# TSUNAMIS: THE RESPONSE OF HARBOURS WITH SLOPING BOUNDARIES TO LONG WAVE EXCITATION

by
Jeffrey Alan Zelt

W.M. Keck Laboratory of Hydraulics and Water Resources
Division of Engineering and Applied Science
CALIFORNIA INSTITUTE OF TECHNOLOGY
Pasadena, California

Report No. KH-R-47

June 1986

# **Tsunamis**: The Response of Harbours with Sloping Boundaries to Long Wave Excitation

by

Jeffrey Alan Zelt

Project Supervisor:

Fredric Raichlen
Professor of Civil Engineering

Supported by:

National Science Foundation
Grant Numbers CEE79–12434, CEE81–15457,
CEE84–10087

W. M. Keck Laboratory of Hydraulics and Water Resources
Division of Engineering and Applied Science
California Institute of Technology
Pasadena, California

Report No. KH–R–47 June 1986

## Acknowledgements

I am indebted to many talented individuals who provided invaluable assistance throughout all phases of this research project.

I would like to thank my advisor, Fredric Raichlen, for his assistance, encouragement, and for providing me with the necessary academic freedom to pursue this research. I am deeply grateful. I would also like to thank Professor John Hall for many fruitful discussions regarding the numerical modelling in this work. His patience and insight will not be forgotten.

The entire staff of the W.M. Keck Hydraulics Laboratory have been good friends throughout my stay here at Caltech. Special mention is due to Joan Mathews who cheerfully answered all my questions and cleared up every problem I brought to her, large or small. Rayma Harrison and Gunilla Hastrup also lightened my load by providing expert assistance in tracking down obscure references to books and papers needed throughout this project. The assistance and advice of Elton Daly, Rich Eastvedt, and Joe Fontana in the design and construction of the experimental apparatus is also appreciated.

I consider myself very fortunate to have had the opportunity to receive a first class education here at Caltech. In particular, I would like to thank Professors G.B. Whitham and Theodore Y. Wu, for providing me a priceless insight to fluid mechanics. I would also like to thank Lou DeMacedo for teaching me that physics is phun.

This manuscript was typeset with the program TEX on one of many HP 9836C computers donated to Caltech by Hewlett Packard. The numerical work of this

research was performed on an IBM 4341, donated to Caltech by IBM, and on a Floating Point Systems FPS 164, courtesy of Professor Herb Keller.

This study was funded, in part, by the National Science Foundation under Grant Numbers CEE79-12434, CEE81-15457, and CEE84-10087. I would like to thank the Canadian government, who, through the Natural Sciences and Engineering Research Council, provided me with four years of personal financial support.

This report is essentially the thesis of the same title submitted by the writer on May 9, 1986 to the California Institute of Technology, in partial fulfillment of the requirements for the degree of Doctor of Philosophy in Civil Engineering.

# Abstract

The influence of sloping boundaries on the long wave response of bays and harbours is studied in this work. Laboratory experiments are performed to help validate the theoretical analysis which is applicable to nonbreaking waves.

A set of long wave equations in the Lagrangian description is derived which includes terms to account for nonlinear, dispersive, and dissipative processes for wave propagation in two horizontal coordinates. A finite element model is developed based on these equations which is capable of treating arbitrary geometry and the runup of nonbreaking waves on a beach.

An analytical harbour response model, capable of treating narrow rectangular harbours with variable bathymetry and sidewall geometry, is developed and applied to several simple geometries. The model shows that for a given harbour length and entrance width, the resonant frequencies and the response of a harbour are very dependent on the harbour sidewall geometry and bathymetry.

Some of the nonlinear effects of the runup of nonbreaking periodic waves on a plane beach are discussed. In particular, the time average of the water surface time history at a fixed spatial location is negative and the wave crests are smaller than the troughs. Nonlinear effects do not alter the runup maxima or minima and the maximum fluid acceleration occurs at the point of maximum rundown of the wave.

Laboratory experiments were performed to determine the long wave reponse of a narrow rectangular harbour whose still water depth decreases linearly between the harbour entrance and the shoreline. Good agreement with the finite element

model was obtained, including the prediction of the depression of the mean water level within the harbour.

A three-dimensional application of the finite element model treats the runup of solitary waves on a coastline with variable bottom topography and a curved shoreline. The results indicate that the model can predict the trapping of wave energy along a sloping coastal margin, a process of fundamental importance for predicting potential tsunami damage.

# TABLE OF CONTENTS

Chapter Page

Chapter Page

# LIST OF FIGURES

Figure Page

Figure Page

Figure Page

Figure Page

# LIST OF TABLES

# CHAPTER 1

## Introduction

It is well known that undersea seismic activity and certain atmospheric conditions can generate long wavelength surface gravity waves in the ocean. The subset of these waves which are generated by large scale, short duration disturbances are known as "tsunamis" and are generally of seismic origin.

In the deep ocean, typical tsunami wavelengths are 100–400 km. This is very long compared with the average depth of the Pacific Ocean which is about 4 km, and yields deep ocean wavelength-to-depth ratios of 25 to 100. Waves with such length to depth ratios propagate as shallow water waves at a speed $c$ determined by the local water depth: $c = \sqrt{gh}$, where $g$ is the acceleration of gravity and $h$ the water depth; hence, typical propagation speeds are of the order of 700 km/ hr. Given these values of the wavelength and propagation speed, and the fact that tsunami amplitudes in this region of the ocean generally are probably less than 1 m, it is clear that they usually pass unnoticed in the deep ocean and pose no harm at all to ships of any size. The rise and fall of the water surface by a metre, over a period of several minutes, would be masked entirely by the wind generated sea and swell.

However, as a tsunami propagates up the continental slope and across the continental shelf, its amplitude increases and its wavelength decreases as the wave shoals. Through the processes of refraction, diffraction, shoaling and reflection the wave can be greatly distorted as it approaches the coast. Indeed, by the time

a tsunami reaches the shoreline it may bear little resemblance to its appearance in the deep ocean. Its amplitude can grow large enough to cause considerable damage. A tsunami that is practically invisible in the deep ocean can transform into a very menacing threat along the coastal margin. The Japanese coast is particularly susceptible to tsunami attack because Japan's offshore sea bed is geologically prone to tsunamigenic seismic activity and because its coastline is highly populated. In addition, much of its coastline is very irregular, containing many harbours and bays which can amplify and trap long wavelength waves. However, many other areas of the world are also vulnerable to tsunami attack, especially those regions bordering the seismically active Pacific "Ring of Fire." For a historical compilation of the vast number of recorded tsunamis in this region see Soloviev & Go (1974, 1975).

For both economic and social reasons the world's ocean coastlines have historically attracted large populations to live near and to visit for recreation. In addition, a vast amount of capital is invested in nearshore coastal structures and moored ships. Hence, a tsunami attack can be potentially a very devastating event, measured in loss of both life and money.

Over the past one hundred years there has been, on average, approximately one destructive tsunami per year, which has caused loss of life or serious property damage somewhere in the world. The eruption of the Krakatoa volcano on August 27,1883 generated a 30 m tsunami which killed 36,000 people in Indonesia. A strong earthquake, felt in northern Japan on June 15, 1896, also generated a tsunami with devastating consequences. The greatest damage occurred along the Sanriku coast. According to official accounts, over 27,000 people died, more than 10,500 buildings were destroyed and over 9,000 people injured. The water rose 24 m at Yoshihama and a runup of 30 m was recorded at Ryori. In more recent times, a catastrophic earthquake in southern Chile on May 22, 1960 generated

a very large tsunami. About 1000 people were killed in Chile, 60 people in the Hawaiian Islands, and 200 people in Japan. The maximum tsunami runup reported was approximately 20 m in Chile, 10.5 m in the Hawaiian Islands, 6.5 m in Japan and the USSR, and 3.5 m in the United States. In addition to the deaths caused in Japan, the tsunami was also strong enough to move large boats significant distances inland. This is a remarkable feat, considering this is after the tsunami had propagated over 15,000 km across the Pacific Ocean from the southern coast of South America. The tsunami generated by the Alaska earthquake of March 28, 1964 was responsible for at least 121 deaths in Alaska, Oregon, and California. Damage was estimated to be in excess of $100,000,000. The Nihonkai-Chubu tsunami, generated by an earthquake in the Sea of Japan on May 26, 1983, was responsible for 101 deaths in Japan and 3 deaths in Korea. The maximum runup recorded was 14.9 m on Minehama beach in Akita prefecture. Damage along the coast of Japan amounted to more than $800,000,000.

The nearshore bathymetry and coastline geometry are often a crucial factor with respect to the destructive power of a tsunami. In particular, if a tsunami enters an inlet or a man-made harbour which has a natural period of oscillation near the dominant period of a tsunami, its amplitude may be amplified greatly by the process of resonance. In effect, this amplification occurs because a wave which reflects from the head of the basin propagates back offshore toward the sea but has some of its energy reflected at the harbour entrance back into the basin, thereby trapping some of the wave's energy within the harbour. The tsunami amplitude can be greatly enhanced if the trapped waves are in phase with the incident waves entering the harbour from the open sea, resulting in heavy damage to moored ships, coastal structures, and low lying coastal communities. It is not surprising that "tsunami" is a Japanese word which translates to "harbour wave." As an example of this process, consider the town of Port Alberni located 65 km

from the coast at the head of Alberni Inlet on Vancouver Island, British Columbia. Alberni Inlet is connected with the open ocean through Trevor Channel. The town was inundated with waves whose maximum amplitude exceeded 5.2 m generated by the 1964 Alaska earthquake (Murty 1977). However, at the exposed town of Tofino (which does not lie within an inlet or a harbour), only 65 km up the coast, the amplitude never exceeded 2.5 m. The large amplification measured in Alberni Inlet has been largely attributed to resonance. The tsunami contained a significant amount of energy in a frequency band which closely matched a natural oscillation frequency of the combined Alberni Inlet, Trevor Channel waterway (Murty & Boilard 1970 and Thomson 1981).

## 1.1 Objective of this Study

The protection of life and property from tsunami attacks depends primarily on understanding the physical processes involved and on being able to predict both the damage caused by a hypothetical tsunami attack at a given location and the consequences of engineering attempts to help mitigate future losses in the area. Therefore, the hope is that as better models are developed, better decisions can be made to help improve the safety of future coastal developments and to help protect existing ones as well. It is in this spirit that this investigation was carried out. The objective of this study is to investigate the runup of nonbreaking waves on both straight and irregular beaches and to incorporate this process into a comprehensive nonlinear, dispersive, numerical model, which will be capable of predicting the dynamic response of harbours excited by long waves such as tsunamis. The model will handle problems with arbitrary geometry.

The long wave dynamic response characteristics of a harbour are determined largely by its bathymetry, shoreline and entrance geometry. The offshore topog-

raphy exterior to the harbour may also have an influence. Some harbours are bounded by vertical boundaries, or at least have very steep shores which can be approximated by vertical boundaries. It is reasonable to analyze such harbours or bays with long wave models which make the vertical boundary approximation. Such a boundary is relatively easy to incorporate into a model because its location is known. However, if the harbour is bounded by a sloping boundary, the shoreline position is not fixed and will move as waves run up and down the boundary. If the wave amplitude is large, this motion of the shoreline must be handled properly to compute the correct wave field and harbour response. Therefore, for a sloping beach the runup of waves can be an important process that may influence the response of a harbour to long wave excitation. It is a process which must be coupled with a harbour response model to predict quantitative estimates of the wave field within a basin excited by long waves. Perhaps the biggest influence that a sloping boundary can have on a wave field is that the waves may break as they propagate towards the shoreline. This is an exceedingly complex process which can dissipate much of the available wave energy. If this is the case, little energy will be reflected back towards the harbour entrance so resonance is not likely. This investigation will not consider breaking waves. It will be assumed that the slopes of the boundaries are large enough to prevent breaking, although nonlinear runup effects may still be large.

The treatment of moving boundaries in a numerical model cast in the Eulerian description is awkward, though possible. An alternate approach is to cast the model in the Lagrangian description. This is the description most widely used in solid mechanics but it can also be applied to fluid problems as well. In the Lagrangian description material boundaries (such a a shoreline for nonbreaking waves) are fixed with respect to the Lagrangian coordinate system, even though these boundaries may move in the more traditional Eulerian coordinate system.

Therefore, to facilitate the treatment of wave runup along sloping boundaries, it was decided to develop the numerical model in the Lagrangian description. Analytical work and laboratory experiments on wave runup and harbour resonance were also done. These results will be used to test the validity of the numerical model.

## 1.2 Report Outline

In Chapter 2 a review of previous work relevant to this study is presented. Chapter 3 contains the theoretical analysis performed for this investigation. This analysis consists of a derivation of the long wave equations of motion in the Lagrangian description for two horizontal coordinates, a derivation of a harbour resonance model applicable to long narrow harbours with otherwise arbitrary bathymetry and geometry, a presentation of some nonlinear effects associated with wave runup on linear sloping beaches, and finally the development of a nonlinear, dispersive finite element numerical model based on the long wave equations of motion derived earlier in the chapter. The experimental equipment and procedures used in the study are described in Chapter 4. In Chapter 5 finite element model calculations are compared with both the analytical theory of Chapter 3 and the results of laboratory experiments outlined in Chapter 4. The major conclusions drawn from this investigation are presented in Chapter 6. Appendix A contains a simplified derivation of the nonlinear, nondispersive, long wave equations of motion in the Lagrangian description that is based on physical and geometrical reasoning.

# CHAPTER 2

## Literature Review

Accounts of coastal tsunami damage can be traced back more than two thousand years. Many of these old records give highly detailed qualitative descriptions and most are of great statistical interest to scientists and engineers. However, it is only in the past 50 years or so that careful scientific measurements and investigations have actively addressed the tsunami problem. According to Van Dorn (1965) modern tsunami research began in Japan, following the tsunami generated by the Sanriku earthquake of March 3, 1933. More than 3,000 residents died and more than 6,000 structures and 12,000 boats were washed away and destroyed (Soloviev & Go 1974). Since then, a large body of work has been compiled on the generation and propagation of tsunamis. No attempt will be made to offer an exhaustive review of previous work in this field. For a general survey of tsunami related topics see Wiegel (1964), Van Dorn (1965), and Carrier (1971). For a compilation of more recent work see Hwang & Lee (1979), and Iida & Iwasaki (1983). Previous reviews and further references related to the excitation of harbours and bays by long waves can be found in Raichlen (1966, 1976), Wilson (1972), Miles (1974), and Lepelletier (1980).

This review will be limited to previous work on wave-induced oscillations in harbours or bays and on runup studies that have relevance to this topic. The literature which strictly relates to harbour or bay oscillation and does not consider runup will be reviewed first. This literature will be further divided into linear and

nonlinear studies. Then the literature on wave runup with relevance to harbour oscillations will be covered. It will be divided into three groups, reflecting the different techniques used to to study this process.

## 2.1 Harbour Oscillations

Many early methods for treating wave propagation were based on ray techniques borrowed from linear geometric optics theory. These techniques are well suited to treating problems with arbitrary geometry. However, without significant modification they cannot treat diffraction or reflection from objects or shorelines. In addition, they cannot quantitatively predict runup. Therefore, these methods are not directly applicable to harbour oscillation studies, so the related literature will not be reviewed. In the next section literature related to studies of harbour or bay oscillations that neglected nonlinear effects will be reviewed. Then, following that, literature related to studies which did include nonlinear effects will be reviewed.

### 2.1.1 Linear Investigations

Early work on oscillations in harbours or bays made the assumption that at resonance either a node or an antinode existed at the mouth, depending on the entrance geometry. This imposed a constraint on the coupling between the basin and the exterior body of water. Unless viscous losses were included, the wave heights within the basin could grow unbounded, since energy was prevented from escaping from the harbour or bay at resonance. This problem was solved by Miles & Munk (1961), who investigated the coupling of a harbour to the open sea. They specialized their theory to treat long wave harbour oscillations induced through the entrance of a constant depth rectangular harbour. By modelling the

process by which energy is radiated out of the harbour through the entrance to the open sea, they showed that the amplitude within the harbour was finite even at resonance. They were also able to compute the effect of changing the width of the entrance on the wave amplitude in the harbour. They found that as the entrance width was reduced to zero, the response of the harbour increased without bound at resonance. The authors named this effect the "harbour paradox." This apparent paradox arose because viscous dissipation at the mouth of the harbour was neglected. If this is properly accounted for, the wave amplitude remains bounded as the entrance width is reduced to zero, even at resonance, and the paradox is resolved.

Ippen & Raichlen (1962) looked at the problem of simulating the open sea in laboratory studies. They conducted experiments to study the response of a small rectangular harbour connected to a large, highly reflective rectangular wave basin. They found that there was a high degree of coupling between the small harbour and the outer basin. They obtained a large number of closely spaced spikes in the harbour response curve, much different than the peaks associated with the resonant modes of a rectangular harbour connected to the open sea. Their observations agreed fairly well with a simple theoretical model they developed, except near resonance, since nonlinearities and viscous losses were not considered. Their work stressed the need for using efficient wave absorbers and filters to accurately simulate the open sea in small experimental wave basin facilities.

Ippen & Goda (1963) studied experimentally the response of a constant depth narrow rectangular harbour connected to the open sea, using deep water waves. They also developed a linear dispersive theoretical model which agreed reasonably well with the experiments, provided they installed efficient wave absorbers in the wave basin to simulate the open ocean exterior to the harbour. Although they did introduce a correction factor for laminar viscous losses in the boundary layers along

the side walls, they did not account for energy dissipation due to the formation of eddies at the harbour entrance, so their theory tended to overpredict the harbour response at resonance.

Both Lee (1969, 1971) and Hwang & Tuck (1970) studied linear inviscid harmonic harbour oscillations using boundary integral techniques to solve the Helmholtz equation. Both models treated arbitrary harbour geometry but were limited to domains with constant water depth. Lee's method expresses the solution as a distribution of sources and dipoles along the boundary, whereas Hwang & Tuck used only sources. Hwang & Tuck compared their model to the theory of Ippen & Goda (1963) for a narrow rectangular harbour connected to the sea and found good agreement, although their model predicted a larger response at resonance than Ippen & Goda's theory. At the first resonant mode the difference was approximately 12%. They also presented numerical results for an arbitrary shaped bay. Lee compared his numerical model to analytical solutions and also to experimental results for both a narrow rectangular harbour and for a circular harbour. He obtained good agreement, although near resonance his numerical and analytical theory overpredicted the amplification within the harbour. This is likely because his did not model viscous losses, especially near the harbour entrance where flow separation can occur. He also constucted a model of the East and West Basins of Long Beach Harbour, Long Beach, California. His experimentally determined harbour response characteristics agreed quite well with the predictions of his numerical model.

Olsen & Hwang (1971) presented a linear nondispersive numerical technique for investigating long wave oscillations in a bay or harbour. They combined a finite difference solution of the Helmholz equation within the bay with an open sea integral solution outside the bay. Variations in depth could be treated but the bay was bounded by vertical walls. Arbitrary planform geometry within the

bay was treated by approximating the boundary by straight line segments of the grid system. Thus, normal boundary derivatives were in only one of the two coordinate directions. They compared their results with field data available for Keauhou Bay, Hawaii. Their model showed general agreement with the field data but there were some discrepancies for the lower frequencies which they attributed to shelf resonance and edge wave effects.

Chen & Mei (1974) developed a linear inviscid nondispersive hybrid finite element model for treating arbitrary planform geometry and variable water depth. They used the model to study the steady-state harmonic response characteristics of an offshore harbour. The domain of the problem was divided into an inner and an outer region. In the inner region, the solution was obtained using standard finite element techniques. In the outer region, the solution was represented as the sum of a known incident wave and a radiated wave expressed as a series solution. The outer analytic solution was matched to the inner finite element solution along their common boundary. In addition, the model could treat sharp-ended breakwaters by expressing the solution in a small region around the breakwater tip as a series solution and then matching it with the finite element solution along their common boundary.

Houston (1978) studied the interaction of tsunamis with the Hawaiian Islands. Using sea floor deformation estimates for both the 1960 Chilean earthquake and the 1964 Alaskan earthquake, he used a numerical model to generate the resulting tsunamis and to propagate them across the Pacific Ocean to determine their deep water signatures near the Hawaiian Islands. He used this information as input to a linear nondispersive hybrid finite element model modified from Chen & Mei (1974). He reported good agreement with tide gauge records from the actual events at several different locations. This indicated that nonlinear and dispersive processes may not have played a large role in the interaction of the tsunamis with

the Hawaiian coast at the locations studied.

Behrendt, Jonsson & Skovgaard (1983) modified the finite element model of Chen & Mei (1974) to include an absorbing boundary condition. This boundary condition was used to simulate the full or partial absorption of wave energy along a boundary, presumably by wave breaking. The boundary condition corresponded to the simple admittance radiation condition for plane progressive waves in water of constant depth, although they introduced a parameter to vary the amount of transmission and reflection. Even though the boundary condition was based on plane waves propagating in water of constant depth, they applied it to more general conditions, so its physical significance is difficult to assess theoretically. They did not comment on how one could choose the adjustable parameter to simulate real boundary dissipation mechanisms. However, their work does reflect the need to incorporate boundary dissipation in tsunami models, especially if the waves break. They also investigated the effect of varying the angle of the incident waves. They found that even though the amplitudes in the open sea were heavily influenced by the angle of incidence, the response of the harbour was relatively insensitive to it.

### 2.1.2 Nonlinear Investigations

Most of the linear numerical models reviewed in the previous section computed steady-state harmonic solutions. More general cases could be treated using Fourier superposition. However, nonlinear problems cannot be solved with simple Fourier superposition (except for certain spectral methods). Therefore, nonlinear problems are generally solved in the time domain with a time-marching scheme.

Leendertse (1967) developed a nonlinear nondispersive finite difference model to treat the propagation of long waves. Friction was modelled by a bottom stress

proportional to the square of the velocity. The model results were often very sensitive to the choice of the friction coefficient. In those cases the friction coefficient had to be determined iteratively by comparing the computed results with field measurements. A weakness of the model was that the surface displacement time history had to be completely specified along a boundary of the domain. Therefore, waves reflected or scattered from boundaries could not leave the solution domain unless their time histories were known *a priori*. In general, these time histories are not known, since they are part of the solution to be computed.

Peregrine (1967) derived equations of motion in the Eulerian description for long waves propagating in water of varying depth in two horizontal space dimensions. His derivation retained terms which modelled the effects of nonlinearities and of frequency dispersion. As an example, he computed numerically the climb of a solitary wave on a beach of uniform slope. However, he terminated the simulation before the wave reached the shore, so no runup information was obtained. A method similar to Peregrine's will be used in this work to derive a set of nonlinear dispersive long wave equations in Lagrangian coordinates.

Iwagaki & Murakami (1972) performed laboratory experiments to investigate the response of a narrow constant depth rectangular harbour excited by perodic nonharmonic long waves. Incident waves were generated which contained three, two, or just one main harmonic component. They found that the resonant characterisics of the harbour for the composite waves were different from that obtained by linearly superimposing the resonant characteristics for each of the harmonic components of the composite waves. They concluded that the differences were due to nonlinear interactions between the different harmonics in the composite waves.

Houston & Garcia (1978) used model of Leendertse (1967) to predict the 100 and 500-year runup elevations along the west coast of the continental United

States. The generation and deep ocean propagation of the tsunami generated by the 1964 Alaskan earthquake was simulated by a linear nondispersive long wave model described by Houston & Garcia (1974). It was originally developed by Hwang, Butler & Divoky (1972). The output of this model was used as input to the model of Leendertse to compute the detailed nearshore propagation. The coastal boundary was treated as a perfectly reflecting vertical wall. It was assumed that the tsunami runup heights would be equal to the coastline wave elevations. For steep beaches this is a good assumption, but clearly this may be only a crude estimate for more gently sloped beaches.

Rogers & Mei (1978) studied steady-state nonlinear resonant excitation of a long and narrow rectangular bay of constant depth. They argued that the radiated wave away from the bay entrance was small enough to allow a linear analysis of the motion in the open ocean outside the bay. Within the bay they used weakly nonlinear equations of the Boussinesq class. They restricted their analysis to one-dimensional wave motion within the harbour, since two-dimensionality was only important in the immediate vicinity of the bay entrance. They also performed laboratory experiments with three bays of different lengths, corresponding to the first three linear resonant modes. They found that at resonance nonlinearities tended to decrease the amplitude of the fundamental harmonic as energy was spread to higher harmonics. The nonlinear generation of higher harmonics led to additional resonant peaks in the harbour response curve. They also showed that nonlinear effects produced a mean setup at the backwall; i.e., the mean water level at the backwall was positive. From their calculations and experiments they concluded that for a short bay entrance losses may be more important than intrinsic nonlinear effects, but for long bays the reverse is true. However, it should be noted that their laboratory experimental conditions were such that the dispersive effects were probably stronger than the Boussinesq equations are capable of treating ac-

curately. Hence, the validity of some of their comparisions between theory and experiment may be questionable.

In the linear harmonic numerical models reviewed in the previous section the open ocean could be treated by expressing the radiated portion of the solution as a sum or integral over a particular set of singular solutions. This has the physical interpretation of expressing the radiated solution as either a superposition of point source wave solutions along a two-dimensional curve or as a superposition of multipole wave solutions at a single point in space. Unfortunately, the expressions for the multipole solutions are frequency dependent, so this technique to simulate the open sea cannot be used easily in the time domain. A different approach is needed. The technique most widely used is to specify a radiation boundary condition at the outer boundary of the domain to allow the radiated wave to pass out of the solution domain without reflecting back in to contaminate the solution. Mungall & Reid (1978) derived and numerically experimented with a boundary condition of this type using a linear finite difference model. It permitted radially propagating long waves to pass freely through the outer boundary of a domain. They found it was very effective provided the boundary condition was not applied too close to the point where the waves were generated. Although the boundary condition applies to radially spreading waves, they obtained good results using a rectangular domain. The boundary condition is linear, but if it is applied sufficiently far from the source of the waves it can be applied to nonlinear problems as well. Hebenstreit & Reid (1980) and Hebenstreit, Bernard & Vastano (1980) modified the linear model of Bernard & Vastano (1977) to include this boundary condition. Lepelletier (1980) successfully implemented the boundary condition in his numerical model. The same boundary condition will be used in this work as well, although in a form suited to the Lagrangian description.

Wu (1979,1981) developed a nonlinear dispersive shallow water theory in two

horizontal coordinates. Starting with three "layer-mean-transport" equations representing the conservation of mass and horizontal momentum, he obtained three coupled long wave equations of the Boussinesq class. These were valid, in particular, for Ursell numbers of $O(1)$. Solutions of these equations were slightly rotational (if the still water depth was not constant). Therefore, the horizontal fluid velocity could not be expressed in terms of a standard velocity potential. However, by introducing a *depth averaged* velocity potential he was able to reduce the three equations of motion down to a *single* equation involving this pseudopotential. This was important from a numerical point of view since only a single scalar field needed to be computed. After the pseudo-potential was determined, the two components of velocity and the water surface displacement could then be computed, although they were not needed explicitly in the formulation.

Lepelletier (1980) extended the equations of Wu (1979, 1981) slightly by including a term to account for viscous losses in a thin boundary layer along the bottom and along a free surface contaminated with surfactants. Lepelletier's model was based on the finite element technique and could treat problems with arbitrary geometry, although his formulation could not treat moving boundaries and hence was not directly applicable to runup studies. He looked in detail, experimentally and numerically, at the response of a constant depth long narrow rectangular harbour excited by periodic and transient nonlinear long waves. He found that if the wave length of the incident waves was greater than four times the harbour length, then nonlinearities had little effect on the response characteristics of the harbour. However, for smaller wavelengths he found that a nonlinear dispersive theory was necessary to get good agreement with experimental results, especially at resonance. His numerical model also predicted secondary resonant peaks in the response curve of the harbour, which were not predicted by linear theory. These were confirmed by experiments. He also looked briefly at the transient response

of three long narrow harbours: 1) rectangular with a constant water depth, 2) rectangular with a depth that decreased by a factor of two linearly from the mouth to the backwall (the backwall was vertical), and 3) trapezoidal with a constant depth. Agreement between the experiments and the model was good. As a practical application of his model, he simulated the response of Ofunato Bay, Japan, to a tsunami. Raichlen, Lepelletier, & Tam (1983) used the model to determine the long wave response of Hilo Harbour, Hawaii. Lepelletier stressed that viscous losses due to flow separation at the entrance of a harbour were very important, especially if the entrance is partially blocked by a breakwater. An accurate treatment of this process in a model is difficult, and he suggested that further work on this topic was warranted.

Most studies of oscillations in bays or harbours have approximated the open ocean outside the bay or harbour by a region where the still water depth is constant. In many cases this may be a reasonable approximation, but often the depth variations are not so simple and, in fact, there may be large depth variations, particularly if the continental shelf is narrow. Noiseux (1983) looked at the effect of depth variations near the mouths of very idealized harbour-like geometries on the transmission properties of wave radiation from a cavity into an outer region. Using linear nondispersive theory, he showed that there are combinations of planforms and depth variations for which the wave energy in selected modes would not leak out. In addition, for more realistic geometries the trapping of energy within the cavity can still be effective, resulting in very large $e$-folding times for some modes. Therefore, he stressed that the offshore depth variations may also be important in determining the resonance characteristics of a bay or harbour, in addition to the geometry of the harbour itself.

## 2.2 Runup Models

The runup of waves on a sloping beach is an exceedingly complex process. For that reason most models that deal with this process are numerical in nature and rely heavily on the use of computers. A notable exception to this is the elegant work of Carrier & Greenspan (1958). They showed that it is possible to transform the nonlinear nondispersive shallow water equations for one horizontal coordinate into a *single linear* differential equation for the case where the still water depth increases linearly offshore. Using this transformation they were able to show that there exist solutions that can climb a sloping beach without breaking. Later, Spielvogel (1975) used the Carrier & Greenspan transformation to look at the nearshore amplification of tsunamis.

The runup of waves on sloping boundaries is generally more difficult to incorporate into models than the more traditional boundary condition for vertical boundaries where the normal mass flux is zero. Many different techniques have been proposed to treat this problem. The simplest technique is to introduce an imaginary vertical barrier near boundaries, which otherwise would experience a moving shoreline. The water depth at this barrier is always nonzero. The position of the shoreline can then be approximated by a horizontal inland extrapolation from the wave height at this barrier. If the actual shoreline is steep, then such an approximation can be reasonable. However, for large shoreline motions or for gradually sloped beaches this approximation can obviously lead to poor estimates of tsunami runup or inundation. The geography above the still shoreline may influence significantly the runup process. In addition, both mass and momentum are not conserved by such extrapolations (Lynch & Gray 1978).

In this section literature will be reviewed on studies that treat shoreline motions by more sophisticated techniques. These techniques will be divided into three

categories: 1) Eulerian techniques which use fixed numerical grids or meshes, 2) Eulerian techniques which use deforming meshes, and 3) various Lagrangian techniques. Certainly this does not cover all possible techniques investigators have used to model runup, and some models may combine aspects of all three of these, but for the purpose of reviewing the literature these three divisions are convenient.

### 2.2.1 Eulerian Techniques With Fixed Grids

Eulerian techniques that make use of fixed grids or meshes usually treat moving shorelines by turning cells or elements on and off at the boundary, using techniques that conserve mass. They are simpler to implement than techniques that make use of deforming meshes, but they possess other problems. Often the impulsive filling of a cell with fluid can lead to numerical problems unless treated very carefully.

Keller & Keller (1964, 1965) investigated the runup of waves in one horizontal coordinate. They looked at the propagation of time harmonic waves through water of slowly varying depth and derived an expression for the height of a wave at the shoreline given its offshore wavelength, the offshore depth (which may be infinite), and the nearshore beach slope. The analysis was based on linear dispersive theory and was applicable to small beach slopes. They also developed a nonlinear nondispersive finite difference model to treat long wave runup for a single horizontal coordinate. It was based on a fixed grid system, although the exact shoreline position was tracked between the fixed grid points. The model was used to investigate the runup of periodic waves on a uniformly sloping beach. Finally, by combining the theory of weak shock waves with the nonlinear nondispersive shallow water theory they studied analytically the formation and growth of bores on a beach. However, because of the weak shock approximation, the analysis was

not valid at the shoreline.

Reid & Bodine (1968) investigated transient storm surges in Galveston Bay, Texas. They developed a finite difference numerical model based on the linear nondispersive long wave equations, with corrections for rainfall, windstress, and bottom friction. The elevation of the sea bed or of the land was represented by a square grid. The elevation over each grid square was assumed to be constant. Hence, the actual topography was approximated in a stair-step fashion. If the elevation of the water in a flooded square was less than the base elevation of an adjacent dry square, then a zero normal flow boundary condition was applied along their common boundary. However, if the water elevation in a flooded square was *greater* than that of an adjacent dry square, then water was permitted to flow into the dry square. The flow rate between the two squares was determined using an empirical equation for flow over a broad-crested barrier. The overtopping of a barrier (e.g., a sea wall) could be treated also. The model could treat only barriers aligned along the grid mesh divisions. The flow across the barrier was permitted when the water height on one side exceeded the barrier height. If the water height exceeded the barrier height on both sides, then the flow rate was determined using an empirical equation for flow over a submerged weir. The empirical coefficients in the model were determined by iteration, comparing the model with tide data and data from hurricane Carla (September 9–12, 1961). The model was then compared with field data from hurricane Cindy (September, 16–17, 1963). The gross features of the inundation were predicted reasonably well. This model is also applicable to tsunami inundation studies elsewhere in the world, although they did not consider this application. It should be remembered that the empirical coefficients used could be very site-dependent, however.

Xanthopoulos & Koutitas (1976) described a nonlinear finite difference model to study two-dimensional flooding from a dam failure. They assumed a hydrostatic

pressure distribution and neglected the inertial terms in the momentum equations. Thus, pressure gradient forces were balanced entirely by viscous boundary stress forces. They used a fixed rectangular mesh. The shoreline was defined to within the accuracy of one mesh cell. However, they did not describe the details of how these cells were turned on or off. They found that the model could be calibrated using one-dimensional data from laboratory dam break experiments for small initial water heights. However, the accuracy of the model greatly decreased as the initial height of water behind the dam was increased. This is presumably because the unsteady inertial terms in the momentum equation were neglected. The force balance used in this investigation is too restrictive to study the runup and inundation of tsunamis. In order to apply the techniques outlined in this work to tsunamis, the inertial terms would have to be accounted for except, perhaps, at the extreme tip of the runup tongue where the water depth is very shallow and viscous forces can dominate inertia effects.

Yeh & Yeh (1976) described a nonlinear nondispersive numerical model for simulating storm surge. The shoreline in the numerical model moved as the flow inundated low lying land. However, the details of the treatment of this boundary are not given. It appears that the shoreline advanced or retreated in discrete increments of grid cells rather than deforming continuously. They reported good agreement with field data.

Yeh & Chou (1979) developed a nonlinear finite difference surge model. It operated with reference to a fixed rectangular grid system. The shoreline location always coincided with a grid line. Therefore, the shoreline moved in discrete jumps. A new grid point was added to the computations if the surge elevation of any of its neighbours was above the base elevation of that grid point. A slightly more complicated scheme was used to remove the grid point from the calculations during rundown. They compared the model to field results and also with a similar

numerical surge model, which used a fictitious vertical wall instead of a sloping shoreline. They reported that their model showed much better agreement with field data than the fixed boundary model. The fixed boundary model predicted up to 30% higher surge levels than their moving boundary model. The discrepancy was greatest for higher surge values. They explained the descrepancy as being due to the storage effect of the inland region where water can accumulate but which is not part of the computational domain of the fixed boundary model.

Houston & Butler (1979) developed a linear nondisperive tsunami inundation model very similar to that of Reid & Bodine (1968), although Houston & Butler slightly generalized the grid system so that variable sized rectangular cells could be used to represent the topography. Houston & Butler calibrated their model using data recorded from the 1964 Alaskan tsunami in Crescent City, California. The model was then used to predict the 50 and 100-year tsunami runup heights expected in the Hauula-Punaluu region of the Island of Oahu, Hawaii.

Tanaka, Ono & Ishise (1980) developed a nonlinear finite element model which treated tsunami runup and wave overtopping of barriers. The moving shoreline was simulated by adding entire wet elements into the domain of the problem as the shore advanced or by removing dry elements as it receded. The rate of flow into a wet element was determined from an empirical equation. Hence, a flux boundary condition specifying the volume flow rate was applied along the shoreline boundary as it advanced or retreated in discrete steps. However, a fixed finite element mesh was used along boundaries where wave overtopping was simulated. The overtopping flow rate was determined from an empirical equation based on the wave height at the barrier. This flow rate was then used as a flux boundary condition at that point.

### 2.2.2 Eulerian Techniques With Deforming Grids

Very little work with numerical methods that use deforming grids has been applied to long wave runup. This technique tends to be more complicated than methods that use fixed grids. However, the additional work can lead to models that more accurately treat the motion of the fluid near the shoreline.

Lynch & Gray (1978, 1980) outlined a general technique whereby moving boundaries can be treated by finite element Eulerian models. The finite element basis functions are chosen to be functions of time so that the element boundaries track the moving shoreline. They showed how this motion generates extra terms which, if treated properly, reduce the problem to one that can be treated by standard finite element procedures. They showed how to apply the method to treat the propagation and runup of long waves. They looked at two very simple problems involving the runup of waves on plane beaches. The results of these examples did not offer any new insights into the runup process. However, they did show that estimating the runup by extrapolating the wave height at a vertical wall could introduce significant errors. Treating deforming elements is more computationally expensive than fixed ones so they stressed that, in general, one would like to keep elements away from the shoreline fixed, while allowing the ones near and at the shoreline to freely deform. However, they did not offer a method to determine which elements should deform and which should not. Such a problem does not occur in Lagrangian models since *all* fluid particles are free to move. They also recognized the potential problem that can arise if the mesh becomes too geometrically distorted. Should that problem arise, they recommeded that the solution domain be remeshed, even though such an algorithm is generally quite difficult to implement. Although the meshes used for Lagrangian models do not deform, distortion problems can still arise in these models, especially if there exists a mean

flow with shear.

Gopalakrishnan & Tung (1980, 1983) described a nonlinear long wave finite element runup model valid for one horizontal dimension. The model contained terms that accounted for vertical accelerations. The moving shoreline was handled by allowing the shoreline element to deform so that the beach node always tracked the shoreline. If the shoreline element became too "stretched," it split into two elements. The element containing the shoreline node continued to deform but the other new element created by the splitting stayed fixed. From the results of their model they reported that before a positive disturbance reached the beach the shoreline first receded a little before it advanced. They reported that the model could treat the transformation of a solitary wave on a beach into a bore, although they showed no results. They also reported a curious behaviour of the shoreline near the maximum runup point as predicted by their model for the case of periodic waves. As the shoreline approached the maximum runup point, it first receded a little and then continued up to the maximum runup point. They did not show any plots that detailed the rundown process. Presumably, as the shoreline element was compressed during rundown, an element could have been removed from the computations by a process opposite to the one used to split the element on runup. However, no mention of this process was made. There was no reason to expect that the rundown profiles would look the same as the runup profiles for the cases they treated. Therefore, although the technique outlined by the authors seems applicable to tsunami runup, they did not present a thorough or a convincing argument to show that their model could be used reliably for such studies. It should be noted that the techniques in this work cannot be extended easily to include two horizontal dimensions since the element-splitting procedure would be very complex. For example, it would not work well for rectangular elements unless all the shoreline elements split simultaneously.

### 2.2.3 Lagrangian Methods

Lagrangian methods are more suited to treating moving physical boundaries than are Eulerian techniques. In Lagrangian techniques the fluid is represented as a large number of fluid particles that move with the local fluid velocity. Tracking these particles up a beach slope is generally no more difficult than tracking them out in the bulk of the fluid.

Heitner (1969, 1970) and Heitner & Housner (1970) developed a nonlinear model for wave runup based on a Lagrangian method. Heitner's formulation treated only plane waves propagating on water of constant depth or on a linearly sloping beach. His theory included terms representing the kinetic energy of vertical motion. This introduced frequency dispersion and allowed permanent wave solutions over a flat bottom to be computed. By introducing an artificial viscosity term he was able to model the formation and propagation of bores. Although the run*up* of a bore could be examined, the technique had difficulties treating the subsequent run*down* for large waves. If the rundown problems could be solved, his technique might also have application to modelling harbour oscillations.

Shuto (1967) showed how the linear nondispersive long wave equations in the Lagrangian description for one horizontal dimension can be obtained from the exact Lagrangian expressions for mass and momentum conservation. He used these long wave equations to study theoretically the runup of nonbreaking small amplitude long waves on a linearly sloping beach. He compared the theory with laboratory experiments and obtained reasonable agreement for the range of parameters he considered. Shuto (1968) later extended the theory to include two horizontal coordinates but he did not apply it to a problem. Shuto (1972) used the inviscid linear nondispersive Lagrangian long wave equations to study theoretically the runup of periodic waves on a linearly sloping beach joined to a region of

constant depth. The aim of the investigation was to study the runup height and bottom pressure distribution for waves reflecting from a sloping dike. By applying a simple wave breaking condition proposed by Miche (1944) he reported reasonable comparison with laboratory experiments for the wave height at breaking and the reflection coefficient from the dike. Shuto & Goto (1978) developed a simple linear nondispersive finite difference model based on the long wave Lagrangian equations of motion for one horizontal spatial coordinate. It could treat arbitrary water depth. They computed the runup of a harmonic wave on a sloping beach connected to a channel of constant depth (similar to the theoretical work of Shuto 1967, 1972). Their results compared well with the theoretical work of Keller & Keller (1964, 1965). They also used the model to simulate the runup of a tsunami on a beach on the Sanriku Coast, Japan. The purpose of the simulation was to show that more general cases could be treated by their model, but no conclusions could be drawn from their results.

The theoretical work of Shuto (1967, 1968, 1972) and Shuto & Goto (1978) was based on the linear long wave equations in the Lagrangian description. It should be noted that if finite displacement (nonlinear) effects are neglected, there is no fundamental difference between the Lagrangian and Eulerian descriptions. By neglecting the finite amplitude effects, one assumes tacitly that all quantities computed may be evaluated at the equilibrium positions of the fluid particles.

Goto (1979) derived a set of nonlinear nondispersive long wave equations in the Lagrangian description for one horizontal coordinate. Using an explicit finite difference method, he computed the runup of a nonbreaking periodic wave on a linearly sloping beach and reported approximately a 10–20% difference between the linear and nonlinear results. Goto & Shuto (1980) extended the theory to treat two horizontal dimensions. They used a simple finite difference scheme to study the runup of the Meiji Sanriku Tsunami of 1896 in Okkirai Bay, Japan.

They reported good agreement with some of the high water marks recorded in 1896. However, since no wave records of the incident tsunami exist, input to the model was obtained from estimates of the ocean bottom motion caused by the earthquake. Reconstruction of historical tsunamis by this technique is difficult. Therefore, it is difficult to ascertain the accuracy of a runup model that uses such estimates for input.

Pedersen & Gjevik (1983) developed a finite difference numerical model based on a Lagrangian description which was capable of studying the runup of long waves on a beach. The model was based on a set of Boussinesq-type equations, which included both nonlinear and dispersive terms. The model was based on only a single horizontal coordinate, but it could treat the propagation of waves in a channel of slowly varying cross-sectional area. The authors treated the case of the propagation of a solitary wave down a constant depth channel connected to a uniformly sloping beach. They reported that the results compared very well with the experiments of Langsholt (1981). Although the model could not treat breaking waves, they reported that it did predict the formation of a bore during the backwash of the wave, in agreement with Langsholt's experiments.

# CHAPTER 3

# Theoretical Analysis

## 3.1 The derivation of the Long Wave Equations in the Lagrangian Description

In the more traditional Eulerian approach to fluid mechanics the fluid flow is described by a set of field variables, which are considered to be functions of the time $t$ and three spatial coordinates $(x, y, z)$. For any fixed value of $t$ these functions define the fluid motion at that instant at all points in space occupied by the fluid. Similarly, if we fix $(x, y, z)$ these functions describe the time history of the fluid motion at a fixed point in space. For most applications this is the preferred description because it is the easiest and most convenient description to attack a fluid flow problem with either numerical or analytical methods. For most problems the fluid occupies a given fixed domain over which $(x, y, z)$ ranges and over which the solution is sought. However, if this domain is not fixed but varies with time in an unknown manner (i.e., if the domain of the problem depends upon the solution itself), then a fluid mechanical description in Eulerian coordinates becomes awkward. This type of domain behaviour occurs when nonlinear (finite displacement) effects are included in the runup of long waves on a beach. As the waves wash up and down the beach, the two-dimensional horizontal domain of the fluid changes. One boundary of the fluid is the shoreline and this moves with time in a manner that depends upon the solution itself. Therefore, one cannot first

determine the domain of the problem and then the solution. The two must be found together simultaneously.

However, in the Lagrangian description all fluid variables are considered functions of the time $t$ and three variables $(a, b, c)$, which serve to label a particle of fluid. The idea is that one follows infinitesimal particles of fluid and observes how the fluid functions vary in time as they move about. In general, the quantities $a, b, c$ may be any three quanities that identify a particle and that vary continuously from one particle to the next. In this work $(a, b, c)$ will be defined to be the spatial coordinates of the particle at the time $t = 0$. Thus, for any fixed value of $t$ the fluid functions define the fluid motion for all the particles of fluid and if we fix $(a, b, c)$, then these functions describe the time history of the fluid motion as we follow a particular fluid particle. Since the $(a, b, c)$ domain of a problem represents all the initial coordinates of the fluid particles, it is fixed, whether the physical boundaries of the domain move or not. Hence, the Lagrangian description is suited to problems with moving boundaries. That is the motivation for developing a set of long wave equations of motion in the Lagrangian description.

It is expected that the average reader has had more experience and is more comfortable with the Eulerian description of fluid motion. Therefore, rather than simply state these 3-D equations in the Lagrangian description let us first review the equation of motion in the Eulerian description and then use these to derive the corresponding 3-D equations in the Lagrangian description. It is hoped that in this way the reader will feel more comfortable with this alternate description of the fluid motion. Finally, from these 3-D equations in the Lagrangian description we will derive the long wave equations in the Lagrangian description for two horizontal dimensions. For a less rigorous (but more intuitive) derivation of the long wave equations, the reader is referred to Appendix A.

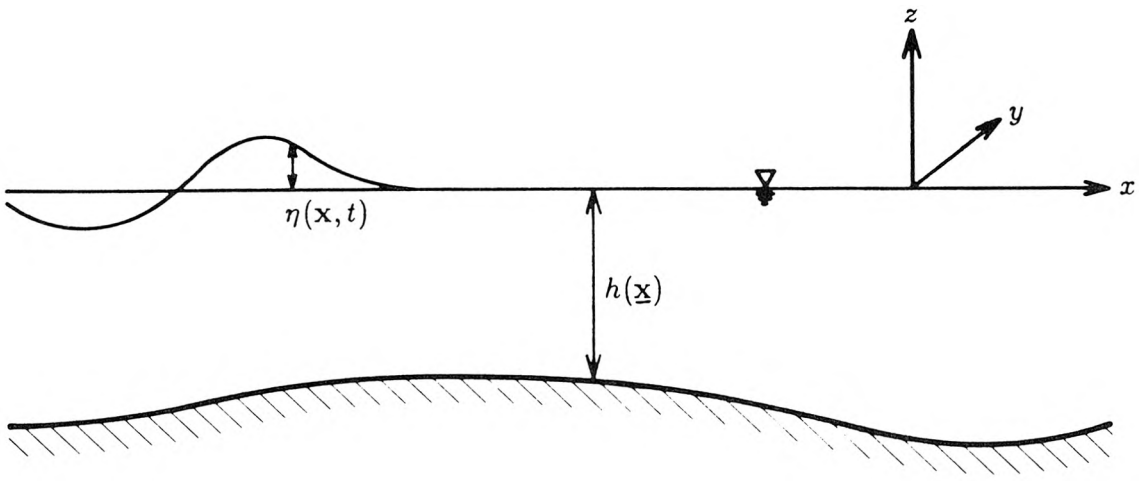


Fig. 3.1.1 Definition sketch of the Eulerian variables.

### 3.1.1 Review of the Three-Dimensional Eulerian Equations of Motion

In the Eulerian system we will denote the independent spatial coordinates by $(x_1, x_2, x_3) = (x, y, z) = \mathbf{X}$. The coordinates $(x, y) = \mathbf{x}$ are in the horizontal plane and $z$ is positive upwards from the still water level. In the analysis which follows, boldface Roman letters will be used to denote vectors. Uppercase bold letters will refer to three-dimensional vectors (i.e., $\mathbf{X}$) and lowercase bold letters will denote the vector whose components are the two horizontal components of the corresponding three-dimensional vector (i.e., $\mathbf{x}$). The still water depth is $h(\mathbf{x})$. The unknowns to be solved for are the vertical displacement of the water surface above the mean water level $\eta(\mathbf{x}, t)$, the pressure $p(\mathbf{X}, t)$, and the three components of velocity parallel to the three coordinate axes $u_1(\mathbf{X}, t) = u$, $u_2(\mathbf{X}, t) = v$, and $u_3(\mathbf{X}, t) = w$. Let $\mathbf{U} = (u, v, w)$ and $\mathbf{u} = (u, v)$. See Fig. 3.1.1 for a sketch defining the geometry. If we assume that the fluid density $\rho$ is con-

stant, the continuity and momentum equations can be written as:

$$\nabla_{\mathrm{E}} \cdot \mathbf{u} + \frac{\partial w}{\partial z} = 0 \tag{3.1.1}$$

$$\frac{\partial \mathbf{u}}{\partial t} + \mathbf{u} \cdot \nabla_{\mathrm{E}} \mathbf{u} + w \frac{\partial \mathbf{u}}{\partial z} = -\frac{1}{\rho} \nabla_{\mathrm{E}} p_d + \nu \left( \nabla_{\mathrm{E}}^2 \mathbf{u} + \frac{\partial^2 \mathbf{u}}{\partial z^2} \right) \tag{3.1.2a}$$

$$\frac{\partial w}{\partial t} + \mathbf{u} \cdot \nabla_{\mathrm{E}} w + w \frac{\partial w}{\partial z} = -\frac{1}{\rho} \frac{\partial p_d}{\partial z} + \nu \left( \nabla_{\mathrm{E}}^2 w + \frac{\partial^2 w}{\partial z^2} \right) \tag{3.1.2b}$$

where

$$\nabla_{\mathrm{E}} = \left(\frac{\partial}{\partial x}, \frac{\partial}{\partial y}\right) \qquad \mathrm{E} \leftrightarrow \text{Eulerian},$$

$p_d$ is the dynamic pressure defined by $p_d = p + \rho g z$, $\nu$ is the kinematic viscosity of the fluid, and the subscript $\mathrm{E}$ refers to the Eulerian description. Let us denote the three-dimensional gradient operator by ${}_3\nabla_{\mathrm{E}}$:

$${}_3\nabla_{\mathrm{E}} = \left(\frac{\partial}{\partial x}, \frac{\partial}{\partial y}, \frac{\partial}{\partial z}\right) \quad .$$

It is understood that all quantities here are in the Eulerian description. We could indicate this by subscripting each variable with the letter $\mathrm{E}$, but since it is clear at this point we will refrain from doing so until there is a possibility of confusion. After we introduce the Lagrangian equations of motion, we will avoid any confusion by following this subscript convention

The viscous terms in Eq. (3.1.2) are responsible for energy dissipation. One can divide the source of this dissipation into two separate regions: the dissipation that occurs in a thin boundary layer region near solid boundaries, and the dissipation due to the internal fluid friction away from these boundaries. As will be shown later in Section 3.1.1.1, this second mechanism is negligible in comparison with the first for the range of physical situations that are of interest in this investigation. Therefore, the viscous terms in Eqs. (3.1.2) are important only in boundary layers, and only along these boundaries will the influence of these terms

be considered in the derivation of the long wave equations. It will also be shown in Section 3.1.1.1 that, for typical physical situations of interest, the boundary layer thickness is negligible in comparison to the total depth, although this condition must of course be violated near a shoreline where the waterdepth goes to zero.

A discussion of these viscous terms is important because they influence the boundary conditions to be imposed to obtain a solution of Eqs. (3.1.1) and (3.1.2). The boundary conditions to be satisfied for the flow *exterior* to the boundary layer (at $z = -h(\mathbf{x})$) are:

$$p_d = \rho g \eta \qquad z = \eta \tag{3.1.3a}$$

$$w = \frac{D\eta}{Dt} = \frac{\partial \eta}{\partial t} + \mathbf{u} \cdot \nabla_{\mathrm{E}} \eta \qquad z = \eta \tag{3.1.3b}$$

$$w = -\frac{Dh}{Dt} = -\mathbf{u} \cdot \nabla_{\mathrm{E}} h \qquad z = -h(\mathbf{x}) \tag{3.1.3c}$$

where

$$\frac{D}{Dt} = \frac{\partial}{\partial t} + \mathbf{U} \cdot {}_3\nabla_{\mathrm{E}} \quad .$$

Here we have neglected the thickness of the boundary layer and applied these conditions directly at the boundaries instead of a distance $\delta$ away, where $\delta$ is the boundary layer thickness. There are two boundary conditions specified at the free surface because the position of this boundary, $\eta$, is unknown *a priori* and must be included as an unknown to be solved for along with the components of velocity and the pressure. The boundary condition described by Eq. (3.1.3b) is the extra boundary condition introduced to determine $\eta$. If we wanted to try to model the viscous terms exactly, then at the free surface we would have to impose Eqs. (3.1.3a), (3.1.3b), as well as a boundary condition of zero shear (assuming the surface is not contaminated with surfactants). At the bottom we would have to impose a no-slip boundary condition.

Let us denote the horizontal velocity *within* the boundary layer by $\mathbf{u}_{\mathrm{bl}}$. Then provided $h(\mathbf{x})$ is a "slowly" varying function of $\mathbf{x}$ and the boundary layer thick-

ness is "small" in comparison to the total water depth (these conditions will be made more precise later), we can obtain an expression for the velocity gradient $\partial \mathbf{u}_{\mathrm{bl}}/\partial z$ at the bottom in terms of the velocity $\mathbf{u}$ just outside the boundary layer, e.g., see Lepelletier (1980). The result is:

$$\frac{\partial \mathbf{u}_{\mathrm{bl}}}{\partial z}(\mathrm{x}, -h(\mathrm{x}), t) = \sqrt{\frac{1}{\pi \nu}} \int_0^\infty \frac{\frac{\partial \mathbf{u}}{\partial t}(t - t')}{\sqrt{t'}}\, dt' \tag{3.1.4}$$

where $\mathbf{u}$ is evaluated just outside the boundary layer. However, it will be shown that under most conditions the boundary layer is thin in comparison with the total water depth, so this value of $\mathbf{u}$ can be approximated by its value at the bottom $z = -h(\mathrm{x})$.

Since the nonlinear advective terms in the equations of motion were neglected in the derivation of Eq. (3.1.4), its accuracy can be expected to diminish as the wave motion increases. In particular, if the boundary layer becomes turbulent, this expression will no longer be valid. However, the boundary layer should remain laminar for most of the laboratory conditions of interest, as will be discussed later in Section 3.1.1.1.

Given the velocity gradient at the bottom, the shear stress and hence the energy dissipation due to the presence of the boundary layer can be computed. Therefore, by the use of Eq. (3.1.4), the boundary layer dissipation can be evaluated simply with the knowledge of the fluid velocity immediately outside the boundary layer.

If we specialize $\mathbf{u}$ to be harmonic, i.e., $\mathbf{u} = \mathbf{u}_0 \cos \omega t$, then Eq. (3.1.4) reduces to:

$$\frac{\partial \mathbf{u}_{\mathrm{bl}}}{\partial z} = \sqrt{\frac{\omega}{\nu}}\, \mathbf{u}_0 \cos(\omega t + \pi/4) \quad . \tag{3.1.5}$$

The shear force per unit area at the bottom is $\mathbf{T} = \mu\, \partial \mathbf{u}_{\mathrm{bl}}/\partial z$ (neglecting a small correction proportional to the slope of the slowly varying bottom), where $\mu$ is

the absolute viscosity of the fluid. Hence, by the use of Eq. (3.1.5), the energy dissipated per period $T$ per unit area is:

$$W = \int_0^T \mathbf{T}\cdot\mathbf{u}\, dt = \frac{\rho}{2}\sqrt{\frac{\omega\nu}{2}}|\mathbf{u}_0|^2 T \quad . \tag{3.1.6}$$

The same energy dissipation results if, instead of Eq. (3.1.5), the following expression for the bottom velocity gradient is used:

$$\frac{\partial \mathbf{u}_{bl}}{\partial z} = \sqrt{\frac{\omega}{2\nu}}\,\mathbf{u}_0 \cos\omega t = \sqrt{\frac{\omega}{2\nu}}\,\mathbf{u} \quad . \tag{3.1.7}$$

For waves that contain a spectrum of frequencies, the circular frequency, $\omega$, in Eq. (3.1.7) is not precisely defined, but for cases where there is a dominant frequency present it should yield satisfactory results. This expression is much simpler than Eq. (3.1.4) and will be used in the derivation of the long wave equations to introduce the effect of energy dissipation in the boundary layer.

Finally, since viscous effects can be ignored throughout the bulk of the fluid exterior to the boundary layers, there is no mechanism to generate vorticity unless the free surface intersects with itself. The free surface will intersect with itself only if a wave breaks. However, this investigation will deal only with nonbreaking wave systems. Therefore, provided the flow is irrotational at some point in time, such as if the fluid is at rest at the time $t = 0$, it will remain irrotational thereafter. Then we will have:

$$\left.\begin{aligned} \frac{\partial u}{\partial z} &= \frac{\partial w}{\partial x} \\ \frac{\partial v}{\partial z} &= \frac{\partial w}{\partial y} \\ \frac{\partial v}{\partial x} &= \frac{\partial u}{\partial y} \end{aligned}\right\} \quad . \tag{3.1.8}$$

Since approximations must be made in developing the long wave equations, it is important to nondimensionalize the variables by the appropriate quantities so that the nondimensional variables will be $O(1)$. Then the relative importance of

each of the terms in the equations and boundary conditions can be determined by comparing the magnitudes of the dimensionless constants that appear as a result of the nondimensionalization chosen. Let $\ell$ denote a characteristic horizontal length scale of the problem, $H$ a characteristic wave height, $h_0$ a characteristic water depth, and $\omega$ a characteristic wave frequency. Then based on linear nondispersive inviscid wave theory, the following nondimensionalization will yield dimensionless variables of order unity:

$$\mathbf{x} = \frac{\mathbf{x}^*}{\ell} \qquad z = \frac{z^*}{h_0} \qquad t = t^* \frac{\sqrt{gh_0}}{\ell}$$

$$\eta = \frac{\eta^*}{H} \qquad p_d = \frac{p_d^*}{\rho g H} \qquad h = \frac{h^*}{h_0}$$

$$\mathbf{u} = \frac{\mathbf{u}^*}{\sqrt{gh_0}} \frac{h_0}{H} \qquad w = \frac{w^*}{\sqrt{gh_0}} \frac{\ell}{H}$$

where the starred symbols are the original dimensional variables. For the remainder of this section all variables will be nondimensional unless specifically stated otherwise. As before, $\nabla_{\mathrm{E}}$ will be defined as:

$$\nabla_{\mathrm{E}} = \left(\frac{\partial}{\partial x}, \frac{\partial}{\partial y}\right)$$

although now $x$ and $y$ refer to dimensionless variables. Under this nondimensionalization Eqs. (3.1.1) and (3.1.2) become:

$$\nabla_{\mathrm{E}} \cdot \mathbf{u} + \frac{\partial w}{\partial z} = 0 \tag{3.1.9}$$

$$\frac{\partial \mathbf{u}}{\partial t} + \alpha \mathbf{u} \cdot \nabla_{\mathrm{E}} \mathbf{u} + \alpha w \frac{\partial \mathbf{u}}{\partial z} = -\frac{1}{\rho} \nabla_{\mathrm{E}} p_d + \gamma^2 \vartheta \left( \beta \nabla_{\mathrm{E}}^2 \mathbf{u} + \frac{\partial^2 \mathbf{u}}{\partial z^2} \right) \tag{3.1.10a}$$

$$\beta \frac{\partial w}{\partial t} + \alpha\beta \mathbf{u} \cdot \nabla_{\mathrm{E}} w + \alpha\beta w \frac{\partial w}{\partial z} = -\frac{1}{\rho} \frac{\partial p_d}{\partial z} + \beta\gamma^2 \vartheta \left( \beta \nabla_{\mathrm{E}}^2 w + \frac{\partial^2 w}{\partial z^2} \right) \tag{3.1.10b}$$

where:

$$\alpha = \frac{H}{h_0} \tag{3.1.11}$$

$$\beta = \left(\frac{h_0}{\ell}\right)^2 \tag{3.1.12}$$

$$\gamma = \frac{\ell}{h_0}\sqrt{\frac{\omega\nu}{2gh_0}} \tag{3.1.13}$$

$$\vartheta = \frac{2\sqrt{gh_0}}{\omega\ell} \quad . \tag{3.1.14}$$

The vorticity conditions (3.1.8) become:

$$\left.\begin{aligned} \frac{\partial u}{\partial z} &= \beta\frac{\partial w}{\partial x} \\ \frac{\partial v}{\partial z} &= \beta\frac{\partial w}{\partial y} \\ \frac{\partial v}{\partial x} &= \frac{\partial u}{\partial y} \end{aligned}\right\} \quad . \tag{3.1.15}$$

The boundary conditions for the inviscid flow exterior to the boundary layer and the expression for the velocity gradient at the bottom (in the boundary layer) become:

$$p_d = \eta \qquad\qquad z = \alpha\eta \tag{3.1.16a}$$

$$w = \frac{\partial\eta}{\partial t} + \alpha\mathbf{u}\cdot\nabla_{\mathrm{E}}\,\eta \qquad\qquad z = \alpha\eta \tag{3.1.16b}$$

$$w = -\mathbf{u}\cdot\nabla_{\mathrm{E}}\,h \qquad\qquad z = -h(\mathbf{x}) \tag{3.1.16c}$$

$$\frac{\partial\mathbf{u}_{\mathrm{bl}}}{\partial z} = \frac{1}{\gamma\vartheta}\mathbf{u} \qquad\qquad z = -h(\mathbf{x}) \quad . \tag{3.1.17}$$

The two most important dimensionless parameters which emerge from this choice of nondimensionalization are the nonlinear parameter $\alpha$ and the dispersion parameter $\beta$. As their names suggest, $\alpha$ is a measure of the importance of the nonlinear (finite amplitude) effects and $\beta$ is a measure of the importance of frequency dispersion. The ratio of these two parameters is called the Ursell number after Ursell (1953), $U_r = \alpha/\beta = H\ell^2/h_0^3$. If $U_r < O(1)$, then dispersive effects dominate so that a linear dispersive theory is appropriate. If $U_r > O(1)$, then nonlinear effects dominate and a nonlinear nondispersive theory is appropriate.

If $U_r = O(1)$ both nonlinear and dispersive effects are important, so a nonlinear dispersive theory should be used.

The parameters $\gamma$ and $\vartheta$ also appear, although only in the combination $\gamma^2\vartheta$, where from Eqs. (3.1.13) and (3.1.14):

$$\gamma^2\vartheta = \frac{1}{h_0^2}\frac{\nu\ell}{\sqrt{gh_0}} \quad . \tag{3.1.18}$$

Notice that the quantity $\gamma^2\vartheta$ does not depend on $\omega$, so the characteristic frequency $\omega$ is not actually needed in this nondimensionalization. It was not necessary to introduce both $\gamma$ and $\vartheta$ as independent parameters at this point (a single parameter $\gamma' \equiv \gamma^2\vartheta$ could have been introduced instead). However, it is the parameter $\gamma$ which will appear later in the long wave equations, so both $\gamma$ and the scaling factor $\vartheta$ have been introduced here for later reference. The characteristic frequency $\omega$ will be introduced through Eq. (3.1.7), when boundary layer dissipation is treated in detail. It is clear that $\vartheta = O(1)$ for long waves. The quantity $\gamma^2\vartheta$ (and hence also $\gamma$) is a measure of the importance of viscous dissipation in the boundary layers.

So far, no approximations to the equations of motion have been made except for the assumption of incompressibility. Now that our choice of nondimensionalization has been made, the assumptions that will be used in the derivation of the long wave equations can be stated. It will be assumed that:

(i) The ratio $\alpha = H/h_0$ of the characteristic wave height $H$ to the characteristic water depth $h_0$ is small but not infinitesimal.

(ii) The ratio $\beta = (h_0/\ell)^2$ of the characteristic water depth $h_0$ to the characteristic wavelength $\ell$ is small but not infinitesimal.

(iii) The kinematic viscosity $\nu$ of the fluid is small so that the parameter $\gamma = \ell/h_0\sqrt{\omega\nu/2gh_0}$ is small but not infinitesimal.

(iv) The slopes $\partial h^*/\partial x^*$ and $\partial h^*/\partial y^*$ are $O(h_0/\ell)$ and the curvatures $\partial^2 h^*/\partial x^{*2}$, $\partial^2 h^*/\partial x^*\partial y^*$, and $\partial^2 h^*/\partial y^{*2}$ are $O(h_0/\ell^2)$, so that $\partial h/\partial x$, $\partial h/\partial y$, $\partial^2 h/\partial x^2$, $\partial^2 h/\partial x\partial y$, and $\partial^2 h/\partial y^2$ are all $O(1)$.

In addition, it will be assumed that the small parameters $\alpha$, $\beta$, and $\gamma$ are of the same small order of magnitude; i.e.,

$$O(\alpha) = O(\beta) = O(\gamma) < O(1) \quad . \tag{3.1.19}$$

Therefore, in the derivation of the long wave equations only terms up to order $\alpha$, $\beta$, and $\gamma$ will be retained. All terms that are quadratic in these quantities or of even smaller order will be discarded.

Notice that the viscous terms in Eq. (3.1.10a) appear to be $O(\gamma^2)$. This shows that the viscous dissipation throughout the bulk of the fluid external to the boundary layers can be neglected. However, dissipation in the boundary layers cannot be neglected because according to Eq. (3.1.17) $\partial \mathbf{u}_{\rm bl}/\partial z$ is $O(1/\gamma)$, so that the actual order of the boundary layer dissipation terms will be $O(\gamma)$. The reason why the velocity gradient $\partial \mathbf{u}_{\rm bl}/\partial z$ is $O(1/\gamma)$ and not $O(1)$ is that the nondimensionalization used was chosen based on linear nondispersive inviscid theory where boundary layers do not appear. Hence, if this nondimensionalization is used within a boundary layer, one would not expect $\partial \mathbf{u}_{\rm bl}/\partial z$ to be $O(1)$. One would have to choose a vertical length scale based on the boundary layer thickness to achieve this.

If we ignore the terms quadratic in small quantities, then Eqs. (3.1.9) and (3.1.10) reduce to:

$$\nabla_{\rm E}\cdot\mathbf{u} + \frac{\partial w}{\partial z} = 0 \tag{3.1.20}$$

$$\frac{\partial \mathbf{u}}{\partial t} + \alpha\mathbf{u}\cdot\nabla_{\rm E}\,\mathbf{u} + \alpha w\frac{\partial \mathbf{u}}{\partial z} = -\frac{1}{\rho}\nabla_{\rm E}\,p_d + \gamma^2\vartheta\frac{\partial^2 \mathbf{u}}{\partial z^2} + O(\beta\gamma^2) \tag{3.1.21a}$$

$$\beta \frac{\partial w}{\partial t} = -\frac{1}{\rho} \frac{\partial p_d}{\partial z} + O(\alpha\beta, \beta\gamma^2) \quad . \tag{3.1.21b}$$

### 3.1.1.1 Laminar Boundary Layers in Oscillatory Flow

Let us now justify the claims made in the previous section regarding a boundary layer in an oscillatory flow subject to the range of laboratory conditions of interest to this investigation. First, it will be shown that the boundary layer will be thin in comparison with the total water depth. Then it will be shown that internal dissipation is much less than dissipation that occurs near solid boundaries in thin boundary layers. Finally, it will be shown that we can expect the boundary layer to remain laminar.

An estimate of the boundary layer thickness $\delta$ is:

$$\delta = \sqrt{\frac{2\nu}{\omega}} \quad . \tag{3.1.22}$$

This is called the Stokes length after G. G. Stokes (1851). Typical laboratory conditions for experiments performed in this investigation are: $h_0 \approx 10\,\mathrm{cm}$, wave period $T = 2\,\mathrm{sec}$; i.e., $\omega \approx \pi\,\mathrm{sec}^{-1}$, and $\nu \approx 0.01\,\mathrm{cm}^2\mathrm{sec}^{-1}$. Using these values the relative boundary layer thickness is:

$$\frac{\delta}{h_0} = \frac{1}{h_0}\sqrt{\frac{2\nu}{\omega}} \approx 0.008 \quad . \tag{3.1.23}$$

Hence, the boundary layer is indeed very small in comparison with a typical water depth. It is interesting now to note the physical significance of the dissipation parameter $\gamma$ as defined by Eq. (3.1.13). For weakly dispersive long waves the first order approximation, $gh_0 = (\omega^2/k^2)[1 + O(\beta)]$, can be made where $k = 2\pi/\lambda$ is the wavenumber of a sinusoidal wave and $\lambda$ is its wavelength. If we substitute this expression for $gh_0$ into Eq. (3.1.13) and define the characteristic length scale

$\ell$ to be the wavelength $\lambda$ we get (neglecting higher order terms):

$$\gamma = \frac{\pi}{h_0}\sqrt{\frac{2\nu}{\omega}} = \pi\frac{\delta}{h_0} \quad . \tag{3.1.24}$$

Hence, the dissipation parameter $\gamma$ is proportional to the ratio of the typical boundary layer thickness to the characteristic water depth. Therefore, the assumption that $\gamma$ is of small order is *equivalent* to the assumption that $\delta/h_0$ is of small order.

We have already indicated that the internal dissipation can be neglected in comparison to the boundary layer dissipation. This can be shown more directly. Using linear dispersive theory Lighthill (1978) showed that the proportional energy density loss per period (the ratio of the energy per unit surface area lost per period to the instantaneous energy per unit surface area) due to boundary layer dissipation is:

$$\Delta \mathrm{E}_{\mathrm{bl}} = \frac{2\pi}{h_0}\sqrt{\frac{\nu}{2\omega}}\frac{2kh_0}{\sinh 2kh_0} \quad . \tag{3.1.25}$$

This is an approximate result which is valid provided the boundary layer thickness is much less than $h_0$. He also showed that the proportional energy density loss per period due to internal dissipation is:

$$\Delta \mathrm{E}_{\mathrm{int}} = \frac{8\pi\nu k^2}{\omega} \quad . \tag{3.1.26}$$

This is an exact result (using linear dispersive theory) and was first obtained by G. G. Stokes. Again, if we let $\ell = \lambda = 2\pi/k$ and use Eq. (3.1.24), expressions (3.1.25) and (3.1.26) reduce to:

$$\Delta \mathrm{E}_{\mathrm{bl}} = \pi\frac{\delta}{h_0}[1 + O(\beta)] = \gamma + O(\gamma\beta) \tag{3.1.27a}$$

$$\Delta \mathrm{E}_{\mathrm{int}} = 16\pi\beta\gamma^2[1 + O(\beta)] = O(\beta\gamma^2) \quad . \tag{3.1.27b}$$

Hence, the internal dissipation is $O(\beta\gamma^2)$ and can be neglected since it is a third order quantity. If nonlinear effects were included, the same conclusion would be

reached provided the boundary layer remained laminar since only terms of $O(\alpha\gamma)$ would be added to Eq. (3.1.27a) and terms of $O(\alpha\beta\gamma^2)$ to Eq. (3.1.27b).

Finally, let us examine the range of laboratory conditions under which the boundary layer can be expected to remain laminar under oscillatory waves. According to Jonsson (1978), boundary layer transition on a smooth bottom occurs for $\mathrm{Re}_\delta \approx 563$, where $\mathrm{Re}_\delta = U\delta/\nu$ is the Reynolds number based on the Stokes length $\delta$, and $U$ is the maximum fluid particle velocity immediately outside the boundary layer. An estimate for $U$ from linear nondispersive theory is $U = (H/h_0)\sqrt{gh_0} = \alpha\sqrt{gh_0}$. Hence, using Eq. (3.1.22) the condition for the boundary layer to remain laminar is:

$$563 > \frac{\alpha\sqrt{gh_0}}{\nu}\sqrt{\frac{2\nu}{\omega}} = \alpha\sqrt{\frac{2gh_0}{\omega\nu}} \quad . \tag{3.1.28}$$

As before, with $h_0 = 10\,\mathrm{cm}$ and $\omega = \pi\,\mathrm{sec}^{-1}$ this implies $\alpha < 0.71$, which is a very large value of the nonlinear parameter $\alpha$. Therefore, under most laboratory conditions the boundary layer is expected to remain laminar.

### 3.1.2 The Three-Dimensional Lagrangian Equations of Motion

Now let us derive the three-dimensional Lagrangian equations of motion. It will be assumed at this point in the discussion that all quantities will be in the Lagrangian description unless otherwise stated or if the variable is subscripted with the letter E (e.g., $\mathbf{u}_\mathrm{E}$), and that all variables are dimensional unless otherwise stated. The variables $(x, y, z) = \mathbf{X}$ will now denote the position at time $t$ of a fluid particle, which at time $t = 0$ was located at $(a, b, c) = \mathbf{A}$. Let $\mathbf{x} = (x, y)$; $\mathbf{a} = (a, b)$. This relation between $(a, b, c)$ and $(x, y, z)$ should be considered as simply a transformation of variables from the $(a, b, c)$ plane to the $(x, y, z)$ plane. The time $t$ simply plays the role of a parameter, so the transformation is

different for different values of $t$ (although it varies continuously with $t$). It will be necessary to introduce the Jacobian of the transformation between the $(x, y, z)$ variables and the $(a, b, c)$ variables. The three-dimensional Jacobian $J$ is defined as:

$$J = \frac{\partial(x, y, z)}{\partial(a, b, c)} = \begin{vmatrix} \frac{\partial x}{\partial a} & \frac{\partial x}{\partial b} & \frac{\partial x}{\partial c} \\ \frac{\partial y}{\partial a} & \frac{\partial y}{\partial b} & \frac{\partial y}{\partial c} \\ \frac{\partial z}{\partial a} & \frac{\partial z}{\partial b} & \frac{\partial z}{\partial c} \end{vmatrix} \tag{3.1.29}$$

where the vertical bars are used to denote the determinant of the enclosed matrix. Let $a_1 = a$, $a_2 = b$, $a_3 = c$. From this point on, the subscripts $i, j, k$, and $l$ will range over the integers 1,2,3. The Einstein summation convention will be used (sum over repeated subscripts) unless stated otherwise. The *minor* of $\partial x_j / \partial a_k$ will be denoted by $\mathrm{M}_{jk}$. The minor $\mathrm{M}_{jk}$ is defined to be the $2 \times 2$ submatrix obtained by deleting the $j^{\text{th}}$ row and the $k^{\text{th}}$ column of the matrix that appears in Eq. (3.1.29). The *cofactor* of $\partial x_j / \partial a_k$ will be denoted by $\mathrm{A}_{jk}$. It is a number defined as $\mathrm{A}_{jk} = (-1)^{j+k} |\mathrm{M}_{jk}|$. For example:

$$\begin{aligned} \mathrm{A}_{23} &= (-1)^{2+3} \begin{vmatrix} \frac{\partial x}{\partial a} & \frac{\partial x}{\partial b} \\ \frac{\partial z}{\partial a} & \frac{\partial z}{\partial b} \end{vmatrix} \\ &= (-1)^{2+3} \frac{\partial(x, z)}{\partial(a, b)} = -\left(\frac{\partial x}{\partial a}\frac{\partial z}{\partial b} - \frac{\partial x}{\partial b}\frac{\partial z}{\partial a}\right) \end{aligned} \tag{3.1.30}$$

where $\dfrac{\partial(x, z)}{\partial(a, b)}$ denotes the two-dimensional Jacobian of $x$ and $z$ with respect to $a$ and $b$.

So far we have considered $x$, $y$, and $z$ to be functions of $a$, $b$, and $c$; i.e., $x_i = x_i(a, b, c, t)$ or $\mathbf{X} = \mathbf{X}(\mathbf{A}, t)$. However, it is equally correct to think of $a$, $b$, and $c$ to be functions of $x$, $y$, and $z$; i.e., $a_i = a_i(x, y, z, t)$ or $\mathbf{A} = \mathbf{A}(\mathbf{X}, t)$. This inverse exists because the Jacobian of the transformation, Eq. (3.1.29), is never zero. In fact, the Jacobian, $J$, must be unity (for incompressible flow).

This will be obvious when the continuity equation is considered. In this case, given the time $t$ and the position of a fluid particle $(x, y, z)$, we can obtain the initial position of the particle. Then we must have:

$$\delta_{ij} = \frac{\partial x_i}{\partial x_j} = \frac{\partial x_i}{\partial a_k}\frac{\partial a_k}{\partial x_j} \tag{3.1.31}$$

where $\delta_{ij}$ is the Kronecker $\delta$ symbol defined as $\delta_{ij} = 1$ if $i = j$; $\delta_{ij} = 0$ if $i \neq j$. If we write (3.1.31) out in matrix notation we get:

$$\begin{pmatrix} \frac{\partial x}{\partial a} & \frac{\partial x}{\partial b} & \frac{\partial x}{\partial c} \\ \frac{\partial y}{\partial a} & \frac{\partial y}{\partial b} & \frac{\partial y}{\partial c} \\ \frac{\partial z}{\partial a} & \frac{\partial z}{\partial b} & \frac{\partial z}{\partial c} \end{pmatrix} \begin{pmatrix} \frac{\partial a}{\partial x} & \frac{\partial a}{\partial y} & \frac{\partial a}{\partial z} \\ \frac{\partial b}{\partial x} & \frac{\partial b}{\partial y} & \frac{\partial b}{\partial z} \\ \frac{\partial c}{\partial x} & \frac{\partial c}{\partial y} & \frac{\partial c}{\partial z} \end{pmatrix} = \begin{pmatrix} 1 & 0 & 0 \\ 0 & 1 & 0 \\ 0 & 0 & 1 \end{pmatrix} \quad . \tag{3.1.32}$$

We can solve for $\partial a_k / \partial x_i$ by computing the inverse of the first matrix. We get (e.g., Kolman 1970):

$$\frac{\partial a_k}{\partial x_i} = \frac{\mathrm{A}_{ik}}{J} \quad . \tag{3.1.33}$$

Now consider an arbitrary function $g(\mathbf{A}, t)$. Let $g_{\mathrm{E}}$ denote its Eulerian description; i.e.,

$$g_{\mathrm{E}}(\mathbf{X}, t) = g(\mathbf{A}(\mathbf{X}, t), t) \quad . \tag{3.1.34}$$

This equation simply states that the value at time $t$ of an arbitrary function expressed in the Eulerian description evaluated at an arbitrary location $\mathbf{X}$ must be the same as the value of this function expressed in the Lagrangian description evaluated at the initial location of the particle, which at time $t$ has reached the location $\mathbf{X}$. If we take the derivative of $g_{\mathrm{E}}$ with respect to $x_i$ and use Eq. (3.1.33), we get:

$$\frac{\partial g_{\mathrm{E}}}{\partial x_i} = \frac{\partial g}{\partial a_k}\frac{\partial a_k}{\partial x_i} = \frac{1}{J}\frac{\partial g}{\partial a_k}\mathrm{A}_{ik} \quad . \tag{3.1.35}$$

For $i = 1$, this is just $1/J$ times the cofactor expansion of the determinant:

$$\begin{vmatrix} \frac{\partial g}{\partial a} & \frac{\partial g}{\partial b} & \frac{\partial g}{\partial c} \\ \frac{\partial y}{\partial a} & \frac{\partial y}{\partial b} & \frac{\partial y}{\partial c} \\ \frac{\partial z}{\partial a} & \frac{\partial z}{\partial b} & \frac{\partial z}{\partial c} \end{vmatrix} = \frac{\partial(g, y, z)}{\partial(a, b, c)} \tag{3.1.36}$$

about the first row (e.g., Kolman 1970). In general, we get:

$$\frac{\partial g_{\mathrm{E}}}{\partial x} = \frac{1}{J}\frac{\partial(g, y, z)}{\partial(a, b, c)} \qquad \frac{\partial g_{\mathrm{E}}}{\partial y} = \frac{1}{J}\frac{\partial(x, g, z)}{\partial(a, b, c)} \qquad \frac{\partial g_{\mathrm{E}}}{\partial z} = \frac{1}{J}\frac{\partial(x, y, g)}{\partial(a, b, c)} . \tag{3.1.37}$$

This result will be used to derive the momentum equations in the Lagrangian description.

For brevity, it will be convenient to denote the partial derivative of a function $g$ with respect to the coordinate $q$ by $g_q$; e.g., $\partial y/\partial c = y_c$, $\partial^2 x/\partial t^2 = x_{tt}$. This should not be confused with the italic subscripts $i$, $j$, $k$, and $l$, which refer to elements of a vector or a matrix.

So far, only stated mathematical relations and definitions have been stated without reference to the physics of the problem. This has been necessary to provide a clear derivation of the three-dimensional Lagrangian equations of motion, which we are now in a position to do.

The equation of continuity takes on a simple form in the Lagrangian description. Consider the small element of fluid in Fig. 3.1.2, which at time $t = 0$ occupies an infinitesimal parallelepiped with one reference corner located at the point $(a, b, c)$ and with edges of length $da$, $db$, and $dc$, each parallel to one of the coordinate axes. Its volume is $da\,db\,dc$. At some later time $t$, this element has deformed and now forms an oblique parallelepiped with the reference corner located at $(x(a, b, c, t), y(a, b, c, t), z(a, b, c, t))$. If we look upon the relation between $(a, b, c)$ and $(x, y, z)$ as simply a change of variables, it is clear (e.g., Greenspan

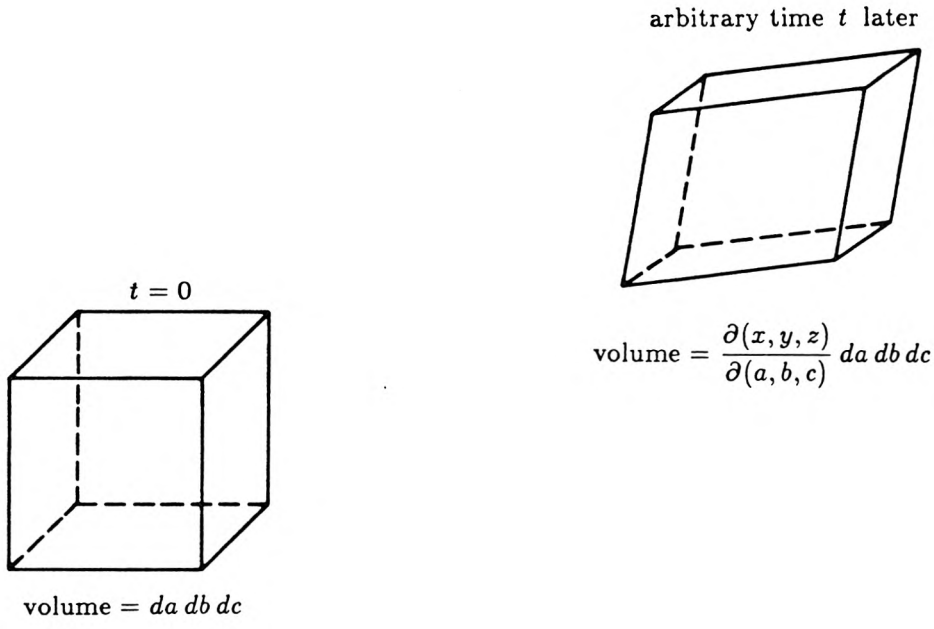


Fig. 3.1.2 Deformation of a differential element of fluid.

& Benney 1973) that the new volume of this element is $\dfrac{\partial(x,y,z)}{\partial(a,b,c)} da\, db\, dc$. Since mass must be conserved, we get:

$$\rho(\mathbf{A},0)\, da\, db\, dc = \rho(\mathbf{A},t) \frac{\partial(x,y,z)}{\partial(a,b,c)}\, da\, db\, dc \quad . \tag{3.1.38}$$

For incompressible flow $\rho =$ is constant and therefore, using Eq. (3.1.29), the continuity equation for incompressible flow in the Lagrangian description is:

$$J = 1 \quad . \tag{3.1.39}$$

This appears to be a simple equation. However, Eq. (3.1.39) is, in fact, a nonlinear differential equation since, if $J$ were expanded as given by Eq. (3.1.29), we would obtain six nonlinear terms one of which is, for example, $x_a\, y_b\, z_c$. The nonlinearity arises because a small element of fluid (e.g., Fig. 3.1.2) may undergo large deformations as time progesses. For arbitrary motion, the statement of continuity, $J = 1$, can be linearized only if a short differential time interval is considered,

since all deformations over such an interval will be small. However, over a larger time interval the nonlinear terms cannot be neglected. In contrast, the Eulerian continuity equation (3.1.1) is linear. The linearity is a consequence of the fact that the statement of continuity in the Eulerian description is local in both space and time; at each point in time the local divergence of the velocity field must be zero to conserve mass. There is no need to consider the time evolution of an element of fluid, as in the Lagrangian case.

The momentum equations will be derived next. The $i^{\text{th}}$ component of velocity of a particle is:

$$\frac{\partial x_i}{\partial t}(\mathbf{A},t) \quad . \tag{3.1.40}$$

At any time $t$ this velocity must of course be equal to the $i^{\text{th}}$ component of the Eulerian velocity at the present position of the fluid particle; i.e.,

$$\frac{\partial x_i}{\partial t}(\mathbf{A},t) = u_{i_{\text{E}}}(\mathbf{X}(\mathbf{A},t),t) \quad . \tag{3.1.41}$$

Stated in words, this says that the velocity at time $t$ of a fluid particle whose initial coordinates were $\mathbf{A}$ is equal to the Eulerian velocity at time $t$ evaluated at the present location of that particle. The $i^{\text{th}}$ component of the acceleration of this particle of fluid is:

$$\frac{\partial^2 x_i}{\partial t^2}(\mathbf{A},t) \quad . \tag{3.1.42}$$

But this must equal the $i^{\text{th}}$ component of the Eulerian advective acceleration at the present position of the fluid particle; i.e.,

$$\frac{\partial^2 x_i}{\partial t^2}(\mathbf{A},t) = \frac{Du_{i_{\text{E}}}}{Dt}(\mathbf{X}(\mathbf{A},t),t) \quad . \tag{3.1.43}$$

Now it is straightforward to transform the Eulerian momentum equations to the Lagrangian description. The Eulerian equations can be written as:

$$\frac{Du_{i_{\text{E}}}}{Dt} + g\delta_{i3} = -\frac{1}{\rho}\frac{\partial p_{\text{E}}}{\partial x_i} + \nu\frac{\partial^2 u_{i_{\text{E}}}}{\partial x_j \partial x_j} \qquad i = 1,2,3 \quad . \tag{3.1.44}$$

If we substitute Eq. (3.1.43) into this expression we get:

$$\frac{\partial^2 x_i}{\partial t^2} + g\delta_{i3} = -\frac{1}{\rho}\frac{\partial p}{\partial x_i} + F_i \qquad i = 1,2,3 \tag{3.1.45}$$

where the pressure is now considered a function of the Lagrangian coordinates $(a,b,c)$. The $F_i$ are the terms that result from transforming the viscous terms into the Lagrangian description. Their exact expressions will be complicated and will not be presented here since we will be interested only in the first order (linear) quantities. Equation (3.1.45) is awkward because, although $p$ is a function of the $a_i$, it is differentiated with respect to the $x_i$. Further simplification leads to two different forms of the momentum equations in the Lagrangian description. The first form can be obtained by using Eq. (3.1.37) with $g = p$ (and with $J = 1$ from Eq. (3.1.39)). Then Eq. (3.1.45) becomes:

$$\left.\begin{aligned} \frac{\partial^2 x}{\partial t^2} &= -\frac{1}{\rho}\frac{\partial(p,y,z)}{\partial(a,b,c)} + F_1 \\ \frac{\partial^2 y}{\partial t^2} &= -\frac{1}{\rho}\frac{\partial(x,p,z)}{\partial(a,b,c)} + F_2 \\ \frac{\partial^2 z}{\partial t^2} + g &= -\frac{1}{\rho}\frac{\partial(x,y,p)}{\partial(a,b,c)} + F_3 \end{aligned}\right\} \quad . \tag{3.1.46}$$

This is the form of the momentum equations that will be used to derive the long wave equations. Notice that in these equations the acceleration terms are linear but the pressure gradient terms are nonlinear, in contrast to the momentum equations in the Eulerian description where the opposite is true. The nonlinearity in the pressure terms in Eq. (3.1.46) occurs because the pressure gradient at the present location of a fluid particle depends on how the surrounding fluid has deformed from the initial instant, $t = 0$. These deformations can be large and, hence, nonlinear.

Another form of the momentum equations can be obtained by multiplying

Eq. (3.1.45) by $\partial x_i/\partial a_j$ (and then summing over $i$). The result is

$$\begin{aligned}(\frac{\partial^2 x_i}{\partial t^2} + g\delta_{i3})\frac{\partial x_i}{\partial a_j} &= -\frac{1}{\rho}\frac{\partial p}{\partial x_i}\frac{\partial x_i}{\partial a_j} + F_i\frac{\partial x_i}{\partial a_j} \\ &= -\frac{1}{\rho}\frac{\partial p}{\partial a_j} + F_i\frac{\partial x_i}{\partial a_j} \qquad j = 1,2,3\end{aligned}$$

or in matrix form:

$$\begin{pmatrix} x_a & y_a & z_a \\ x_b & y_b & z_b \\ x_c & y_c & z_c \end{pmatrix}\begin{pmatrix} x_{tt} \\ y_{tt} \\ z_{tt}+g \end{pmatrix} + \frac{1}{\rho}\begin{pmatrix} p_a \\ p_b \\ p_c \end{pmatrix} = \begin{pmatrix} F_i\frac{\partial x_i}{\partial a} \\ F_i\frac{\partial x_i}{\partial b} \\ F_i\frac{\partial x_i}{\partial c} \end{pmatrix} \quad . \tag{3.1.46b}$$

Equations (3.1.46a) and (3.1.46b) compare to (3.1.2) in the Eulerian description. Notice that in Eq. (3.1.46a) the acceleration terms are linear but the pressure gradient terms are nonlinear. In the Eulerian description the opposite is true, as is the case with the alternate form of the momentum equations in the Lagrangian description, Eq. (3.1.46b).

Now let us look at the irrotationality conditions, Eq. (3.1.8). These can be written concisely using the permutation symbol $\varepsilon_{ijk}$ defined as: $\varepsilon_{123} = \varepsilon_{312} = \varepsilon_{231} = 1$, $\varepsilon_{213} = \varepsilon_{321} = \varepsilon_{132} = -1$, $\varepsilon_{ijk} = 0$ otherwise. Then Eq. (3.1.8) can be written as:

$$0 = \varepsilon_{ijk}\frac{\partial u_{k_E}}{\partial x_j} \qquad i = 1,2,3 \quad . \tag{3.1.47}$$

If we use the Lagrangian description of the velocity from Eq. (3.1.41), and then use Eq. (3.1.33) with $J = 1$, Eq. (3.1.47) becomes:

$$\begin{aligned}0 &= \varepsilon_{ijk}\frac{\partial u_k}{\partial a_l}\frac{\partial a_l}{\partial x_j} \\ &= \varepsilon_{ijk}\frac{\partial}{\partial t}(\frac{\partial x_k}{\partial a_l})\frac{\partial a_l}{\partial x_j} \\ &= \varepsilon_{ijk}\frac{\partial}{\partial t}(\frac{\partial x_k}{\partial a_l})\mathrm{A}_{jl} \qquad i = 1,2,3 \quad .\end{aligned} \tag{3.1.48}$$

Alternately, we can use Eq. (3.1.37) with $g_{\mathrm{E}} = u_{k_{\mathrm{E}}}$ $k = 1,2,3$ and (3.1.41). Then Eq. (3.1.47) reduces to:

$$\left.\begin{aligned} \frac{\partial(x, z_t, z)}{\partial(a, b, c)} &= \frac{\partial(x, y, y_t)}{\partial(a, b, c)} \\ \frac{\partial(x, y, x_t)}{\partial(a, b, c)} &= \frac{\partial(z_t, y, z)}{\partial(a, b, c)} \\ \frac{\partial(y_t, y, z)}{\partial(a, b, c)} &= \frac{\partial(x, x_t, z)}{\partial(a, b, c)} \end{aligned}\right\} \quad . \tag{3.1.49}$$

These are the irrotationality conditions to be used in the derivation of the long wave equations. They compare with Eq. (3.1.8). Note they are nonlinear. It is also important to note that because the irrotationality conditions in the Lagrangian description are fundamentally different from that in the Eulerian description where they are expressed by the vanishing of the curl of the velocity, there will not, in general, be a velocity potential analogous to that in the Eulerian description.

Assuming all motion starts from rest at time $t = 0$, the boundary conditions for the irrotational flow external to the boundary layers are:

$$p = 0 \qquad c = 0 \tag{3.1.50a}$$

$$z = -h(\mathrm{x}) \qquad c = -h(\mathrm{a}) \quad . \tag{3.1.50b}$$

Eq. (3.1.50a) corresponds to the dynamic boundary condition (3.1.3a) in the Eulerian description. It is evaluated at $c = 0$. That refers to particles that lie at the free surface at time $t = 0$. However, since the free surface is a material surface, these particles must remain at the free surface. Hence, $c = 0$ describes the free surface for all time and, therefore, Eq. (3.1.50a) states that the pressure is zero at the free surface for all time. Boundary condition (3.1.50b) corresponds to Eq. (3.1.3c). It states that particles which lie at the bottom at time $t = 0$; i.e., particles for which $c = -h(\mathrm{a})$, remain on the bottom thereafter. It is, in general, nonlinear unless $h(\mathrm{a})$ is a linear function of $a$ and $b$.

Notice that there is only one boundary condition to impose at the free surface. In the Eulerian description there were two because the position of the free surface is an extra unknown to be solved for as part of the problem. However, since the free surface is a material surface, its position is fixed in the Lagrangian description. In our case it corresponds to $c = 0$. Therefore, an extra variable need not be introduced to keep track of the position of the free surface. However, for *convenience*, we we will make the following definition:

$$\eta(a,b,t) \equiv z(a,b,0,t) \quad . \tag{3.1.51}$$

This definition is analogous to boundary condition (3.1.3b) in the Eulerian description. However, Eq. (3.1.51) is not an extra boundary condition that the flow must satisfy. It merely states that we will denote $z(\mathbf{a}, c = 0, t)$ by $\eta(\mathbf{a}, t)$.

Now let us look at the relationship between the Eulerian and the Lagrangian descriptions. In particular, if we are given the set of fluid functions describing the flow in one description, how do we transform them into the other description? First, suppose we are given the three components of the velocity in the Eulerian description, $\mathbf{U}_{\text{E}}(\mathbf{X}, t)$. These are three functions defined for $t > 0$ at all points in space occupied by fluid particles at time $t$. From them we want to determine the three functions $\mathbf{X}(\mathbf{A}, t)$, which give the location of any particle of fluid at time $t$, given its initial position, $\mathbf{A}$. To do that we must integrate Eq. (3.1.41) with respect to time:

$$\mathbf{X}(\mathbf{A},t) = \mathbf{A} + \int_0^t \mathbf{U}_{\text{E}}(\mathbf{X}(\mathbf{A},t'),t')\,dt' \quad . \tag{3.1.52}$$

In general, it will be very difficult to obtain $\mathbf{X}(\mathbf{A}, t)$ because, as can be seen, it involves solving three coupled integral equations. However, if we *can* obtain $\mathbf{X}(\mathbf{A}, t)$, then an arbitrary function $g_{\text{E}}(\mathbf{X}, t)$ in the Eulerian description can be

transformed very simply to the Lagrangian description:

$$g(\mathbf{A},t) = g_{\text{E}}(\mathbf{X}(\mathbf{A},t),t) \tag{3.1.53}$$

where $\mathbf{X}(\mathbf{A},t)$ is determined from Eq. (3.1.52).

On the other hand, suppose we are given $\mathbf{X}(\mathbf{A},t)$, the location of any particle of fluid at time $t$, whose initial position is $\mathbf{A}$. In theory, this can be inverted to get $\mathbf{A}(\mathbf{X},t)$, the initial coordinate of any particle of fluid which at time $t$ is located at the position $\mathbf{X}$. The inversion is possible because the Jacobian of the transformation is always nonzero from Eq. (3.1.39). Given $\mathbf{A}(\mathbf{X},t)$, any function in the Lagragian description, $g(\mathbf{A},t)$, can be transformed to the Eulerian description using in Eq. (3.1.34):

$$g_{\text{E}}(\mathbf{X},t) = g(\mathbf{A}(\mathbf{X},t),t) \quad . \tag{3.1.54}$$

This states that the Eulerian description of an arbitrary function $g$ is obtained by evaluating the function in the Lagrangian description at the initial coordinate of the particle that reaches the location $\mathbf{X}$ at time $t$. Clearly, all of the effort to transform from the Lagrangian to the Eulerian description involves inverting $\mathbf{X}(\mathbf{A},t)$ to obtain $\mathbf{A}(\mathbf{X},t)$.

The present variables are inconvenient for numerical work or for the derivation of the long wave equations. It is more convenient to work with the deviations of these variables from their initial values. In the Eulerian description this is analogous to working with the dynamic pressure instead of the static pressure. This will allow us to do a consistent nondimensionalization so that the importance of the various terms in the equations can be determined easily. Therefore, let:

$$\mathbf{x}^* = \hat{\mathbf{x}}^* - \hat{\mathbf{a}}^* \qquad z^* = \hat{z}^* - \hat{c}^* \qquad p^* = \hat{p}^* + \rho g \hat{c}^*$$

$$\mathbf{a}^* = \hat{\mathbf{a}}^* \qquad c^* = \hat{c}^* \qquad t^* = \hat{t}^*$$

where $\hat{\mathbf{x}}^*$, $\hat{z}^*$, $\hat{p}^*$, $\hat{\mathbf{a}}^*$, $\hat{c}^*$, and $\hat{t}^*$ refer to $\mathbf{x}$, $z$, $p$, $\mathbf{a}$, $c$, and $t$ in the analysis up to this point; i.e., $(\hat{a}^*, \hat{b}^*, \hat{c}^*)$ are the initial (dimensional) coordinates of a particle which at time $t$ is located at $(\hat{x}^*, \hat{y}^*, \hat{z}^*)$. Now let us nondimensionalize. The nondimensionalization which is consistent with that previously used in Eulerian description is:

$$\mathbf{a} = \frac{\mathbf{a}^*}{\ell} \qquad c = \frac{c^*}{h_0} \qquad t = t^* \frac{\sqrt{gh_0}}{\ell}$$

$$p = \frac{p^*}{\rho g H} \qquad h = \frac{h^*}{h_0}$$

$$\mathbf{x} = \frac{\mathbf{x}^*}{\ell}\frac{h_0}{H} \qquad z = \frac{z^*}{H} \quad .$$

As before, the quantities $H$, $\ell$, $h_0$ refer to a characteristic wave height, horizontal length, and water depth. In this section the nondimensional parameters $\alpha$, $\beta$, $\gamma$, and $\vartheta$ are defined as in Section 3.1.1:

$$\alpha = \frac{H}{h_0}$$

$$\beta = \left(\frac{h_0}{\ell}\right)^2$$

$$\gamma = \frac{\ell}{h_0}\sqrt{\frac{\omega\nu}{2gh_0}}$$

$$\vartheta = \frac{2\sqrt{gh_0}}{\omega\ell} \quad .$$

From now on all quantities will be nondimensional unless specifically stated otherwise. The operators $\nabla$ and ${}_3\nabla$ will be defined as:

$$\nabla = \left(\frac{\partial}{\partial a}, \frac{\partial}{\partial b}\right) \qquad {}_3\nabla = \left(\frac{\partial}{\partial a}, \frac{\partial}{\partial b}, \frac{\partial}{\partial c}\right) \quad . \tag{3.1.55}$$

With this change of variables and nondimensionalization, the Lagrangian functions $\mathbf{X}(\mathbf{A}, t)$ no longer specify the absolute coordinates of a fluid particle,

only its deviation from its initial position; its absolute coordinates are $\hat{\mathbf{X}} = \hat{\mathbf{X}}^*/\ell$. In terms of the displacements $\hat{\mathbf{X}}$ or $\hat{\mathbf{x}}$ we get:

$$\hat{\mathbf{X}}(\mathbf{A},t) = \mathbf{A} + \alpha\mathbf{X}(\mathbf{A},t) \quad \text{or} \quad \hat{\mathbf{x}}(\mathbf{A},t) = \mathbf{a} + \alpha\mathbf{x}(\mathbf{A},t) \quad . \tag{3.1.56}$$

The first equation can be inverted to get $\mathbf{A}(\hat{\mathbf{X}},t)$. Then $\mathbf{A}(\hat{\mathbf{X}},t)$ must satisfy:

$$\mathbf{A}(\hat{\mathbf{X}},t) = \hat{\mathbf{X}} - \alpha\mathbf{X}(\mathbf{A}(\hat{\mathbf{X}},t),t) \quad . \tag{3.1.57}$$

These relations can now be used to obtain the dimensionless form of the transformation equations between the Lagrangian and Eulerian description given by Eqs. (3.1.52), (3.1.53), and (3.1.54). In terms of the nondimensional variables Eq. (3.1.52) becomes:

$$\mathbf{X}(\mathbf{A},t) = \int_0^t \mathbf{U}_{\text{E}}(\mathbf{A} + \alpha\mathbf{X}(\mathbf{A},t'),t')\,dt' \quad . \tag{3.1.58}$$

Now let us make the assumption, of Eq. (3.1.19); i.e.:

$$O(\alpha) = O(\beta) = O(\gamma) < O(1) \quad . \tag{3.1.59}$$

If we expand $\mathbf{U}_{\text{E}}$ in a Taylor series, Eq. (3.1.58) becomes:

$$\mathbf{X}(\mathbf{A},t) = \int_0^t \mathbf{U}_{\text{E}}(\mathbf{A},t')\,dt' + \alpha\int_0^t \mathbf{X}(\mathbf{A},t')\cdot{}_3\nabla_{\text{E}}\mathbf{U}_{\text{E}}(\mathbf{A},t')\,dt' + O(\alpha^2) \; . \tag{3.1.60}$$

We can solve for $\mathbf{X}(\mathbf{A},t)$ to get:

$$\mathbf{X}(\mathbf{A},t) = \int_0^t \mathbf{U}_{\text{E}}(\mathbf{A},t')\,dt' + \alpha\int_0^t \left[\int_0^{t'} \mathbf{U}_{\text{E}}(\mathbf{A},t'')\,dt''\right]\cdot{}_3\nabla_{\text{E}}\mathbf{U}_{\text{E}}(\mathbf{A},t')\,dt' + O(\alpha^2) \; . \tag{3.1.61}$$

This is a first order approximate solution to Eq. (3.1.58). It is an explicit formula to compute $\mathbf{X}(\mathbf{A},t)$, the location of any particle of fluid at time $t$, if we are given

the three components of the velocity in the Eulerian description, $\mathbf{U}_{\text{E}}(\mathbf{X},t)$. If we differentiate it with respect to $t$, we obtain:

$$\frac{\partial \mathbf{X}}{\partial t}(\mathbf{A},t) = \mathbf{U}_{\text{E}}(\mathbf{A},t) + \alpha \left[ \int_0^t \mathbf{U}_{\text{E}}(\mathbf{A},t')\, dt' \right] \cdot_3 \nabla_{\text{E}} \mathbf{U}_{\text{E}}(\mathbf{A},t) + O(\alpha^2) \quad . \tag{3.1.62}$$

Now let us return to the transformation from the Eulerian to the Lagrangian description. In terms of these new variables Eq. (3.1.53) becomes:

$$g(\mathbf{A},t) = g_{\text{E}}(\mathbf{A} + \alpha \mathbf{X}(\mathbf{A},t),t) \quad . \tag{3.1.63}$$

This expression is used to transform an arbitrary function in the Eulerian description to the Lagrangian description. To use it, $\mathbf{X}(\mathbf{A},t)$ must first be computed from Eq. (3.1.61) (with an error of $O(\alpha^2)$).

In terms of these new variables Eq. (3.1.54) becomes:

$$g_{\text{E}}(\hat{\mathbf{X}},t) = g(\mathbf{A}(\hat{\mathbf{X}},t),t) \quad . \tag{3.1.64}$$

Using Eq. (3.1.57), this becomes:

$$\begin{aligned} g_{\text{E}}(\hat{\mathbf{X}},t) &= g(\hat{\mathbf{X}} - \alpha \mathbf{X}(\mathbf{A}(\hat{\mathbf{X}},t),t),t) \\ &= g(\hat{\mathbf{X}},t) - \alpha \mathbf{X}(\mathbf{A}(\hat{\mathbf{X}},t),t) \cdot_3 \nabla g(\hat{\mathbf{X}},t) + O(\alpha^2) \quad . \end{aligned} \tag{3.1.65}$$

But from Eq. (3.1.57), $\mathbf{A}(\hat{\mathbf{X}},t) = \hat{\mathbf{X}} + O(\alpha)$, and so this last expression can be written as:

$$g_{\text{E}}(\hat{\mathbf{X}},t) = g(\hat{\mathbf{X}},t) - \alpha \mathbf{X}(\hat{\mathbf{X}},t) \cdot_3 \nabla g(\hat{\mathbf{X}},t) + O(\alpha^2) \quad . \tag{3.1.66}$$

Given $\mathbf{X}(\mathbf{A},t)$, any function can be transformed from the Lagrangian description to the Eulerian description using this expression (with an error of $O(\alpha^2)$). Notice that the quantities on the right hand side of Eq. (3.1.66) in the Lagrangian

description are all evaluated at the location of interest, $\hat{\mathbf{X}}$, and not at the initial position of the particle that reached that location at time $t$, $\mathbf{A}(\hat{\mathbf{X}},t)$. For example, if $g = \eta$ we get:

$$\eta_{\text{E}}(\hat{\mathbf{x}},t) = \eta(\hat{\mathbf{x}},t) - \alpha \mathbf{x}(\hat{\mathbf{X}},t)\cdot\nabla\eta(\hat{\mathbf{x}},t) + O(\alpha^2) \quad . \tag{3.1.67}$$

Now let us obtain expressions for the viscous terms, $F_i$, which appear in (3.1.46). From Eqs. (3.1.37) and (3.1.56) we get:

$$\frac{\partial g_{\text{E}}}{\partial x_j} = \frac{\partial g}{\partial a_j} + O(\alpha) \quad . \tag{3.1.68}$$

If we apply this twice with $g_{\text{E}} = u_{i_{\text{E}}}(\mathbf{X},t)$ we get:

$$\frac{\partial^2 u_{i_{\text{E}}}}{\partial x_j^2}(\hat{\mathbf{X}},t) = \frac{\partial^2 u_i}{\partial a_j^2}(\mathbf{A}(\hat{\mathbf{X}},t),t) + O(\alpha) \quad . \tag{3.1.69}$$

Using this result and the relation $u_i = \partial x_i/\partial t$ we can transform the viscous terms in Eq. (3.1.10) to the Lagrangian description. We get:

$$F_1 = \gamma^2\vartheta\frac{\partial^3 x}{\partial c^2\partial t} + O(\alpha\gamma^2,\beta\gamma^2) \tag{3.1.70a}$$

$$F_2 = \gamma^2\vartheta\frac{\partial^3 y}{\partial c^2\partial t} + O(\alpha\gamma^2,\beta\gamma^2) \tag{3.1.70b}$$

$$F_3 = O(\beta\gamma^2) \quad . \tag{3.1.70c}$$

Similarly, the Lagrangian representation of Eq. (3.1.17) is:

$$\frac{\partial^2 \mathbf{x}_{\text{bl}}}{\partial c\partial t} = \frac{1}{\gamma\vartheta}\frac{\partial \mathbf{x}}{\partial t} + O(\frac{\alpha}{\gamma}) \qquad c = -h(\mathbf{a}) \tag{3.1.71}$$

where $\mathbf{x}_{\text{bl}}$ is the horizontal fluid particle displacement vector in the boundary layer.

Now let us return to the equations of motion. In terms of the new dimensionless variables the continuity equation (3.1.39), the momentum equations (3.1.46a) and the irrotationality conditions (3.1.49) become:

Continuity:

$$x_a + y_b + z_c + \alpha\left[\frac{\partial(x,y)}{\partial(a,b)} + \frac{\partial(x,z)}{\partial(a,c)} + \frac{\partial(y,z)}{\partial(b,c)}\right] + \alpha^2\frac{\partial(x,y,z)}{\partial(a,b,c)} = 0 \qquad (3.1.72)$$

Momentum:

$$\left.\begin{aligned} x_{tt} + p_a + z_a + \alpha\left[\frac{\partial(p,y)}{\partial(a,b)} + \frac{\partial(p,z)}{\partial(a,c)} + \frac{\partial(z,y)}{\partial(a,b)}\right] + \alpha^2\frac{\partial(p,y,z)}{\partial(a,b,c)} &= F_1 \\ y_{tt} + p_b + z_b + \alpha\left[\frac{\partial(x,p)}{\partial(a,b)} + \frac{\partial(p,z)}{\partial(b,c)} + \frac{\partial(x,z)}{\partial(a,b)}\right] + \alpha^2\frac{\partial(x,p,z)}{\partial(a,b,c)} &= F_2 \\ \beta z_{tt} + p_c - x_a - y_b + \alpha\left[\frac{\partial(x,p)}{\partial(a,c)} + \frac{\partial(y,p)}{\partial(b,c)} - \frac{\partial(x,y)}{\partial(a,b)}\right] + \alpha^2\frac{\partial(x,y,p)}{\partial(a,b,c)} &= F_3 \end{aligned}\right\} \qquad (3.1.73)$$

Irrotationality:

$$y_{ct} + \alpha\left[\frac{\partial(x,y_t)}{\partial(a,c)} + \frac{\partial(y,y_t)}{\partial(b,c)}\right] + \alpha^2\frac{\partial(x,y,y_t)}{\partial(a,b,c)} = \beta z_{bt} + \alpha\beta\left[\frac{\partial(x,z_t)}{\partial(a,b)} + \frac{\partial(z_t,z)}{\partial(b,c)}\right] + \alpha^2\beta\frac{\partial(x,z_t,z)}{\partial(a,b,c)} \qquad (3.1.74a)$$

$$x_{ct} + \alpha\left[\frac{\partial(x,x_t)}{\partial(a,c)} + \frac{\partial(y,x_t)}{\partial(b,c)}\right] + \alpha^2\frac{\partial(x,y,x_t)}{\partial(a,b,c)} = \beta z_{at} + \alpha\beta\left[\frac{\partial(z_t,y)}{\partial(a,b)} + \frac{\partial(z_t,z)}{\partial(a,c)}\right] + \alpha^2\beta\frac{\partial(z_t,y,z)}{\partial(a,b,c)} \qquad (3.1.74b)$$

$$y_{at} + \alpha\left[\frac{\partial(y_t,y)}{\partial(a,b)} + \frac{\partial(y_t,z)}{\partial(a,c)}\right] + \alpha^2\frac{\partial(y_t,y,z)}{\partial(a,b,c)} = x_{bt} + \alpha\left[\frac{\partial(x,x_t)}{\partial(a,b)} + \frac{\partial(x_t,z)}{\partial(b,c)}\right] + \alpha^2\frac{\partial(x,x_t,z)}{\partial(a,b,c)} \qquad (3.1.74c)$$

In terms of the nondimensional variables, the boundary conditions (3.1.50a) and (3.1.50b) become:

$$p = 0 \qquad c = 0 \qquad (3.1.75a)$$

$$z = \frac{h(\mathrm{a}) - h(\mathrm{a} + \alpha\mathrm{x})}{\alpha} \qquad c = -h(\mathrm{a}) \qquad (3.1.75b)$$

plus the definition:

$$\eta = z \qquad\qquad c = 0 \quad . \tag{3.1.76}$$

Now if we neglect all terms quadratic in small quantities and use Eq. (3.1.70) for the $F_i$, the equations of motion (3.1.72)-(3.1.74) and the boundary conditions (3.1.75) reduce to the following approximate expressions:

Continuity:

$$x_a + y_b + z_c + \alpha\left[\frac{\partial(x,y)}{\partial(a,b)} + \frac{\partial(x,z)}{\partial(a,c)} + \frac{\partial(y,z)}{\partial(b,c)}\right] = O(\alpha^2) \tag{3.1.77}$$

Momentum:

$$x_{tt} + p_a + z_a + \alpha\left[\frac{\partial(p,y)}{\partial(a,b)} + \frac{\partial(p,z)}{\partial(a,c)} + \frac{\partial(z,y)}{\partial(a,b)}\right] - \gamma^2\vartheta x_{cct} = O(\alpha^2) \tag{3.1.78a}$$

$$y_{tt} + p_b + z_b + \alpha\left[\frac{\partial(x,p)}{\partial(a,b)} + \frac{\partial(p,z)}{\partial(b,c)} + \frac{\partial(x,z)}{\partial(a,b)}\right] - \gamma^2\vartheta y_{cct} = O(\alpha^2) \tag{3.1.78b}$$

$$\beta z_{tt} + p_c - x_a - y_b + \alpha\left[\frac{\partial(x,p)}{\partial(a,c)} + \frac{\partial(y,p)}{\partial(b,c)} - \frac{\partial(x,y)}{\partial(a,b)}\right] = O(\alpha^2) \tag{3.1.79}$$

Irrotationality:

$$\left.\begin{aligned} y_{ct} - \beta z_{bt} + \alpha\left[\frac{\partial(x,y_t)}{\partial(a,c)} + \frac{\partial(y,y_t)}{\partial(b,c)}\right] &= O(\alpha\beta,\alpha^2) \\ x_{ct} - \beta z_{at} + \alpha\left[\frac{\partial(x,x_t)}{\partial(a,c)} + \frac{\partial(y,x_t)}{\partial(b,c)}\right] &= O(\alpha\beta,\alpha^2) \\ y_{at} - x_{bt} + \alpha\left[\frac{\partial(y_t,y)}{\partial(a,b)} + \frac{\partial(y_t,z)}{\partial(a,c)} - \frac{\partial(x,x_t)}{\partial(a,b)} - \frac{\partial(x_t,z)}{\partial(b,c)}\right] &= O(\alpha^2) \end{aligned}\right\} \tag{3.1.80}$$

The boundary conditions become:

$$p = 0 \qquad \text{at} \qquad c = 0 \tag{3.1.81a}$$

and

$$z = -h_a x - h_b y - \alpha\left[\frac{x^2}{2}h_{aa} + xyh_{ab} + \frac{y^2}{2}h_{bb}\right] + O(\alpha^2) \qquad \text{at} \quad c = -h(\mathbf{a}) \ . \tag{3.1.81b}$$

Equations (3.1.77)–(3.1.81) are approximate expressions for the three-dimensional equations of motion in the Lagrangian description valid for small $\alpha$, $\beta$, and $\gamma$. In the next section these equations will be manipulated to reduce them to a set of long wave equations in two horizontal coordinates, independent of the vertical coordinate, $c$.

### 3.1.3 The Long Wave Lagrangian Equations

To simplify subsequent manipulations, let us write the horizontal momentum equations, Eqs. (3.1.78a) and (3.1.78b), in vector notation. To do that, notice that the vector:

$$\left( \frac{\partial(p,z)}{\partial(a,c)}, \frac{\partial(p,z)}{\partial(b,c)} \right) \tag{3.1.82}$$

can be written as: $z_c \nabla p - p_c \nabla z$. We also can write:

$$\left(\frac{\partial(p,y)}{\partial(a,b)} + \frac{\partial(z,y)}{\partial(a,b)} \ , \ \frac{\partial(x,p)}{\partial(a,b)} + \frac{\partial(x,z)}{\partial(a,b)}\right) = \nabla(p+z)\cdot\underline{\mathbf{D}}$$

where $\underline{\mathbf{D}}$ is the second order tensor whose representation in this coordinate system is:

$$\underline{\mathbf{D}} = \begin{pmatrix} y_b & -x_b \\ -y_a & x_a \end{pmatrix} \quad . \tag{3.1.83}$$

Hence, in vector notation, Eqs. (3.1.78a) and (3.1.78b) can be written as:

$$\mathbf{x}_{tt} + \nabla(p+z) + \alpha\left[z_c \nabla p - p_c \nabla z + \nabla(p+z)\cdot\underline{\mathbf{D}}\right] - \gamma^2 \vartheta \frac{\partial^3 \mathbf{x}}{\partial c^2 \partial t} = O(\alpha^2) \ . \tag{3.1.84}$$

To introduce the effect of boundary layer dissipation into the long wave equations, we will integrate this equation with respect to the variable $c$ from $c = -h(\mathbf{a})$ to $c = 0$ and then use Eq. (3.1.71) to eliminate the boundary layer gradient term

which results from the integration. The result is:

$$\int_{-h(\mathbf{a})}^{0} \left\{ \mathbf{x}_{tt} + \nabla(p+z) + \alpha\left[z_c \nabla p - p_c \nabla z + \nabla(p+z)\cdot\underline{\mathbf{D}}\right] \right\} dc + \gamma \frac{\partial \mathbf{x}}{\partial t}(\mathbf{a}, -h(\mathbf{a}), t)$$

$$= O(\alpha^2, \alpha\gamma) \quad . \qquad (3.1.85)$$

Here we assumed that $\partial^2 \mathbf{x}/\partial c\,\partial t$ was zero at $c = 0$. This will be true if there is no horizontal shear at the free surface. This will not be true if the surface is contaminated with surfactants and this will be discussed later in Section 5.2 of Chapter 5.

Now let us assume that the unknowns can be expanded in a power series in $\alpha$. Peregrine (1967) used expansions of this type to derive a set of equations in the Eulerian description for long waves in water of varying depth. Let:

$$\mathbf{x} = \sum_{n=0}^{\infty} \alpha^n \mathbf{x}_n(\mathbf{a}, c, t) \qquad z = \sum_{n=0}^{\infty} \alpha^n z_n(\mathbf{a}, c, t) \qquad p = \sum_{n=0}^{\infty} \alpha^n p_n(\mathbf{a}, c, t) \; . \qquad (3.1.86)$$

Numbers used as subscripts will denote the order of the term in these expansions. As usual, the subscripts $a$, $b$, $c$, and $t$ will denote differentiation with respect to these quantities (i.e., $z_{0c} = \partial z_0/\partial c$). In the following, the subscripts 0 and 1 refer to the zero and first order terms in the expansions of Eq. (3.1.86) (i.e., $n = 0, 1$).

If we substitute these expansions into Eqs. (3.1.77), (3.1.85), (3.1.80), (3.1.81), and (3.1.76) and collect terms of similar order in $\alpha$, we get (assuming $\beta = O(\alpha)$ and $\gamma = O(\alpha)$):

To the lowest order, $O(\alpha^0)$:

Continuity:

$$\nabla\cdot\mathbf{x}_0 + z_{0c} = 0 \qquad (3.1.87)$$

Momentum:

$$\int_{-h(\mathbf{a})}^{0} [\mathbf{x}_{0tt} + \nabla(p_0 + z_0)]\, dc = 0 \tag{3.1.88a}$$

$$p_{0c} - \nabla\cdot\mathbf{x}_0 = 0 \tag{3.1.88b}$$

Irrotationality:

$$y_{0ct} = 0 \tag{3.1.89a}$$

$$x_{0ct} = 0 \tag{3.1.89b}$$

$$y_{0at} - x_{0bt} = 0 \tag{3.1.89c}$$

Boundary conditions:

$$p_0 = 0 \qquad c = 0 \tag{3.1.90a}$$

$$z_0 = -\nabla h\cdot\mathbf{x}_0 \qquad c = -h(\mathbf{a}) \tag{3.1.90b}$$

and:

$$z_0 = \eta_0 \qquad c = 0 \quad . \tag{3.1.91}$$

To the next order, $O(\alpha)$:

Continuity:

$$\nabla\cdot\mathbf{x}_1 + z_{1c} + z_{0c}\nabla\cdot\mathbf{x}_0 - x_{0c}z_{0a} - y_{0c}z_{0b} + \frac{\partial(x_0, y_0)}{\partial(a, b)} = 0 \tag{3.1.92}$$

Momentum:

$$\int_{-h(\mathbf{a})}^{0} \left\{ \mathbf{x}_{1tt} + \nabla(p_1 + z_1) + z_{0c}\nabla p_0 - p_{0c}\nabla z_0 + \nabla(p_0 + z_0)\cdot\underline{\mathbf{D}}_0 \right\} dc + \frac{\gamma}{\alpha}\frac{\partial \mathbf{x}_0}{\partial t}(\mathbf{a}, -h(\mathbf{a}), t) = 0 \tag{3.1.93a}$$

$$\frac{\beta}{\alpha} z_{0tt} + p_{1c} - \nabla\cdot\mathbf{x}_1 + p_{0c}\nabla\cdot\mathbf{x}_0 - x_{0c}p_{0a} - y_{0c}p_{0b} - \frac{\partial(x_0, y_0)}{\partial(a, b)} = 0 \tag{3.1.93b}$$

Irrotationality:

$$y_{1ct} - \frac{\beta}{\alpha} z_{0bt} + \frac{\partial(x_0, y_{0t})}{\partial(a,c)} + \frac{\partial(y_0, y_{0t})}{\partial(b,c)} = 0 \qquad (3.1.94a)$$

$$x_{1ct} - \frac{\beta}{\alpha} z_{0at} + \frac{\partial(x_0, x_{0t})}{\partial(a,c)} + \frac{\partial(y_0, x_{0t})}{\partial(b,c)} = 0 \qquad (3.1.94b)$$

$$y_{1at} - x_{1bt} + \frac{\partial(y_{0t}, y_0)}{\partial(a,b)} + \frac{\partial(y_{0t}, z_0)}{\partial(a,c)} - \frac{\partial(x_0, x_{0t})}{\partial(a,b)} - \frac{\partial(x_{0t}, z_0)}{\partial(b,c)} = 0 \qquad (3.1.94c)$$

Boundary conditions:

$$p_1 = 0 \qquad c = 0 \qquad (3.1.95a)$$

$$z_1 = -\nabla h \cdot \mathbf{x}_1 - \frac{1}{2} \mathbf{x}_0 \cdot \underline{\mathbf{H}} \cdot \mathbf{x}_0 \qquad c = -h(\mathbf{a}) \qquad (3.1.95b)$$

and:

$$z_1 = \eta_1 \qquad c = 0 \qquad (3.1.96)$$

where

$$\underline{\mathbf{D}}_0 = \begin{pmatrix} y_{0b} & -x_{0b} \\ -y_{0a} & x_{0a} \end{pmatrix} \qquad \underline{\mathbf{H}} = \begin{pmatrix} h_{aa} & h_{ab} \\ h_{ba} & h_{bb} \end{pmatrix} \qquad (3.1.97)$$

so that $\mathbf{x}_0 \cdot \underline{\mathbf{H}} \cdot \mathbf{x}_0 = x_0^2 h_{aa} + 2 x_0 y_0 h_{ab} + y_0^2 h_{bb}$ .

The procedure now will be to "depth average" these equations to eliminate the vertical coordinate $c$, and then to use these averaged equations to obtain an approximate set of equations of motion that will be accurate to $O(\alpha, \beta, \gamma)$. One way to proceed is to solve the order zero equations, substitute these solutions into the order one equations, and then solve these. As explained by Peregrine (1967), such a procedure will yield a solution valid only for small values of $t$. A better way to proceed is to combine the order zero equations with the order one equations to obtain a single set of equations that includes both the order zero and the order one effects. We must choose the variables that will appear in these equations. For the water surface elevation the only clear choice is the variable $\varsigma(\mathbf{a}, t)$ defined as:

$$\varsigma(\mathbf{a}, t) \equiv \eta_0(\mathbf{a}, t) + \alpha \eta_1(\mathbf{a}, t) \quad . \qquad (3.1.98)$$

Clearly $\zeta(\mathbf{a},t) = \eta(\mathbf{a},t) + O(\alpha^2)$. However, there is not as clear a choice for the particle displacement variables. We cannot define the variables to be $\mathbf{x}_0(\mathbf{a},c,t) + \alpha\mathbf{x}_1(\mathbf{a},c,t)$, analogous to Eq. (3.1.98), because the long wave equations will be independent of $c$, so the variables corresponding to the fluid particle displacements must also be independent of $c$. There are two obvious choices for these variables:

$$\mathbf{x}'(\mathbf{a},t) \equiv \mathbf{x}_0(\mathbf{a},0,t) + \alpha\mathbf{x}_1(\mathbf{a},0,t) \tag{3.1.99}$$

and

$$\overline{\mathbf{x}}(\mathbf{a},t) \equiv \frac{1}{h(\mathbf{a})} \int_{-h(\mathbf{a})}^{0} \{\mathbf{x}_0(\mathbf{a},c,t) + \alpha\mathbf{x}_1(\mathbf{a},c,t)\}\, dc \quad . \tag{3.1.100}$$

The vector $\mathbf{x}'$ corresponds to the displacements of the fluid particles at the free surface and the vector $\overline{\mathbf{x}}$ corresponds to "depth averaged" fluid displacements. We will derive one set of equations of motion for the variables $\zeta$ and $\mathbf{x}'$, and another set of equations for the variables $\zeta$ and $\overline{\mathbf{x}}$. Both sets of equations will be accurate to $O(\alpha,\beta,\gamma)$.

It is worth noting the role that the three vorticity conditions will take in the derivation of the long wave equations. The three vorticity conditions (that each component of the vorticity must be zero) are not additional constraints which the variables $x$, $y$, $z$, and $p$ must satisfy <u>in addition</u> to the continuity equation and the three momentum equations. Since we have only four unknowns, we need only four equations (continuity and momentum). The vorticity conditions can be derived from the continuity and momentum equations (given the appropriate initial conditions). Hence, the three vorticity conditions are consistent and contained in the continuity and momentum equations. Therefore, it is perfectly consistent to use the vorticity conditions in the derivation of the long wave equations if they are useful, but it is <u>not necessary</u> that we do. In fact, it is only the two horizontal

components of vorticity that are found to be convenient in the derivation.

Now from Eqs. (3.1.89a) and (3.1.89b) we get that the zero order horizontal particle displacements are independent of $c$:

$$\mathbf{x}_0 = \mathbf{x}_0(\mathbf{a}, t) \quad . \tag{3.1.101}$$

If we integrate the zero order continuity equation, (3.1.87), from $c = -h(\mathbf{a})$ to any arbitrary value of $c$ and then use the boundary conditions (3.1.90b) and (3.1.101), we can solve for the zero order vertical displacement variable, $z_0$:

$$z_0 = -\nabla\cdot(h\mathbf{x}_0) - c\nabla\cdot\mathbf{x}_0 \quad . \tag{3.1.102}$$

From now on we will denote $h(\mathbf{a})$ simply by $h$. If we evaluate Eq. (3.1.102) at $c = 0$ and use the definition of $\eta_0$, Eq. (3.1.91), we get:

$$\eta_0 = -\nabla\cdot(h\mathbf{x}_0) \quad . \tag{3.1.103}$$

This is the zero order approximation of the long wave continuity equation. Let us now add the continuity equation (3.1.87) to the vertical momentum equation (3.1.88b), integrate this expression with respect to $c$ from any arbitrary value of $c$ up to $c = 0$, and then use the dynamic free surface condition, Eq. (3.1.90a), and the definition of $\eta_0$, Eq. (3.1.91). The result is:

$$p_0 + z_0 = \eta_0 \quad . \tag{3.1.104}$$

This is simply the hydrostatic equation. Finally, if we substitute this last expression into Eq. (3.1.88a) and perform the integration (remembering that $\mathbf{x}_0$ is independent of $c$) we get:

$$\mathbf{x}_{0tt} + \nabla\eta_0 = 0 \quad . \tag{3.1.105}$$

This is the zero order approximation of the long wave momentum equation. This ends the order zero manipulations.

Now let us look at the order one equations. If we substitute Eq. (3.1.101) into the horizontal components of the vorticity equation (3.1.94a) and (3.1.94b), we get:

$$\mathbf{x}_{1c} = \frac{\beta}{\alpha}\nabla z_0 \quad . \tag{3.1.106}$$

Now we can substitute the Eq. (3.1.102) for $z_0$ into this and integrate with respect to $c$ from any arbitrary value of $c$ to $c = 0$. The result is:

$$\mathbf{x}_1 = \mathbf{x}_1\,|_{c=0} - \frac{\beta}{\alpha}\left\{c\nabla[\nabla\cdot(h\mathbf{x}_0)] + \frac{c^2}{2}\nabla(\nabla\cdot\mathbf{x}_0)\right\} \quad . \tag{3.1.107}$$

This is the first order correction to the horizontal particle displacement vector. The lowest order contribution, Eq. (3.1.101), is independent of the vertical coordinate $c$. However, the additional term, $\mathbf{x}_1$, is dependent on $c$; it represents the effect of nonhydrostatic vertical fluid accelerations that lead to frequency dispersion when wave propagation is considered.

Now if we add Eqs. (3.1.92) and (3.1.93b) and use Eqs. (3.1.101) and (3.1.104) the result reduces to:

$$\frac{\partial}{\partial c}(p_1 + z_1) = -\frac{\beta}{\alpha}z_{0tt} \quad . \tag{3.1.108}$$

If we integrate this expression from any arbitrary value of $c$ to $c = 0$ and make use of Eqs. (3.1.95a), (3.1.96), and (3.1.102) we get:

$$p_1 + z_1 = \eta_1 + \frac{\beta}{\alpha}\left\{c\nabla\cdot(h\mathbf{x}_{0tt}) + \frac{c^2}{2}\nabla\cdot\mathbf{x}_{0tt}\right\} \quad . \tag{3.1.109}$$

This equation represents the deviation of the pressure from hydrostatic due to vertical fluid accelerations. If we substitute Eqs. (3.1.102), (3.1.104), (3.1.107), and (3.1.109) into the integrated horizontal momentum equations (3.1.93a), use Eq. (3.1.101), and perform the integration over the variable $c$ we get:

$$\mathbf{x}_{1tt}\,|_{c=0} + \nabla\eta_1 - (\nabla\cdot\mathbf{x}_0)\nabla\eta_0 + \nabla\eta_0\cdot\underline{\mathbf{D}}_0 + \frac{\gamma}{\alpha h}\mathbf{x}_{0t} = 0 \quad . \tag{3.1.110}$$

Finally, if we solve Eq. (3.1.92) for $z_{1c}$, integrate with respect to $c$ from $c = -h$ to $c = 0$ and use Eqs. (3.1.90b), (3.1.91), (3.1.95b), (3.1.96), (3.1.101), and (3.1.107), we can solve for $\eta_1$ to get:

$$\eta_1 = -\frac{1}{2}\mathbf{x}_0\cdot\underline{\mathbf{H}}\cdot\mathbf{x}_0 - \nabla\cdot[h\mathbf{x}_1|_{c=0}] - \nabla\cdot\mathbf{x}_0[\eta_0 + \nabla h\cdot\mathbf{x}_0] - h\frac{\partial(x_0,y_0)}{\partial(a,b)} \\ - \frac{\beta}{\alpha}\nabla\cdot\left\{\frac{h^2}{2}\nabla[\nabla\cdot(h\mathbf{x}_0)] - \frac{h^3}{6}\nabla(\nabla\cdot\mathbf{x}_0)\right\} \quad . \tag{3.1.111}$$

Now for the moment let us just consider the variables $\zeta$ and $\mathbf{x}'$. We can obtain the long wave continuity equation in terms of these variables by adding Eq. (3.1.103) to $\alpha$ times Eq. (3.1.111) and using Eqs. (3.1.98) and (3.1.99):

$$\boxed{\begin{aligned}\zeta = & -\nabla h\cdot\mathbf{x}' - \frac{\alpha}{2}\mathbf{x}'\cdot\underline{\mathbf{H}}\cdot\mathbf{x}' - h\frac{\left[\nabla\cdot\mathbf{x}' + \alpha\frac{\partial(x',y')}{\partial(a,b)}\right]}{1+\alpha\nabla\cdot\mathbf{x}'} \\ & - \beta\nabla\cdot\left\{\frac{h^2}{2}\nabla[\nabla\cdot(h\mathbf{x}')] - \frac{h^3}{6}\nabla(\nabla\cdot\mathbf{x}')\right\} \quad + O(\alpha\beta,\alpha^2)\end{aligned}} \quad . \tag{3.1.112}$$

The momentum equations can be obtained in the same way by adding Eq. (3.1.105) to $\alpha$ times Eq. (3.1.110) and using Eqs. (3.1.98) and (3.1.99):

$$\mathbf{x}'_{tt} + \frac{\gamma}{h}\mathbf{x}'_t + \nabla\zeta(1-\alpha\nabla\cdot\mathbf{x}') + \alpha\nabla\zeta\cdot\underline{\mathbf{D}}' = O(\alpha\beta,\alpha\gamma,\alpha^2) \tag{3.1.113}$$

where the definition of $\underline{\mathbf{D}}'$ is the same as that for $\underline{\mathbf{D}}$ in Eq. (3.1.83), but with primes on each of its entries. If we multiply Eq. (3.1.113) by $(1+\alpha\nabla\cdot\mathbf{x}')$ we get:

$$\boxed{(1+\alpha\nabla\cdot\mathbf{x}')[\mathbf{x}'_{tt} + \frac{\gamma}{h}\mathbf{x}'_t] + \alpha\nabla\zeta\cdot\underline{\mathbf{D}}' + \nabla\zeta = O(\alpha\beta,\alpha\gamma,\alpha^2)} \quad . \tag{3.1.114}$$

These are the momentum equations in terms of the variables $\zeta$ and $\mathbf{x}'$.

Now let us consider the variables $\zeta$ and $\overline{\mathbf{x}}$. We can obtain an expression for $\overline{\mathbf{x}}$ in terms of $\mathbf{x}_0(\mathbf{a},t)$, and $\mathbf{x}_1(\mathbf{a},0,t)$ if we substitute Eqs. (3.1.101) and (3.1.107) into Eq. (3.1.100) and perform the integration:

$$\overline{\mathbf{x}} = \mathbf{x}_0 + \alpha \mathbf{x}_1 \,|_{c=0} + \beta\left\{\frac{h}{2}\nabla[\nabla\cdot(h\mathbf{x}_0)] - \frac{h^2}{6}\nabla(\nabla\cdot\mathbf{x}_0)\right\} \quad . \tag{3.1.115}$$

Comparing this with the expression for $\mathbf{x}'$, Eq. (3.1.99), we see that:

$$\overline{\mathbf{x}} = \mathbf{x}' + \beta\left\{\frac{h}{2}\nabla[\nabla\cdot(h\mathbf{x}_0)] - \frac{h^2}{6}\nabla(\nabla\cdot\mathbf{x}_0)\right\} \quad . \tag{3.1.116}$$

Along a shoreline where $h \to 0$ we have $\overline{\mathbf{x}} = \mathbf{x}'$. In terms of $\zeta$ and $\overline{\mathbf{x}}$ the long wave continuity and momentum equations are:

$$\boxed{\zeta = -\nabla h\cdot\overline{\mathbf{x}} - \frac{\alpha}{2}\overline{\mathbf{x}}\cdot\underline{\mathbf{H}}\cdot\overline{\mathbf{x}} - h\frac{\left[\nabla\cdot\overline{\mathbf{x}} + \alpha\frac{\partial(\overline{x},\overline{y})}{\partial(a,b)}\right]}{1+\alpha\nabla\cdot\overline{\mathbf{x}}} + O(\alpha\beta,\alpha^2)} \tag{3.1.117}$$

$$\boxed{(1+\alpha\nabla\cdot\overline{\mathbf{x}})[\overline{\mathbf{x}}_{tt} + \frac{\gamma}{h}\overline{\mathbf{x}}_t] + \alpha\nabla\zeta\cdot\overline{\underline{\mathbf{D}}} + \nabla\zeta = \beta\left\{\frac{h}{2}\nabla[\nabla\cdot(h\overline{\mathbf{x}}_{tt})] - \frac{h^2}{6}\nabla(\nabla\cdot\overline{\mathbf{x}}_{tt})\right\} + O(\alpha\beta,\alpha\gamma,\alpha^2)} \tag{3.1.118}$$

where the definition of $\overline{\underline{\mathbf{D}}}$ is the same as that for $\underline{\mathbf{D}}$ in Eq. (3.1.83) but with bars over each of its entries. Equations (3.1.117) and (3.1.118) are the long wave equations which will be used in the finite element numerical model. Note that in Eqs. (3.1.117) and (3.1.118) the dispersion terms are contained in the momentum equations, whereas in Eqs. (3.1.112) and (3.1.114) they are contained in the continuity equation.

Note that to the same order of accuracy the continuity equation (3.1.117) can be written as:

$$\boxed{\varsigma = \frac{1}{\alpha}\left\{\frac{h(\mathbf{a})}{1+\alpha\nabla\cdot\overline{\mathbf{x}}+\alpha^2\frac{\partial(\overline{x},\overline{y})}{\partial(a,b)}} - h(\mathbf{a}+\alpha\overline{\mathbf{x}})\right\} + O(\alpha\beta,\alpha^2)} \quad . \qquad (3.1.119)$$

This equation does not explicitly contain any spatial derivatives of $h$ since they have been absorbed into the term $h(\mathbf{a}+\alpha\overline{\mathbf{x}})$. This equation can be used in place of Eq. (3.1.117). However, for clarity, the development of the finite element model in Section 3.4 will treat only Eq. (3.1.117).

Now let us look at the vorticity. Notice that we did not use the vertical component of irrotationality condition represented by Eqs. (3.1.89c) and (3.1.94c) in deriving the long wave equations. As mentioned earlier, this does not mean that we still need to enforce this condition on the solution. It is merely a statement of what condition the *exact* solution $\mathbf{x}$ and $z$ will satisfy. Let us see what this condition implies for the *approximate* solutions $\mathbf{x}'$ and $\overline{\mathbf{x}}$. If we use Eq. (3.1.101) and combine Eqs. (3.1.89c) and (3.1.94c), the irrotationality condition can be written as:

$$y_{at} - x_{bt} + \alpha\left\{\frac{\partial(y_t,y)}{\partial(a,b)} + \frac{\partial(x_t,x)}{\partial(a,b)}\right\} = O(\alpha^2) \qquad (3.1.120)$$

or

$$\mathcal{W}[\mathbf{x}] = O(\alpha^2) \qquad (3.1.121)$$

where $\mathcal{W}$ represents the vorticity operator in Eq. (3.1.120). Equation (3.1.120) must be satisfied by any solution to the three-dimensional continuity and momentum equations (exterior to the boundary layers where viscous effects can be ignored), provided the vorticity is zero at some point in time. Using Eqs. (3.1.99), (3.1.101), and (3.1.107) we can write this vorticity condition in terms of $\mathbf{x}'$. The

result is:

$$\mathcal{W}[\mathbf{x}'] = O(\alpha\beta, \alpha^2) \quad ; \tag{3.1.122}$$

i.e., $\mathbf{x}'$ is an irrotational vector field. This is to be expected because $\mathbf{x}(\mathbf{a}, c, t)$ is irrotational and from Eq. (3.1.99) $\mathbf{x}'(\mathbf{a}, t)$ differs from $\mathbf{x}(\mathbf{a}, 0, t)$ by terms of only $O(\alpha^2)$. We can also obtain the vorticity condition satisfied by $\overline{\mathbf{x}}$. Using Eqs. (3.1.120), (3.1.116), and (3.1.122) we get:

$$\mathcal{W}[\overline{\mathbf{x}}] = \beta\left\{\frac{1}{2}h_a\frac{\partial}{\partial b}\nabla\cdot(h\overline{\mathbf{x}}_t) - \frac{1}{2}h_b\frac{\partial}{\partial a}\nabla\cdot(h\overline{\mathbf{x}}_t) + \frac{h}{3}h_b\frac{\partial}{\partial a}\nabla\cdot\overline{\mathbf{x}}_t - \frac{h}{3}h_a\frac{\partial}{\partial b}\nabla\cdot\overline{\mathbf{x}}_t\right\}$$
$$+ O(\alpha\beta, \alpha^2) \quad . \tag{3.1.123}$$

Therefore, provided $\nabla h \neq 0$ and the flow is not restricted to one horizontal coordinate, $\overline{\mathbf{x}}$ is in general a rotational vector field with vorticity of $O(\beta)$. Variations in the still water depth $h(\mathbf{a})$ generate the vorticity represented by the right hand side of Eq. (3.1.123) (e.g., see Wu 1981). That is perfectly acceptable; the vector $\mathbf{x}(\mathbf{a}, c, t)$ must be irrotational but its "depth average" $(1/h)\int_{-h}^{0}\mathbf{x}\,dc$ need not be.

### 3.1.3.1 Dispersive Range of Validity of the Long Wave Equations

The long wave equations derived in Section 3.1.3 are based on the assumption that the parameters $\alpha$, $\beta$, and $\gamma$ satisfiy: $O(\alpha) = O(\beta) = O(\gamma) < O(1)$. Therefore, these equations will cease to be valid as $\alpha$, $\beta$, and $\gamma$ grow large and become $O(1)$. It is impossible to set a precise upper bound on how large these parameters can become before the solution is invalid. However, we can get an idea of the range of validity of the dispersive correction terms in the long wave equations of motion. Since we can solve the fully dispersive linear inviscid case exactly for constant depth, we can check the results of this theory with the results of the long wave model equations and see how the two differ as we vary the amount of dispersion. Unfortunately, we cannot solve the nonlinear problem

exactly, so we cannot make a similar comparison to investigate the nonlinear range of validity.

It is well known that according to linear inviscid dispersive theory in a region of constant depth, $h_0$, the dispersion relation, phase speed, and group speed for a plane harmonic wave are given, respectively, by the following expressions:

$$\omega^2 = gk \tanh kh_0 \tag{3.1.124}$$

$$c = \sqrt{gh_0}\sqrt{\frac{\tanh kh_0}{kh_0}} \tag{3.1.125}$$

$$c_g = \frac{c}{2}\left(1 + \frac{2kh_0}{\sinh 2kh_0}\right) \quad . \tag{3.1.126}$$

We can expand these expressions in powers of $kh_0$ as:

$$\omega^2 = gh_0k^2\left(1 - \frac{1}{3}(kh_0)^2 + \frac{2}{15}(kh_0)^4 + O(kh_0)^6\right) \tag{3.1.127}$$

$$c = \sqrt{gh_0}\left(1 - \frac{1}{6}(kh_0)^2 + \frac{19}{360}(kh_0)^4 + O(kh_0)^6\right) \tag{3.1.128}$$

$$c_g = \sqrt{gh_0}\left(1 - \frac{1}{2}(kh_0)^2 + \frac{19}{72}(kh_0)^4 + O(kh_0)^6\right) \quad . \tag{3.1.129}$$

Here, the quantity $(kh_0)^2$ plays the role of the dispersion parameter, $\beta$.

If we neglect the nonlinear and dissipative terms and specialize the long wave equations (3.1.117) and (3.1.118) to one horizontal dimension for a constant depth, $h_0$, we can eliminate the particle displacement variable $\overline{x}$ between the two equations and obtain a single equation for the water surface elevation, which we will denote by $\eta$. In dimensional variables we get:

$$\eta_{tt} - gh_0\eta_{aa} = \frac{h_0^2}{3}\eta_{aatt} \quad . \tag{3.1.130}$$

The term on the right hand side of this equation is the dispersive correction term. If we assume a solution of the form $\eta \sim e^{i(ka-\omega t)}$, we obtain the following dispersion

relation (e.g., see Whitham 1974):

$$\omega^2 = \frac{gh_0k^2}{1+\frac{1}{3}(kh_0)^2} = gh_0k^2\left(1-\frac{1}{3}(kh_0)^2+\frac{1}{9}(kh_0)^4+O(kh_0)^6\right) . \quad (3.1.131)$$

Comparing this with Eq. (3.1.127) we see that the model dispersion relation agrees with the exact one to $O(kh_0)^2$. We find the same sort of agreement regarding the phase and group speeds. From Eq. (3.1.131) the phase and group speeds are:

$$c = \frac{\sqrt{gh_0}}{\left[1+\frac{1}{3}(kh_0)^2\right]^{1/2}} = \sqrt{gh_0}\left(1-\frac{1}{6}(kh_0)^2+\frac{1}{24}(kh_0)^4+O(kh_0)^6\right) \quad (3.1.132)$$

$$c_g = \frac{\sqrt{gh_0}}{\left[1+\frac{1}{3}(kh_0)^2\right]^{3/2}} = \sqrt{gh_0}\left(1-\frac{1}{2}(kh_0)^2+\frac{5}{24}(kh_0)^4+O(kh_0)^6\right) \quad (3.1.133)$$

In contrast, the classic nondispersive long wave expressions for $c$ and $c_g$ are:

$$c = c_g = \sqrt{gh_0} \quad . \quad (3.1.134)$$

In Table 3.1.1 the exact linear dispersive expressions for $c$ and $c_g$ given by Eqs. (3.1.125) & (3.1.126) are compared with both the dispersive long wave expressions of Eqs. (3.1.132) & (3.1.133) and with the nondispersive result of Eq. (3.1.134). The first column lists values of the parameter $h_0/\lambda$ and the second column lists the corresponding values of $kh_0 = 2\pi h_0/\lambda$, where $\lambda$ denotes the wavelength. Increasing values of these parameters correspond to increasing the importance of dispersion. The two columns labelled "Nondispersive Theory" list the deviations of the nondispersive results of Eq. (3.1.134) from the exact linear result of Eqs. (3.1.125) & (3.1.126), and the last two columns, labelled "$1^{st}$ Order Theory," list the deviations of the dispersive long wave expressions of Eqs. (3.1.132) & (3.1.133) from the exact linear expressions. The deviations listed in this table for the phase speed $c$ are the percentage errors defined as $(c_{\text{approx}} - c_{\text{exact}})/c_{\text{exact}} \times 100$. Here $c_{\text{exact}}$ denotes the exact linear expression of Eq. (3.1.125) and $c_{\text{approx}}$

denotes either the nondispersive result of Eq. (3.1.134) for the deviations in the third column or the dispersive long wave result of Eq. (3.1.132) for the fifth column. The percentage errors for $c_g$ are defined similarly.

In Table 3.1.1 note that the first order dispersive theory is much more accurate than the classical nondispersive long wave theory. Note also that the nondispersive theory consistently overpredicts $c$ and $c_g$, whereas the opposite is true for the $1^{st}$ order theory. The classic upper limit of applicability of nondispersive theory is usually taken to be $h_0/\lambda = 0.05$ (Eagleson & Dean 1966). Beyond this value, the error between nondispersive theory and exact linear dispersive theory can grow unacceptable for many applications. The line in Table 3.1.1 corresponding to this limit is written in boldface. For the nondispersive theory there is an error of approximately 1.6 % in $c$ and 5 % in $c_g$ at this value of $h_0/\lambda$. The group speed $c_g$ is always less than $c$, so the error in $c_g$ is always greater than that in $c$. However, for the $1^{st}$ order theory the errors in $c$ and $c_g$ are extremely small, only about 0.01 % and 0.05 %, respectively.

The other line in Table 3.1.1 that is written in boldface corresponds to the analogous upper limit of applicability of the $1^{st}$ order theory; it lies at $h_0/\lambda = 0.17$. At this value of $h_0/\lambda$ the error in $c_g$ for the $1^{st}$ order theory is about 5 %, the same error in $c_g$ for the nondispersive theory at the classic limit, $h_0/\lambda = 0.05$. Note that at $h_0/\lambda = 0.17$ the corresponding error in $c$ is less than 1 % for the $1^{st}$ order theory, whereas the errors in $c$ and $c_g$ for the nondispersive theory are very large, about 16 % and 54 %, respectively. The last line of the table, $h_0/\lambda = 0.17$, corresponds to $h_0/\lambda = 0.2$. This is the value of $h_0/\lambda$ for which the error in the phase speed $c$ for the $1^{st}$ order theory is about 1.6 %, the same error in $c$ for the nondispersive theory at the classic limit, $h_0/\lambda = 0.05$. Therefore, this could also be defined as the upper limit of applicability of the $1^{st}$ order theory. However, the group speed $c_g$ is of greater dynamical interest than the phase speed $c$, so

Table 3.1.1

Percent error in phase speed $c$ and group speed $c_g$ from that computed by linear dispersive theory.

| | | Nondispersive Theory | | 1st Order Theory | |
|---|---|---|---|---|---|
| $h_0/\lambda$ | $kh_0$ | $c$ | $c_g$ | $c$ | $c_g$ |
| 0.00 | 0.000 | 0.00 | 0.00 | -0.00 | -0.00 |
| 0.01 | 0.063 | 0.07 | 0.20 | -0.00 | -0.00 |
| 0.02 | 0.126 | 0.26 | 0.79 | -0.00 | -0.00 |
| 0.03 | 0.188 | 0.59 | 1.77 | -0.00 | -0.01 |
| 0.04 | 0.251 | 1.04 | 3.15 | -0.00 | -0.02 |
| **0.05** | **0.314** | **1.62** | **4.92** | **-0.01** | **-0.05** |
| 0.06 | 0.377 | 2.32 | 7.07 | -0.02 | -0.11 |
| 0.07 | 0.440 | 3.13 | 9.61 | -0.04 | -0.20 |
| 0.08 | 0.503 | 4.06 | 12.53 | -0.06 | -0.33 |
| 0.09 | 0.565 | 5.09 | 15.81 | -0.10 | -0.51 |
| 0.10 | 0.628 | 6.22 | 19.46 | -0.15 | -0.76 |
| 0.11 | 0.691 | 7.44 | 23.46 | -0.21 | -1.09 |
| 0.12 | 0.754 | 8.75 | 27.79 | -0.29 | -1.49 |
| 0.13 | 0.817 | 10.14 | 32.45 | -0.38 | -2.00 |
| 0.14 | 0.880 | 11.60 | 37.42 | -0.49 | -2.60 |
| 0.15 | 0.942 | 13.13 | 42.69 | -0.63 | -3.31 |
| 0.16 | 1.005 | 14.72 | 48.19 | -0.78 | -4.13 |
| **0.17** | **1.068** | **16.37** | **53.96** | **-0.95** | **-5.06** |
| 0.18 | 1.131 | 18.07 | 59.95 | -1.14 | -6.11 |
| 0.19 | 1.194 | 19.80 | 66.12 | -1.36 | -7.27 |
| 0.20 | 1.257 | 21.58 | 72.47 | -1.59 | -8.54 |

the upper limit of applicability of the 1st order theory, $h_0/\lambda = 0.17$, was based on the error in $c_g$, not $c$.

Therefore, although this does not set an absolute upper limit on the range of validity of the 1st order theory, it does suggest that the inclusion of the 1st order dispersive correction terms in the long wave equations permits us to accurately simulate waves with a time scale or length scale at least three times smaller than that possible without the correction terms (for a given water depth). This is important even if an incident wave system does satisfy $h_0/\lambda < 0.05$ because

nonlinear effects within a bay or harbour may generate higher harmonics that lie outside the classic long wave limit.

## 3.2 Response of Variable Depth Narrow Harbours

To investigate the effect of variable depth on the response of harbours to long wave excitation, let us specialize to narrow harbours so that the complexity of the problem can be reduced and we can extract important information using analytical tools. We will neglect the nonlinear terms in the equations of motion, so it is immaterial whether we choose the Lagrangian or the Eulerian description. Let us choose the Eulerian description. Since there will be no conflict in this section, we will not subscript the Eulerian variables with the letter E. Much of the analysis of this section will be valid for any narrow harbour with arbitrary bathymetry where the flow within the harbour can be approximated by two-dimensional wave theory within the harbour with wave propagation in a single coordinate direction.

The solution domain is divided into two nonoverlapping regions, I and II. See Fig. 3.2.1 for a definition sketch of the problem. The stars refer to the dimensional variable; i.e., $x^*$ is the dimensional horizontal coordinate measuring distance away from the still shoreline. The variable $\tilde{x}^*$ is similar but it measures distance away from the harbour entrance. The coordinate $x^*$ is convenient for describing the flow within the harbour, whereas the coordinate $\tilde{x}^*$ is convenient for describing the flow in the outer region. Figure 3.2.1 shows the still water depth gradually diminishing to zero at the shore CD but this need not be so. Instead, the still water depth may be non zero along CD in which case CD would correspond to a vertical wall. In addition, the points C and D may coalesce to a single point. Region I consists of the harbour itself and Region II is the open ocean outside the harbour. Where confusion is possible, variables in the two regions will be

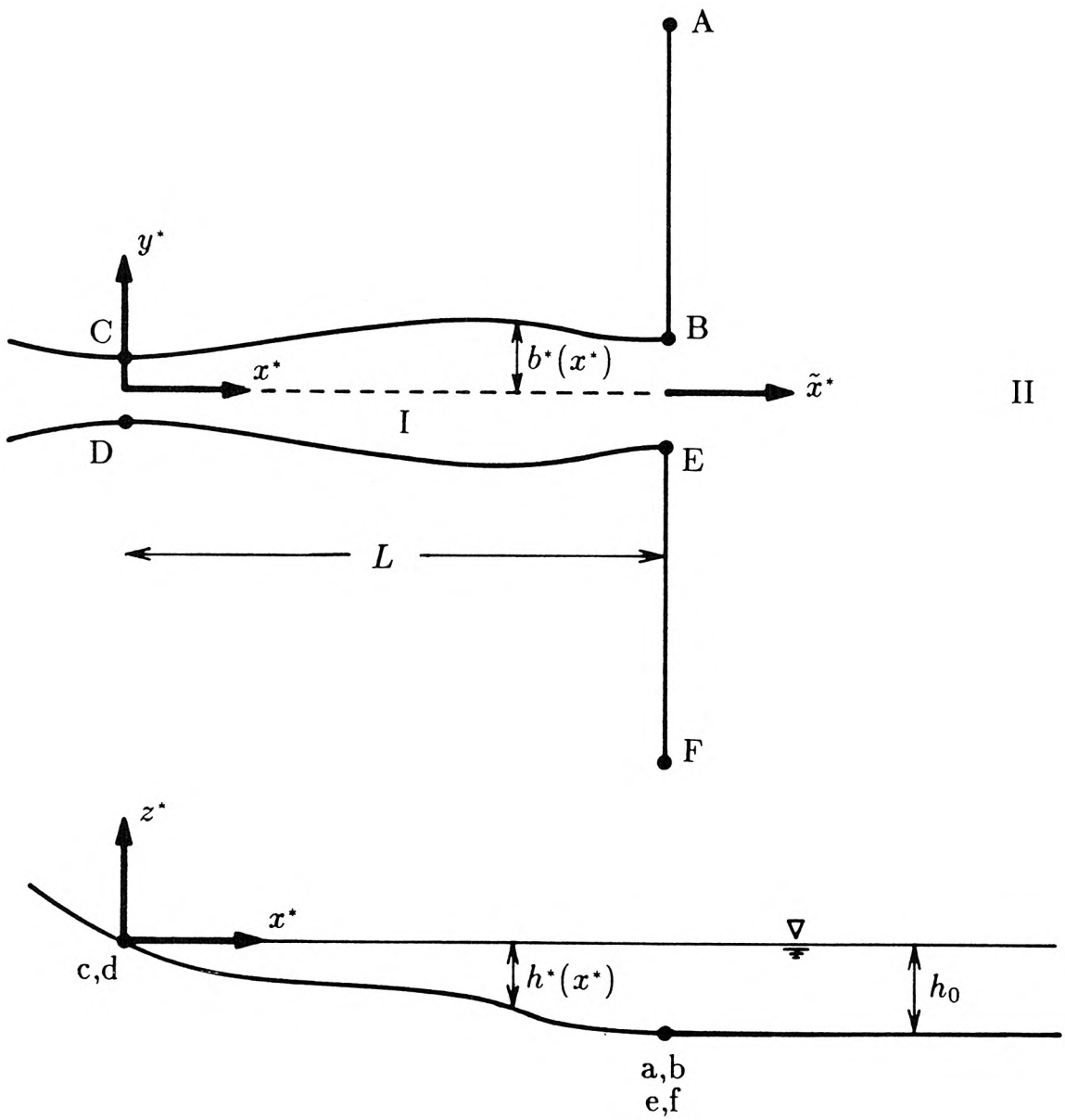


Fig. 3.2.1 Definition sketch of harbour geometry.

differentiated with the subscripts I and II (e.g., $\eta_{\rm I}$ and $\eta_{\rm II}$). It will be assumed that the incident wave propagates normal to the coastline.

We will quantify the response of the harbour in two different ways. First, we will compute its amplification factor $R$, which is traditionally defined as one-half of the ratio of the amplitude of the wave motion at $x = 0$ to the amplitude of the incident wave. The factor of one-half is included because the amplitude at a plane vertical wall with no harbour present is twice that of the incident wave (for normal incidence). The amplification factor, $R$, can be evaluated in places other than at the shore, $x = 0$. In fact, the laboratory experiments that were performed to compare with this theory, and which will be discussed later in Section 5.2 of Chapter 5, measured the harbour response at the centre, $x = 1/2$. However, for clarity, in this derivation of the harbour response theory we will consider only the amplification factor, $R$, evaluated at the shore or backwall, $x = 0$.

Although the amplification factor, $R$, defined in the manner just described is important, it can be misleading because it incorporates two separate effects. The wave amplitude at $x = 0$ is dependent not only on the trapping of energy within the harbour due to an abrupt change in the wave impedance at the harbour entrance, but also on the shoaling and geometrical amplification of the waves due to variable bathymetry and harbour sidewall geometry within the harbour. Therefore, it is of interest to define an alternate amplification factor, $R'$, which quantifies only the energy trapping due to the coupling of the harbour at its entrance with the semi-infinite ocean but which does not include the wave amplification due to variable bathymetry and sidewall geometry *within* the harbour. Therefore, let us define $S$ to be the amplification factor for the same harbour which is connected to an infinitely long constant depth channel, instead of a semi-infinite open sea (the width of the channel is chosen to be the same as the width of the entrance of the harbour so the width is continuous across the entrance). Then $S$ will quantify

the shoaling and geometrical amplification of waves due to variable bathymetry and sidewall geometry within the harbour. The possible abrupt change of the bathymetry and harbour sidewall geometry at the entrance between the harbour and the channel may also cause a small amount of energy to be reflected, so $S$ may also exhibit resonant behaviour at certain frequencies, but, in general, the effect is much smaller than the resonant amplification that results from the coupling of the harbour with the semi-infinite ocean. The alternate amplification factor, $R'$, can then be defined as the ratio of the traditional amplification factor, $R$, which includes both wave amplification processes, with the amplification factor, $S$, which includes only the wave shoaling and geometrical amplification processes; i.e.,

$$R' \equiv \frac{R}{S} \quad . \tag{3.2.1}$$

Both of the amplification factors $R$ and $R'$ are obtained by normalizing the wave amplitude at $x = 0$ in Fig. 3.2.1 by some quantity. For $R$, this quantity is the amplitude which would be measured at the entrance of the harbour if the harbour entrance were closed off and the incident wave reflected from a plane vertical wall. For $R'$, this quantity is the amplitude which would be measured at the shore of the harbour, $x = 0$, if the harbour were connected to an infinitely constant depth channel instead of a semi-infinite ocean. For a constant depth rectangular harbour, both of these quantities will be the same. Hence, for a constant depth rectangular harbour, $R'$ will be identical to $R$ but for other types of harbours they will, in general, be different.

### 3.2.1 General Assumptions

We will make the following assumptions:

(i) still water depth:

a) The still water depth in region II is constant and equal to $h_0$.

b) Within the harbour the still water depth, $h^*$, is a function of $x^*$ only.

(ii) boundaries:

a) The coastlines AB and EF are straight and extend out to $y^* \pm \infty$. All energy is perfectly reflected.

b) The harbour sidewalls BC and DE are vertical and perfectly reflecting.

c) The wave height is finite and all energy is reflected at the shoreline CD.

d) The width of the harbour, $2b^*(x^*)$, varies slowly with $x^*$.

e) The ratio of the width of the harbour to its length, $2b^*(x^*)/L$, is small.

(iii) incident wave system:

a) The propagation direction of the incident wave system is normal to the coastline.

b) The departure of the water surface from its still level is small everywhere so that the nonlinear terms in the equations of motion may be neglected.

c) The ratio of the still water depth to a characteristic wavelength scale is small so that dispersive effects may be neglected.

d) The ratio of the width of the harbour to a characteristic wavelength scale is small.

We will consider only one source of viscous dissipation: entrance flow separation losses due to flow passing through the entrance of the harbour BG. However, this analysis will also model the radiation of energy from the harbour entrance to the open sea and this process can also be viewed as a source of (inviscid) dissipation as far at the response of the harbour is concerned.

### 3.2.2 Equations of Motion

The equations of motion can be obtained by specializing the long wave equations derived in Section 3.1 to one horizontal coordinate and by discarding the nonlinear, dispersive, and laminar viscous terms. The continuity equation and momentum equations reduce to the following familiar expressions in the Eulerian description:

$$\frac{\partial \eta^*}{\partial t^*} = -\frac{\partial}{\partial x^*}(h^* u^*) - \frac{\partial}{\partial y^*}(h^* v^*) \tag{3.2.2}$$

$$\frac{\partial u^*}{\partial t^*} = -g\frac{\partial \eta^*}{\partial x^*} \tag{3.2.3}$$

$$\frac{\partial v^*}{\partial t^*} = -g\frac{\partial \eta^*}{\partial y^*} \tag{3.2.4}$$

where $h^*$ is the (dimensional) still water depth.

Let us assume the incident wave is a harmonic plane wave:

$$\eta^*_{\text{inc}}(\tilde{x}^*, t^*) = A^*_{\text{inc}} e^{+ik(\tilde{x}^* + \sqrt{gh_0}\, t^*)} \quad . \tag{3.2.5}$$

Let us choose the following nondimensionalization:

$$x = \frac{x^*}{L}, \quad \tilde{x} = \frac{\tilde{x}^*}{L} \qquad y = \frac{y^*}{b^*(L)} \qquad t = t^*\frac{\sqrt{gh_0}}{L}$$

$$u = \frac{u^*}{\sqrt{gh_0}}\frac{h_0}{H} \qquad v = \frac{v^*}{\sqrt{gh_0}} \qquad \eta = \frac{\eta^*}{h_0}$$

$$h = \frac{h^*}{h_0} \qquad b = \frac{b^*}{b^*(L)} \quad .$$

In terms of these variables the governing equations and incident wave system become:

$$\frac{\partial \eta}{\partial t} = -\frac{\partial}{\partial x}(hu) - \frac{1}{\epsilon}\frac{\partial}{\partial y}(hv) \tag{3.2.6}$$

$$\frac{\partial u}{\partial t} = -\frac{\partial \eta}{\partial x} \tag{3.2.7}$$

$$\frac{\partial v}{\partial t} = -\frac{\partial \eta}{\partial y} \tag{3.2.8}$$

$$\eta_{\text{inc}} = A_{\text{inc}} e^{+i\kappa(\tilde{x}+t)} \tag{3.2.9}$$

where

$$A_{\text{inc}} = \frac{A^*_{\text{inc}}}{h_0} \qquad \kappa = kL \qquad \epsilon = \frac{b^*(L)}{L} \quad . \tag{3.2.10}$$

We have chosen a nondimensionalization based on the harbour geometry and the still water depth instead of on the characteristics of the incident wave system. This is because we would like to imagine the harbour geometry as fixed and then determine the response of the harbour as we vary the wavelength of the incident wave system. However, the laboratory experiments to be discussed in Chapters 4 and 5 actually determined the harbour response by varying the harbour dimensions and keeping the incident wave constant.

For region II we can combine Eqs. (3.2.6)-(3.2.8) (with h=1) to obtain a single equation for $\eta$:

$$\frac{\partial^2 \eta}{\partial t^2} = \frac{\partial^2 \eta}{\partial x^2} + \frac{1}{\epsilon^2}\frac{\partial^2 \eta}{\partial y^2} \quad . \tag{3.2.11}$$

By virtue of assumptions (ii) d) and (iii) d), we will treat the flow as two-dimensional with wave propagation in a single coordinate direction in region I. We can obtain the appropriate continuity equation for this region by integrating Eq. (3.2.6) across the width of the harbour under the assumption that $\eta$ and $u$ are independent of $y$:

$$\begin{aligned}\frac{\partial \eta}{\partial t} &= -\frac{\partial}{\partial x}(hu) - \frac{1}{2\epsilon\, b(x)} \int_{-b(x)}^{+b(x)} \frac{\partial}{\partial y}(hv)\, dy \\ &= -\frac{\partial}{\partial x}(hu) - \frac{h}{2\epsilon\, b(x)} \left[ v|_{y=+b(x)} - v|_{y=-b(x)} \right] \quad . \end{aligned} \tag{3.2.12}$$

We can approximate the velocities $v$ at $y = \pm b(x)$ by:

$$v\,|_{y=\pm b(x)} = \pm \epsilon u \frac{db}{dx} \quad . \tag{3.2.13}$$

Then Eq. (3.2.12) becomes:

$$\frac{\partial \eta}{\partial t} = -\frac{1}{b}\frac{\partial}{\partial x}(hbu) \quad . \tag{3.2.14}$$

We can combine this with Eq. (3.2.7) to get the following equation for the wave motion in region I:

$$\frac{\partial^2 \eta}{\partial t^2} = \frac{1}{b}\frac{\partial}{\partial x}(hb\frac{\partial \eta}{\partial x}) \quad . \tag{3.2.15}$$

### 3.2.3 Matching Conditions

The solution for the wave motion in regions I and II will be obtained by the following general method. The solution in region I will be found by solving Eq. (3.2.15). It will contain an unknown amplitude and phase parameter. Then, the solution in region II will be found by solving Eq. (3.2.11) in terms of these same two parameters. Finally, these two parameters will be determined by connecting the two solutions, using the appropriate matching conditions. Since there are two parameters, there must be two matching conditions.

The first matching condition introduces a head loss across the entrance BG, and therefore introduces dissipation. The introduction of harbour entrance losses removes the well known harbour paradox phenomenon (Miles & Munk 1961). Without these losses the response of a harbour can grow unbounded at its resonant frequencies as the harbour entrance is made narrower and narrower. This is because radiation damping decreases and approaches zero as the harbour entrance width goes to zero. However, entrance dissipation does not scale in this manner and therefore, if it is included in the analysis, the harbour response remains well behaved in this limit.

In most inviscid wave theories it is generally assumed that the fluid moves tangential to all solid boundaries, even if the boundary contains sharp corners.

In reality, viscous effects will force the flow to separate if there is an unfavorable pressure gradient, and the generation of turbulence by this separated flow can be responsible for a significant amount of energy dissipation. An example of this is the case where waves propagate through a narrow constriction at a harbour entrance. This is of particular interest to this research. For such a case the following dimensional quadratic head loss formula in the Eulerian description has been used with success; e.g., see Mei, Liu & Ippen (1974):

$$\eta^- - \eta^+ = \frac{f}{2g} u|u| + \frac{L}{g}\frac{\partial u}{\partial t} \tag{3.2.16}$$

$$u^- = u^+ \tag{3.2.17}$$

where $\eta^-$ and $\eta^+$ are the free surface displacements on each side of the constriction and $u$ is the averaged horizontal velocity through the constriction. Dimensional variables will be used in this section until stated otherwise. The velocity $u$ is positive for flow moving from the $\eta^-$ side to the $\eta^+$ side of the gap. The parameters $f$ and $L$ are empirical coefficients. For the geometry shown in Fig. 3.2.1, $\eta^-$ and $\eta^+$ would correspond to $\eta_{\rm I}$ and $\eta_{\rm II}$, respectively, and $u$ would correspond to the $x$-component of the horizontal velocity through the entrance BG.

Mei, Liu & Ippen (1974) looked at the transmission of long waves through a narrow gap using Eqs. (3.2.16) & (3.2.17). They showed that for the transmission of long waves through a narrow gap, the inertia term in Eq. (3.2.16) can usually be neglected leaving:

$$\eta^- - \eta^+ = \frac{f}{2g} u|u| \quad . \tag{3.2.18}$$

The Lagrangian forms of Eqs. (3.2.17) and (3.2.18) will be used in the finite element model to be discussed in Section 3.4. Equation (3.2.18) has been used by several investigators to introduce dissipation into long wave models. Ünlüata & Mei (1975) developed a purely analytical model using this equation to study the

response of a harbour with simple geometry. Their results showed that Eq. (3.2.18) was responsible for the generation of higher harmonics not necessarily present in the incident waves, although the amplitudes of these harmonics were in general quite small. They did not significantly alter the harbour response characteristics. Ito (1970) and Horikawa & Nishimura (1970) used an entrance loss defined by Eq. (3.2.18) in both finite difference numerical and simplified analytical wave models to model the dissipation produced by tsunami breakwaters. Murakami & Noguchi (1977) modified the theory of Ippen & Goda (1963) using an approximate technique to include the head loss formula of Eq. (3.2.18).

Equation (3.2.17) may appear to be inconsistent with Eq. (3.2.18) because conservation of mass requires that $u^-(h_0 + \eta^-) = u^+(h_0 + \eta^+)$. Hence, if the jump in $\eta$, $\Delta\eta \equiv \eta^- - \eta^+$, is nonzero then the jump in $u$, $\Delta u \equiv u^- - u^+$, must also be nonzero. However, it is clear from the head loss formula, Eq. (3.2.18), that $\Delta\eta$ is $O(A_{\rm inc}/h_0)^2$. Conservation of mass then requires that $\Delta u$ is $O(A_{\rm inc}/h_0)^3$. Now since assumption (iii) b) requires that $A_{\rm inc}/h_0$ is small, we can neglect terms of $O(A_{\rm inc}/h_0)^3$ in comparison with terms $O(A_{\rm inc}/h_0)^2$, so the matching condition $\Delta u = 0$ is actually consistent to the order of accuracy of interest to this investigation.

Although Eq. (3.2.18) can be implemented in numerical models without an inordinate amount of work, its highly nonlinear nature makes it difficult to be used in purely analytical models. For analytical models a simplified "equivalent head loss" formula of the form $\eta^- - \eta^+ = c\,u$ can be used. The dimensional constant $c$ can be obtained by equating the energy loss over one period of a harmonic wave using this expression and Eq. (3.2.18). The rate, per unit width, at which energy

is dissipated across the gap is:

$$\left\{\frac{\rho g}{2}(h+\eta^-)^2+\frac{1}{2}\rho u^{-2}(h+\eta^-)\right\}u^- - \left\{\frac{\rho g}{2}(h+\eta^+)^2+\frac{1}{2}\rho u^{+2}(h+\eta^+)\right\}u^+ . \tag{3.2.19}$$

If this expression is integrated over one period of the wave's motion for both head loss formulae and the results equated to each other, the constant $c$ is found to be $4fu_{\max}/3\pi g$, i.e.,

$$\eta^- - \eta^+ = \frac{4f}{3\pi g}u_{\max}u \tag{3.2.20}$$

where $u_{\max}$ is the maximum horizontal velocity through the gap. The maximum velocity, $u_{\max}$, is not a function of time. This expression can be applied to periodic flow which is not sinusoidal, although its accuracy diminishes as more energy is placed in other harmonics. This formula has also been used with success. Using Eq. (3.2.20), Rogers & Mei (1978) concluded that for a short harbour or bay, entrance losses may be more important than intrinsic nonlinear effects throughout the fluid, but for long harbours the opposite is more likely.

The evaluation of the entrance loss coefficient $f$ is not easy. It will depend upon the geometry of the constriction in question. For the case of a fully open rectangular harbour with sharp corners at the entrance (no breakwater present), Lepelletier (1980) reports that

$$f = \begin{cases} 0.8u_{\max}/2b\omega & \text{for} \quad u_{\max}/2b\omega < 1 \\ 0.8 & \text{for} \quad u_{\max}/2b\omega \geq 1 \end{cases} \tag{3.2.21}$$

where $2b$ is the width of the harbour and $\omega$ is a typical frequency associated with the motion. Equation (3.2.21) was obtained by comparing the results of a finite element model with corresponding experiments. This form for $f$, especially its maximum value of $0.8$, is somewhat dependent on the particular numerical algorithm employed and the particular finite element mesh used for the simulations. When empirical coefficients, such as $f$, are determined from the comparison

of experimental results with numerical results, this dependence should always be kept in mind. Indeed, it will be shown later in Section 5.1.3 that it is likely that Eq. (3.2.21) underestimates $f$ somewhat.

Now let us return to nondimensional variables introduced in the previous section: If we write Eq. (3.2.20) in nondimensional form we get:

$$\eta_{\rm I}(t) - \eta_{\rm II}(y,t) = \frac{4f}{3\pi} u_{\max} u_{\rm I}(t) \qquad |y| \le 1 \quad . \tag{3.2.22}$$

Here all the variables are evaluated at the harbour entrance (i.e., $x = 1$ or $\tilde{x} = 0$) and $u_{\max} \equiv \max_t \Re\{u_{\rm I}|_{x=1}\}$ and $\Re\{\ \}$ denote the real part of a complex quantity. Note that across the entrance to the harbour $\eta_{\rm II}$, in general, depends on $y$ but $\eta_{\rm I}$ does not, since we assumed that the flow was one-dimensional in region I. Let us therefore propose an alternate matching condition where we replace $\eta_{\rm II}(y,t)$ by its average value across the entrance:

$$\eta_{\rm I}(t) - \frac{1}{2}\int_{-1}^{+1} \eta_{\rm II}(y,t)\, dy = \frac{4f}{3\pi} u_{\max} u_{\rm I}(t) \qquad x = 1, \quad |y| \le 1 \quad . \tag{3.2.23}$$

This is the form of the head loss matching condition which will be used to join the two solutions in regions I and II.

The second matching condition, Eq. (3.2.17), is that the jump in the velocity, $u$, is zero. We need to write this matching condition in terms of $\eta$. Since $u$ is continuous along BG, $u_t$ must be continuous also. Now the $x$ component of the momentum equation in region II is $u_t = -\eta_x$. Hence, if $u_t$ is continuous, $\eta_x$ must be also. Hence, the second matching condition can be written as:

$$\left.\frac{\partial \eta}{\partial x}\right|_{\rm I} = \left.\frac{\partial \eta}{\partial x}\right|_{\rm II} \qquad x = 1, \quad |y| \le 1 \quad . \tag{3.2.24}$$

Now in general, the first term in this equation, $\eta_{x_{\rm I}}$, does not depend on $y$ but the second term, $\eta_{x_{\rm II}}$, does. However, when the two solutions are matched, we can force $\eta_{x_{\rm II}}$ to be independent of $y$, so there will be no inconsistency.

### 3.2.4 Solution Inside the Harbour

Let us write the solution of Eqs. (3.2.6)–(3.2.8) or of Eq. (3.2.15) in region I in the form:

$$\eta(x,t) = A\mathcal{H}(\kappa,x)\, e^{i\kappa t} \tag{3.2.25a}$$

$$u(x,t) = -iA\mathcal{U}(\kappa,x)\, e^{i\kappa t} \quad . \tag{3.2.25b}$$

The functions $\mathcal{H}(\kappa,x)$ and $\mathcal{U}(\kappa,x)$ contain the spatial variations of $\eta$ and $u$ in region I, corresponding to the nondimensional frequency $\kappa$. The functions $\mathcal{H}$ and $\mathcal{U}$ are real but in general $A$ is complex. The function $\mathcal{H}(\kappa,x)$ will be referred to as the "harbour function." $\mathcal{U}(\kappa,x)$ is related to $\mathcal{H}(\kappa,x)$ through Eq. (3.2.7):

$$\mathcal{U}(\kappa,x) = -\frac{1}{\kappa}\frac{\partial \mathcal{H}}{\partial x}(\kappa,x) \quad . \tag{3.2.26}$$

We will choose $\mathcal{H}(\kappa,x)$ so that:

$$\mathcal{H}(\kappa,0) = 1 \quad . \tag{3.2.27}$$

Then the amplification factor of the harbour will be:

$$R = \frac{|A|}{2|A_{\text{inc}}|} \quad . \tag{3.2.28}$$

Also, with this form for $u(x,t)$ we find that the temporal maximum of the velocity at the entrance ($x = 1$) is:

$$u_{\max} = |A||\mathcal{U}(\kappa,1)| = \frac{|A|}{\kappa}\left|\frac{\partial \mathcal{H}}{\partial x}(\kappa,1)\right| \quad . \tag{3.2.29}$$

As mentioned earlier, to compute $R'$ we must normalize $|A|$ by the amplitude at $x = 0$ which would exist if the harbour were connected at its entrance ($x = 1$) to an infinitely long channel of unit depth ($h = 1$). Let us denote that amplitude by $A_S$; then $R' = |A|/|A_S|$. In the channel the wave motion will be harmonic

in space and time. Since from assumption (ii) c) all energy is reflected at the shoreline $x = 0$, the amplitude in the channel will be $2|A_{\text{inc}}|$:

$$\eta(x,t) = 2A_{\text{inc}} \sin(\kappa x + \phi) e^{i\kappa t} \qquad x > 1 \qquad \text{(3.2.30a)}$$

$$u(x,t) = i2A_{\text{inc}} \cos(\kappa x + \phi) e^{i\kappa t} \qquad x > 1 \qquad \text{(3.2.30b)}$$

where $\phi$ is some phase angle. From Eqs. (3.2.25) and (3.2.26) the solution in the harbour will be:

$$\eta(x,t) = A_S \mathcal{H}(\kappa,x) e^{i\kappa t} \qquad x < 1 \qquad \text{(3.2.31a)}$$

$$u(x,t) = iA_S \frac{1}{\kappa} \frac{\partial \mathcal{H}}{\partial x}(\kappa,x) e^{i\kappa t} \qquad x < 1\,. \qquad \text{(3.2.31b)}$$

We want to determine $|A_S|$, the wave amplitude at $x = 0$. To match this solution with Eq. (3.2.30) at the harbour entrance ($x = 1$), we must force both the water surface elevation and the velocity to be continuous at $x = 1$; i.e.,

$$A_S \mathcal{H}(\kappa,1) = 2A_{\text{inc}} \sin(\kappa + \phi) \qquad \text{(3.2.32a)}$$

$$A_S \frac{1}{\kappa} \frac{\partial \mathcal{H}}{\partial x}(\kappa,1) = 2A_{\text{inc}} \cos(\kappa + \phi)\,. \qquad \text{(3.2.32b)}$$

The phase angle $\phi$ does not concern us here. If we solve for $|A_S|$ we get:

$$|A_S| = \frac{2|A_{\text{inc}}|}{\left\{ \left( \mathcal{H}(\kappa,1) \right)^2 + \left( \frac{1}{\kappa} \frac{\partial \mathcal{H}}{\partial x}(\kappa,1) \right)^2 \right\}^{1/2}}\,. \qquad \text{(3.2.33)}$$

Hence, the alternate amplification factor $R'$ is:

$$R' = \frac{|A|}{|A_S|} = \frac{|A|}{2|A_{\text{inc}}|} \left\{ \left( \mathcal{H}(\kappa,1) \right)^2 + \left( \frac{1}{\kappa} \frac{\partial \mathcal{H}}{\partial x}(\kappa,1) \right)^2 \right\}^{1/2}$$

$$= R \left\{ \left( \mathcal{H}(\kappa,1) \right)^2 + \left( \frac{1}{\kappa} \frac{\partial \mathcal{H}}{\partial x}(\kappa,1) \right)^2 \right\}^{1/2}\,. \qquad \text{(3.2.34)}$$

For a constant depth rectangular harbour we will have $\mathcal{H}(\kappa,x) = \cos\kappa x$. Then, as mentioned earlier, $R = R'$. Let us define the factor multiplying $R$ in (3.2.34) as $1/S$; i.e.,

$$S = \left\{ \left(\mathcal{H}(\kappa,1)\right)^2 + \left(\frac{1}{\kappa}\frac{\partial\mathcal{H}}{\partial x}(\kappa,1)\right)^2 \right\}^{-1/2} \quad . \tag{3.2.35}$$

Then, as mentioned earlier, the modified amplification factor for the harbour, $R'$, can be obtained from:

$$R' = \frac{R}{S} \tag{3.2.36}$$

where $S$ is defined by Eq. (3.2.35). The quantity $S$ is solely a function of $\kappa$. The amplification factor $R$ is a function of $\kappa$ but may also depend on other parameters as well.

The key step to determine the amplification factors $R$ and $R'$ will be to obtain the harbour function, $\mathcal{H}(\kappa,x)$. An equation for $\mathcal{H}(\kappa,x)$ can be obtained if we substitute Eq. (3.2.25a) into Eq. (3.2.15):

$$\frac{1}{b}\frac{\partial}{\partial x}\left(hb\frac{\partial\mathcal{H}}{\partial x}\right) + \kappa^2\mathcal{H} = 0 \quad . \tag{3.2.37}$$

In order to apply the results to be derived later in this section, let us obtain explicit forms for $\mathcal{H}(\kappa,x)$ for special cases of the functions $h(x)$ and $b(x)$.

### 3.2.4.1 Rectangular Harbour, Linear Bottom

$$h(x) = \begin{cases} x/s & x < s \\ 1 & s \le x \le 1 \end{cases} \tag{3.2.38}$$

$$b(x) = 1 \tag{3.2.39}$$

Here we have a rectangular harbour where the still water depth is constant ($h(x) = 1$) for $x > s$. For $x < s$ the bottom slopes linearly and

intersects the still water level at $x = 0$. The length of the sloping region, $s$, is arbitrary and will appear as a parameter in the solution.

In the region $x < s$, where the bottom slopes linearly, Eq. (3.2.37) is:

$$\frac{x}{s}\frac{\partial^2 \mathcal{H}}{\partial x^2} + \frac{1}{s}\frac{\partial \mathcal{H}}{\partial x} + \kappa^2 \mathcal{H} = 0 \quad . \tag{3.2.40}$$

With the change of variables $\xi = 2\kappa\sqrt{sx}$ this equation reduces to Bessel's equation of order zero:

$$\frac{d^2 \mathcal{H}}{d\xi^2} + \frac{1}{\xi}\frac{d\mathcal{H}}{d\xi} + \mathcal{H} = 0 \quad . \tag{3.2.41}$$

There are two linearly independent solutions to this equations, the Bessel functions of the first and second kinds of order zero, $J_0(\xi)$ and $Y_0(\xi)$. To satisfy assumption (ii) c), the $Y_0$ solution must be excluded since $Y_0(\xi)$ has a logarithmic singularity at $\xi = 0$. Therefore, the solution which satisfies Eq. (3.2.27) is:

$$\mathcal{H}(\kappa, x) = J_0(2\kappa\sqrt{sx}) \qquad x < s \tag{3.2.42a}$$

$$\frac{\partial \mathcal{H}}{\partial x}(\kappa, x) = -\kappa\sqrt{\frac{s}{x}}\, J_1(2\kappa\sqrt{sx}) \quad x < s \, . \tag{3.2.42b}$$

For $x > s$, where the depth is uniform, $\mathcal{H}$ will be harmonic:

$$\mathcal{H}(\kappa, x) = \quad a_1 \cos\kappa x + a_2 \sin\kappa x \qquad s < x < 1 \tag{3.2.43a}$$

$$\frac{\partial \mathcal{H}}{\partial x}(\kappa, x) = -a_1\kappa \sin\kappa x + a_2\kappa\cos\kappa x \quad s < x < 1 \, . \tag{3.2.43b}$$

The parameters $a_1$ and $a_2$ must be determined by matching these two solutions together at $x = s$. The matching conditions are the same as those that will be used to match the solution in region I to the solution in region II, except that the head loss is assumed to be zero. In other words, we can determine $a_1$ and $a_2$ by forcing $\eta$ and $\partial\eta/\partial x$ to be continuous at $x = s$. The result is:

$$a_1 = J_0(2\kappa s)\cos\kappa s + J_1(2\kappa s)\sin\kappa s \tag{3.2.44a}$$

$$a_2 = J_0(2\kappa s)\sin\kappa s - J_1(2\kappa s)\cos\kappa s \quad . \tag{3.2.44b}$$

Hence, in the region $s < x < 1$ the expressions for $\mathcal{H}$ and $\partial\mathcal{H}/\partial x$ are:

$$\mathcal{H}(\kappa, x) = \quad J_0(2\kappa s)\cos\kappa(x-s) - J_1(2\kappa s)\sin\kappa(x-s) \tag{3.2.45a}$$

$$\frac{\partial\mathcal{H}}{\partial x}(\kappa, x) = -\kappa\left[J_1(2\kappa s)\cos\kappa(x-s) + J_0(2\kappa s)\sin\kappa(x-s)\right] . \tag{3.2.45b}$$

With this solution we can investigate the response of a constant depth rectangular harbour with a vertical endwall $(s = 0)$, a rectangular harbour with a bottom which slopes linearly from the harbour mouth to the shoreline $(s = 1)$, or a harbour anywhere between these two cases.

### 3.2.4.2 Triangular Harbour, Linear Bottom

$$h(x) = \begin{cases} x/s & x < s \\ 1 & s \le x \le 1 \end{cases} \tag{3.2.46}$$

$$b(x) = x \tag{3.2.47}$$

This is the same as the example just described except that the vertical harbour side walls converge linearly to a vertex at $x = 0$; i.e., the points C and D in Fig. 3.2.1 coalesce to a single point.

In the region $x < s$, Eq. (3.2.37) becomes:

$$\frac{x}{s}\frac{\partial^2\mathcal{H}}{\partial x^2} + \frac{2}{s}\frac{\partial\mathcal{H}}{\partial x} + \kappa^2\mathcal{H} = 0 \quad . \tag{3.2.48}$$

Although this is very similar to Eq. (3.2.40), the behaviour of $\mathcal{H}$ is very different. With the change of variables $\xi = 2\kappa\sqrt{sx}$ and $H = \xi\mathcal{H}$ this equation reduces to Bessel's equation of order one:

$$\xi^2\frac{d^2H}{d\xi^2} + \xi\frac{dH}{d\xi} + (\xi^2 - 1)H = 0 \quad . \tag{3.2.49}$$

Now as $\xi \to 0$, $Y_1(\xi) \sim 1/\xi$. Hence, in order to satisfy assumption (ii) c) we must discard this part of the solution. Then the solution that satisfies Eq. (3.2.27) is:

$$\mathcal{H}(\kappa, x) = \frac{J_1(2\kappa\sqrt{sx})}{\kappa\sqrt{sx}} \qquad x < s \tag{3.2.50a}$$

$$\frac{\partial \mathcal{H}}{\partial x}(\kappa, x) = -\frac{J_2(2\kappa\sqrt{sx})}{x} \qquad x < s \quad . \tag{3.2.50b}$$

In the region $x > s$ Eq. (3.2.37) takes the form:

$$\frac{\partial^2 \mathcal{H}}{\partial x^2} + \frac{1}{x}\frac{\partial \mathcal{H}}{\partial x} + \kappa^2 \mathcal{H} = 0 \quad . \tag{3.2.51}$$

With the substitution $\xi = \kappa x$, this equation reduces to Bessel's equation of order zero. Hence, we get:

$$\mathcal{H}(\kappa, x) = a_1 J_0(\kappa x) + a_2 Y_0(\kappa x) \qquad s < x < 1 \tag{3.2.52a}$$

$$\frac{\partial \mathcal{H}}{\partial x}(\kappa, x) = -a_1 \kappa J_1(\kappa x) - a_2 \kappa Y_1(\kappa x) \quad s < x < 1 \quad . \tag{3.2.52b}$$

As for the previous case, we must determine $a_1$ and $a_2$ by forcing $\eta$ and $\partial\eta/\partial x$ (i.e., $\mathcal{H}$ and $\partial\mathcal{H}/\partial x$) to be continuous at $x = s$. This condition yields:

$$a_1 = \frac{\pi}{2}\left[J_2(2\kappa s)Y_0(\kappa s) - J_1(2\kappa s)Y_1(\kappa s)\right] \tag{3.2.53a}$$

$$a_2 = \frac{\pi}{2}\left[J_1(2\kappa s)J_1(\kappa s) - J_2(2\kappa s)J_0(\kappa s)\right] \tag{3.2.53b}$$

where we used the identity $J_{n+1}(\xi)\,Y_n(\xi) - J_n(\xi)\,Y_{n+1}(\xi) = 2/(\pi\xi)$. Hence, the solution for $x > s$ is:

$$\begin{aligned}\mathcal{H}(\kappa, x) = {} & \frac{\pi}{2} J_0(\kappa x)\left[J_2(2\kappa s)Y_0(\kappa s) - J_1(2\kappa s)Y_1(\kappa s)\right] \\ & + \frac{\pi}{2} Y_0(\kappa x)\left[J_1(2\kappa s)J_1(\kappa s) - J_2(2\kappa s)J_0(\kappa s)\right]\end{aligned} \tag{3.2.54a}$$

$$\begin{aligned}\frac{\partial \mathcal{H}}{\partial x}(\kappa, x) = {} & \frac{\pi\kappa}{2} J_1(\kappa x)\left[J_1(2\kappa s)Y_1(\kappa s) - J_2(2\kappa s)Y_0(\kappa s)\right] \\ & + \frac{\pi\kappa}{2} Y_1(\kappa x)\left[J_2(2\kappa s)J_0(\kappa s) - J_1(2\kappa s)J_1(\kappa s)\right] \quad .\end{aligned} \tag{3.2.54b}$$

### 3.2.4.3 Rectangular Harbour, Parabolic Bottom

$$h(x) = x(2-x) \tag{3.2.55}$$

$$b(x) = 1 \tag{3.2.56}$$

In this case the still water depth decreases quadratically from the mouth of the harbour to the shoreline at $x = 0$. The slope of the bottom is continuous at the mouth of the harbour (i.e., equal to zero) and is equal to two at the shoreline.

For this case Eq. (3.2.37) becomes:

$$x(2-x)\frac{\partial^2 \mathcal{H}}{\partial x^2} + 2(1-x)\frac{\partial \mathcal{H}}{\partial x} + \kappa^2 \mathcal{H} = 0 \quad . \tag{3.2.57}$$

With the change of variables $\xi = 1 - x$, this equation reduces to:

$$(1-\xi^2)\frac{\partial^2 \mathcal{H}}{\partial \xi^2} - 2\xi\frac{\partial \mathcal{H}}{\partial \xi} + \kappa^2 \mathcal{H} = 0 \quad . \tag{3.2.58}$$

This is Legendre's equation of order $\nu$ where $\kappa^2 = \nu(\nu+1)$. There are two fundamental solutions to this equation: $\mathcal{H}(\kappa, x) = P_\nu(1-x)$ and $\mathcal{H}(\kappa, x) = Q_\nu(1-x)$, where $P_\nu(\xi)$ and $Q_\nu(\xi)$ are Legendre Functions of the first and second kind, respectively, of degree $\nu$. (See Magnus, Oberhettinger & Soni (1966) for a description of the properties of these functions.) We must exclude the function $Q_\nu(\xi)$, since it has a logarithmic singularity at $\xi = 1$ ($x = 0$):

$$Q_\nu(\xi) \overset{\xi \to 1}{\longrightarrow} -\frac{1}{2}\ln\left(\frac{1-\xi}{2}\right) - \gamma - \psi(\nu+1) \qquad \nu \neq -1, -2, -3, \ldots \tag{3.2.59}$$

where $\gamma = 0.57721\ldots$ is Eulers constant and $\psi(z)$ is the psi or digamma function defined as:

$$\psi(z) = \frac{d}{dz}\ln\Gamma(z+1) \tag{3.2.60}$$

and $\Gamma(z)$ is the gamma function. Hence, $\mathcal{H}$ must be proportional to $P_\nu(1-x)$. Since the function $P_\nu(1-x)$ is unity at the shore ($x = 0$), the constant of proportionality must be 1 in order to satisfy Eq. (3.2.27). Therefore, we must have:

$$\mathcal{H}(\kappa, x) = P_\nu(1-x) \qquad \nu = -\frac{1}{2} + \sqrt{\frac{1}{4} + \kappa^2} \quad . \tag{3.2.61}$$

For later use we will need expressions for $\mathcal{H}(\kappa, 1)$ and $\partial\mathcal{H}(\kappa, 1)/\partial x$. They are:

$$\mathcal{H}(\kappa, 1) = P_\nu(0) = \frac{1}{\sqrt{\pi}} \cos\frac{\pi\nu}{2} \frac{\Gamma\left(\frac{\nu+1}{2}\right)}{\Gamma\left(\frac{\nu}{2}+1\right)} \tag{3.2.62a}$$

$$\frac{\partial\mathcal{H}}{\partial x}(\kappa, 1) = -\frac{\partial P_\nu}{\partial x}(0) = -\frac{2}{\sqrt{\pi}} \sin\frac{\pi\nu}{2} \frac{\Gamma\left(\frac{\nu}{2}+1\right)}{\Gamma\left(\frac{\nu+1}{2}\right)} \quad . \tag{3.2.62b}$$

### 3.2.4.4 Parabolic Harbour, Horizontal Bottom

$$h(x) = 1 \tag{3.2.63}$$

$$b(x) = \sqrt{x} \tag{3.2.64}$$

In this case the harbour side walls vary parabolically and there is no vertex at $x = 0$ as there was for the triangular harbour in Section 3.2.4.2.

For this case Eq. (3.2.37) becomes:

$$\frac{\partial^2\mathcal{H}}{\partial x^2} + \frac{1}{2x}\frac{\partial\mathcal{H}}{\partial x} + \kappa^2\mathcal{H} = 0 \quad . \tag{3.2.65}$$

With the change of variables $\xi = \kappa x$ and $H = \xi^{-1/4}\mathcal{H}$, this equation reduces to:

$$\xi^2\frac{d^2H}{d\xi^2} + \xi\frac{dH}{d\xi} + (\xi^2 - \frac{1}{16})H = 0 \quad . \tag{3.2.66}$$

This is Bessel's equation of order $\frac{1}{4}$. Hence, two linearly independent solutions to Eq. (3.2.65) are:

$$x^{1/4} J_{\frac{1}{4}}(\kappa x) \qquad \text{and} \qquad x^{1/4} J_{-\frac{1}{4}}(\kappa x) \quad . \tag{3.2.67}$$

Although both of these solutions are finite at $x = 0$, the slope of the first one diverges as $1/\sqrt{x}$ as $x \to 0$. To satisfy Eq. (3.2.27) and the vertical wall boundary condition $\partial \mathcal{H}/\partial x = 0$ at $x = 0$, we must have:

$$\mathcal{H}(\kappa, x) = \frac{\Gamma(3/4)}{2^{1/4}} (\kappa x)^{1/4} J_{-\frac{1}{4}}(\kappa x) \tag{3.2.68a}$$

$$\frac{\partial \mathcal{H}}{\partial x}(\kappa, x) = -\frac{\Gamma(3/4)}{2^{1/4}} \kappa (\kappa x)^{1/4} J_{\frac{3}{4}}(\kappa x) \quad . \tag{3.2.68b}$$

#### 3.2.4.5 Other Geometries

Geometries other than those presented in Sections 3.2.4.1–3.2.4.4 can also be treated analytically. However, the geometries presented here are, in many cases, quite good approximations to many natural bays, inlets, and man-made harbours. However, if much more irregular geometries must be treated, then the harbour function, $\mathcal{H}(\kappa, x)$, can be determined numerically. This can be done quite easily since it is not necessary to couple the motion within the harbour (region I in Fig. 3.2.1) to that in the open ocean region (region II in Fig. 3.2.1). The coupling will be treated later in Section 3.2.6, when the solutions in regions I and II are matched.

### 3.2.5 Solution Outside the Harbour

The solution outside the harbour must satisfy the two-dimensional wave equation (3.2.11). The boundary conditions are obtained from assumption (ii) a)

in Section 3.2.1, matching condition (3.2.24), and expressions (3.2.9) and (3.2.25a):

$$\frac{\partial \eta}{\partial \tilde{x}}(0,y,t) = \begin{cases} A\dfrac{\partial \mathcal{H}}{\partial x}(\kappa,1)\, e^{i\kappa t} & |y| \le 1 \\ 0 & |y| > 1 \end{cases} \tag{3.2.69}$$

$$\eta \rightarrow 2A_{\text{inc}} \cos \kappa \tilde{x}\; e^{i\kappa t} \qquad \tilde{x}^2 + y^2 \rightarrow \infty \quad . \tag{3.2.70}$$

In addition, the radiated wave must satisfy the radiation condition that all energy must be outgoing as $\tilde{x}^2 + y^2 \rightarrow \infty$. The wave represented by Eq. (3.2.70) is simply the incident-reflected wave which would exist if the harbour were not present. The radiated wave is the difference between the incident-reflected wave in Eq. (3.2.70) and the actual amplitude $\eta$. Now the two-dimensional harmonic point source solution of the wave equation (3.2.11) is (e.g., Whitham 1974):

$$-\frac{1}{4\pi} \int_{-\infty}^{+\infty} e^{-i\kappa\sqrt{\tilde{x}^2+\epsilon^2 y^2}\,\cosh\zeta}\, d\zeta\, e^{i\kappa t} = \frac{i}{4} H_0^{(2)}\left(\kappa\sqrt{\tilde{x}^2+\epsilon^2 y^2}\right) e^{i\kappa t} \tag{3.2.71}$$

where $H_0^{(2)}(z)$ is the Hankel function of the second kind of order zero defined as $J_0(z) - iY_0(z)$, where $J_0(z)$ and $Y_0(z)$ are Bessel functions of the first and second kind, respectively, of order zero. The Hankel function of the *second* kind was chosen to satisfy the radiation condition. To see that Eq. (3.2.71) does indeed correspond to outgoing waves at infinity we can replace the Hankel function by its asymptotic form for large argument (e.g., Abramowitz & Stegun 1972):

$$H_0^{(2)}(z) \sim \sqrt{\frac{2}{\pi z}}\; e^{-(z-\pi/4)} \qquad |z| \rightarrow \infty \quad . \tag{3.2.72}$$

Using this asymptotic form for the Hankel function, the point source solution of Eq. (3.2.71) far from the harbour entrance becomes:

$$\frac{i/\sqrt{4\pi}}{\left(\tilde{x}^2+\epsilon^2 y^2\right)^{1/4}}\, e^{-i\kappa\left(\sqrt{\tilde{x}^2+\epsilon^2 y^2}-t\right)} \quad . \tag{3.2.73}$$

This is an outgoing cylindrical wave. The Hankel function of the first kind satisfies the same asymptotic form but with $i$ replaced by $-i$. It therefore corresponds to an incoming wave. Our solution can be obtained by superposing point sources (i.e., integrating the point source solution) along $x = 0$ in order to satisfy the boundary condition (3.2.69). The result is:

$$\eta(\tilde{x}, y, t) = 2A_{\text{inc}} \cos \kappa \tilde{x}\ e^{i\kappa t} + \frac{i}{2} \epsilon A \frac{\partial \mathcal{H}}{\partial x}(\kappa, 1) \int_{-1}^{+1} H_0^{(2)}(\kappa \sqrt{\tilde{x}^2 + \epsilon^2 (y - y')^2}\,)\, dy'\ e^{i\kappa t}. \tag{3.2.74}$$

### 3.2.6 Matching the Solutions

The amplitude parameter $A$ is still undetermined. To determine its value we must match the solution within the harbour with the solution outside the harbour, using the remaining matching condition (3.2.23). If we substitute Eqs. (3.2.25) and (3.2.74) into Eq. (3.2.23) with $\mathcal{U}(\kappa, x)$ given by Eq. (3.2.26) and $u_{\max}$ given by Eq. (3.2.29), we get:

$$A = 2A_{\text{inc}} \left\{ \mathcal{H}(\kappa, 1) - \frac{i\epsilon}{4} \frac{\partial \mathcal{H}}{\partial x}(\kappa, 1) \int_{-1}^{+1} dy \int_{-1}^{+1} H_0^{(2)}(\kappa \epsilon |y - y'|)\, dy' \right.$$
$$\left. - \frac{4if}{3\pi\kappa^2} |A| \left| \frac{\partial \mathcal{H}}{\partial x}(\kappa, 1) \right| \frac{\partial \mathcal{H}}{\partial x}(\kappa, 1) \right\}^{-1} . \tag{3.2.75}$$

This expression can be simplified. Incident wave systems of interest will have wavelengths of the same order of magnitude as the length of the harbour $L$; i.e.,

$$\kappa = kL = O(1) \quad . \tag{3.2.76}$$

According to assumption (iii) d), the width of the harbour is small compared to the wavelength of the incident wave; i.e., $kb < O(1)$. Combining this with Eq. (3.2.76) we get $b/L < O(1)$; i.e., $\epsilon \ll 1$ (say $\epsilon < 0.1$). Then the argument of the Hankel

function in Eq. (3.2.75) will be small and we can approximate $H_0^{(2)}(\kappa\epsilon|y-y'|)$ by the following expression which is valid for small values of $\epsilon$ (Abramowitz & Stegun 1972):

$$H_0^{(2)}(\kappa\epsilon|y-y'|) = 1 - \frac{2i}{\pi}\left\{\ln\frac{\kappa\epsilon}{2}|y-y'| + \gamma\right\} + O(\epsilon^2 \ln\epsilon) \qquad (3.2.77)$$

where $\gamma$ is Euler's constant. If we substitute this approximate expression for $H_0^{(2)}$ into Eq. (3.2.75) and perform the integration, the equation for $A$ reduces to:

$$A = 2A_{\text{inc}}\left\{\mathcal{H}(\kappa,1) - i\epsilon\frac{\partial\mathcal{H}}{\partial x}(\kappa,1)\left\{1 - \frac{2i}{\pi}[\ln\epsilon\kappa + \gamma - 3/2]\right\}\right.$$
$$\left. - \frac{4if}{3\pi\kappa^2}|A|\left|\frac{\partial\mathcal{H}}{\partial x}(\kappa,1)\right|\frac{\partial\mathcal{H}}{\partial x}(\kappa,1)\right\}^{-1} . \qquad (3.2.78)$$

Hence:

$$R = \left|\mathcal{H}(\kappa,1) - \frac{2\epsilon}{\pi}\frac{\partial\mathcal{H}}{\partial x}(\kappa,1)[\ln\epsilon\kappa + \gamma - 3/2]\right.$$
$$\left. + i\left(-\epsilon\frac{\partial\mathcal{H}}{\partial x}(\kappa,1) - \frac{8f}{3\pi\kappa^2}R|A_{\text{inc}}|\left|\frac{\partial\mathcal{H}}{\partial x}(\kappa,1)\right|\frac{\partial\mathcal{H}}{\partial x}(\kappa,1)\right)\right|^{-1} . \qquad (3.2.79)$$

Given an arbitrary harbour function $\mathcal{H}(\kappa,x)$, these expressions determine the complex amplitude of the wave system in the harbour, $A$ (defined in Eq. 3.2.25a), and the amplification factor, $R$. The modified amplification factor, $R'$, which removes from $R$ the effects of shoaling and geometrical amplification within the harbour, can then be obtained by substituting Eq. (3.2.79) into Eq. (3.2.34). Notice that because of the nonlinear nature of the head loss matching condition, $R$ is a function of the magnitude of the incident amplitude, $|A_{\text{inc}}|$.

Now we can substitute the results for the special cases of Sections 3.2.4.1–3.2.4.4 into Eqs. (3.2.34), (3.2.35) and (3.2.79) to obtain the response curves for those harbours. Figures 3.2.2, 3.2.3 and 3.2.4 show the results for the case where the ratio of the width of the harbour entrance to the length of the harbour is 0.2;

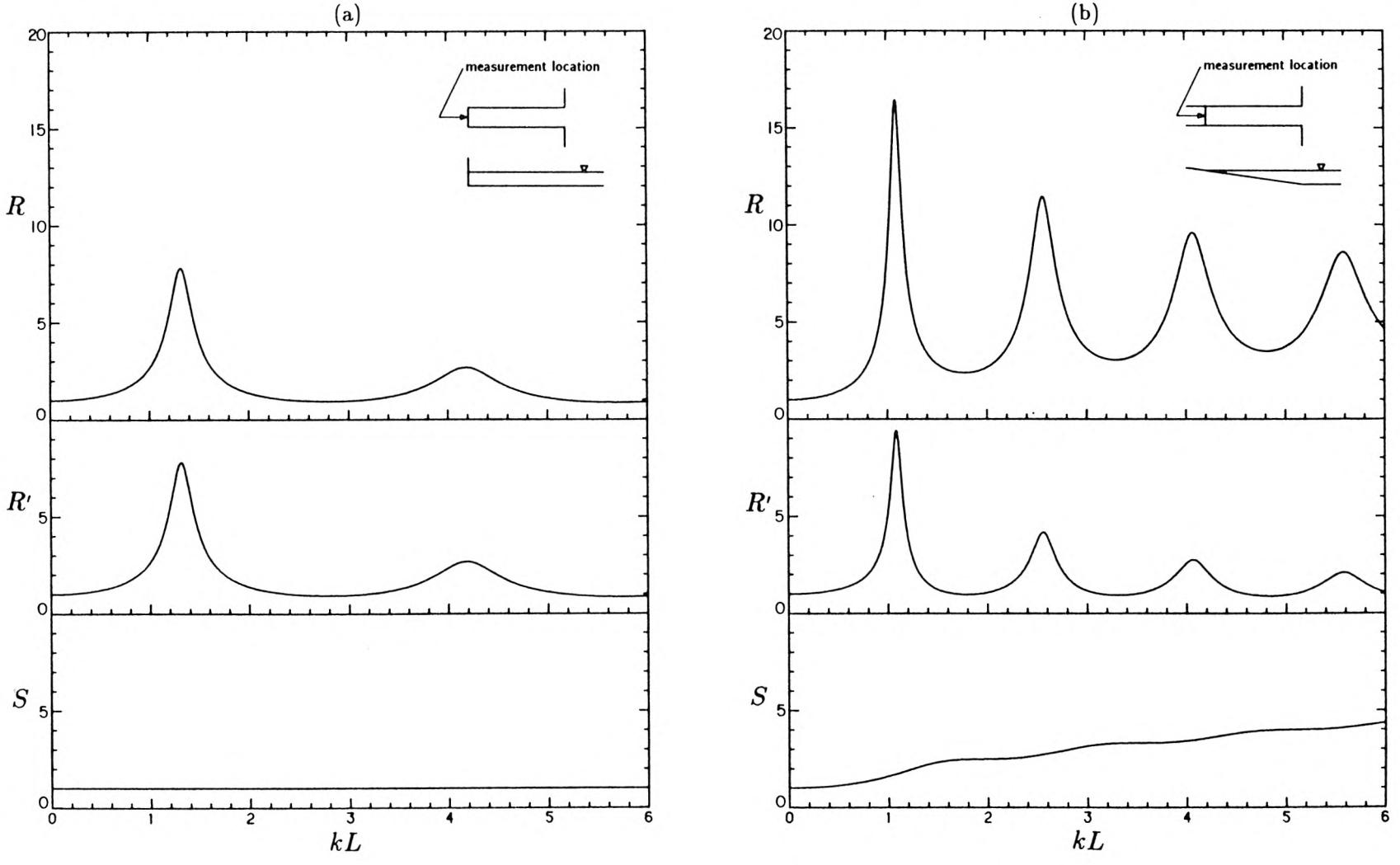


Fig. 3.2.2 Harbour response curves for rectangular harbours. $\epsilon = 0.1$ $f = 0$;
(a) constant depth, (b) linearly sloping bottom.

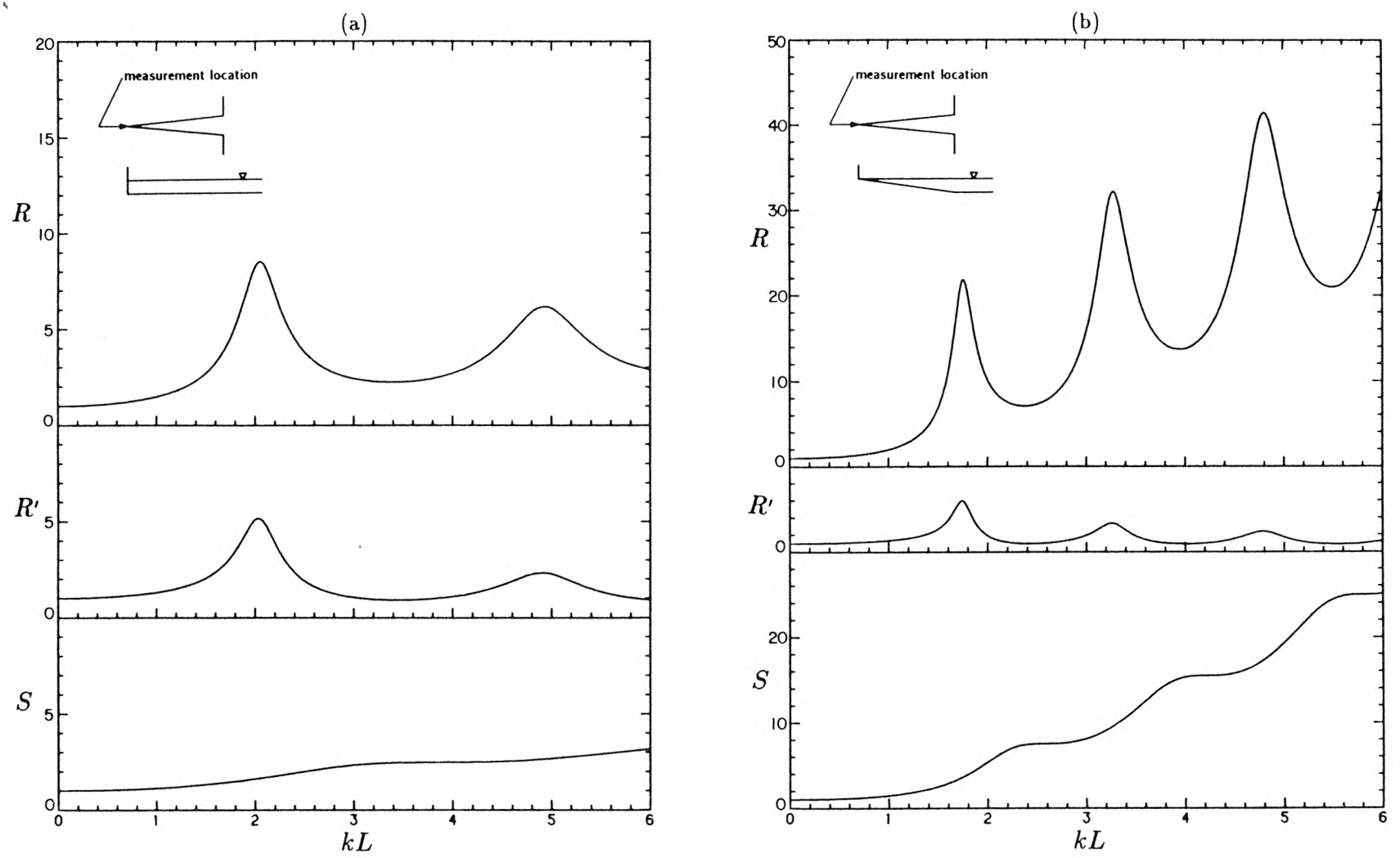


Fig. 3.2.3 Harbour response curves for harbours with linearly converging sides. $\epsilon = 0.1 \quad f = 0$; (a) constant depth, (b) linearly sloping bottom.

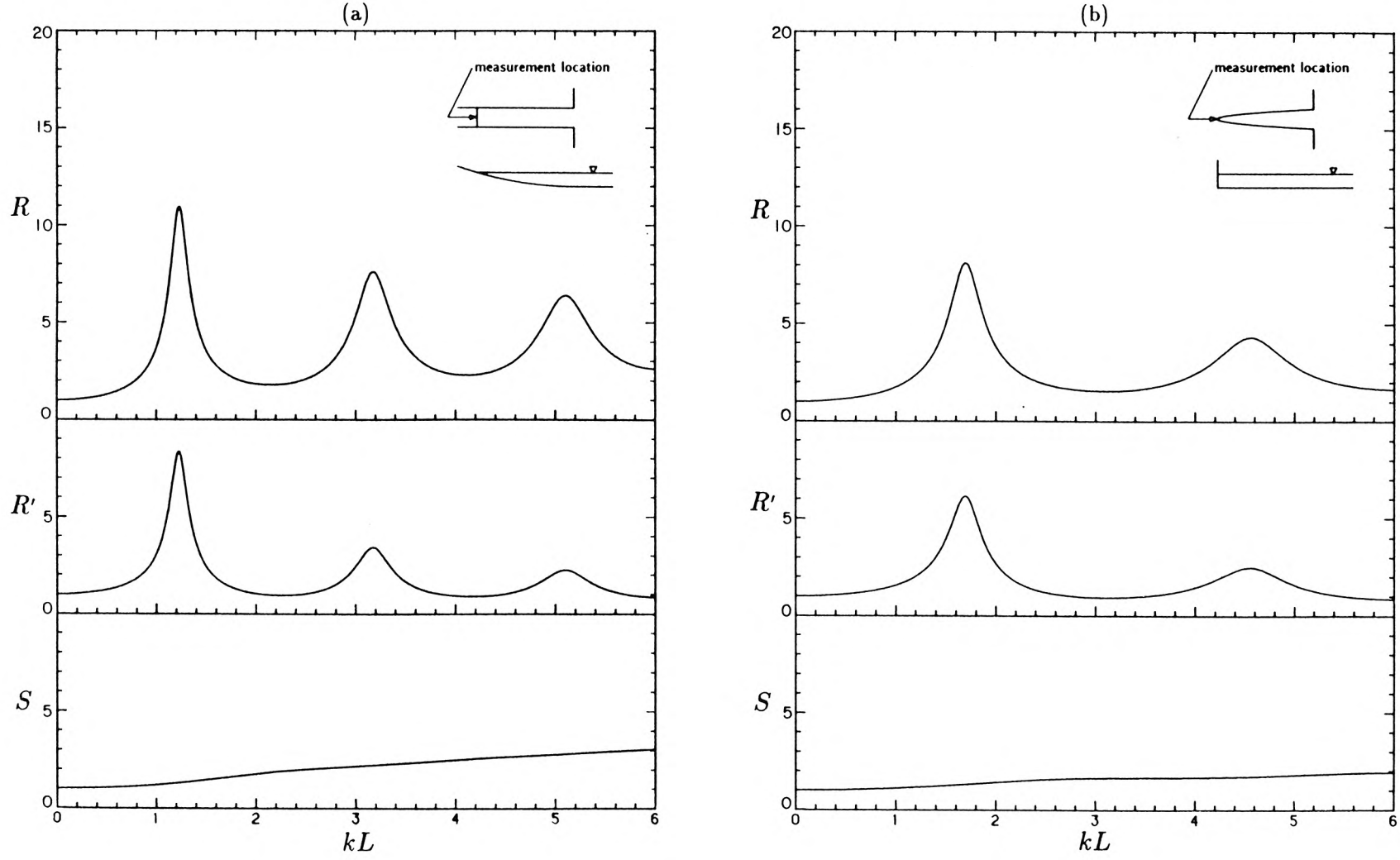


Fig. 3.2.4 Harbour response curves. $\epsilon = 0.1 \quad f = 0$; (a) rectangular harbour with a parabolic bottom, (b) parabolic harbour with a flat bottom.

i.e., $2b^*(L)/L = 0.2$ or $\epsilon = 0.1$ ( $\epsilon$ is defined in Eq. (3.2.10)). Entrance losses are neglected ( $f = 0$ ). Each figure shows the results for two different geometries. For each geometry the two amplification factors, $R$ and $R'$, as well as the factor $S$ are plotted as a function of $kL$.

Figure 3.2.2a shows the results for a constant depth rectangular harbour. Notice that $S \equiv 1$ as remarked earlier. This means that there is no amplification at the backwall of the harbour because of depth or sidewall variations within the harbour. As a consequence, both $R$ and $R'$ are identical. Figure 3.2.2b then shows the effects of a linearly sloping bottom. There are significant differences between Figs. 3.2.2a and 3.2.2b. The factor $S$ now steadily increases with $kL$. This is simply because, for a constant slope, shorter wavelengths shoal more than longer wavelengths. Due to this shoaling the total response of the harbour, $R$, is much greater than for the constant depth case in Fig. 3.2.2a. However, the magnitudes of the alternate amplification factors, $R'$, are of comparable size.

Both of the harbours in Fig. 3.2.3 have sidewalls that converge linearly to a vertex. Figure 3.2.3a treats the case of constant depth and Fig. 3.2.3b treats the case where the bottom slopes linearly from the harbour entrance to the shore. Notice that $S$ is very large in Fig. 3.2.3b, where *both* the width and depth of the harbour decrease from its entrance to the shore. That is a result of both shoaling and geometrical amplification. As a result, the total response, $R$, is extremely large. In fact, the shoaling and geometrical amplification increases so fast with $kL$ that the total response, $R$, also increases rapidly with $kL$, although $R$ also shows much resonant structure. However, the alternate amplification factor, $R'$, behaves much like all the $R'$ factors for the other harbours.

Figure 3.2.4 shows the results for a rectangular harbour with a parabolic bottom and for a parabolic harbour with a flat bottom. The effect of shoaling due to the decrease in water depth is stronger than the effect of geometrical amplifi-

cation due to the decrease in harbour width, so the parameter $S$ is greater for the harbour with the parabolic bottom. As a result, the total response, $R$, for the harbour with the parabolic bottom is greater than for the harbour with the parabolic sides.

Tables 3.2.1 and 3.2.2 summarize the important quantities in Figs. 3.2.2, 3.2.3 and 3.2.4 for the first two resonant modes. The first column shows the plan and side views of the harbour. The second column gives the corresponding harbour function $\mathcal{H}(\kappa, x)$. The third column lists the values of $\kappa_{\text{res}}$, the values of $\kappa$ $(= kL)$ at resonance. These are the values of $\kappa$ that maximize $R$. The last three columns list the values of $R$, $R'$ and $S$ corresponding to $\kappa_{\text{res}}$. Since $dS/d\kappa \geq 0$ for the special cases considered, the values of $\kappa$ that maximize $R'$ will be slightly smaller than $\kappa_{\text{res}}$ or equal to it for the constant depth rectangular harbour where $S(\kappa) \equiv 1$. The harbours are listed in order of increasing values of $\kappa_{\text{res}}$ for the first resonant mode.

All the harbours have the same length and the same width and depth at their entrances, but their response curves are very different. Not only do the magnitudes of the resonant peaks differ greatly but their locations do so as well. The values of $\kappa_{\text{res}}$ vary by almost a factor of two for both the first and second modes. Thus, the harbour length, entrance width and depth are not at all sufficient to yield an estimate of the resonant frequencies of a harbour. The details of the harbour planform and bathymetry must also be considered. Shoaling and geometrical amplification caused by decreasing water depth and harbour width both tend to increase the shoreline amplitudes although it is difficult to quantify this effect for the general case. Green's law is not valid for most of these harbours. It states that the amplitude for a wave system varies as $b^{-1/2}h^{-1/4}$ and this clearly is useless if $b \to 0$ or $h \to 0$.

The periods of free oscillation of the harbours shown in Tables 3.2.1 and 3.2.2

Table 3.2.1

First resonant mode response for six harbours with different geometries. $\epsilon = 0.1 \quad f = 0.$

| | | First Resonant Mode | | | |
|---|---|---|---|---|---|
| Harbour Geometry | Harbour Function | $\kappa_{\text{res}}$ | $R_{\text{res}}$ | $R'_{\text{res}}$ | $S_{\text{res}}$ |
| 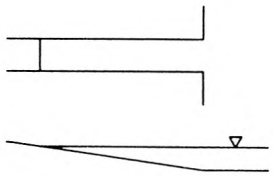 | $J_0(2\kappa\sqrt{x})$ | 1.089 | 16.43 | 9.40 | 1.75 |
| 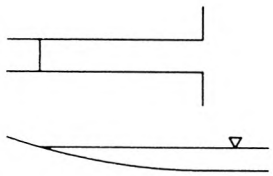 | $P_\nu(1-x)$<br>$\nu = -\frac{1}{2} + \sqrt{\frac{1}{4} + \kappa^2}$ | 1.229 | 10.96 | 8.36 | 1.31 |
| 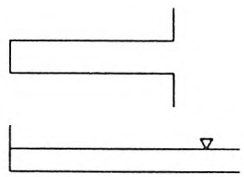 | $\cos \kappa x$ | 1.315 | 7.81 | 7.81 | 1.00 |
| 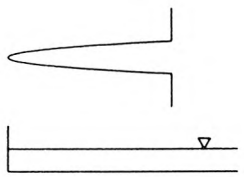 | $\Gamma(\frac{3}{4})\left(\frac{\kappa x}{2}\right)^{\frac{1}{4}} J_{-\frac{1}{4}}(\kappa x)$ | 1.696 | 8.12 | 6.14 | 1.32 |
| 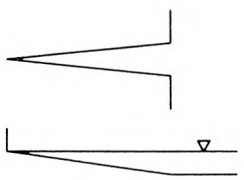 | $\frac{J_1(2\kappa\sqrt{x})}{\kappa\sqrt{x}}$ | 1.757 | 21.85 | 5.91 | 3.70 |
| 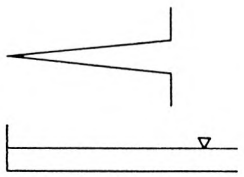 | $J_0(\kappa x)$ | 2.050 | 8.50 | 5.14 | 1.65 |

Table 3.2.2

Second resonant mode response for six harbours with different geometries. $\epsilon = 0.1 \quad f = 0.$

| | | Second Resonant Mode | | | |
|---|---|---|---|---|---|
| Harbour Geometry | Harbour Function | $\kappa_{\text{res}}$ | $R_{\text{res}}$ | $R'_{\text{res}}$ | $S_{\text{res}}$ |
| 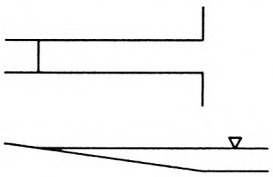 | $J_0(2\kappa\sqrt{x})$ | 2.565 | 11.45 | 4.18 | 2.74 |
| 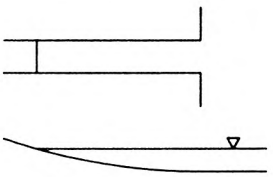 | $P_\nu(1-x)$<br>$\nu = -\frac{1}{2} + \sqrt{\frac{1}{4} + \kappa^2}$ | 3.177 | 7.61 | 3.43 | 2.22 |
| 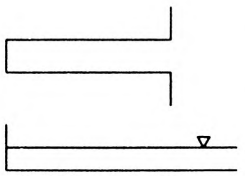 | $\cos \kappa x$ | 4.182 | 2.68 | 2.68 | 1.00 |
| 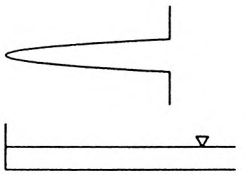 | $\Gamma(\frac{3}{4}) \left(\frac{\kappa x}{2}\right)^{\frac{1}{4}} J_{-\frac{1}{4}}(\kappa x)$ | 4.559 | 4.32 | 2.49 | 1.73 |
| 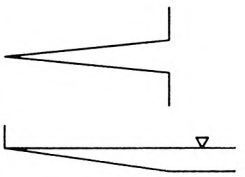 | $\frac{J_1(2\kappa\sqrt{x})}{\kappa\sqrt{x}}$ | 3.280 | 32.18 | 3.33 | 9.67 |
| 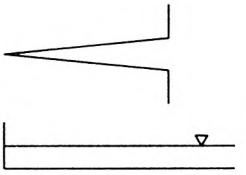 | $J_0(\kappa x)$ | 4.926 | 6.19 | 2.33 | 2.65 |

have been estimated by a number of investigators in the past (e.g., see Lamb 1945). However, this early work determined these periods by assuming a node existed at the harbour entrance. This is equivalent to treating an infinitesimally narrow harbour where there is no radiation damping. Hence, such an analysis cannot yield an estimate of the amplification factor at resonance since the neglect of radiation damping results in unbounded motion within the harbour at resonance. By including the effect of finite entrance width, a realistic estimate of the amplification factor can be determined. The resonant frequencies are a weak function of the entrance width and, in general, the values of $\kappa_{\text{res}}$ in Tables 3.2.1 and 3.2.2 are lower than the corresponding ones for zero entrance width. The first attempt to model the effects of the radiation of energy from the mouth of a harbour appears to be due to Miles & Munk (1961). However, they did not consider entrance losses. For narrow mouthed harbours this source of dissipation must usually be considered, especially near resonance.

It can be seen from Tables 3.2.1 and 3.2.2 that decreasing water depth has an opposite effect on the values of $\kappa_{\text{res}}$ than decreasing the harbour width. The resonant frequencies for a harbour with a still water depth which decreases as one moves toward the shoreline are *lower* than for a similar harbour with a constant depth. This can be seen clearly by comparing Figs. 3.2.2a and 3.2.2b. This effect can be explained because, as the wave shoals, its speed decreases. Hence, it takes longer for a wave to propagate to the shoreline and reflect back to the harbour entrance. Such a delay could also be produced by keeping the still water depth constant and increasing the harbour length and this, of course, would lower the resonant frequencies of the harbour. On the other hand, it can be seen that the resonant frequencies for a harbour whose *width* decreases toward the shoreline are *higher* than for a similar harbour with straight parallel sides. This can be seen clearly by comparing Figs. 3.2.2a and 3.2.3a.

Although the factor $S$ is a monotonic function of $kL$ in Figs. 3.2.2–3.2.4, it seems to show more structure for certain harbour geometries than for others. This waviness in $S$ is due to the reflection of wave energy at the harbour entrance due to an abrupt change in the slope of the bottom. Reflections can also occur if the sidewalls are not parallel at the harbour entrance because the factor $S$ was defined by joining the harbour with a channel of constant width. The waviness is greatest in Fig. 3.2.3b where the bottom slope jumps from zero outside the harbour to a constant value inside the harbour *and* where the sidewalls are not parallel at the entrance. The waviness in $S$ is the least noticeable in Figs. 3.2.2a, 3.2.4a, and 3.2.4b. For these harbours the bottom slope is continuous (equal to zero) at the harbour entrance and, in addition, the sidewalls are parallel at the entrance.

Harbour response curves for a nonzero entrance loss coefficient, $f \neq 0$, can also be computed from Eq. (3.2.79). These will be shown later in Section 5.1.3 of Chapter 5 when they will be compared with response curves obtained by numerically solving the long wave equations of Section 3.1.3 using the finite element model.

### 3.2.7 Behaviour Near Resonance

Now let us look in detail at the behaviour of the harbour response near resonance. It is clear from Eq. (3.2.79) for the amplification factor $R$ that as the relative harbour entrance width goes to zero ($\epsilon \to 0$) and as the amplitude of the incident wave goes to zero ($|A_{\text{inc}}| \to 0$), resonance will occur for those values of $\kappa$ ($= kL$) which satisfy $\mathcal{H}(\kappa, 1) = 0$. Let us denote these values of $\kappa$ by $\kappa_i$ $i = 1, 2, \ldots$; i.e.,

$$H(\kappa_i, 1) = 0 \qquad i = 1, 2, \ldots \tag{3.2.80}$$

As $\kappa$ approaches one of these values the harbour response tends to infinity unless

we include the effect of finite harbour entrance width ($\epsilon > 0$) or entrance losses ($|A_{\text{inc}}| > 0$). However, for nonzero values of $\epsilon$ and $|A_{\text{inc}}|$ it is not obvious from Eq. (3.2.79) how $R$ depends on the various parameters of the problem, especially at resonance. Clearly we can solve Eq. (3.2.79) numerically for $R$. This was done to obtain the values of $R_{\text{res}}$ in Tables 3.2.1 and 3.2.2. However, since $R$ depends on at least three parameters: $\kappa$, $\epsilon$, and $|A_{\text{inc}}|$ (assuming that $f$ is constant), this is not the most desirable way to investigate the dependence of $R$ on these parameters. Most of the important information can be extracted much more easily if we proceed analytically. In this discussion the focus will be on the behaviour of $R$ when $\kappa$ corresponds to a resonant harbour mode; i.e., $\kappa = \kappa_{\text{res}}$. It will be shown that at resonance $R$ depends very differently on $\epsilon$ and $|A_{\text{inc}}|$, depending on the relative magnitude of these two parameters. This is because Eq. (3.2.79) represents a quartic polynomial for the determination of $R$, and the coefficients of the higher order powers of $R$ in this equation are proportional to powers of the small parameters $\epsilon$ and $|A_{\text{inc}}|$. Hence, the behaviour of $R$ near resonance must be determined by singular perturbation techniques. Depending on the relative magnitude of $\epsilon$ and $A_{\text{inc}}$, different terms in the equation are dominant; therefore, the dependence of $R$ on these parameters near resonance will be different as well.

If $\epsilon$ and $A_{\text{inc}}$ are small but finite, resonance will occur for $\kappa$ near $\kappa_i$, and the corresponding harbour response will be bounded. Let us look at the harbour response near resonance and define the deviation of $\kappa$ from $\kappa_i$ as $\kappa'$:

$$\kappa = \kappa_i + \kappa' \qquad \kappa' < O(1) \quad . \tag{3.2.81}$$

Then we will have (using Eq. 3.2.80):

$$\mathcal{H}(\kappa, 1) = \kappa' \frac{\partial \mathcal{H}}{\partial \kappa}(\kappa_i, 1) + O(\kappa'^2) \tag{3.2.82a}$$

$$\frac{\partial \mathcal{H}}{\partial x}(\kappa,1) = \frac{\partial \mathcal{H}}{\partial x}(\kappa_i,1) + O(\kappa') \quad . \tag{3.2.82b}$$

If we substitute these expressions into Eq. (3.2.79) we get:

$$\begin{aligned}\frac{1}{R} = \Bigg| & \kappa' \frac{\partial \mathcal{H}}{\partial \kappa}(\kappa_i,1) - \frac{2\epsilon}{\pi}\frac{\partial \mathcal{H}}{\partial x}(\kappa_i,1)[\ln \epsilon\kappa_i + \gamma - 3/2] \\ & + i\Big(-\epsilon\frac{\partial \mathcal{H}}{\partial x}(\kappa_i,1) - \frac{8f}{3\pi\kappa_i^2}R|A_{\rm inc}|\left|\frac{\partial \mathcal{H}}{\partial x}(\kappa_i,1)\right| \frac{\partial \mathcal{H}}{\partial x}(\kappa_i,1)\Big)\Bigg| \\ & + O(\kappa'^2, \kappa'\epsilon\ln\epsilon, R|A_{\rm inc}|\kappa')\end{aligned} \quad . \tag{3.2.83}$$

At resonance we will have $\partial R/\partial\kappa' = 0$ (and $\partial^2 R/\partial\kappa'^2 < 0$). Let us denote the values of quantities evaluated at resonance with the subscript "res," i.e., $\kappa'_{\rm res}$ and $R_{\rm res}$. If we differentiate Eq. (3.2.83) with respect to $\kappa'$ and then solve for $\kappa'_{\rm res}$, we get:

$$\kappa'_{\rm res} = \frac{2\epsilon}{\pi}\frac{\dfrac{\partial \mathcal{H}}{\partial x}(\kappa_i,1)}{\dfrac{\partial \mathcal{H}}{\partial \kappa}(\kappa_i,1)}[\ln\epsilon\kappa_i + \gamma - 3/2] + O(\epsilon^2\ln^2\epsilon, R_{\rm res}|A_{\rm inc}|\epsilon\ln\epsilon) \; . \tag{3.2.84}$$

We still have not determined the amplification factor at resonance, $R_{\rm res}$, but when we do we must check that it is consistent with Eq. (3.2.83):

$$R_{\rm res} < O\left(\frac{1}{A_{\rm inc}}\right) \quad . \tag{3.2.85}$$

If this condition is not satisfied, the terms neglected in Eq. (3.2.83) could be as important as the ones retained. Notice that $\kappa'_{\rm res}$ is independent of $|A_{\rm inc}|$ or $f$. To this approximation the entrance loss dissipation does not affect the frequency at which resonance occurs (although it does, of course, greatly affect the amplification factor at resonance).

The ratio of the derivatives in Eq. (3.2.84) has a significance. We have defined $\kappa_i$ to be the solutions to $\mathcal{H}(\kappa_i,1) = 0$; i.e., $\kappa_i$ are the zero order approximations

to the values of $kL$ at resonance for a harbour of length $L$ (nondimensional length $= 1$). For a harbour of length $xL$ (nondimensional length $= x$), the zero order approximations to the values of $\kappa$ at resonance would be determined by $\mathcal{H}(\kappa_i, x) = 0$. This would define $\kappa_i(x)$, the zero order approximations of $kL$ at resonance for a harbour of length $xL$. With this definition of $\kappa_i(x)$, the ratio of derivatives in Eq. (3.2.84) is simply $-d\kappa_i(1)/dx$, and so:

$$\kappa'_{\rm res} = -\frac{2\epsilon}{\pi}\frac{d\kappa_i}{dx}(1)[\ln \epsilon\kappa_i + \gamma - 3/2] + O(\epsilon^2 \ln^2\epsilon, R_{\rm res}|A_{\rm inc}|\epsilon \ln \epsilon) \ . \qquad (3.2.86)$$

In general, $\kappa_i$ is a decreasing function of $x$ (since the resonant frequencies will decrease as the harbour length increases). Hence, $d\kappa_i(1)/dx$ is negative. Therefore, for small $\epsilon$:

$$\kappa'_{\rm res} < 0 \quad . \qquad (3.2.87)$$

Hence, $\kappa_{\rm res} < \kappa_i$. This means that the resonant frequencies of a harbour decrease as its entrance width increases. The resonant frequencies approach the theoretical values, $\kappa_i$, only if the relative entrance width goes to zero ($\epsilon \to 0$).

Now let us look at the behaviour of $R$ near resonance, in particular its dependence on $\epsilon$ and $|A_{\rm inc}|$. If Eq. (3.2.84) is substituted into (3.2.83), the following approximate expression is obtained to determine $R_{\rm res}$.

$$R_{\rm res} = \frac{1}{\left|\epsilon\frac{\partial\mathcal{H}}{\partial x}(\kappa_i,1) + \frac{8f}{3\pi\kappa_i^2}R_{\rm res}|A_{\rm inc}|\left|\frac{\partial\mathcal{H}}{\partial x}(\kappa_i,1)\right|\frac{\partial\mathcal{H}}{\partial x}(\kappa_i,1)\right| + \text{H.O.T.}} \qquad (3.2.88)$$

where H.O.T. refers to higher order terms of smaller magnitude. The solution to this equation is:

$$R_{\rm res} = \frac{\epsilon}{|A_{\rm inc}|}\frac{\sqrt{1 + \frac{32f}{3\pi\kappa_i^2}\frac{|A_{\rm inc}|}{\epsilon^2}} - 1}{\frac{16f}{3\pi\kappa_i^2}\left|\frac{\partial\mathcal{H}}{\partial x}(\kappa_i,1)\right|} + \text{H.O.T.} \quad . \qquad (3.2.89)$$

This expresion is valid for any relative magnitude of $\epsilon$ and $|A_{\rm inc}|$ (provided that they are both small). In particular this is the expression that must be used when both entrance losses and radiation are equally important. We can see that the condition for this is $|A_{\rm inc}| = O(\epsilon^2)$. There are two important cases of interest where this expression can be simplified.

Case I $\quad |A_{\rm inc}| < O(\epsilon^2)$ :

In this case the amplitude of the incident wave system is very small. Therefore, entrance losses do not contribute a significant amount to the total dissipation. Radiation of energy from the mouth of the harbour is the dominant source of dissipation and it is this mechanism that limits the harbour response at resonance. The amplification factor at resonance becomes:

$$R_{\rm res} = \frac{1}{\epsilon \left| \frac{\partial \mathcal{H}}{\partial x}(\kappa_i, 1) \right|} + \text{H.O.T.} \qquad (3.2.90a)$$

$$= O(\frac{1}{\epsilon}) \quad . \qquad (3.2.90b)$$

Notice that $R_{\rm res}$ is inversely proportional to the width of the harbour. This behaviour has been called the harbour paradox (Miles & Munk 1961). If the effect of entrance losses is not included in the analysis of the harbour response of a narrow rectangular harbour, the wave amplitude will grow unbounded at resonance as its entrance is made narrower and narrower. It may appear from Eq. (3.2.90) that even with entrance losses the wave amplitude will grow unbounded as $\epsilon \to 0$, but that is not so. As $\epsilon \to 0$, it is true that $R_{\rm res} \to \infty$, but Eq. (3.2.90) is valid only for $|A_{\rm inc}| < O(\epsilon^2)$ and so, even if $R_{\rm res}$ is large the actual wave amplitude in the harbour will be small:

$$|A_{\rm res}| = 2R_{\rm res}|A_{\rm inc}| < O(\frac{1}{\epsilon})\, O(\epsilon^2) < O(\epsilon) \quad . \qquad (3.2.91)$$

Case II $\quad |A_{\text{inc}}| > O(\epsilon^2)$ :

In this case dissipation is dominated by entrance losses and we find the following behaviour for $R_{\text{res}}$ :

$$R_{\text{res}} = \frac{1}{|A_{\text{inc}}|^{1/2}} \frac{\sqrt{3\pi\kappa_i^2/8f}}{\left|\frac{\partial \mathcal{H}}{\partial x}(\kappa_i, 1)\right|} + \text{H.O.T.} \tag{3.2.92a}$$

$$= O\left(\frac{1}{|A_{\text{inc}}|^{1/2}}\right) \quad . \tag{3.2.92b}$$

Here the harbour response is limited by the amplitude of the incident wave system. Again there is no paradox.

Notice that from Eqs. (3.2.89), (3.2.90b) and (3.2.92b), $R_{\text{res}}$ does satisfy Eq. (3.2.85), so the analysis is consistent.

So far we have considered the geometry and bathymetry of the harbour fixed, so $\epsilon$ and $|A_{\text{inc}}|$ have been the only parameters of the problem that determine $R_{\text{res}}$. However, we can also investigate the dependence of $R_{\text{res}}$ on the geometry and bathymetry of the harbour. Its effect enters the problem through the harbour function $\mathcal{H}(\kappa, x)$. Different harbour geometry and bathymetry will generate different harbour functions. Now consider the incident wave and relative harbour width fixed so that $\epsilon$ and $|A_{\text{inc}}|$ are constant. From Eqs. (3.2.89), (3.2.90), and (3.2.92) we see that the behaviour of $R$ at resonance depends on the parameters $\kappa_i$ and the slope of the harbour function $\mathcal{H}$ at the harbour entrance, i.e., $\partial \mathcal{H}(\kappa_i, 1)/\partial x$. For cases I and II the behaviour is:

Case I : $$R_{\text{res}} \sim \frac{1}{\left|\frac{\partial \mathcal{H}}{\partial x}(\kappa_i, 1)\right|} \qquad i = 1, 2, \ldots \tag{3.2.93a}$$

Case II : $$R_{\text{res}} \sim \frac{\kappa_i}{\left|\frac{\partial \mathcal{H}}{\partial x}(\kappa_i, 1)\right|} \qquad i = 1, 2, \ldots \tag{3.2.93b}$$

Now let us look at the behaviour of the modified amplification factor, $R'$, at resonance. From Eq. (3.2.36), it is obtained by dividing $R$ by the factor $S$,

where $S$ is defined by Eq. (3.2.35). The quantity $S$ measures the amount by which the amplitude of a plane harmonic wave is amplified as it travels from the harbour entrance to the shore, due to shoaling and geometrical amplification. By dividing out the amplification due to these processes, the modified amplification factor, $R'$, is a better measure of the amplification directly attributable to the resonance process. If Eq. (3.2.82) is substituted into Eq. (3.2.35) we get:

$$S_{\text{res}} = \left| \frac{1}{\kappa_i} \frac{\partial \mathcal{H}}{\partial x}(\kappa_i, 1) \right|^{-1} + \text{H.O.T.} \quad . \tag{3.2.94}$$

If this expression and Eq. (3.2.89) are substituted into Eq. (3.2.34), one obtains:

$$R'_{\text{res}} = \frac{\epsilon}{|A_{\text{inc}}|} \frac{3\pi\kappa_i^2}{16f} \left\{ \sqrt{1 + \frac{32f}{3\pi\kappa_i^2} \frac{|A_{\text{inc}}|}{\epsilon^2}} - 1 \right\} + \text{H.O.T.} \quad . \tag{3.2.95}$$

For Case I and Case II this expression can be reduced to:

$$\text{Case I} \qquad |A_{\text{inc}}| < O(\epsilon^2) \qquad R'_{\text{res}} = \frac{1}{\kappa_i \epsilon} + \text{H.O.T.} \tag{3.2.96}$$

$$\text{Case II} \qquad |A_{\text{inc}}| > O(\epsilon^2) \qquad R'_{\text{res}} = \frac{1}{|A_{\text{inc}}|^{1/2}} \sqrt{\frac{3\pi}{8f}} + \text{H.O.T.} \quad . \tag{3.2.97}$$

For $f$ constant, $R'_{\text{res}}$ is solely a function of the relative harbour entrance width, $\epsilon$, the incident wave amplitude $|A_{\text{inc}}|$, and the zero order approximation to the nondimensional frequency of resonant mode $i$, $\kappa_i$. The particular harbour geometry and bathymetry enter only through its influence on the nondimensional resonant wave frequency, $\kappa_i$, where $\kappa_i$ is determined from Eq. (3.2.80). Notice that, in Case II, $R'_{\text{res}}$ is independent of the particular resonant mode (i.e., $R'_{\text{res}}$ does not depend on $i$). In fact, it is even independent of the particular harbour geometry and bathymetry. Hence, we expect fairly uniform response at each of the resonant modes. However, in Case I, $R'_{\text{res}} \sim 1/\kappa_i$; hence, the resonant response will decrease for the higher modes as $\kappa_i$ increases. This behaviour can be seen in the results presented in Tables 3.2.1 and 3.2.2. For the general case, the

harbour response will behave in a manner intermediate between these two cases. In addition, the higher order terms neglected in this analysis will modify these results a little.

This analysis shows that for a fixed relative harbour entrance width, $\epsilon$, and incident wave amplitude, $|A_{\text{inc}}|$, the harbour response $R'_{\text{res}}$ at the first resonant mode will be maximized (minimized) by the harbour whose geometry and bathymetry minimizes (maximizes) the lowest nondimensional resonant frequency, $\kappa_1$. However, as just mentioned, the harbour geometry and bathymetry will have little influence if the entrance dissipation is large (as shown by Eq. (3.2.97)).

For applications, this analysis is valid only for the lower resonant modes, i.e., for modes where $i$ or $\kappa_i$ is small. In order to use a one-dimensional theory within the harbour, it was necessary to make the assumption that the ratio of the width of the harbour to a characteristic wavelength scale was small; i.e.,

$$kb^*(L) \ll 1 \quad . \tag{3.2.98}$$

Since $\kappa = kL$ and $\epsilon = b^*(L)/L$, this can be rewritten as:

$$\kappa\epsilon \ll 1 \quad . \tag{3.2.99}$$

If the geometry of the harbour is fixed, i.e., $\epsilon = \text{const}$, then this assumption must be violated for the higher modes where $\kappa \rightarrow \infty$. It was also assumed that the effects of frequency dispersion were negligible. Therefore, the condition:

$$kh_0 \ll 1 \tag{3.2.100}$$

must also be satisfied for this analysis to be valid. Since $\kappa = kL$, this can be rewritten as:

$$\kappa\left(\frac{h_0}{L}\right) \ll 1 \quad . \tag{3.2.101}$$

If the ratio of the water depth to the harbour length is held constant, then this ratio can be made arbitrarily large by letting $\kappa \to \infty$. Therefore, dispersive effects cannot be ignored for the higher resonant modes, and a dispersive theory must be used to treat those cases. Of course, if the ratio $h_0/L$ in Eq.(3.2.101) were reduced at the same rate as $\kappa$ increased then Eq. (3.2.100) would remain valid but this is not possible, except in laboratory experiments. Since both Eq. (3.2.99) and (3.2.101) must be satisfied, the upper limit of applicability of this theory will depend on how small $\epsilon$ and $h_0/L$ are. However, the fact that this analysis is not valid as $i \to \infty$ is not a problem because in general we will be interested only in the lowest resonant modes since they are responsible for the largest amplification factors.

### 3.2.8 General Case

The more general case where the incident wave is not purely sinusoidal can be treated by the method of Fourier superposition; i.e., Eqs. (3.2.25a) and (3.2.25b) can be generalized to:

$$\eta(x,t) = \sum_{n=1}^{\infty} A_n \mathcal{H}_n(\kappa, x)\, e^{in\kappa_0 t} \tag{3.2.102a}$$

$$u(x,t) = -i \sum_{n=1}^{\infty} A_n \mathcal{U}_n(\kappa, x)\, e^{in\kappa_0 t} \quad . \tag{3.2.102b}$$

If entrance losses are neglected, the amplitude of the $n^{\text{th}}$ Fourier component within the harbour, $A_n$, can be expressed in terms of the $n^{\text{th}}$ Fourier component of the incident wave using Eq. (3.2.78) with $f = 0$. However, if entrance losses are included ( $f \neq 0$ ), the situtation is more complicated because the nonlinear nature of the headloss matching condition prevents a simple uncoupling of the Fourier components. The coupling arises because the expression for the maximum velocity

through the harbour entrance, $u_{\max}$, which appears in the matching condition of Eq. (3.2.23), depends on *all* of the Fourier components; i.e., Eq. (3.2.29) for $u_{\max}$ must be replaced by a more general expression involving all of the Fourier components:

$$u_{\max} = \max_t \Re \left\{ -i \sum_{n=1}^{\infty} A_n \mathcal{U}_n(\kappa, 1)\, e^{in\kappa_0 t} \right\} \quad . \tag{3.2.103}$$

This coupling can be treated effectively using a simple numerical algorithm which computes the Fourier coefficients, $\{A_n\}$, using an iterative scheme. This scheme will be used in Chapter 5 in order to compare this theory with the laboratory experiments and the results of the finite element model. The only term that complicates the analysis is Eq. (3.2.103) for $u_{\max}$. Therefore, the scheme involves approximating Eq. (3.2.103) at each iteration by simpler expressions.

The scheme proceeds as follows. If we Assume that the majority of the energy is contained in the first harmonic, as will be the case for the experiments with which this theory will be compared to, then $u_{\max}$ in Eq. (3.2.103) can be approximated by the first term in the sum; i.e.,

$$u_{\max} = |A_1||\mathcal{U}_1(\kappa, 1)| \quad . \tag{3.2.104}$$

This is exactly the same as Eq. (3.2.29). Therefore, a first estimate for the $\{A_n\}$ can be obtained using precisely the theory just presented for the harmonic case. After these values for the $\{A_n\}$ have been computed, a better estimation for $u_{\max}$ can then be obtained by substituting these $\{A_n\}$ into Eq. (3.2.103). By using that estimate of $u_{\max}$, *improved* values for the $\{A_n\}$ can then be generated. This process can be repeated until the $\{A_n\}$ converge to the degree of accuracy required.

While this numerical algorithm will not necessarily converge if the energy is spread over a large band of frequencies, it was found to be very efficient when the

first harmonic was dominant. For the comparison with the harbour response laboratory experiments in Chapter 5, convergence was obtained very quickly, usually within 2 iterations. This algorithm can be simplified by neglecting entrance losses for the first iteration. That is equivalent to making the approximation $u_{\max} = 0$ at the first step, instead of using Eq. (3.2.104). However, it was found that convergence problems could arise if this simplification was made, so Eq. (3.2.104) was used for the first step of the algorithm.

## 3.3 Nonlinear Runup Effects for a Linearly Sloping Bottom

In this section various nonlinear effects relevant to the runup of nonbreaking waves on a beach will be covered. These results will be useful for validating the finite element model (which will be discussed later in Section 5.1.1 of Chapter 5) based on the long wave equations (3.1.117) and (3.1.118).

Due to the nonlinear nature of the equations that govern the runup of nonbreaking waves on a beach, it is difficult to extract information about this process with only analytical techniques. However, if one specializes the geometry to the case of a linearly sloping beach and neglects dispersive and dissipative effects, it is possible to obtain some interesting results. These results can provide an indication of the effects of the nonlinear terms in the equations of motion on the runup of nonbreaking waves on beaches for other cases where such an analysis is not possible.

Therefore, let us specialize to the case where the still water depth varies linearly with the dimensional horizontal coordinate, $x^*$, as shown in Fig. 3.3.1. Since all of the work in this section will be in the Eulerian description it will not be necessary to subscript variables with the letter E to emphasize that the variable

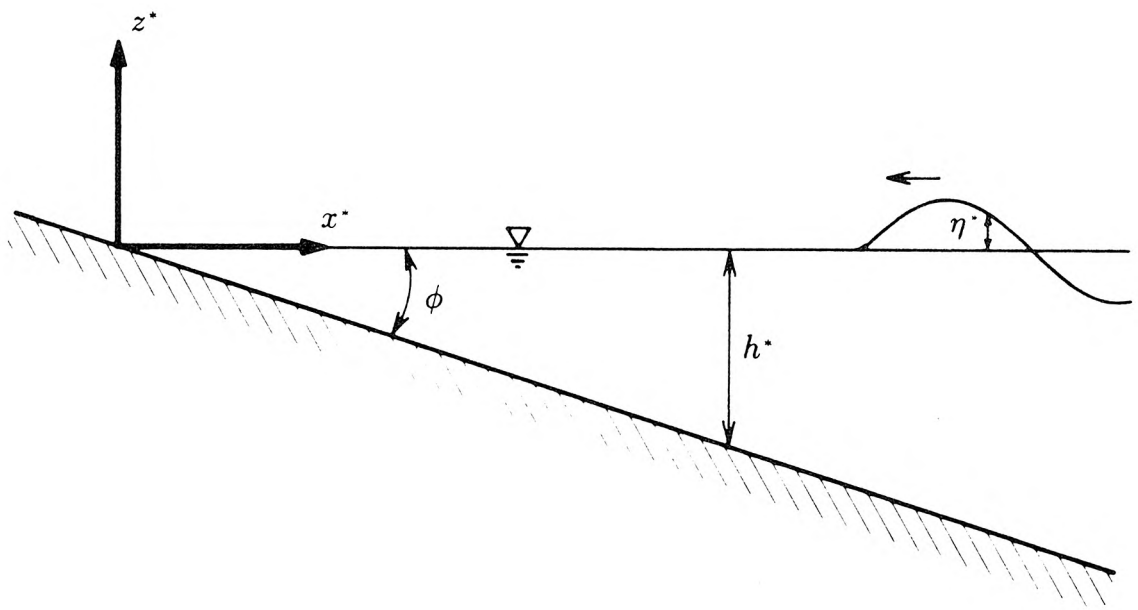


Fig. 3.3.1 Definition Sketch for the Runup of Waves on a Linearly Sloping Beach.

is a function of Eulerian variables. For a small beach angle, $\phi$, we have:

$$h^* = \phi x^* \quad . \tag{3.3.1}$$

The problem is strictly two-dimensional. There are no variations in the $y^*$ direction. Since frequency dispersion will be neglected, this analysis cannot be physically valid as $x^* \to \infty$, since as the water gets deeper and deeper, dispersive effects become more important. Far offshore the wave must eventually transform into a deep water wave where the horizontal fluid particle velocities decay rapidly with depth. Frequency dispersion cannot be neglected in this region. Therefore, this analysis will be valid only in the near shore region where dispersive effects

are small; i.e., the wavelengths are large relative to the depth. The shallow water continuity and momentum equations are well known and may be found in many books on water wave theory (e.g., Stoker 1957). In dimensional form they are:

$$\frac{\partial \eta^*}{\partial t^*} + \frac{\partial}{\partial x^*}[(\eta^* + h^*)u^*] = 0 \tag{3.3.2a}$$

$$\frac{\partial u^*}{\partial t^*} + u^* \frac{\partial u^*}{\partial x^*} + g\frac{\partial \eta^*}{\partial x^*} = 0 \tag{3.3.2b}$$

where $g$ is the acceleration of gravity. Let $\ell$ be a characteristic horizontal length scale of the wave motion. It will depend on the particular problem being studied. Based on shallow water linear wave theory, a characteristic wave celerity can be defined:

$$C = \sqrt{g\ell\phi} \quad . \tag{3.3.3}$$

Then we can define a time scale, $T = \ell/C$, and velocity scale, $u_0 = \ell/T$, as follows:

$$T = \sqrt{\frac{\ell}{\phi g}} \tag{3.3.4}$$

$$u_0 = \sqrt{\phi g \ell} \quad . \tag{3.3.5}$$

Let us choose the following nondimensionalization:

$$x = \frac{x^*}{\ell} \qquad t = \frac{t^*}{T} \qquad h = \frac{h^*}{\phi\ell} = x$$

$$h = \frac{h^*}{\phi\ell} = x \qquad u = \frac{u^*}{u_0} \tag{3.3.6}$$

and make the definition:

$$c^2 = \frac{h^* + \eta^*}{\phi\ell} = h + \eta = x + \eta \quad . \tag{3.3.7}$$

Here $c$ can be interpreted loosely as a local wave celerity. It will not be confused with the independent Lagrangian vertical coordinate $a_3 = c$ since all work in this

section will be in the Eulerian description. With these definitions the equations of motion become:

$$\eta_t + [(\eta + x)u]_x = 0 \tag{3.3.8a}$$

$$u_t + uu_x + \eta_x = 0 \quad . \tag{3.3.8b}$$

For the rest of this section all variables will be nondimensional unless stated otherwise.

If the still water depth is constant, the shallow water equations can be solved by the method of characteristics. In that analysis it is convenient to introduce the wave speed as a dependent variable. That is also convenient in this case. In terms of $u$ and $c$ Eqs. (3.3.8) become:

$$2c_t + 2uc_x + cu_x = 0 \tag{3.3.9a}$$

$$u_t + uu_x + 2cc_x - 1 = 0 \quad . \tag{3.3.9b}$$

Through an elegant series of transformations, Carrier & Greenspan (1958) were able to transform this problem, with two coupled nonlinear equations, into a new problem with only one *linear* equation. A brief derivation based on Whitham (1979) will be presented. This development is included as a convenience for the reader to aid the interpretation of the subsequent analysis.

If Eqs. (3.3.9) are added and subtracted we get:

$$\frac{d}{dt}(u \pm 2c - t) = 0 \qquad \text{along} \qquad \frac{dx}{dt} = u \pm c \quad . \tag{3.3.10}$$

Let us define the characteristic variables $\alpha$ and $\beta$ by:

$$\alpha = \quad u + 2c - t \tag{3.3.11a}$$

$$\beta = -u + 2c + t \quad . \tag{3.3.11b}$$

Hence, Eq. (3.3.10) becomes:

$$\alpha = \text{const} \qquad \text{along} \qquad \frac{dx}{dt} = u + c \tag{3.3.12a}$$

$$\beta = \text{const} \qquad \text{along} \qquad \frac{dx}{dt} = u - c \quad . \tag{3.3.12b}$$

Now let us consider $x$ and $t$ to be functions of $\alpha$ and $\beta$. Then for $\alpha = \text{const}$ or $\beta = \text{const}$ we get:

$$\frac{dx}{dt} = \frac{\dfrac{\partial x}{\partial \beta}}{\dfrac{\partial t}{\partial \beta}} \qquad \text{if} \quad \alpha = \text{const} \tag{3.3.13a}$$

$$\frac{dx}{dt} = \frac{\dfrac{\partial x}{\partial \alpha}}{\dfrac{\partial t}{\partial \alpha}} \qquad \text{if} \quad \beta = \text{const} \quad . \tag{3.3.13b}$$

Combining these relations with Eqs. (3.3.11) and (3.3.12) we obtain the two relations:

$$x_\beta = t_\beta(3\alpha - \beta)/4 + (t^2/2)_\beta \tag{3.3.14a}$$

$$x_\alpha = t_\alpha(\alpha - 3\beta)/4 + (t^2/2)_\alpha \quad . \tag{3.3.14b}$$

The last terms in these two equations, $(t^2/2)_\alpha$ and $(t^2/2)_\beta$, arise from the linear variation of the still water depth with $x$. If the still water depth were constant, these two terms would be zero and the equations would be linear. However, for the special case considered here, where the still water depth varies linearly with $x$, the nonlinear terms can be eliminated by simply differentiating the first equation with respect to $\alpha$, the second equation with respect to $\beta$, and then subtracting one from the other to get:

$$2(\alpha + \beta)t_{\alpha\beta} + 3(t_\alpha + t_\beta) = 0 \quad . \tag{3.3.15}$$

This is a linear partial differential equation for $t(\alpha,\beta)$. It is convenient to introduce new variables $\sigma$ and $\lambda$ by:

$$\lambda = \beta - \alpha = 2(t-u) \tag{3.3.16a}$$

$$\sigma = \alpha + \beta = 4c \quad . \tag{3.3.16b}$$

Then Eq. (3.3.15) beomes:

$$t_{\lambda\lambda} = t_{\sigma\sigma} + \frac{3}{\sigma} t_\sigma \quad . \tag{3.3.17}$$

Now since from Eq. (3.3.16a), $t = \lambda/2 + u$, $u$ must also satsify Eq. (3.3.17):

$$u_{\lambda\lambda} = u_{\sigma\sigma} + \frac{3}{\sigma} u_\sigma \quad . \tag{3.3.18}$$

Finally, if we introduce a "potential" $\varphi(\sigma,\lambda)$ so that

$$u = \frac{\varphi_\sigma}{\sigma} \tag{3.3.19}$$

then Eq. (3.3.18) reduces to the two-dimensional radially symmetric wave equation in polar coordinates where $\lambda$ plays the role of time and $\sigma$ plays the role of the radial coordinate:

$$\varphi_{\lambda\lambda} = \varphi_{\sigma\sigma} + \frac{1}{\sigma} \varphi_\sigma \quad . \tag{3.3.20}$$

The problem has now been reduced to solving Eq. (3.3.20), which is a single linear partial differential equation. The boundary condition at the shoreline also becomes very simple. In the original nonlinear equations, where $x$ and $t$ were the independent variables, the shoreline moved and its motion had to be determined as part of the problem. However, in this case the shoreline is fixed in terms of the coordinate $\sigma$. At the shoreline the total water depth must be identically zero (for all time). This means that at the shoreline $c = 0$, or from Eq. (3.3.16b):

$$\sigma = 0 \qquad \text{(at the shoreline)} \quad . \tag{3.3.21}$$

This simplifies the problem even further. It may be noted here that the shoreline also becomes a fixed boundary when the equations of motion are written in the Lagrangian description. However, in that description the equations are still nonlinear. The transformation outlined here also linearizes the equations of motion (for the special case of a linearly sloping bottom). It is not equivalent to transforming to the Lagrangian description.

In terms of the variables $\sigma$ and $\lambda$ and the potential $\varphi(\sigma,\lambda)$, the expressions for $t$, $x$, $\eta$, $u$, and $c$ are:

$$t = \frac{\lambda}{2} + u = \frac{\lambda}{2} + \frac{\varphi_\sigma}{\sigma} \tag{3.3.22}$$

$$x = \frac{1}{2}u^2 + c^2 + \frac{1}{4}\varphi_\lambda = \frac{1}{2}\left(\frac{\varphi_\sigma}{\sigma}\right)^2 + \frac{1}{4}\varphi_\lambda + \frac{\sigma^2}{16} \tag{3.3.23}$$

$$\eta = c^2 - x = \frac{\sigma^2}{16} - x = -\frac{1}{4}\varphi_\lambda - \frac{1}{2}u^2 = -\frac{1}{4}\varphi_\lambda - \frac{1}{2}\left(\frac{\varphi_\sigma}{\sigma}\right)^2 \tag{3.3.24}$$

$$u = \frac{\varphi_\sigma}{\sigma} \tag{3.3.25}$$

$$c = \frac{\sigma}{4} \quad . \tag{3.3.26}$$

Although Eq. (3.3.20) is certainly much simpler to solve than the two original coupled nonlinear equations (3.3.8a) and (3.3.8b), it is difficult to obtain $\eta$ or $u$ as explicit functions of $x$ and $t$. If $\varphi(\sigma,\lambda)$ is given, then Eqs. (3.3.22)–(3.3.25) will give $t$, $x$, $\eta$, and $u$ all parametrically in terms of the variables $\sigma$ and $\lambda$. In general, it will be very difficult to eliminate $\sigma$ and $\lambda$ to obtain direct functional relationships for $\eta$ and $u$ in terms of $x$ and $t$. In fact, this may be impossible if the Jacobian of the transformation between the $(x,t)$ variables and the $(\sigma,\lambda)$ variables vanishes. In such cases the solution becomes multivalued, and there will be no unique functional relationship for $\eta$ and $u$ in terms of $x$ and $t$. Such a situation indicates that a bore should be fitted to the solution. However, even with this drawback, important information can still be obtained.

An important result concerns the effect of the nonlinear terms in the original equations of motion on the maximum and minimum runup heights predicted at the shoreline. To compare the linear and nonlinear theories, the same transformations outlined above can also be applied to the *linearized* shallow water equations. The same second order partial differential equation identical to Eq. (3.3.20) is obtained, but the expressions for $t$, $x$, $\eta$, $u$, and $c$ in terms of $\sigma$, $\lambda$ and $\varphi(\sigma,\lambda)$ are simpler. For completeness, the governing differential equation is repeated here with the five new expressions for $t$, $x$, $\eta$, $u$, and $c$:

$$\varphi_{\lambda\lambda} = \varphi_{\sigma\sigma} + \frac{1}{\sigma}\varphi_{\sigma} \tag{3.3.27}$$

where

$$t = \frac{\lambda}{2} \tag{3.3.28}$$

$$x = \frac{\sigma^2}{16} \tag{3.3.29}$$

$$\eta = -\frac{1}{4}\varphi_{\lambda} \tag{3.3.30}$$

$$u = \frac{\varphi_{\sigma}}{\sigma} \tag{3.3.31}$$

$$c = \frac{\sigma}{4} \quad . \tag{3.3.32}$$

In this case it is easy to eliminate $\sigma$ and $\lambda$ from the problem, but for the purposes of comparing the linear theory with the nonlinear theory it is convenient not to do that.

Now suppose that we are given a solution $\varphi(\sigma,\lambda)$ to Equation (3.3.20) or (3.3.27). Provided the solution decays as $x \to \infty$, the nonlinear effects will also decay as $x \to \infty$ and both the linear and the nonlinear solutions will agree with each other. The more important region is at and near the shoreline. The shoreline corresponds to $\sigma = 0$. At the points of maximum and minimum runup,

the velocity at the shoreline must be zero. Hence, from Eq. (3.3.25) or (3.3.31), maximum and minumum runup must occur when:

$$\left.\frac{\varphi_\sigma}{\sigma}\right|_{\sigma\to 0} = 0 \quad . \tag{3.3.33}$$

If this equation has solutions, it will determine a set of one or more values for $\lambda$: $\lambda_1$, $\lambda_2$, .... The $\lambda_i$ will be identical for both the linear and nonlinear theories because $\varphi(\sigma,\lambda)$ is the same for both theories. Each $\lambda_i$ will correspond to a relative maximum or minimum runup height (recall that $\lambda$ is time-like). From Eq. (3.3.33) the nonlinear term in Eq. (3.3.24), $1/2(\varphi_\sigma/\sigma)^2$, is exactly zero for $\sigma = 0$, $\lambda = \lambda_i$. Therefore, the corresponding runup heights, $\eta_i$, are the same according to both the nonlinear theory of Eq. (3.3.24) and the linear theory of Eq. (3.3.30):

$$\eta_i = -\frac{1}{4}\varphi_\lambda \Big|_{\substack{\sigma=0\\ \lambda=\lambda_i}} \quad . \tag{3.3.34}$$

Hence, both the linear and nonlinear theories predict the same maximum and minimum runup. The times at which the runup extrema occur are also the same according to both theories:

$$t_i = \frac{\lambda_i}{2} \quad . \tag{3.3.35}$$

However, in general, the wave profiles at these times and the trajectory of the shoreline in $(x,t)$ space will not be the same.

Now let us look at a particular case. A simple solution of Eq. (3.3.20) or (3.3.27) pointed out by Carrier & Greenspan (1958) is:

$$\varphi(\sigma,\lambda) = -\frac{8A_0}{\varrho} J_0(\varrho\frac{\sigma}{2}) \sin \varrho\frac{\lambda}{2} \tag{3.3.36}$$

where $A_0$ is an arbitrary amplitude parameter and $\varrho$ is a separation constant. Without loss of generality let us set $\varrho = 1$ and assume that $A_0 > 0$. This potential corresponds to a standing wave solution resulting from the perfect reflection from

the shore of a wave of unit frequency ( $\varrho = 1$ ). From Eqs. (3.3.28)-(3.3.30) this potential, i.e., Eq. (3.3.36), corresponds to the linear solution:

$$\eta = A_0 J_0(2\sqrt{x}) \cos t \quad . \tag{3.3.37}$$

With the choice of length scale $\ell = \phi g/\omega^2$, this solution can be expressed in dimensional units as:

$$\eta^* = A_0^* J_0(2\omega\sqrt{\frac{x^*}{\phi g}}) \cos \omega t^* \tag{3.3.38}$$

where

$$A_0^* = \frac{\phi^2 g A_0}{\omega^2} \quad . \tag{3.3.39}$$

Both the linear and nonlinear theories predict maximum and minimum runup heights of $\pm A_0$. The Jacobian of the transformation between the $(\sigma, \lambda)$ coordinates and the $(x, t)$ coordinates is nonzero for small $A_0$ and first becomes zero for $A_0 = 1$ (e.g., see Whitham 1979). Consequently, the nonlinear solution corresponding to Eq. (3.3.36) is valid only for $A_0 \leq 1$. For $A_0 = 1$, the tangent to the water surface displacement, $\eta$, is vertical at the maximum rundown point. Therefore, in all that follows we will assume that $A_0 \leq 1$.

From Eq. (3.3.37), linear theory predicts that nodes will occur for:

$$x_s = \frac{1}{4} j_s^2 \qquad \text{i.e.,} \qquad \sigma_s = 2 j_s \qquad s = 1, 2, \ldots \tag{3.3.40}$$

where $j_s$ is the $s^{\text{th}}$ zero of $J_0(z)$. It is interesting to examine the behaviour of the nonlinear solution at these values of $x = x_s$ $s = 1, 2, \ldots$ . It will be shown that according to the nonlinear theory these locations are not nodes in the strict sense of the word, but the behaviour of the solution at these points does display some of the characteristics seen at true node points. Therefore, we will refer to these points as "node" points, using quotation marks. In fact, we will show that the water surface height at these "node" points is always either negative or at

most zero and is equal to zero exactly twice every period of the incident wave. In particular, let us examine the behaviour of the solution at these points precisely at the time of maximum or minimum runup at the shoreline, i.e., at $t = t_i = \lambda_i/2$ as given by Eq. (3.3.35). If we substitute Eq. (3.3.36) into Eq. (3.3.22) we get:

$$t_i = \frac{\lambda_i}{2} = i\pi \qquad i = 0, \pm 1, \pm 2, \ldots \tag{3.3.41}$$

At these times the water surface profile is:

$$\eta = (-1)^i A_0 J_0(\frac{\sigma}{2}) \tag{3.3.42a}$$

$$x = \frac{\sigma^2}{16} - (-1)^i A_0 J_0(\frac{\sigma}{2}) \tag{3.3.42b}$$

$$u \equiv 0 \quad . \tag{3.3.42c}$$

Note that $u \equiv 0$ (everywhere) at the times of maximum and minimum runup. Linear theory also predicts this behaviour. The even values of $i$ correspond to maximum runup and the odd values of $i$ correspond to minimum runup (maximum rundown). At the points $x = j_s^2/4$, Eq. (3.3.42b) is satisfied for $\sigma = 2j_s$, $s = 1, 2, \ldots$ exactly as in the linear case. Hence, at a "node" point:

$$\eta = 0 \qquad x = j_s^2/4, \quad t = i\pi \quad . \tag{3.3.43}$$

This is also the same as linear theory. Now let us examine $\partial\eta/\partial t$ and $\partial^2\eta/\partial t^2$ at the "node" points at the times of maximum and minimum runup. Linear theory, of course, predicts $\partial\eta/\partial t = \partial^2\eta/\partial t^2 = 0$ (in fact, it predicts that all the time derivatives of $\eta$ are zero since it predicts $\eta$ is identically zero). At the "node" points $x = j_s^2/4$, the variables $\sigma$ and $\lambda$ are solely functions of the time $t$. If Eq. (3.3.24) for $\eta$ is differentiated with respect to $t$ holding $x$ constant the result is:

$$\left.\frac{\partial\eta}{\partial t}\right|_{x=\text{const}} = \frac{\sigma}{8}\frac{d\sigma}{dt} \tag{3.3.44a}$$

$$\left.\frac{\partial^2\eta}{\partial t^2}\right|_{x=\text{const}} = \frac{\sigma}{8}\frac{d^2\sigma}{dt^2} + \frac{1}{8}\left(\frac{d\sigma}{dt}\right)^2 \quad . \tag{3.3.44b}$$

In order to get an expression for $d\sigma/dt$ at a "node" point at the time of maximum or minimum runup, expression (3.3.36) for $\varphi(\sigma,\lambda)$ (with $\varrho = 1$) can be substituted into Eq. (3.3.23) for $x$. This expression is then differentiated with respect to $t$ holding $x$ constant. At the time of maximum or minimum runup at a "node" point we then get:

$$0 = \left\{j_s - 2(-1)^i A_0 J_1(j_s)\right\}\frac{d\sigma}{dt} \quad . \tag{3.3.45}$$

Now for $A_0 < 1$:

$$j_s - 2(-1)^i A_0 J_1(j_s) > 0 \qquad A_0 < 1 \quad \text{for all } s \quad . \tag{3.3.46}$$

Hence, Eq. (3.3.45) reduces to:

$$\frac{d\sigma}{dt} = 0 \qquad \text{at} \quad x = j_s^2/4, \quad t = i\pi \quad . \tag{3.3.47}$$

Substituting this into Eq. (3.3.44a) yields the result that $\partial\eta/\partial t = 0$ at a "node" point at the times of maximum or minimum runup:

$$\left.\frac{\partial\eta}{\partial t}\right|_{x=j_s^2/4} = 0 \qquad \text{at} \quad t = i\pi \quad . \tag{3.3.48}$$

This again is the same as linear theory. However, when we look at $\partial^2\eta/\partial t^2$ we get a very interesting result which differs from linear theory. From Eq. (3.3.44b) we see that we must obtain an expression for $d^2\sigma/dt^2$. If we substitute Eq. (3.3.36) into Eq. (3.3.23) and differentiate twice with respect to $t$ holding $x$ fixed and make use of (3.3.47), then at the time of maximum or minimum runup at a "node" point we find:

$$\frac{d^2\sigma}{dt^2} = -\frac{\left[2A_0\dfrac{J_1(j_s)}{j_s}\dfrac{d\lambda}{dt}\right]^2}{j_s + 2(-1)^i A_0 J_1(j_s)} \qquad \text{at} \quad x = j_s^2/4, \quad t = i\pi \quad . \tag{3.3.49}$$

To evaluate this expression we need an expression for $d\lambda/dt$. That can be obtained by substituting Eq. (3.3.36) into Eq. (3.3.22) and differentiating with respect to $t$, holding $x$ fixed. The result is:

$$\frac{d\lambda}{dt} = \frac{2j_s}{j_s + 2(-1)^i A_0 J_1(j_s)} \qquad \text{at} \quad x = j_s^2/4, \quad t = i\pi \quad . \tag{3.3.50}$$

The important thing is that $d\lambda/dt \neq 0$. If this expression for $d\lambda/dt$ and Eqs. (3.3.49) and (3.3.47) is substituted into Eq. (3.3.44b) then at the time of maximum and minimum runup we find that at the "node" points the second time derivative of the water surface displacement is given by the following expression:

$$\frac{\partial^2 \eta}{\partial t^2} = -j_s \frac{\left[2A_0 J_1(j_s)\right]^2}{\left[j_s + 2(-1)^i A_0 J_1(j_s)\right]^3} < 0 \qquad \text{at} \quad x = j_s^2/4, \quad t = i\pi \, . \tag{3.3.51}$$

Equation (3.3.46) shows that the denominator is positive in this expression. For $s$ odd, the curvature is greater at the time of minimum runup ($i$ odd), but if $s$ is even, the curvature is greater at the time of maximum runup ($i$ even). This is a very interesting result because when it is combined with the previous results of Eqs. (3.3.43) and (3.3.48), it shows that $\eta$ must have at least two maxima for every period of the wave's motion. With the addition of some numerical work one can show that $\eta$ has exactly two maxima for every period.

To evaluate $\eta(x,t)$ for arbitrary $x$ and $t$, Eqs. (3.3.22)-(3.3.24) must be solved using a numerical technique, since the parameters $\sigma$ and $\lambda$ can not be eliminated by analytical methods. With the $\varphi(\sigma,\lambda)$ given by Eq. (3.3.36), Eqs. (3.3.22) to (3.3.24) represent three nonlinear parametric equations for $t$, $x$, and $\eta$ in terms of $\sigma$ and $\lambda$. Using Newton's method, $\eta(x,t)$ can easily be obtained. At and near the first "node" point $x = j_1^2/4$, the time history of $\eta$ is plotted in Fig. 3.3.2 for two periods of the incident wave. Notice how there are two relative maxima every period of $2\pi$. Far offshore ($x \to \infty$) the motion is sinusoidal with period $2\pi$. The other important observation is that at the "node" point the water surface

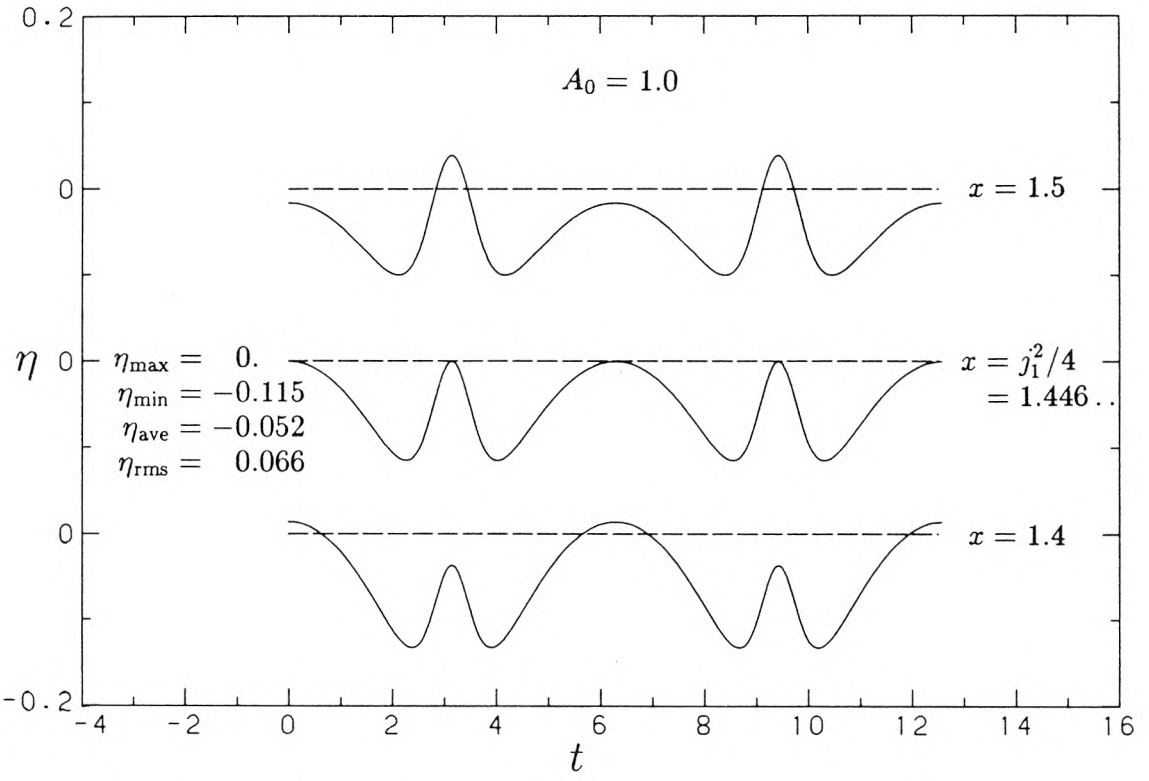


Fig. 3.3.2 Time record of the water surface elevation at and near the first "node." $A_0 = 1$ $(\eta = \eta^* \omega^2/\phi^2 g \quad t = \omega t^*)$.

elevation is always either zero or negative. Hence, the mean value of $\eta$ must be negative. This is characteristic of wave setdown, although setdown normally refers only to *progressive* waves which propagate in water of decreasing depth (Dean & Dalrymple 1984). For breaking waves there is also a region of wave set*up* within the breaker zone, but it is not predicted by this solution because the theory being presented here does not model wave breaking. In the linear case the time average of $\eta$ is zero everywhere. Figures 3.3.3 and 3.3.4 contrast the wave profiles predicted by linear theory $(A_0 \to 0)$ and nonlinear theory. All the results were obtained by numerically solving Eqs. (3.3.22)-(3.3.24) for the case where $\varphi$ is given by Eq. (3.3.36). In the nonlinear case, the amplitude $A_0$ was chosen to be unity to emphasize the nonlinear effects. By following the free surface at the "node" in Fig. 3.3.4, one can see how the wave system manages to exhibit two peaks per

period in this region but only one elsewhere. The mean value of $\eta$ is negative everywhere and increases in magnitude monotonically for decreasing values of $x$. For $A_0 = 1$ the mean value of the water surface profile at the maximum rundown point $(x = +1)$ is $\sim -0.118$.

This double peak phenomenon was observed by Kato & Hattori (1980) from laboratory pressure measurements made under nonbreaking waves on a sloping beach. The pressure measurements showed two maxima for every period of the incident wave. They showed that this effect was predicted by the runup theory of Shuto (1967). When they used Shuto's theory to compute the free surface, they found that it also displayed the same two-peak behaviour in this region. However, they did not discuss the drop in the mean water level near the shore, even though this effect was evident from the theoretical results they presented.

As the parameter $A_0$ is increased the wave becomes more and more distorted near the shore and when $A_0$ reaches unity the wave profile exhibits a vertical tangent at the shoreline at the time of maximum rundown, as shown in Fig. 3.3.4 at $t = \pi$. For $A_0$ near unity the vertical accelerations at the rundown point are large enough so that the assumption of a hydrostatic pressure distribution, which is implicit in the shallow water theory of Eq. (3.3.8) being applied here, is no longer valid. This can be shown quantitatively, since explicit formulae for the variables $\eta$ and $u$ and their time derivatives at the point of maximum rundown can be obtained. If Eq. (3.3.36) (with $\varrho = 1$) is substituted into Eqs. (3.3.22)-(3.3.25) and the expressions are evaluated at the shoreline, i.e., $\sigma = 0$, we get:

$$t = \frac{\lambda}{2} + A_0 \sin\frac{\lambda}{2} \tag{3.3.52}$$

$$x = -A_0 \cos\frac{\lambda}{2} + \frac{A_0^2}{2}\sin^2\frac{\lambda}{2} \tag{3.3.53}$$

$$\eta = -x = A_0 \cos\frac{\lambda}{2} - \frac{A_0^2}{2}\sin^2\frac{\lambda}{2} \tag{3.3.54}$$

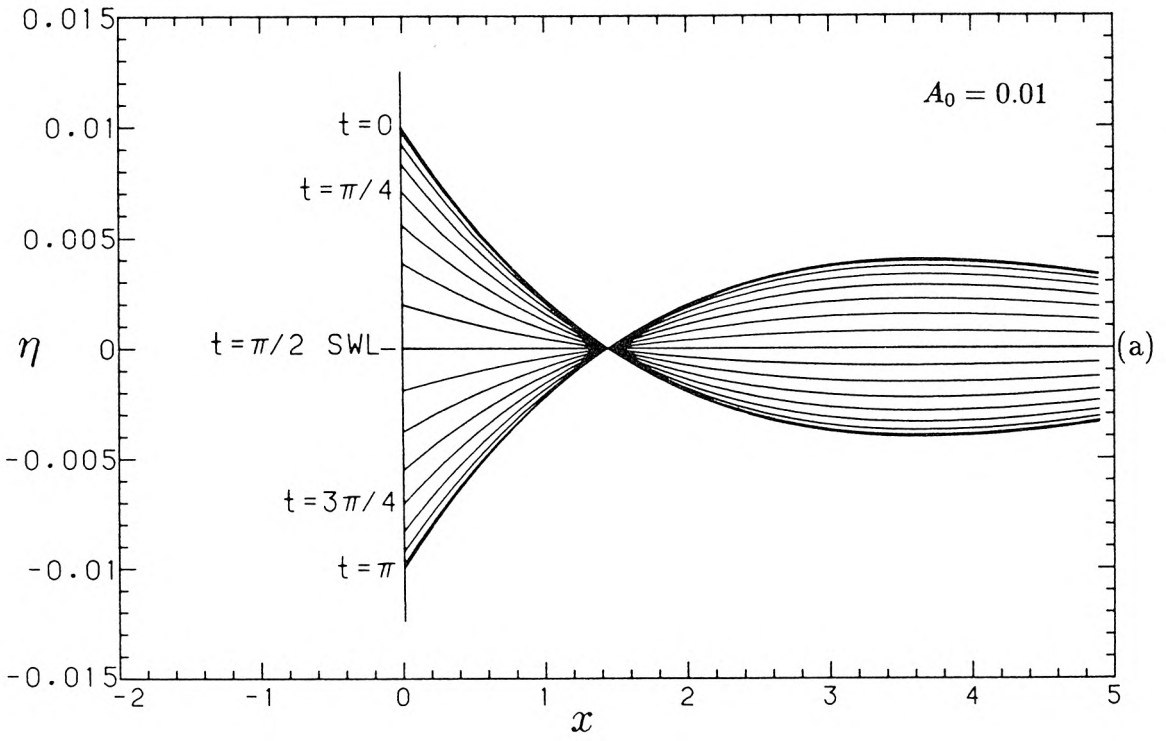


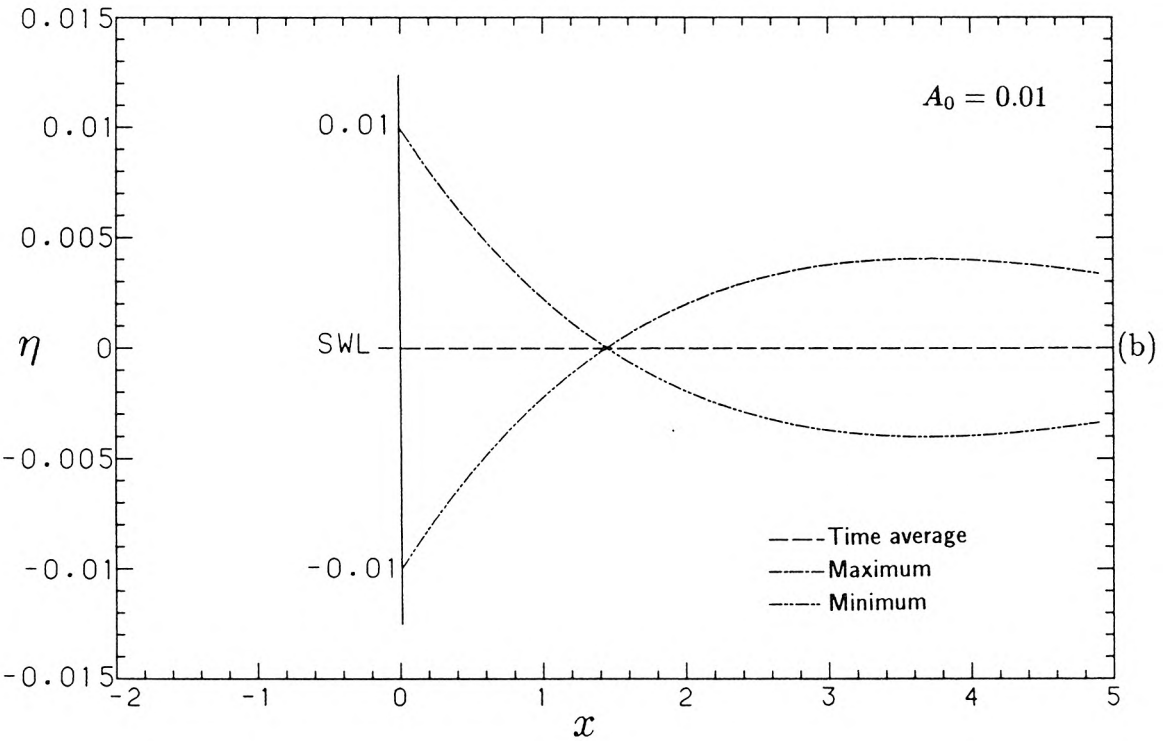


Fig. 3.3.3 Linear theory $(A_0 \to 0)$; (a) wave profiles at successive time intervals, (b) wave envelope and mean value. $(\eta = \eta^* \omega^2/\phi^2 g \quad x = x^* \omega^2/\phi g)$

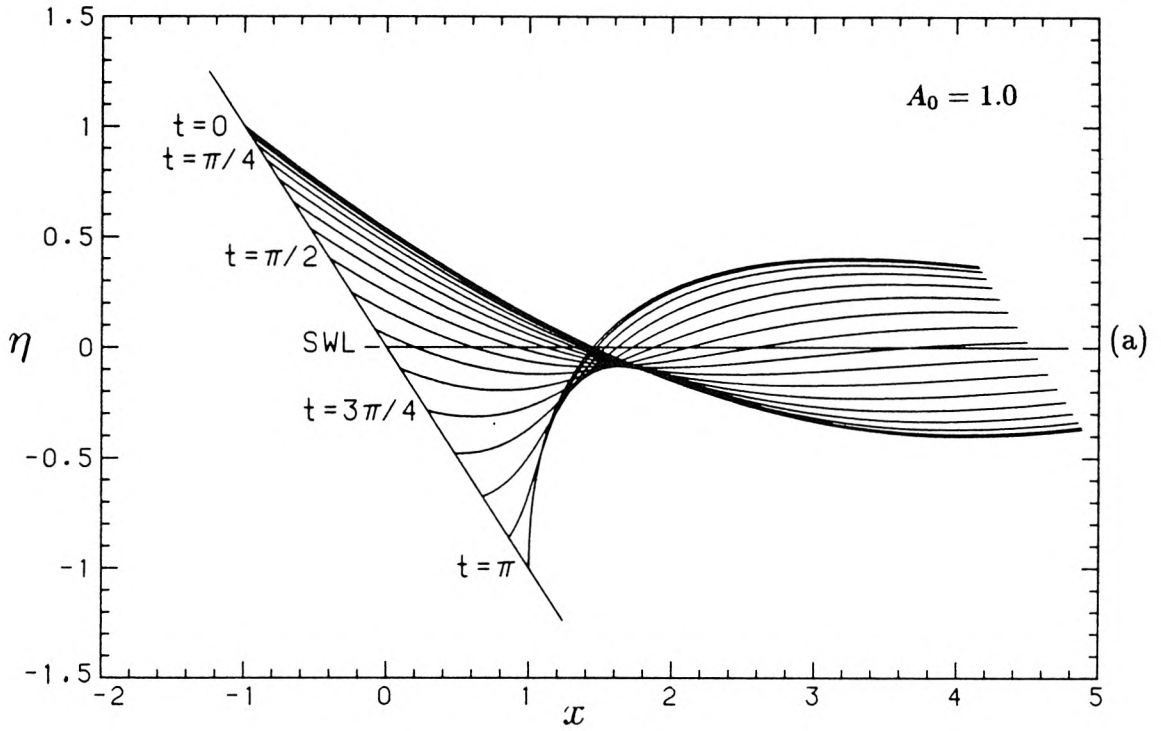


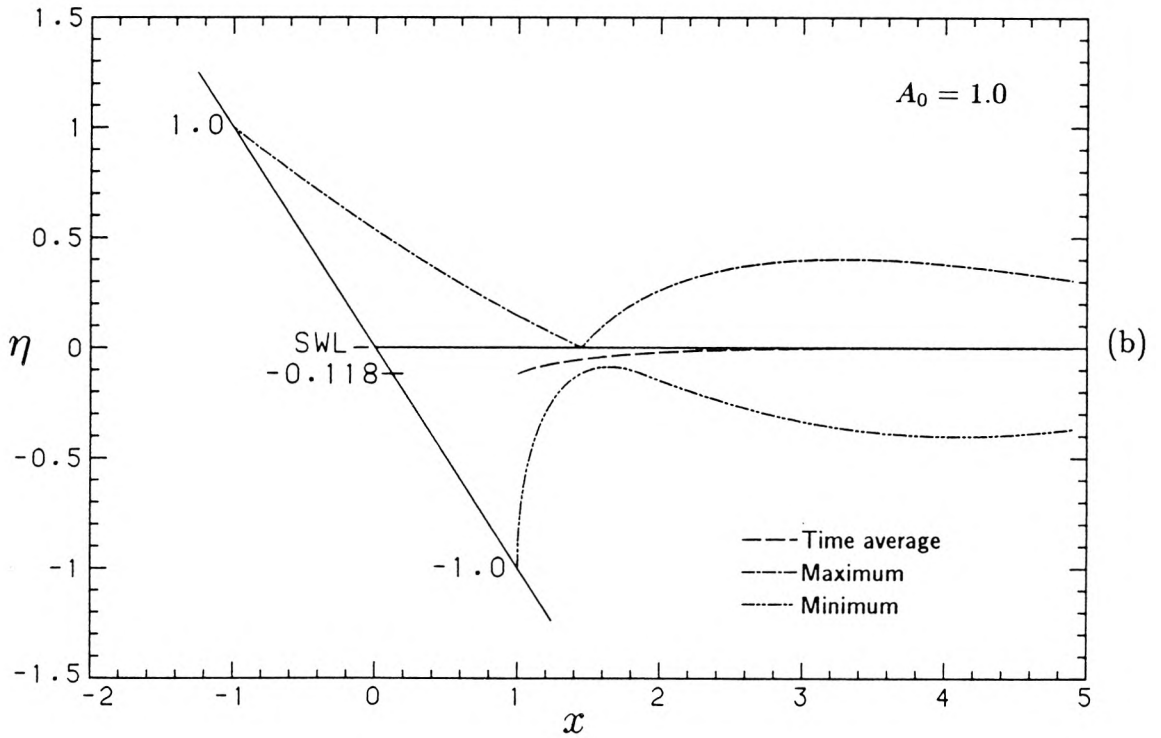


Fig. 3.3.4 Nonlinear theory $(A_0 = 1)$; (a) wave profiles at successive time intervals, (b) wave envelope and mean value. $(\eta = \eta^* \omega^2/\phi^2 g \quad x = x^* \omega^2/\phi g)$.

$$u = A_0 \sin \frac{\lambda}{2} \quad . \tag{3.3.55}$$

The horizontal acceleration of the fluid at the shoreline is then

$$\begin{aligned} \frac{du}{dt} &= \frac{A_0}{2} \cos \frac{\lambda}{2} \frac{d\lambda}{dt} \\ &= \frac{A_0 \cos \lambda/2}{1 + A_0 \cos \lambda/2} \quad . \end{aligned} \tag{3.3.56}$$

The maximum rundown point corresponds to $\lambda/2 = (2i-1)\pi \quad i = 1, 2, \ldots$ . At this point the horizontal fluid acceleration is:

$$\frac{du}{dt} = -\frac{A_0}{1 - A_0} \quad . \tag{3.3.57}$$

Hence, as $A_0 \to 1 \quad du/dt \to -\infty$. If the horizontal acceleration becomes infinite, then so also must the vertical acceleration, since the beach has a finite slope. However, this is physically impossible. To treat the flow more accurately near the rundown point for $A_0$ near unity, a nonlinear shallow water theory that is not based on the assumption of a hydrostatic pressure distribution must be used.

Figure 3.3.5 shows two periods of the motion of the shoreline as given by Eqs. (3.3.52), (3.3.54) and (3.3.55) for six different values of $A_0$, ranging from zero up to one. Each value of $A_0$ is plotted at the same height as the amplitude of the corresponding runup record. Fig. 3.3.5a shows the runup of the wave as a function of time. The runup oscillates between $-A_0$ and $+A_0$. For small amplitudes the motion is approximately sinusoidal, as predicted by linear theory, but as $A_0 \to 1$ the motion becomes very distorted. The shoreline remains above the still water line much longer than it does below it. Near the point of maximum runup the shoreline moves very slowly. It gradually starts to run down and slowly increases its speed. Its speed continues to increase almost all the way up to the point of maximum rundown. Near the rundown point it quickly decelerates and

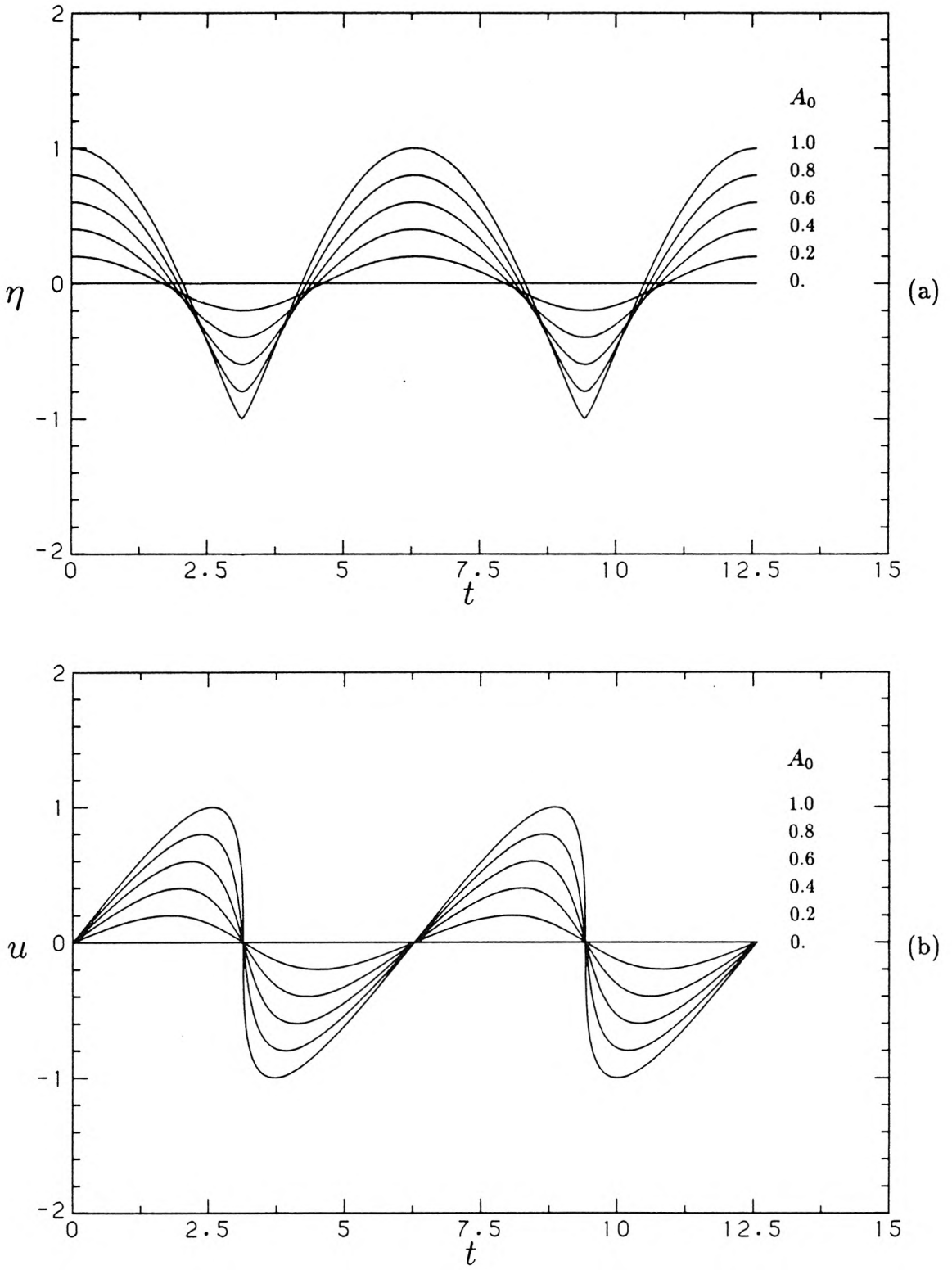


Fig. 3.3.5 Shoreline motion; (a) shoreline elevation $\eta$ computed from Eqs. (3.3.52) and (3.3.54), (b) shoreline velocity $u$ computed from Eqs. (3.3.52) and (3.3.55) ( $t = \omega t^*$ $\eta = \eta^* \omega^2 / \phi^2 g$ $u = u^* \omega / \phi g$ ).

at the rundown point it immediately reverses direction and quickly "snaps" back above the still water line where it slowly returns to the point of maximum runup. Therefore, although the nonlinear theory predicts that $u = 0$ everywhere at the time of maximum rundown (Eq. (3.3.42c)), the velocity at the shoreline for the case $A_0 \to 1$ is only near zero for an infinitesimally short length of time.

The wave height as a function of time for a fixed value of $x$ differs markedly from that shown in Fig. 3.3.5. Figure 3.3.6 shows two periods of the wave height and horizontal velocity at the location $x = 1$ for a range of amplitude parameters, $A_0$. The location $x = 1$ is special since it is the location of the point of maximum rundown for the limiting case of the maximum possible amplitude, $A_0 = 1$. For $A_0 < 1$ the point of maximum rundown occurs for $x < 1$. A continuous plot of the wave height as a function of time for $A_0 = 1$ cannot be made at a point where $x < 1$ since the point will be exposed to dry bed for some portion of the wave's motion near the time of maximum rundown. The velocity records at $x = 1$ in Fig. 3.3.6b are very similar to the shoreline velocity records in Fig. 3.3.5b. Again the infinite acceleration at the rundown point for $A_0 = 1$ is reflected by the vertical tangent of the velocity records at those points. However, the wave height records in Fig. 3.3.6a are very different from the shoreline elevation records in Fig. 3.3.5a. Notice in Fig. 3.3.6a that as the amplitude parameter, $A_0$, increases, the magnitude of the *minimum* wave height increases much faster than the *maximum* wave height. In contrast, the shoreline runup elevation in Fig. 3.3.5a always oscillates between equally spaced extrema at $\eta = \pm A_0$. For $A_0 = 1.0$ the minimum wave height is $\eta = -1$ (i.e., the dry bed is *just* exposed at $x = 1$) and the maximum wave height is only $\eta \sim 0.114$. This behaviour can easily be seen in the series of wave profiles shown in Fig. 3.3.4a for the case $A_0 = 1$. Another noticeable difference between the records in Fig. 3.3.5a and 3.3.6a is that as $A_0 \to 1$ the wave records at $x = 1$ exhibit a cusp at the rundown

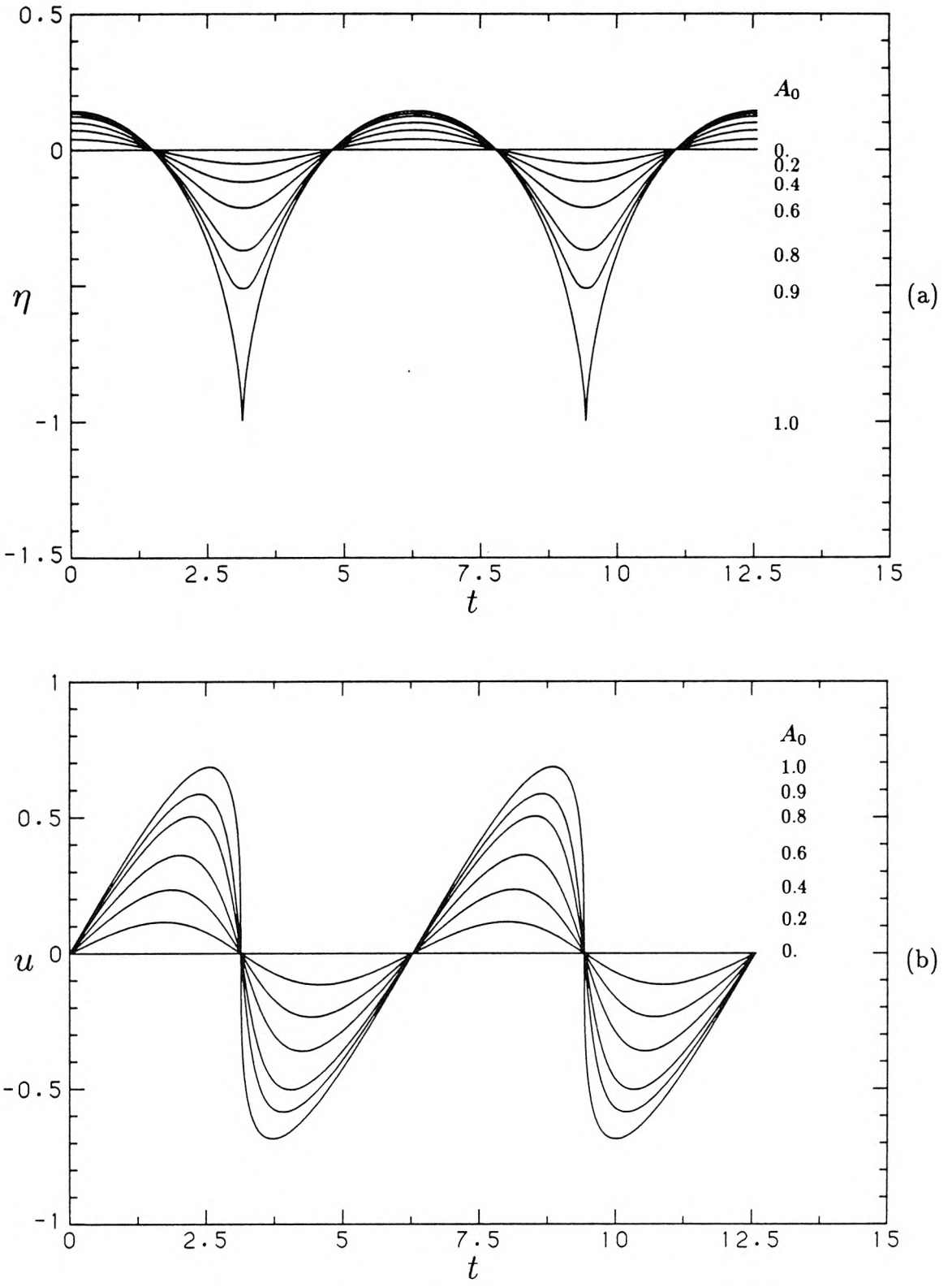


Fig. 3.3.6 Wave motion @ $x = 1$ computed from Eqs. (3.3.22) – (3.3.25); (a) wave height $\eta$, (b) horizontal velocity $u$. ($t = \omega t^*$ $\eta = \eta^* \omega^2 / \phi^2 g$ $u = u^* \omega / \phi g$).

point. This behaviour is not seen in Fig. 3.3.5a. These two results are consistent with each other. The time derivative of the records in Fig. 3.3.5a represents the material time derivative, $d\eta/dt$, since these runup records represent the wave height following a fluid particle at the shoreline. This derivative is well behaved and bounded, as one would expect. However, the time derivative of the records in Fig. 3.3.6a represents the local time derivative, $\partial\eta/\partial t$, for fixed $x$. It need not be bounded for the case $A_0 = 1$. For the case $A_0 = 1$ the tangent to the wave surface at the shoreline is vertical at the rundown point. Hence, the shoreline need only move an infinitesimal distance and the wave height at $x = 1$ will jump by a large amount. This effect produces the cusps in Fig. 3.3.6a for $A_0 = 1$. This behaviour can also be shown analytically but the effort does not provide a better understanding of the solution, so it will not be presented here.

In summary, it should be stated that although the nonlinear solution corresponding to Eq. (3.3.36) is mathematically valid for $A_0 \leq 1$, its range of validity is reduced even further when the physical requirement of small vertical accelerations is imposed. However, the results of this section are still important and they do indicate some of the general effects of the nonlinear terms in the equations of motion. For the general case of a beach that does not slope linearly or that exhibits variations in the $y$ direction, it is difficult to obtain quantitative results analogous to those found for this special case. However, the slopes of many beaches are approximately linear and it is reasonable to extend these results, at least qualitatively, to those cases as well.

## 3.4 Finite Element Model

One cannot hope to solve the nonlinear, dispersive, dissipative long wave equations derived in Section 3.1 for arbitrary geometry, using only analytical meth-

ods. A numerical approach is required if we desire detailed quantitative results. Therefore, a time marching finite element model, which includes the nonlinear, dispersive, and dissipative terms, was written to solve these equations. Since the equations are expressed in the Lagrangian description, this allows the nonlinear effects of the runup of nonbreaking waves on a beach to be modelled easily. In addition, the model is able to treat arbitrary geometry so that the runup of waves along an irregular beach can be investigated. In the following sections the development and implementation of this model will be described.

### 3.4.1 Analytical Formulation

Before we can obtain a finite element formulation of the problem, we first must set up the problem analytically. See Fig. 3.4.1 for a definition sketch of the geometry that the model will deal with. The finite element model will be applied to several problems. The geometry in Fig. 3.4.1 will be used to develop the finite element model because it is the most general. All problems treated with the model will be special cases of this harbour geometry. In Fig. 3.4.1 all quantities have been nondimensionalized by the nondimensionalization chosen in Section 3.1.2. To keep the following derivations and notation as clear as possible, it will be assumed that the domain of the problem contains only one constriction where entrance losses will be modelled. There is no added complexity in treating an arbitrary number of these constrictions. Therefore, for clarity, only one constriction will be included in the formulation and it will be denoted by $\Gamma_{HM}$, joining points C and E in Fig. 3.4.1. We will compute the solution over a finite domain $\Omega$, where $\Omega$ will be comprised of the union of three nonoverlapping regions $\Omega_H$, $\Omega_M$, and $\Omega_O$; i.e.,

$$\Omega = \Omega_H \cup \Omega_M \cup \Omega_O \quad . \tag{3.4.1}$$

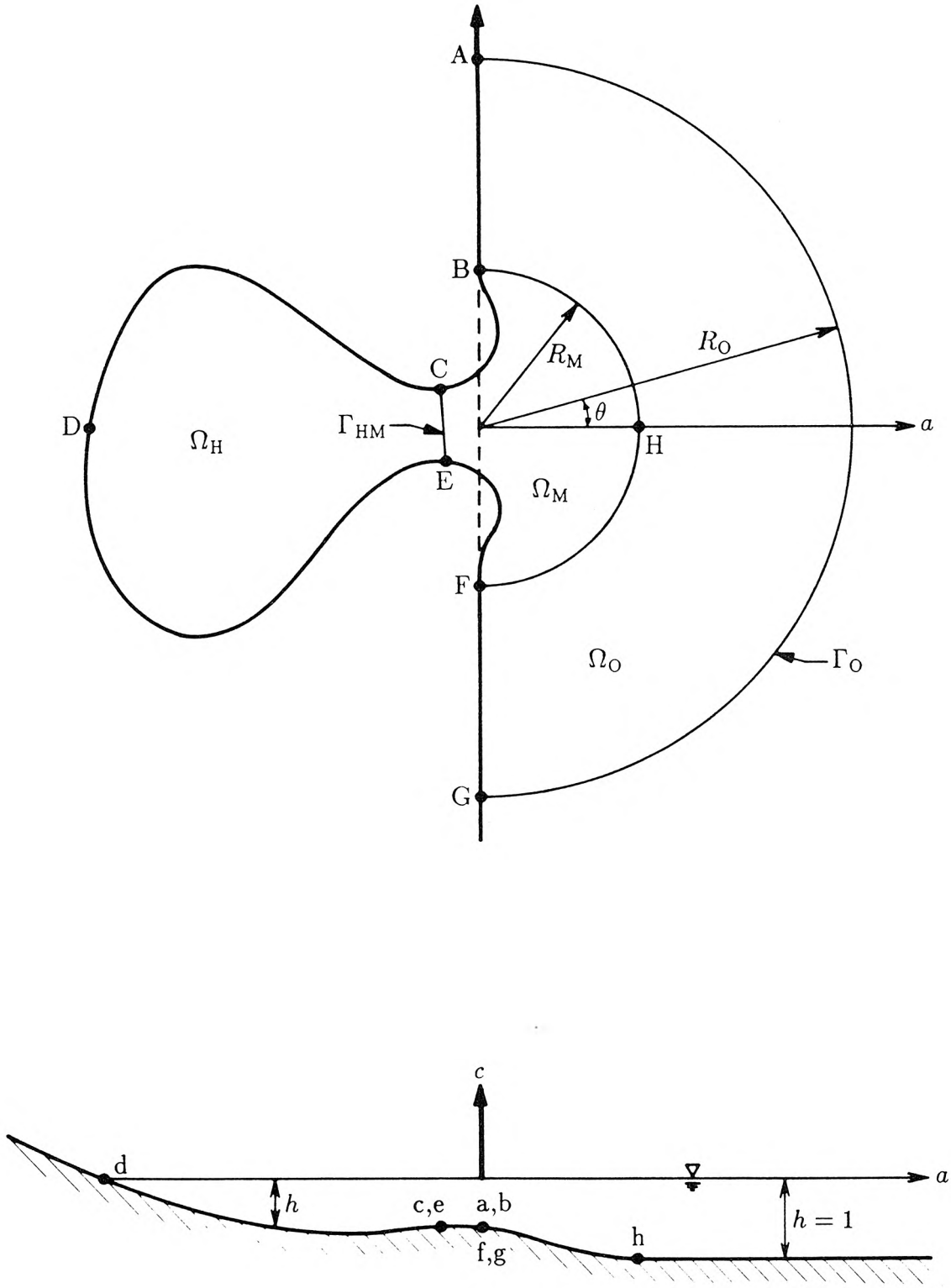


Fig. 3.4.1 Definition Sketch of the Model Geometry

The boundary of $\Omega$, $\partial\Omega$, is the union of the boundary $\Gamma_O$ and the curve ADG. Note that the soution domain $\Omega$ has been drawn in the $(a,b)$ plane. Therefore, it represents the physical domain which the fluid particles occupy at time $t = 0$. For $t > 0$ the instantaneous physical domain will in general be different, particularly where the waves run up and down sloping boundaries.

The region $\Omega_H$ is the inner harbour region bounded by the harbour entrance $\Gamma_{HM}$ and the curve CDE. As shown in the definition sketch, the water depth may continuously decrease to zero at the shoreline. The harbour may also be bounded by vertical walls or by a combination of vertical walls and sloping boundaries. All energy is reflected by the boundary CDE, whether or not the walls slope or are vertical.

The region $\Omega_M$ is the area comprising the harbour mouth out to the boundary denoted by $\Gamma_{MO}$. In the definition sketch this boundary is shown as a semicircle of radius $R_M$ but in general $\Gamma_{MO}$ can be of arbitrary shape. The boundary $\Gamma_{MO}$ is chosen far enough away from the harbour mouth that the wave heights are small enough so that the nonlinear terms in the equations of motion are small in comparison with the linear terms. The reason for this will be explained subsequently.

The outermost region $\Omega_O$ is bounded by $\Gamma_{MO}$, $\Gamma_O$, and the the physical boundaries AB and FG. This region is used to model the open ocean. By assumption, the boundaries AB and FG are vertical and perfectly reflecting. The water depth is constant and equal to $h_0$. The reason why the boundary $\Gamma_{MO}$ is chosen so that nonlinear terms in the equations of motion are small exterior to this boundary is so the solution in region $\Omega_O$ can be linearly decomposed into an "incident-reflected" wave system and a "radiated" wave system. The incident-reflected wave system is defined as the wave system which would be present if the water depth was constant everywhere and the harbour was absent with the vertical wall extended from point A to point G on the definition sketch. This wave system

is known once we have specified the incident wave system. The radiated wave system is then defined simply as the difference between the actual wave system in region $\Omega_O$ and the incident-reflected wave system. It represents the radiation of energy from the mouth of the harbour out to infinity. This decomposition is important because, by subtracting off the incident-reflected wave system, only the radiated wave system need be computed. This system asymptotically satisfies a known radiation condition away from the harbour mouth. Hence, if we choose the boundary $\Gamma_O$ sufficiently far from the harbour entrance and apply this radiation condition along $\Gamma_O$, we can compute the solution on a finite domain even though the open ocean extends out to infinity in the right half-plane. This radiation condition allows the radiated waves to pass through the boundary $\Gamma_O$ without being reflected. Boundary $\Gamma_O$ need not be chosen as a semicirle as shown in the definition sketch. However, a semicirle is the most logical choice for the boundary since the radiated wave system is a radially spreading system. Since the radiated wave system satisfies only the radiation condition asymptotically as one moves away from the harbour entrance, $R_O$ must be chosen sufficiently large enough so this condition is satisfied to a desired degree of accuracy. However, it is also desirable to keep $R_O$ as small as possible to minimize the amount of computation. A further discussion on the choices for $R_M$ and $R_O$ will be given later in this section.

In regions $\Omega_H$ and $\Omega_M$ the full long wave equations of Section 3.1 will be solved. This means that nonlinear, dispersive, and laminar viscous loss effects will be modelled. In the outer region $\Omega_O$ these effects will not be modelled. If we denote the water surface elevation by $\eta(\mathbf{a},t)$ and the water particle displacement vector by $\mathbf{x}(\mathbf{a},t)$ then the long wave equations (3.1.117) and (3.1.118) are:

$$\eta = -\nabla h\cdot\mathbf{x} - \frac{\alpha}{2}\mathbf{x}\cdot\underline{\mathbf{H}}\cdot\mathbf{x} - h\frac{\left[\nabla\cdot\mathbf{x} + \alpha\frac{\partial(x,y)}{\partial(a,b)}\right]}{1+\alpha\nabla\cdot\mathbf{x}} \tag{3.4.2}$$

$$(1+\alpha\nabla\cdot\mathbf{x})[\mathbf{x}_{tt} + \frac{\gamma}{h}\mathbf{x}_t] + \alpha\nabla\eta\cdot\underline{\mathbf{D}} + \nabla\eta = \beta\left\{\frac{h}{2}\nabla[\nabla\cdot(h\mathbf{x}_{tt})] - \frac{h^2}{6}\nabla(\nabla\cdot\mathbf{x}_{tt})\right\}. \tag{3.4.3}$$

These equations are accurate to $O(\alpha,\beta,\gamma)$ where $\alpha$, $\beta$, and $\gamma$ are defined exactly as in Section 3.1:

$$\alpha = \frac{H}{h_0} \qquad \beta = \left(\frac{h_0}{\ell}\right)^2 \qquad \gamma = \frac{\ell}{h_0}\sqrt{\frac{\omega\nu}{2gh_0}} \quad . \tag{3.4.4}$$

$H$, $\ell$, and $\omega$ denote a characteristic wave height, length, and frequency and will depend on the particular problem being modelled. $\underline{\mathbf{D}}$ and $\underline{\mathbf{H}}$ are defined by Eqs. (3.1.83) and (3.1.97). Eqs. (3.4.2) and (3.4.3) are the model equations for regions $\Omega_H$ and $\Omega_M$. In region $\Omega_O$, where the nonlinear, dispersive, and dissipative effects are not modelled, they reduce to (setting $\alpha = \beta = \gamma = 0$):

$$\eta = -\nabla\cdot(h\mathbf{x}) \tag{3.4.5}$$

$$\mathbf{x}_{tt} = -\nabla\eta \quad . \tag{3.4.6}$$

A variety of different boundary conditions can be applied along $\partial\Omega$. There are approximately four different ones of interest:

1) Along a sloping boundary where the still water depth decreases continuously to zero (a beach), the water surface elevation is related to the still water depth as:

$$\begin{aligned}\eta &= -\frac{1}{\alpha}h(\mathbf{a}+\alpha\mathbf{x}) \\ &= -\nabla h\cdot\mathbf{x} - \frac{\alpha}{2}\mathbf{x}\cdot\underline{\mathbf{H}}\cdot\mathbf{x} + O(\alpha^2) \quad .\end{aligned} \tag{3.4.7}$$

For regions of a beach above the still waterline $h$ is negative. *Along* the still water line we have $h(\mathbf{a}) = 0$.

2) Along a boundary where the still water depth is nonzero, we may simply specify the water surface elevation as a given function of time $t$ and initial fluid particle position $\mathbf{a}$; i.e.,

$$\eta = \eta_s(\mathbf{a}, t) \quad . \tag{3.4.8}$$

This would be used if one knew what the water surface displacement time history was, along a given boundary. This would be known if, for instance, one had previously measured it with a series of wave gauges.

3) Along a vertical wall, fluid particles which lie against the wall at time $t = 0$ must remain against it for all subsequent times. Hence, the motion of a fluid particle must be perpendicular to the wall outward normal, $\mathbf{n}$, at the present position of the particle:

$$\mathbf{x}_t \cdot \mathbf{n}(\mathbf{a} + \alpha\mathbf{x}) = 0 \quad . \tag{3.4.9}$$

Note that as the particle moves, the outward normal will in general change direction if the wall is curved. Therefore, since $\mathbf{n}$ is in general a function of $\mathbf{x}$ we <u>cannot</u> integrate this expression to get:

$$\mathbf{x} \cdot \mathbf{n} = 0 \quad .$$

4) Along $\Gamma_O$ the radiated wave will satisfy a radiation condition for radially spreading nondispersive in a region of constant depth. Written in the Lagrangian description, the boundary condition is:

$$\eta = \frac{\partial r}{\partial t} - \frac{1}{2R_O} \int_0^t \eta \, dt \tag{3.4.10}$$

where $r = r(\mathbf{a}, t)$ is the radial component of displacement of a fluid particle; i.e.,

$$r(\mathbf{a}, t) = x(\mathbf{a}, t) \cos\theta + y(\mathbf{a}, t) \sin\theta = \mathbf{x} \cdot \mathbf{n}_\theta \tag{3.4.11}$$

where $\theta(a,b)$ is the polar angle of the position of the particle at time $t = 0$ (see Fig. 3.4.1). The quantity $R_O$ is the distance from the coordinate origin to the boundary $\Gamma_O$. Mungall & Reid (1978) showed that this boundary condition is relatively insensitive to the coordinate origin, provided the origin is chosen reasonably close to the origin of the radiated waves. The term with the integral of $\eta$ represents a correction factor to account for the curvature of the radially spreading wavefronts. The further away from the origin that the radiation boundary is taken, the smaller the effect of this term. A derivation of this radiation condition in the Eulerian description can be found in Mungall & Reid (1978). They incorporated this boundary condition into a depth integrated finite difference long wave model (in the Eulerian description). By comparing the results of the model with known analytical solutions they were able to test this condition and verify its effectiveness for modelling radially spreading gravity waves. Unfortunately, Eq. (3.4.10) is awkward to implement in its present form (in either the Eulerian or the Lagrangian description) because of the presence of the correction factor which involves the time integral of $\eta$. Mungall & Reid simply approximated this integral with its value at the previous time step. In the Lagrangian description, an alternate radiation condition can be derived, similar to Eq. (3.4.10), which does not have this difficulty. It can readily be obtained from Eq. (3.4.10) by solving for $\eta$ iteratively, making use of the fact that the correction term is small.

$$\begin{aligned} \eta &= \frac{\partial r}{\partial t} - \frac{1}{2R_O} \int_0^t \left( \frac{\partial r}{\partial t} - \frac{1}{2R_O} \int_0^{t'} \eta \, dt' \right) dt \\ &= \frac{\partial r}{\partial t} - \frac{r}{2R_O} + \text{H.O.T.} \end{aligned} \tag{3.4.12}$$

This is a much easier boundary condition to implement than Eq. (3.4.10).

Using a procedure similar to that used by Mungall & Reid, one can derive this alternate radiation condition directly without first obtaining Eq. (3.4.10). It is then clear that the higher order terms neglected in the derivations of both Eq. (3.4.10) and Eq. (3.4.12) are of similar order. Therefore, Eq. (3.4.12) will be used in the finite element model.

Since one would like to minimize $R_O$ to reduce the amount of computation, a criterion must be used to set the lower limit for $R_O$ instead of obtaining it by trial and error. Let us denote a typical harbour entrance width by $b_0$. Let $\lambda$ denote a typical wavelength of an incident wave with $k = 2\pi/\lambda$. Then for $kb_0 < 0.5$ a simple error analysis (e.g., Lepelletier 1980) shows that Eq. (3.4.10) will be accurate to within a few percent, provided:

$$R_O^* \geq 0.6\lambda \tag{3.4.13}$$

or, since $R_O = R_O^*/\ell$:

$$R_O \geq 0.6\frac{\lambda}{\ell} \quad . \tag{3.4.14}$$

If we choose $\ell = \lambda$ this criterion reduces to $R_O \geq 0.6$. If $kb_0 > 0.5$, then $R_O$ must be increased beyond this lower limit to achieve the same accuracy. For large $kb_0$, $R_O$ must be increased so much that the use of the radiation condition approach is no longer an economical way to simulate the open ocean.

An estimate for the value of $R_M$ also can be made. Lepelletier (1980) also shows that the nonlinear interactions between the incident-reflected wave system and the radiated wave system can be neglected for a narrow mouthed harbour ($kb_0 \ll 1$) provided:

$$R_M^* \geq 0.1\lambda \quad ; \tag{3.4.15}$$

i.e.,

$$R_M \geq 0.1\frac{\lambda}{\ell} \quad . \tag{3.4.16}$$

Again, as the width of the harbour entrance increases, so also must $R_M$. It should be emphasized that these are only rough estimates for $R_M$ and $R_O$. Their final choice may be dependent on the particular problem being studied. Equations (3.4.14) and (3.4.16) will be used to choose the parameters $R_O$ and $R_M$ when the results of the finite element model are compared with the harbour response laboratory experiments (to be discussed in Section 5.2 of Chapter 5).

As mentioned earlier, the solution domain will be divided into three regions:

(i) Inner Harbour Region $\Omega_H$ :

In this region we will solve the nonlinear, dispersive, and dissipative long wave equations (3.4.2) and (3.4.3). Along the boundary CDE any combination of the beach boundary condition (3.4.7), specified wave height boundary condition (3.4.8), or vertical wall boundary condition (3.4.9) may be specified.

(ii) Harbour Mouth Region $\Omega_M$ :

In this region the same model equations will be solved, and along boundaries BC and EF the same boundary conditions may be specified as in the inner harbour region, $\Omega_H$ .

(iii) Outer Region $\Omega_O$ :

In this region the solution will be decomposed into an incident and reflected wave (denoted by $x_{IR}$ and $\eta_{IR}$ ) and a radiated wave (denoted by $x_R$ and $\eta_R$ ). Each system of waves will satisfy the linear equations of motion (3.4.5) and (3.4.6). The total wave system $x$ and $\eta$ will be a linear superposition

of these two systems:

$$\mathbf{x} = \mathbf{x}_{IR} + \mathbf{x}_{R} \tag{3.4.17a}$$

$$\eta = \eta_{IR} + \eta_{R} \quad . \tag{3.4.17b}$$

It is assumed that the form of the incident wave is known either from a wave record or from a mathematical formula. The reflected wave (for a vertical wall joining the points A and G), which satisfies the no flow boundary condition along $a = 0$ and the linear equations of motion (3.4.5) and (3.4.6), can easily be found. For example, if the incident wave is a plane wave travelling in the $-a$ direction normal to the coastline, i.e.,

$$\eta_{\text{incident}} = f(t + a) \quad , \tag{3.4.18}$$

then the reflected wave will have the same form but will travel in the opposite direction:

$$\eta_{\text{reflected}} = f(t - a) \quad . \tag{3.4.19}$$

The wave speed has been normalized to unity in these formulae. If the incident wave does not approach the coastline in a perpendicular direction, the reflected wave will be related in a similar way to the incident waves system except that the propagation direction of this reflected wave must satisfy the familiar geometrical optics law: the angle of incidence equals the angle of reflection.

For the special case $\eta_{\text{incident}} = f(\xi)$ where $\xi = t + a$, the particle displacements $x_{\text{incident}}$ can be obtained by integrating Eq. (3.4.6). In that case Eq. (3.4.6) reduces to

$$\frac{\partial x_{\text{incident}}}{\partial \xi} = -\eta_{\text{incident}} \quad . \tag{3.4.20}$$

This can easily be integrated to give $x_{\text{incident}}$ as a function of $t + a$. The particle displacement corresponding to $\eta_{\text{reflected}}$ can be obtained by the same general procedure except that the equation to integrate in this case is:

$$\frac{\partial x_{\text{reflected}}}{\partial \chi} = \eta_{\text{reflected}} \tag{3.4.21}$$

where $\chi = t - a$.

Since we know the incident-reflected wave we need compute only the radiated wave $\mathbf{x}_R$ and $\eta_R$ in region $\Omega_O$. Hence, in region $\Omega_O$ we will only compute $\mathbf{x}_R$ and $\eta_R$, using the linear model equations (3.4.5) and (3.4.6). Along the boundaries AB and FG where we assumed the walls were vertical, this radiated wave system must satisfy the wall boundary condition (3.4.9). Along the outer radiative boundary $\Gamma_O$ the radiated wave system must satisfy the radiation boundary condition (3.4.12).

The three regions must be joined together by applying the appropriate matching conditions along their common boundaries $\Gamma_{HM}$ and $\Gamma_{MO}$.

Joining Regions $\Omega_H$ and $\Omega_M$:

Across $\Gamma_{HM}$ a head loss occurs which, in the Eulerian description, is given by Eq. (3.2.18). If this equation is written in nondimensional variables in the Lagrangian description we get:

$$\Delta\eta = \eta_{\text{Region}\Omega_H} - \eta_{\text{Region}\Omega_M} = \frac{\alpha f}{2}\overline{U}\left|\overline{U}\right| \tag{3.4.22}$$

where $U$ is the component of particle velocity across $\Gamma_{HM}$ in the direction of the outward unit normal of region $\Omega_H$:

$$U = \mathbf{x}_t \cdot \mathbf{n}_{\Omega_H} \tag{3.4.23}$$

and $\overline{U}$ is the average of $U$ across the entrance $\Gamma_{HM}$. From Eqs. (3.2.17) and (3.2.18) the jump in the particle displacement vector $\mathbf{x}$ is zero across $\Gamma_{HM}$:

$$\Delta \mathbf{x} = \mathbf{x}_{\text{Region}\Omega_H} - \mathbf{x}_{\text{Region}\Omega_M} = 0 \quad . \tag{3.4.24}$$

Expressions (3.4.22) and (3.4.24) are the two conditions used to join the solution in region $\Omega_H$ with the solution in region $\Omega_M$.

Joining Regions $\Omega_M$ and $\Omega_O$:

Across $\Gamma_{MO}$ there will be a jump in both the computed water surface elevations *and* the particle displacements because in region $\Omega_O$ the incident-reflected wave system, $\mathbf{x}_{IR}$ and $\eta_{IR}$, is subtracted from the total wave system, $\mathbf{x}$ and $\eta$, and only the radiated wave system, $\mathbf{x}_R$ and $\eta_R$, is computed. Hence, across $\Gamma_{MO}$ we must have:

$$\eta_{\text{Region}\Omega_M} - \eta_R = \eta_{IR} \tag{3.4.25a}$$

$$\mathbf{x}_{\text{Region}\Omega_M} - \mathbf{x}_R = \mathbf{x}_{IR} \quad . \tag{3.4.25b}$$

### 3.4.2 Finite Element Formulation

The finite element model will be based on the weighted residual method. Let $\hat{x}$, $\hat{y}$ and $\hat{\eta}$ represent a trial or test function corresponding to the $x$ and $y$ momentum equations and the continuity equations, respectively. If we multiply the continuity equations (3.4.2) and (3.4.5) by $\hat{\eta}$ and then integrate over the entire domain of the problem we get:

$$\iint_{\Omega} \eta\hat{\eta}\, da\, db = -\iint_{\Omega_H \cup \Omega_M} \left\{ \nabla h \cdot \hat{\mathbf{x}} + \frac{\alpha}{2} \mathbf{x} \cdot \underline{\mathbf{H}} \cdot \mathbf{x} + h \frac{\left[ \nabla \cdot \mathbf{x} + \alpha \frac{\partial(x,y)}{\partial(a,b)} \right]}{1 + \alpha \nabla \cdot \mathbf{x}} \right\} \hat{\eta}\, da\, db$$
$$- \iint_{\Omega_O} \nabla \cdot (h\mathbf{x}) \hat{\eta}\, da\, db \quad . \tag{3.4.26}$$

Notice that the nonlinear and dispersive terms have been neglected in the outer region $\Omega_O$ in accordance with the assumptions made previously.

We can also weight the momentum equations (3.4.3) and (3.4.6) with $\hat{x}$ and $\hat{y}$ and integrate over the domain of the problem:

$$\iint_{\Omega_H \cup \Omega_M} \left\{ (1 + \alpha \nabla \cdot \mathbf{x})(\mathbf{x}_{tt} + \frac{\gamma}{h} \mathbf{x}_t) \cdot \hat{\mathbf{x}} + \alpha \nabla \eta \cdot \underline{\mathbf{D}} \cdot \hat{\mathbf{x}} + \nabla \eta \cdot \hat{\mathbf{x}} \right\} da\, db$$
$$-\beta \iint_{\Omega_H \cup \Omega_M} \left\{ \frac{h}{2} \nabla \left[ \nabla \cdot (h\mathbf{x}_{tt}) \right] - \frac{h^2}{6} \nabla (\nabla \cdot \mathbf{x}_{tt}) \right\} \cdot \hat{\mathbf{x}}\, da\, db \tag{3.4.27}$$
$$+ \iint_{\Omega_O} (\mathbf{x}_{tt} + \nabla \eta) \cdot \hat{\mathbf{x}}\, da\, db \quad = 0$$

where $\hat{\mathbf{x}} = (\hat{x}, \hat{y})$. By taking the dot product of the vector momentum equation with $\hat{\mathbf{x}}$ this appears to give only one equation, but since $\hat{x}$ and $\hat{y}$ are independent of each other, it actually represents two equations, one equation with $\hat{x}$ equal to zero and one equation with $\hat{y}$ equal to zero. The vector notation is used because it simplifies the derivation of the finite element formulation of the problem.

It is important to eliminate all of the second order spatial derivatives of the components of $\mathbf{x}$ since they are difficult to handle in a finite element scheme. Therefore, let us derive an alternate expression, which does not contain second order spatial derivatives, to replace the dispersive terms in Eq. (3.4.27). These derivatives can be eliminated by applying the two-dimensional version of Gauss'

theorem (divergence theorem):

$$\iint\limits_{\Omega_H} \left\{ \frac{h}{2} \nabla \left[ \nabla \cdot (h \mathbf{x}_{tt}) \right] - \frac{h^2}{6} \nabla (\nabla \cdot \mathbf{x}_{tt}) \right\} \cdot \hat{\mathbf{x}} \, da \, db \tag{3.4.28}$$

$$= - \iint\limits_{\Omega_H} \left\{ \frac{h^2}{3} \nabla \cdot \mathbf{x}_{tt} \nabla \cdot \hat{\mathbf{x}} + \frac{h}{6} \nabla \cdot \mathbf{x}_{tt} \nabla h \cdot \hat{\mathbf{x}} + \frac{h}{2} \nabla h \cdot \mathbf{x}_{tt} \nabla \cdot \hat{\mathbf{x}} + \frac{1}{2} \nabla h \cdot \mathbf{x}_{tt} \nabla h \cdot \hat{\mathbf{x}} \right\} da \, db$$

$$+ \int\limits_{\partial \Omega_H} \left\{ \frac{h^2}{3} \nabla \cdot \mathbf{x}_{tt} + \frac{h}{2} \nabla h \cdot \mathbf{x}_{tt} \right\} \hat{\mathbf{x}} \cdot \mathbf{n} \, ds$$

where $\mathbf{n}$ is the outward unit vector to region $\Omega_H$. The boundary $\partial \Omega_H$ consists of the curve CDE and the interregion boundary $\Gamma_{HM}$.

We could also write down a similar expression for region $\Omega_M$. We would then pick up a line integral along the boundary $\partial \Omega_M$. This boundary consists of the curves BC and EF as well as the two interregion boundaries $\Gamma_{HM}$ and $\Gamma_{MO}$ (see Fig. 3.4.1). Since from Eq. (3.4.24) the particle displacements are continuous across $\Gamma_{HM}$, the two boundary integrals along $\Gamma_{HM}$ from the regions $\Omega_H$ and $\Omega_M$ will exactly cancel each other since the outward unit vectors are the negative of each other. Since we are not modelling dispersive effects in region $\Omega_O$ we can neglect the boundary integral along $\Gamma_{MO}$, although it would present no extra difficulty to retain it. Then if we combine the integrals over the two regions $\Omega_H$ and $\Omega_M$, we get:

$$\iint\limits_{\Omega_H \cup \Omega_M} \left\{ \frac{h}{2} \nabla \left[ \nabla \cdot (h \mathbf{x}_{tt}) \right] - \frac{h^2}{6} \nabla (\nabla \cdot \mathbf{x}_{tt}) \right\} \cdot \hat{\mathbf{x}} \, da \, db$$

$$= - \iint\limits_{\Omega_H \cup \Omega_M} \left\{ \frac{h^2}{3} \nabla \cdot \mathbf{x}_{tt} \nabla \cdot \hat{\mathbf{x}} + \frac{h}{6} \nabla \cdot \mathbf{x}_{tt} \nabla h \cdot \hat{\mathbf{x}} + \frac{h}{2} \nabla h \cdot \mathbf{x}_{tt} \nabla \cdot \hat{\mathbf{x}} + \frac{1}{2} \nabla h \cdot \mathbf{x}_{tt} \nabla h \cdot \hat{\mathbf{x}} \right\} da \, db$$

$$+ \int\limits_{BDF} \left\{ \frac{h^2}{3} \nabla \cdot \mathbf{x}_{tt} + \frac{h}{2} \nabla h \cdot \mathbf{x}_{tt} \right\} \hat{\mathbf{x}} \cdot \mathbf{n} \, ds \quad . \tag{3.4.29}$$

If we substitute this expression into Eq. (3.4.27), we will eliminate all second spatial derivatives of the components of $\mathbf{x}$.

It is possible to eliminate the surface displacement variable $\eta$ from the the problem by substituting the continuity equation (3.4.2) (and (3.4.5)) into Eq. (3.4.27). The variable $\eta$ would no longer appear. Hence, we would need only to solve the two momentum equations to obtain $\mathbf{x}$; after $\mathbf{x}$ was obtained $\eta$ could be computed with the continuity equation. This would greatly simplify the problem. For this procedure to be useful it is necessary to eliminate all the spatial derivatives of $\eta$ in Eq. (3.4.27), since the expression $\nabla\eta$ involves second derivatives of the components of $\mathbf{x}$. This can be done by making use of Gauss' theorem. However, close examination indicates that although all derivatives of $\eta$ can be eliminated with the use of Gauss' theorem, such a procedure then introduces spatial derivatives of the componenents of $\underline{\mathbf{D}}$. Since from Eq. (3.1.83) $\underline{\mathbf{D}}$ itself is defined in terms of spatial derivatives of $\mathbf{x}$, this appears to produce *second* derivatives of the components of $\mathbf{x}$; therefore, no advantage seems to be gained. However, as we will now show, it is possible to eliminate all derivatives of $\eta$ in Eq. (3.4.27) without generating any second derivatives of $x$ or $y$ since all the derivatives of the components of $\underline{\mathbf{D}}$ must exactly cancel. With the use of Gauss' theorem, the terms involving $\nabla\eta$ in Eq. (3.4.27) can be rewritten:

$$
\begin{aligned}
&\iint_{\Omega_H} \{\alpha\nabla\eta\cdot\underline{\mathbf{D}}\cdot\hat{\mathbf{x}} + \nabla\eta\cdot\hat{\mathbf{x}}\}\, da\, db \\
&= \iint_{\Omega_H} \{\nabla\cdot[\alpha\eta\underline{\mathbf{D}}\cdot\hat{\mathbf{x}} + \eta\hat{\mathbf{x}}] - \alpha\eta\underline{\mathbf{D}}:\nabla\hat{\mathbf{x}} - \alpha\eta(\nabla\cdot\underline{\mathbf{D}})\cdot\hat{\mathbf{x}} - \eta\nabla\cdot\hat{\mathbf{x}}\}\, da\, db \\
&= -\iint_{\Omega_H} \{\alpha\eta\underline{\mathbf{D}}:\nabla\hat{\mathbf{x}} + \alpha\eta(\nabla\cdot\underline{\mathbf{D}})\cdot\hat{\mathbf{x}} + \eta\nabla\cdot\hat{\mathbf{x}}\}\, da\, db \qquad (3.4.30) \\
&\quad + \int_{CDE} \eta\,[\alpha\mathbf{n}\cdot\underline{\mathbf{D}}\cdot\hat{\mathbf{x}} + \hat{\mathbf{x}}\cdot\mathbf{n}]\, ds + \int_{\Gamma_{HM}} \eta\,[\alpha\mathbf{n}\cdot\underline{\mathbf{D}}\cdot\hat{\mathbf{x}} + \hat{\mathbf{x}}\cdot\mathbf{n}]\, ds
\end{aligned}
$$

where the two vertical dots refer to the Gibbs' double dot product:

$$\underline{\mathbf{D}} : \nabla \hat{\mathbf{x}} = D_{ij} \frac{\partial \hat{x}_i}{\partial a_j} \quad . \tag{3.4.31}$$

The expression for $\eta$ in terms of $\mathbf{x}$ could now be substituted into Eq. (3.4.30), and no second spatial derivatives would appear *except* for the term $\nabla \cdot \underline{\mathbf{D}}$ which, as can be seen from Eq. (3.1.83) involves second derivatives of the components of $\mathbf{x}$. However, from the definition of $\underline{\mathbf{D}}$ we see that the divergence of $\underline{\mathbf{D}}$ must be exactly zero!

$$\begin{aligned} \nabla \cdot \underline{\mathbf{D}} &= (y_{ab} - y_{ba} \ , \ -x_{ba} + x_{ab}) \\ &\equiv \mathbf{0} \quad . \end{aligned} \tag{3.4.32}$$

Hence, if we eliminate $\eta$ using the continuity equation, no second spatial derivatives will appear in Eq. (3.4.30).

An expression similar to Eq. (3.4.30) can be written for region $\Omega_{\mathrm{M}}$:

$$\begin{aligned} &\iint\limits_{\Omega_{\mathrm{M}}} \{\alpha \nabla \eta \cdot \underline{\mathbf{D}} \cdot \hat{\mathbf{x}} + \nabla \eta \cdot \hat{\mathbf{x}}\} \, da \, db \\ &= - \iint\limits_{\Omega_{\mathrm{M}}} \{\alpha \eta \underline{\mathbf{D}} : \nabla \hat{\mathbf{x}} + \alpha \eta (\nabla \cdot \underline{\mathbf{D}}) \cdot \hat{\mathbf{x}} + \eta \nabla \cdot \hat{\mathbf{x}}\} \, da \, db \\ &\quad + \int\limits_{\mathrm{BC} \cup \mathrm{EF} \cup \Gamma_{\mathrm{MO}}} \eta \left[\alpha \mathbf{n} \cdot \underline{\mathbf{D}} \cdot \hat{\mathbf{x}} + \hat{\mathbf{x}} \cdot \mathbf{n}\right] ds + \int\limits_{\Gamma_{\mathrm{HM}}} \eta \left[\alpha \mathbf{n} \cdot \underline{\mathbf{D}} \cdot \hat{\mathbf{x}} + \hat{\mathbf{x}} \cdot \mathbf{n}\right] ds \quad . \end{aligned} \tag{3.4.33}$$

This expression can be combined with Eq. (3.4.30) to yield an integral over the region $\Omega_{\mathrm{H}} \cup \Omega_{\mathrm{M}}$. However, since $\eta$ jumps discontinuously across $\Gamma_{\mathrm{HM}}$ as given by Eq. (3.4.22), the two boundary integrals along $\Gamma_{\mathrm{HM}}$ from the regions $\Omega_{\mathrm{H}}$ and $\Omega_{\mathrm{M}}$ will *not* cancel as they did for the dispersive terms. Although $\eta$ jumps across $\Gamma_{\mathrm{HM}}$, $\mathbf{x}$ is continuous as given by Eq. (3.4.24), so $\underline{\mathbf{D}}$ will also be continuous

across $\Gamma_{HM}$. The unit vector for the line integral along $\Gamma_{HM}$ corresponding to region $\Omega_M$ will be the negative of that corresponding to region $\Omega_H$:

$$\mathbf{n}_{\Omega_M} = -\mathbf{n}_{\Omega_H} \quad . \tag{3.4.34}$$

Hence, if we combine the two line integrals along $\Gamma_{HM}$ corresponding to the two regions $\Omega_H$ and $\Omega_M$ and use Eqs. (3.4.22) and (3.4.34), the result is:

$$\begin{aligned}\int_{\Gamma_{HM}} \eta_{\Omega_H} \left[\alpha \mathbf{n}_{\Omega_H} \cdot \underline{\mathbf{D}} \cdot \hat{\mathbf{x}} + \hat{\mathbf{x}} \cdot \mathbf{n}_{\Omega_H}\right] ds + \int_{\Gamma_{HM}} \eta_{\Omega_M} \left[\alpha \mathbf{n}_{\Omega_M} \cdot \underline{\mathbf{D}} \cdot \hat{\mathbf{x}} + \hat{\mathbf{x}} \cdot \mathbf{n}_{\Omega_M}\right] ds \\ = \int_{\Gamma_{HM}} \Delta\eta \left[\alpha \mathbf{n}_{\Omega_H} \cdot \underline{\mathbf{D}} \cdot \hat{\mathbf{x}} + \hat{\mathbf{x}} \cdot \mathbf{n}_{\Omega_H}\right] ds \\ = \int_{\Gamma_{HM}} \frac{\alpha f}{2} \overline{U} \left|\overline{U}\right| \hat{\mathbf{x}} \cdot \mathbf{n}_{\Omega_H} ds + O(\alpha^2) \ . \end{aligned} \tag{3.4.35}$$

Since nonlinear effects are not modelled in region $\Omega_O$, we can neglect nonlinear terms in the boundary integral along $\Gamma_{MO}$, although these could be retained with no extra difficulty. Hence, if we combine the two integrals of the terms containing $\nabla\eta$ from regions $\Omega_H$ and $\Omega_M$ we get:

$$\begin{aligned}\iint_{\Omega_H \cup \Omega_M} \left\{\alpha \nabla\eta \cdot \underline{\mathbf{D}} \cdot \hat{\mathbf{x}} + \nabla\eta \cdot \hat{\mathbf{x}}\right\} da\, db = - \iint_{\Omega_H \cup \Omega_M} \eta \left[\nabla \cdot \hat{\mathbf{x}} + \alpha \underline{\mathbf{D}} : \nabla \hat{\mathbf{x}}\right] da\, db \\ + \int_{BDF} \eta \left[\alpha \mathbf{n} \cdot \underline{\mathbf{D}} \cdot \hat{\mathbf{x}} + \hat{\mathbf{x}} \cdot \mathbf{n}\right] ds \\ + \int_{\Gamma_{HM}} \frac{\alpha f}{2} \overline{U} \left|\overline{U}\right| \hat{\mathbf{x}} \cdot \mathbf{n}_{\Omega_H} ds \\ + \int_{\Gamma_{MO}} \eta \hat{\mathbf{x}} \cdot \mathbf{n}\, ds \quad . \end{aligned} \tag{3.4.36}$$

Here, use was made of Eqs. (3.4.30), (3.4.32), (3.4.33), (3.4.34) and (3.4.35). If this expression is substituted into Eq. (3.4.27), then all spatial derivatives of $\eta$

will be eliminated without introducing second spatial derivatives of $\mathbf{x}$.

Now let us look at the outer region $\Omega_O$ to obtain an equation for the integral over $\Omega_O$ in Eq. (3.4.27). If the decomposition (3.4.17) is substituted into the integral over region $\Omega_O$ in (3.4.27) we get:

$$\iint_{\Omega_O} (\mathbf{x}_{tt} + \nabla\eta)\cdot\hat{\mathbf{x}}\, da\, db = \iint_{\Omega_O} (\mathbf{x}_{R\,tt} + \nabla\eta_R)\cdot\hat{\mathbf{x}}\, da\, db + \iint_{\Omega_O} (\mathbf{x}_{IR\,tt} + \nabla\eta_{IR})\cdot\hat{\mathbf{x}}\, da\, db \quad . \tag{3.4.37}$$

We have assumed that the incident-reflected wave is known and is a solution to the linear nondispersive momentum equation:

$$\mathbf{x}_{IR\,tt} + \nabla\eta_{IR} \equiv 0 \quad . \tag{3.4.38}$$

Hence, the second integral on the right hand side in Eq. (3.4.37) vanishes identically. Gauss' theorem can then be applied to the remaining integral to obtain:

$$\iint_{\Omega_O} (\mathbf{x}_{tt} + \nabla\eta)\cdot\hat{\mathbf{x}}\, da\, db = \iint_{\Omega_O} \{\mathbf{x}_{R\,tt}\cdot\hat{\mathbf{x}} - \eta_R \nabla\cdot\hat{\mathbf{x}}\}\, da\, db + \int_{\Gamma_{MO}} \eta_R\hat{\mathbf{x}}\cdot\mathbf{n}\, ds + \int_{AB\cup FG\cup\Gamma_O} \eta_R\hat{\mathbf{x}}\cdot\mathbf{n}\, ds \quad . \tag{3.4.39}$$

When the line integral along $\Gamma_{MO}$ in this expression is combined with the corresponding one in Eq. (3.4.36), the two will not cancel even though the unit normals are exactly the negative of each other because the computed values of the surface elevation ($\eta$ and $\eta_R$) jump discontinuously across $\Gamma_{MO}$ according to Eq. (3.4.25a). Hence, if these two integrals are combined, the following is ob-

tained:

$$\int_{\Gamma_{MO}} \eta\hat{\mathbf{x}}\cdot\mathbf{n}_{\Omega_M}\,ds + \int_{\Gamma_{MO}} \eta_R\hat{\mathbf{x}}\cdot\mathbf{n}_{\Omega_O}\,ds = \int_{\Gamma_{MO}} \eta_{IR}\hat{\mathbf{x}}\cdot\mathbf{n}_{\Omega_M}\,ds \tag{3.4.40}$$

where $\eta_{IR}$ is a known function of $\mathbf{a}$ and $t$.

Combining expressions (3.4.36), (3.4.39) and (3.4.40) then yields:

$$\begin{aligned}
&\iint_{\Omega_H\cup\Omega_M} \{\alpha\nabla\eta\cdot\underline{\mathbf{D}}\cdot\hat{\mathbf{x}} + \nabla\eta\cdot\hat{\mathbf{x}}\}\,da\,db + \iint_{\Omega_O} (\mathbf{x}_{tt} + \nabla\eta)\cdot\hat{\mathbf{x}}\,da\,db \\
&= -\iint_{\Omega_H\cup\Omega_M} \eta\,[\nabla\cdot\hat{\mathbf{x}} + \alpha\underline{\mathbf{D}}:\nabla\hat{\mathbf{x}}]\,da\,db + \iint_{\Omega_O} \{\mathbf{x}_{R\,tt}\cdot\hat{\mathbf{x}} - \eta_R\nabla\cdot\hat{\mathbf{x}}\}\,da\,db \\
&\quad + \int_{BDF} \eta\,[\alpha\,\mathbf{n}\cdot\underline{\mathbf{D}}\cdot\hat{\mathbf{x}} + \hat{\mathbf{x}}\cdot\mathbf{n}]\,ds + \int_{ABUFGU\Gamma_O} \eta_R\hat{\mathbf{x}}\cdot\mathbf{n}\,ds \\
&\quad + \int_{\Gamma_{HM}} \frac{\alpha f}{2}\overline{U}\,|\overline{U}|\,\hat{\mathbf{x}}\cdot\mathbf{n}_{\Omega_H}\,ds + \int_{\Gamma_{MO}} \eta_{IR}\hat{\mathbf{x}}\cdot\mathbf{n}_{\Omega_M}\,ds \quad .
\end{aligned} \tag{3.4.41}$$

Expressions (3.4.2) and (3.4.5) for $\eta$ and $\eta_R$ in terms of $\mathbf{x}$ and $\mathbf{x}_R$ can be substituted into the area integrals in (3.4.41) to eliminate $\eta$ and $\eta_R$. To satisfy the radiation boundary condition, expressions (3.4.11) and (3.4.12) can be substituted into the line integral along $\Gamma_O$ in Eq. (3.4.41). Then, to eliminate $\eta$ from Eq. (3.4.27) without introducing second spatial derivatives of $\mathbf{x}$, Eqs. (3.4.29) and (3.4.41) can be substituted into Eq. (3.4.27). The final result (neglecting terms of $O(\alpha^2)$) is:

$$\begin{aligned}
0 = &\iint_{\Omega_H\cup\Omega_M} \left\{(1+\alpha\nabla\cdot\mathbf{x})\mathbf{x}_{tt} + \frac{\gamma}{h}\mathbf{x}_t\right\}\cdot\hat{\mathbf{x}}\,da\,db \\
&+ \iint_{\Omega_H\cup\Omega_M} \left[\nabla h\cdot\mathbf{x} + \frac{\alpha}{2}\mathbf{x}\cdot\underline{\mathbf{H}}\cdot\mathbf{x} + h\frac{\left[\nabla\cdot\mathbf{x} + \alpha\frac{\partial(x,y)}{\partial(a,b)}\right]}{1+\alpha\nabla\cdot\mathbf{x}}\right](\nabla\cdot\hat{\mathbf{x}} + \alpha\underline{\mathbf{D}}:\nabla\hat{\mathbf{x}})\,da\,db \\
&+\beta\iint_{\Omega_H\cup\Omega_M} \left\{\frac{h^2}{3}\nabla\cdot\mathbf{x}_{tt}\nabla\cdot\hat{\mathbf{x}} + \frac{h}{6}\nabla\cdot\mathbf{x}_{tt}\nabla h\cdot\hat{\mathbf{x}} + \frac{h}{2}\nabla h\cdot\mathbf{x}_{tt}\nabla\cdot\hat{\mathbf{x}} + \frac{1}{2}\nabla h\cdot\mathbf{x}_{tt}\nabla h\cdot\hat{\mathbf{x}}\right\}da\,db
\end{aligned}$$

$$+\iint_{\Omega_O}\{\mathbf{x}_{R\,tt}\cdot\hat{\mathbf{x}}+\nabla\cdot(h\mathbf{x}_R)\nabla\cdot\hat{\mathbf{x}}\}\,da\,db$$

$$-\beta\int_{BDF}\left\{\frac{h^2}{3}\nabla\cdot\mathbf{x}_{tt}+\frac{h}{2}\nabla h\cdot\mathbf{x}_{tt}\right\}\hat{\mathbf{x}}\cdot\mathbf{n}\,ds$$

$$+\int_{\Gamma_{HM}}\frac{\alpha f}{2}\overline{U}\,|\overline{U}|\,\hat{\mathbf{x}}\cdot\mathbf{n}_{\Omega_H}ds+\int_{\Gamma_{MO}}\eta_{IR}\hat{\mathbf{x}}\cdot\mathbf{n}_{\Omega_M}ds+\int_{\Gamma_O}\left\{\mathbf{x}_t\cdot\mathbf{n}_\theta-\frac{1}{2R_O}\mathbf{x}\cdot\mathbf{n}_\theta\right\}\hat{\mathbf{x}}\cdot\mathbf{n}\,ds$$

$$+\int_{BDF}\eta\left[\alpha\mathbf{n}\cdot\underline{\mathbf{D}}\cdot\hat{\mathbf{x}}+\hat{\mathbf{x}}\cdot\mathbf{n}\right]ds+\int_{ABUFG}\eta_R\hat{\mathbf{x}}\cdot\mathbf{n}\,ds\quad. \tag{3.4.42}$$

This is the finite element formulation which will be used to integrate long wave equations (3.1.117) and (3.1.118). To satisfy boundary conditions (3.4.7) and (3.4.8), those expressions for $\eta$ are substituted into the last two boundary integrals of Eq. (3.4.42) along the portions of the boundary where they apply.

Boundary condition (3.4.9) does not involve specifying the value of $\eta$ along the boundary, and so it must be treated differently than the other three boundary conditions. The treatment of this boundary condition will be covered fully in Section 3.4.5.

### 3.4.3 Spatial Discretization

Now the problem will be discretized to transform it into a matrix problem with a finite number of unknowns. The domain is subdivided into a number of small nonoverlapping regions called elements. Within each element there is a shape function associated with each node bordering on that element. Within the element the shape functions are used to interpolate the values of the unknowns at the nodes of the element.

In order to discretize arbitrary two-dimensional regions, isoparametric elements were chosen. For flexibility, four different types of elements were chosen:

8 node quadrilaterals:

$$N_1(\xi,\eta) = (1+\xi)(1+\eta)(\xi+\eta-1)/4$$
$$N_2(\xi,\eta) = (1-\xi)(1+\eta)(\eta-\xi-1)/4$$
$$N_3(\xi,\eta) = -(1-\xi)(1-\eta)(\xi+\eta+1)/4$$
$$N_4(\xi,\eta) = (1+\xi)(1-\eta)(\xi-\eta-1)/4$$
$$N_5(\xi,\eta) = (1-\xi^2)(1+\eta)/2$$
$$N_6(\xi,\eta) = (1-\eta^2)(1-\xi)/2$$
$$N_7(\xi,\eta) = (1-\xi^2)(1-\eta)/2$$
$$N_8(\xi,\eta) = (1-\eta^2)(1+\xi)/2$$

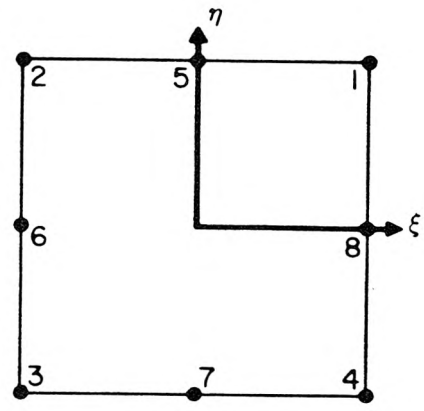


6 node triangles:

$$N_1(\xi,\eta,\varsigma) = (2\xi-1)\xi$$
$$N_2(\xi,\eta,\varsigma) = (2\eta-1)\eta$$
$$N_3(\xi,\eta,\varsigma) = (2\varsigma-1)\varsigma$$
$$N_4(\xi,\eta,\varsigma) = 4\xi\eta$$
$$N_5(\xi,\eta,\varsigma) = 4\eta\varsigma$$
$$N_6(\xi,\eta,\varsigma) = 4\xi\varsigma$$

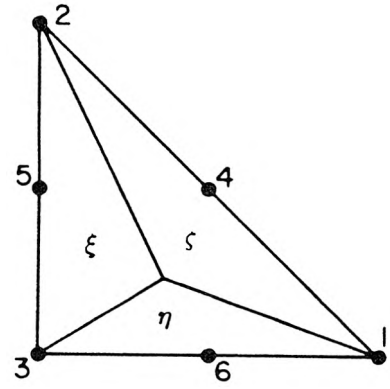


4 node quadrilaterals:

$$N_1(\xi,\eta) = (1+\xi)(1+\eta)/4$$
$$N_2(\xi,\eta) = (1-\xi)(1+\eta)/4$$
$$N_3(\xi,\eta) = (1-\xi)(1-\eta)/4$$
$$N_4(\xi,\eta) = (1+\xi)(1-\eta)/4$$

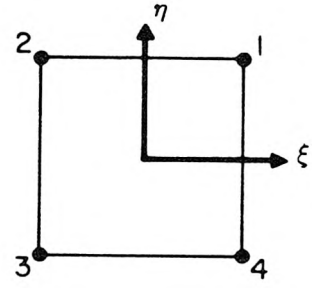


3 node triangles:

$$N_1(\xi,\eta,\varsigma) = \xi$$
$$N_2(\xi,\eta,\varsigma) = \eta$$
$$N_3(\xi,\eta,\varsigma) = \varsigma$$

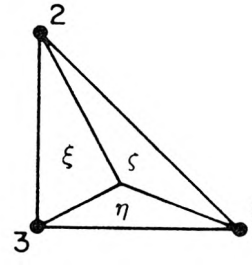


Fig. 3.4.2 Elements used in the Finite Element Model.

8 node quadratic quadrilaterals, 6 node quadratic triangles, 4 node linear quadrilaterals, and 3 node linear triangles. These elements are shown in Fig. 3.4.2 in terms of parent rectangular coordinates $(\xi, \eta)$ for the quadrilaterals and parent area coordinates $(\xi, \eta, \varsigma)$ for the triangles. The vertices of the quadrilaterals lie at $(\xi, \eta) = (\pm 1, \pm 1)$. The vertices of the triangle lie at $(\xi, \eta, \varsigma) = (0,0,1)$, $(0,1,0)$, $(1,0,0)$. Any one of these or any consistent combination of these types of shape functions may be used in the finite element model. These shape functions ensure continuity of the interpolated function along interelement boundaries of adjacent elements.

The nodal and element structure along the interregion boundaries $\Gamma_{HM}$ and $\Gamma_{MO}$ will be discussed in detail in Section 3.4.6. The computed solution jumps abruptly across these boundaries.

The weighting functions $\hat{x}$, $\hat{y}$ and $\hat{\eta}$ have not yet been specified. They will be chosen to be the same as the shape functions. This will result in a particular weighted residual method known as Galerkin's method. It is the most common weighted residual method used with finite element techniques.

The discretization of Eq. (3.4.42) will lead to a system of algebraic equations which can be written in matrix form as :

$$M\ddot{\mathbf{d}} + C\dot{\mathbf{d}} = \mathbf{f} \tag{3.4.43}$$

where the dots represent time derivatives of the components of $\mathbf{d}$. The vector $\mathbf{d}$ contains the particle displacement nodal unknowns:

$$\mathbf{d}(t) = \begin{pmatrix} x_1 \\ y_1 \\ x_2 \\ y_2 \\ \vdots \\ x_N \\ y_N \end{pmatrix} \qquad N = \text{number of nodes.} \tag{3.4.44}$$

The "mass" matrix $M$, dissipation matrix $C$, and the forcing vector $\mathbf{f}$ can be assembled from the element matrices $M^e$ and $C^e$ and element vectors $\mathbf{f}^e$, using standard finite element assembly procedures. Actually $M^e$ and $C^e$ need not both be assembled. Only the combination $M + (\Delta t/2)C$ is needed, as will be shown when the time integration scheme is covered.

For a particular element with $n$ nodes, the element matrix $M^e$ can be expressed as a partitioned matrix of the form:

$$M^e = \left(\begin{array}{c|c|c|c} m_{11} & m_{12} & \cdots & m_{1n} \\ \hline m_{21} & m_{22} & \cdots & m_{2n} \\ \hline \vdots & \vdots & \ddots & \vdots \\ \hline m_{n1} & m_{n2} & \cdots & m_{nn} \end{array}\right) \tag{3.4.45}$$

where each of the $m_{ij}$ are $2 \times 2$ matrices defined as:

$$\begin{aligned} m_{ij} = & \iint_{\Omega^e} (1 + \alpha \nabla \cdot \mathbf{x}) \begin{bmatrix} N_i N_j & 0 \\ 0 & N_i N_j \end{bmatrix} da\, db \\ & + \beta \iint_{\Omega^e} \left\{ \frac{h^2}{3} \begin{bmatrix} \frac{\partial N_i}{\partial a}\frac{\partial N_j}{\partial a} & \frac{\partial N_i}{\partial a}\frac{\partial N_j}{\partial b} \\ \frac{\partial N_i}{\partial b}\frac{\partial N_j}{\partial a} & \frac{\partial N_i}{\partial b}\frac{\partial N_j}{\partial b} \end{bmatrix} + \frac{h}{6} N_i \begin{bmatrix} \frac{\partial h}{\partial a}\frac{\partial N_j}{\partial a} & \frac{\partial h}{\partial a}\frac{\partial N_j}{\partial b} \\ \frac{\partial h}{\partial b}\frac{\partial N_j}{\partial a} & \frac{\partial h}{\partial b}\frac{\partial N_j}{\partial b} \end{bmatrix} \right\} da\, db \\ & + \beta \iint_{\Omega^e} \left\{ \frac{h}{2} N_j \begin{bmatrix} \frac{\partial h}{\partial a}\frac{\partial N_i}{\partial a} & \frac{\partial h}{\partial b}\frac{\partial N_i}{\partial a} \\ \frac{\partial h}{\partial a}\frac{\partial N_i}{\partial b} & \frac{\partial h}{\partial b}\frac{\partial N_i}{\partial b} \end{bmatrix} + \frac{1}{2} N_i N_j \begin{bmatrix} \left(\frac{\partial h}{\partial a}\right)^2 & \frac{\partial h}{\partial a}\frac{\partial h}{\partial b} \\ \frac{\partial h}{\partial a}\frac{\partial h}{\partial b} & \left(\frac{\partial h}{\partial b}\right)^2 \end{bmatrix} \right\} da\, db \\ & - \beta \int_{\partial\Omega^e} \left\{ \frac{h^2}{3} N_i \begin{bmatrix} n_a \frac{\partial N_j}{\partial a} & n_a \frac{\partial N_j}{\partial b} \\ n_b \frac{\partial N_j}{\partial a} & n_b \frac{\partial N_j}{\partial b} \end{bmatrix} + \frac{h}{2} N_i N_j \begin{bmatrix} n_a \frac{\partial h}{\partial a} & n_a \frac{\partial h}{\partial b} \\ n_b \frac{\partial h}{\partial a} & n_b \frac{\partial h}{\partial b} \end{bmatrix} \right\} ds \end{aligned} \tag{3.4.46}$$

where the nonlinear and dispersive terms are included only for elements which lie in the region $\Omega_H \cup \Omega_M$. The terms $n_a$ and $n_b$ are the $a$ and $b$ components of the outward normal unit vector along the boundary of the element domain $\Omega^e$. In the region $\Omega_O$ the nonlinear and dispersive terms are neglected and $\mathbf{x}$ is replaced by $\mathbf{x}_R$. $N_i$ is the shape function for the element corresponding to local node

number $i$. Note that if we neglect dispersion $(\beta = 0)$, $M$ will be symmetric but not otherwise.

The boundary integral in Eq. (3.4.46) is evaluated only along element boundaries which lie along the portion of the boundary BDF where boundary condition (3.4.8) is applied. That is because this integral gives no contribution along the portions of the boundary BDF where either boundary condition (3.4.7) or (3.4.9) are specified. Where boundary condition (3.4.7) is applied we have $h(a,b) = 0$ and hence the integral is identically zero. Where boundary condition (3.4.9) is applied the integral is not zero; however, it gives no contribution since only equations associated with degrees of freedom parallel to the wall are assembled. The component of the outward unit normal vector associated with each of these equations is zero, so there are no contributions (this will be covered in more detail later in Section 3.4.5 when the treatment of the vertical wall boundary condition discussed).

Similarly, the element dissipation matrix $C^e$ can be expressed as:

$$C^e = \left(\begin{array}{c|c|c|c} c_{11} & c_{12} & \cdots & c_{1n} \\ \hline c_{21} & c_{22} & \cdots & c_{2n} \\ \hline \vdots & \vdots & \ddots & \vdots \\ \hline c_{n1} & c_{n2} & \cdots & c_{nn} \end{array}\right) \tag{3.4.47}$$

where each of the $c_{ij}$ are $2 \times 2$ matrices defined as:

$$\begin{aligned} c_{ij} = & \iint_{\Omega^e} \frac{\gamma}{h(a,b)} \begin{bmatrix} N_i N_j & 0 \\ 0 & N_i N_j \end{bmatrix} da\, db \\ & + \int_{\partial\Omega^e} N_i N_j \begin{bmatrix} n_a \cos\theta & n_a \sin\theta \\ n_b \cos\theta & n_b \sin\theta \end{bmatrix} ds \end{aligned} \tag{3.4.48}$$

where the area integral is computed only for elements which lie in the region $\Omega_H \cup \Omega_M$ and the boundary integral is only evaluated along element edges which lie on $\Gamma_O$.

We also can write an expression for the element forcing vector $\mathbf{f}^e$:

$$\mathbf{f}^e = \begin{pmatrix} \mathbf{f}_1 \\ \mathbf{f}_2 \\ \vdots \\ \mathbf{f}_n \end{pmatrix} \tag{3.4.49}$$

where the $\mathbf{f}_i$ are $2 \times 1$ vectors defined as:

$$\begin{aligned}
\mathbf{f}_i = &- \iint_{\Omega^e} \left\{ \begin{pmatrix} 1+\alpha\dfrac{\partial y}{\partial b} \\ -\alpha\dfrac{\partial x}{\partial b} \end{pmatrix} \frac{\partial N_i}{\partial a} + \begin{pmatrix} -\alpha\dfrac{\partial y}{\partial a} \\ 1+\alpha\dfrac{\partial x}{\partial a} \end{pmatrix} \frac{\partial N_i}{\partial b} \right\} \times \\
&\left\{ \nabla h \cdot \mathbf{x} + \frac{\alpha}{2} \mathbf{x} \cdot \underline{\mathbf{H}} \cdot \mathbf{x} + h \frac{\left[ \nabla \cdot \mathbf{x} + \alpha \frac{\partial(x,y)}{\partial(a,b)} \right]}{1 + \alpha \nabla \cdot \mathbf{x}} \right\} da\, db \\
&+ \int_{\partial\Omega^e} \frac{\alpha f}{2} \overline{U} |\overline{U}| \begin{pmatrix} n_a \\ n_b \end{pmatrix} N_i \, ds + \int_{\partial\Omega^e} \eta_{\text{IR}} \begin{pmatrix} n_a \\ n_b \end{pmatrix} N_i \, ds \\
&- \frac{1}{2R_{\text{O}}} \int_{\partial\Omega^e} \mathbf{x} \cdot \mathbf{n}_\theta \begin{pmatrix} n_a \\ n_b \end{pmatrix} N_i \, ds \\
&- \int_{\partial\Omega^e} \left\{ \begin{pmatrix} 1+\alpha\dfrac{\partial y}{\partial b} \\ -\alpha\dfrac{\partial x}{\partial b} \end{pmatrix} n_a + \begin{pmatrix} -\alpha\dfrac{\partial y}{\partial a} \\ 1+\alpha\dfrac{\partial x}{\partial a} \end{pmatrix} n_b \right\} N_i \, \eta \, ds
\end{aligned} \tag{3.4.50}$$

where the nonlinear terms are included only for elements which lie in the region $\Omega_{\text{H}} \cup \Omega_{\text{M}}$ and the boundary integrals are evaluated only for the elements which lie on the appropriate boundaries. In region $\Omega_{\text{O}}$ the nonlinear terms are neglected and $\mathbf{x}$ is replaced by $\mathbf{x}_{\text{R}}$. Boundary conditions (3.4.7) and (3.4.8) are imposed by subsituting the corresponding expressions for $\eta$ into the last boundary integral in Eq. (3.4.50) along the portions of the boundary where they apply. This integral need not be evaluated along the portion of the boundary where boundary condition (3.4.9) is specified. It will give no contribution for the same reason discussed when the expression for $m_{ij}$ in Eq. (3.4.46) was presented.

Initial conditions must also be specified. For motion starting from rest we

must specify:

$$\mathbf{d}(0) = \dot{\mathbf{d}}(0) = \mathbf{0} \quad . \tag{3.4.51}$$

The Galerkin formulation of the continuity equation (3.4.26) can also be discretized to obtain a set of algebraic equations for the nodal values of the surface elevation. However, because $\eta$ was eliminated from the problem, this set of equations need not be solved simultaneously with Eq. (3.4.43). In fact, they are no longer strictly needed to solve the problem. Nevertheless, since the nodal values of the wave elevation are important quantities, they will be computed, once the particle displacements are obtained from Eq. (3.4.43). They can be computed whenever desired, not necessarily at each time step. The matrix representation of these equations is:

$$H\mathbf{e} = \mathbf{p} \tag{3.4.52}$$

where the vector $\mathbf{e}$ contains the nodal values of the water surface elevations:

$$\mathbf{e}(t) = \begin{pmatrix} \eta_1 \\ \eta_2 \\ \vdots \\ \eta_N \end{pmatrix} \qquad N = \text{number of nodes.} \tag{3.4.53}$$

For an element with $n$ nodes the element matrices $H^e$ is of the form:

$$H^e = \begin{pmatrix} h_{11} & h_{12} & \dots & h_{1n} \\ h_{21} & h_{22} & \dots & h_{2n} \\ \vdots & \vdots & \ddots & \vdots \\ h_{n1} & h_{n2} & \dots & h_{nn} \end{pmatrix} \quad \text{where} \quad h_{ij} = \iint\limits_{\Omega^e} N_i N_j \, da \, db \, . \tag{3.4.54}$$

The $i^{\text{th}}$ component of the element forcing vector $\mathbf{p}^e$ is:

$$(\mathbf{p}^e)_i = -\iint\limits_{\Omega^e} \left\{ \nabla h \cdot \mathbf{x} + \frac{\alpha}{2} \mathbf{x} \cdot \underline{\mathbf{H}} \cdot \mathbf{x} + h \frac{\left[ \nabla \cdot \mathbf{x} + \alpha \frac{\partial(x,y)}{\partial(a,b)} \right]}{1 + \alpha \nabla \cdot \mathbf{x}} \right\} N_i \, da \, db \, . \tag{3.4.55}$$

For elements which lie in region $\Omega_O$ the nonlinear terms are neglected and $\mathbf{x}$ is replaced by $\mathbf{x}_R$ .

Assuming that the motion starts from rest, the appropriate initial condition is

$$\mathbf{e}(0) = \mathbf{0} \quad . \tag{3.4.56}$$

All integrations in Eqs. (3.4.46), (3.4.48), (3.4.50), (3.4.54) and (3.4.55) were performed numerically using Gauss quadrature schemes. For the quadrilateral elements, $2\times2$ and $3\times3$ point formulae from Connor & Brebbia (1976) were used for the linear and quadratic elements, respectively. For the triangular elements, 3 point and 6 point formulae from Cowper (1973) were used for the linear and quadratic elements, respectively.

### 3.4.4 Time Integration Scheme

The central difference method was employed for the temporal integration. In this method it is assumed that:

$$\ddot{\mathbf{d}}(t) = \frac{\mathbf{d}(t+\Delta t) - 2\mathbf{d}(t) + \mathbf{d}(t-\Delta t)}{\Delta t^2} \tag{3.4.57}$$

$$\dot{\mathbf{d}}(t) = \frac{\mathbf{d}(t+\Delta t) - \mathbf{d}(t-\Delta t)}{2\Delta t} \quad . \tag{3.4.58}$$

Then, if the discretized value of $\mathbf{d}(t)$ at time $t = n\Delta t$ is denoted by $\mathbf{d}^{(n)}$, Eq. (3.4.43) can be written as:

$$[M + \tfrac{\Delta t}{2} C]\mathbf{d}^{(n+1)} = \Delta t^2 \mathbf{f} + \tfrac{\Delta t}{2} C\mathbf{d}^{(n-1)} + M[2\mathbf{d}^{(n)} - \mathbf{d}^{(n-1)}] \, . \tag{3.4.59}$$

This is an algebraic system of equations for the particle displacement vector $\mathbf{d}$ at time $t = (n+1)\Delta t$:

$$G\mathbf{d}^{(n+1)} = \mathbf{g} \tag{3.4.60}$$

where

$$G = M + \tfrac{\Delta t}{2} C \tag{3.4.61}$$

and

$$\mathbf{g} = \Delta t^2 \mathbf{f} + \tfrac{\Delta t}{2} C \mathbf{d}^{(n-1)} + M[2\mathbf{d}^{(n)} - \mathbf{d}^{(n-1)}] \,. \tag{3.4.62}$$

The matrix $G$ is assembled from the element matrices $M^e$ and $C^e$. The vector $\mathbf{g}$ is assembled from the element matrices $M^e$ and $C^e$, the element vectors $\mathbf{f}^e$, and the element vectors for $\mathbf{d}^{(n)}$ and $\mathbf{d}^{(n+1)}$.

Gray & Lynch (1977) studied ten different schemes for marching finite element long wave solutions through time. They restricted the analysis to propagation in one horizontal coordinate in a fluid of constant depth, neglecting nonlinear and dispersive terms in the equations of motion, although linear dissipation was included. The finite element spatial discretization was done using uniform linear elements. Of those methods, the central difference method employed here was the only one that was conservative (exactly conserved mass and momentum) in the absence of the dissipation terms represented by the matrix $C$, but which damped all wavelengths, even the troublesome short wavelengths of twice the grid spacing when friction was included. The scheme is stable, provided $\Delta t^* < \Delta a^*/\sqrt{3gh}$ where $\Delta a^*$ is the dimensional grid spacing.

For a general nonuniform two-dimensional grid with nonuniform depth variations it is not possible to obtain a general stability constraint of this type but a good estimate is $\Delta t^* < (1/\sqrt{3g})(\Delta s^*/\sqrt{h})_{\min}$ where $\Delta s^*$ represents the distance between any two nodes and $h$ is the average water depth between the nodes. Thus, as $h$ gets smaller, $\Delta s$ can be reduced without the necessity to reduce $\Delta t$. This is important because it allows a finer grid to be used near a shoreline where shoaling causes wavelengths to decrease. If, in addition, nonlinear and dispersive terms are included in the equations of motion, then this time step criterion is not strictly valid but it was found to give a good estimate nonetheless. In practice, a slightly

more conservative estimate was usually used: $\Delta t^* = (0.5/\sqrt{g})(\Delta s^*/\sqrt{h})_{\min}$.

### 3.4.5 Boundary Condition for a Vertical Wall

The boundary condition for a vertical wall, Eq. (3.4.9), does not involve specifying the water surface elevation, $\eta$, along the boundary, so it must be treated differently than the other boundary conditions. Associated with each node point there are usually two degrees of freedom corresponding to the two components of the fluid particle displacement. The wave elevation is not considered to be a third degree of freedom because it has been decoupled from the problem and is completely determined when the nodal values of the particle displacements are known. In order to satisfy boundary condition (3.4.9) there can be only one degree of freedom associated with a node point lying along a vertical wall. This degree of freedom corresponds to the component of particle displacement tangent to the wall at the present location of the fluid particle.

One way to accomplish this would be to proceed as follows. First, assemble the set of algebraic equations (3.4.60) as just described in the previous section. Then perform an orthogonal transformation on these equations which rotates the degrees of freedom associated with nodes along a vertical wall so that one degree of freedom is tangent to the wall and the other one is perpendicular to the wall. Let us denote this orthogonal transformation matrix by $Q$. Then the system of equations (3.4.60) transforms to:

$$G^* \mathbf{d}^{*(n+1)} = \mathbf{g}^* \tag{3.4.63}$$

where

$$\left.\begin{aligned} G^* &= Q^{\mathrm{T}} G Q \\ \mathbf{d}^{*(n+1)} &= Q^{\mathrm{T}} \mathbf{d}^{(n+1)} \\ \mathbf{g}^* &= Q^{\mathrm{T}} \mathbf{g} \end{aligned}\right\} \quad . \tag{3.4.64}$$

Here the $^{\mathrm{T}}$ refers to the transpose of a vector or matrix. The components of acceleration normal to the wall are set to zero and the equation corresponding to these equations of freedom are discarded. Then the remaining equations are solved to obtain the two components of acceleration at the internal nodes and the single tangential component of acceleration at the vertical wall nodes. In fact, instead of setting the normal components of acceleration to zero, these may be specified as non zero, thereby modelling the flow induced by a moving vertical wall, including the effects of finite displacement. If this is done, extra terms are generated on the left hand side of the equal sign. These terms are transferred over to the right hand side into the forcing vector $\mathbf{f}^*$ before the matrix equation is solved. The orthogonal transformation matrix $Q$ may depend on the fluid particle displacements along a wall. If the wall is curved, then the local wall tangents will depend on where the fluid particles are along the wall. Hence, as the fluid particles move, the matrix $Q$ will slowly change. However, if finite displacement (nonlinear) effects are neglected, the matrix $Q$ will be constant.

This is not quite the way that the finite element model handles this boundary condition, although the results are exactly the same. Since the finite element equations are assembled from the element level, the orthogonal transformations are also performed at the element level. Then when the equations are assembled, the equations corresponding to components of displacement normal to a vertical wall are not assembled. Hence, storage is not required for the coefficients in these equations. An element orthogonal transformation matrix for an element with $n$

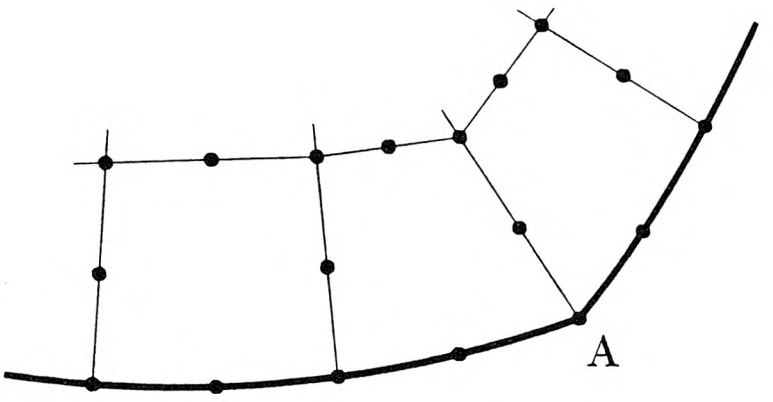


Fig. 3.4.3 Situation where the outward unit normal vector is not uniquely defined at a node point.

nodes is of the form:

$$Q^e = \begin{pmatrix} \cos\theta_1 & -\sin\theta_1 & & & \\ \sin\theta_1 & \cos\theta_1 & & 0 & \\ & & \ddots & & \\ & & & \ddots & \\ & 0 & & \cos\theta_n & -\sin\theta_n \\ & & & \sin\theta_n & \cos\theta_n \end{pmatrix} \tag{3.4.65}$$

where $\theta_i$ is the angle between the $(\nu, \tau)$ axes and the $(a, b)$ axes. $\nu$ is the component of displacement normal to the wall and $\tau$ is the component tangent to the wall. For a node not on a vertical wall $\theta_i$ is chosen to be zero.

The proper choice for $\theta$ must be made because it may not be uniquely defined. This can happen at a corner node of an element located along a vertical wall as shown in Fig. 3.4.3. The outward unit vector $\mathbf{n}$ is well defined along the two sides of the elements shown in the figure, but it changes discontinuously at node A. The

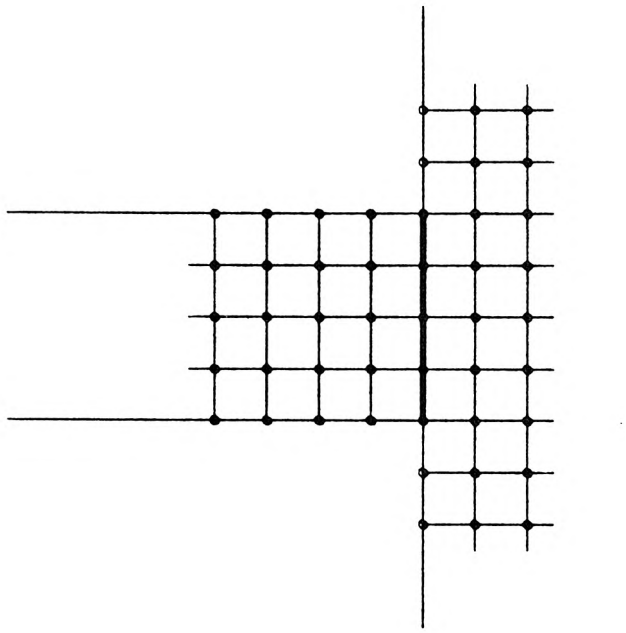

Fig. 3.4.4 Harbour entrance where flow separation occurs.

following definition for $\mathbf{n}_A$ was chosen.

$$\mathbf{n}_A = \frac{\int \mathbf{n} N_A \, ds}{\left| \int \mathbf{n} N_A \, ds \right|} \tag{3.4.66}$$

where $N_A$ is the interpolation function associated with node A. The integration extends along the two element edges adjacent to the wall. Gray (1976) and Pinder & Gray (1977) defined the nodal normal direction in this manner and it was used successfully in finite element wave models by Lynch & Gray (1978), (1979) & (1980). In addition, Wang & Connor (1975) have indicated that this choice of nodal normal direction conserves mass for linear triangular elements.

At a constricted or narrow harbour entrance the boundary geometry may change very abruptly, much more so than as in Fig. 3.4.3. Of interest to this investigation is the case shown in Fig. 3.4.4. The darkened vertical line represents $\Gamma_{HM}$, also depicted in Fig. 3.4.1. At the harbour entrance the boundaries turn

through a very abrupt 90 degrees. The analytical solution to the model equations (3.4.2) and (3.4.3) subject to the boundary condition that the flow remain attached everywhere would exhibit infinite gradients at the corners and very large gradients nearby. It would be pointless to try to model accurately such a flow because real fluid effects will cause the flow to separate at the corners for any fluid motions of interest. Therefore, it is not important to ensure that the fluid particles remain attached and move perfectly tangent to the boundary in this region. In fact, since we know the flow will separate around these corners, especially for flow to the right out of the harbour, we can relax the requirement that this boundary condition be satisfied at the corners and impose an alternate *ad hoc* condition which is closer in agreement with the observed flow in this region. The aim is not so ambitious as to develop a model for flow separation but to impose a condition which is more suited to this particular geometry than the usual requirement that the flow be everywhere tangent to solid boundaries. Across $\Gamma_{HM}$ we can apply Eqs. (3.4.22) and (3.4.24) in order to introduce the dissipation associated with the separated flow but these two conditions are not sufficient to determine the boundary condition associated with the separated flow. For a long narrow harbour a simple condition is to constrain the degrees of freedom associated with particle displacements normal to the entrance to be the same for each of the nodes across the entrance, but not to constrain the transverse degrees of freedom, not even for the corner nodes. Hence, the flow will be free to contract when moving to the right in Fig. 3.4.4 and to contract when moving to the left, but the particles associated with the corner nodes will not be so severely constrained that they remain perfectly attached around the corners. See Fig. 3.4.5. The arrows represent the paths of the fluid particles. In general these paths will be curved and more complex.

This condition can be easily implemented in the numerical model. First, the degrees of freedom associated with nodes across the entrance are rotated, using

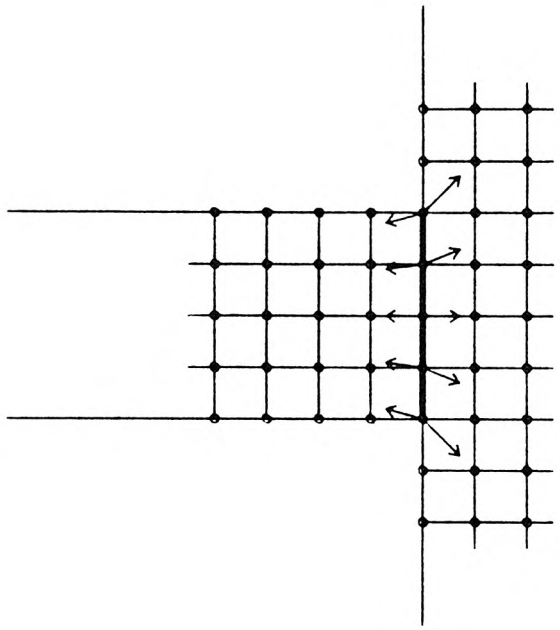

Fig. 3.4.5 Flow through the harbour entrance.

an orthogonal transformation as described in this section so that one degree of freedom for each node is normal to the boundary $\Gamma_{HM}$ and one is tangential to it. Then the coefficients of the element matrices and vectors associated with the normal degrees of freedom are all assembled into the the same equation. However, the coefficients associated with the tangential degrees of freedom are assembled into separate equations so that these components of displacement are not constrained at all.

### 3.4.6 Interregion Boundaries

Across the interregion boundaries $\Gamma_{HM}$ and $\Gamma_{MO}$ the computed solution jumps discontinuously. The numerical treatment of these jumps has not yet been included in the description of the model up to this point. The unknowns

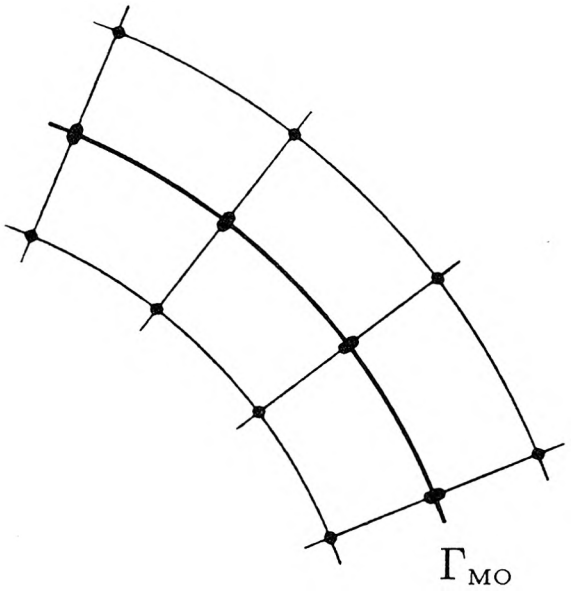


Fig. 3.4.6 Double set of nodes along interregion boundary $\Gamma_{MO}$ .

in the model must be carefully defined along these boundaries. The treatment of the boundary $\Gamma_{HM}$ is actually a special case of the treatment used for boundary $\Gamma_{MO}$ , since across $\Gamma_{MO}$ both the fluid particle displacements and the water surface elevation jump discontinuously, whereas across $\Gamma_{HM}$ only the water surface elevation jumps. Therefore, let us look only at the treatment of the boundary $\Gamma_{MO}$ . The method used for it can then be specialized to $\Gamma_{HM}$ .

The solution along $\Gamma_{MO}$ could be treated by using a double set of nodes along it as shown in Fig. 3.4.6. This is not the way this boundary is treated in the model, but it is necessary to consider this method in order to explain how the boundary is actually treated. For the moment let us assume that this is the method used. When interpolation is done within an element bordering on $\Gamma_{MO}$ , the nodal values along $\Gamma_{MO}$ associated with either $\Omega_M$ or $\Omega_O$ are used, depending on which side

of $\Gamma_{MO}$ the element lies on. There are four particle displacements associated with each double node, two associated with the $\Omega_M$ node and two associated with the $\Omega_O$ node. Using the techniques described in the previous sections, the set of equations represented by Eq. (3.4.43) could be assembled:

$$G\mathbf{d}^{(n+1)} = \mathbf{g} \quad , \tag{3.4.67}$$

but they would not correctly model the flow. This is because the particle displacements at each double node are not independent degrees of freedom. The jumps in the particle displacements are given by Eq. (3.4.25b). Hence, if we are given the particle displacements at one node on $\Gamma_{MO}$, the particle displacements at the bordering node are completely determined by the jump condition (3.4.25b), since $\mathbf{x}_{IR}$ is a given known function. The jump condition represents a series of constraints which the particle displacements at each of the double (or contact) nodes along $\Gamma_{MO}$ must satisfy. These constraints were not included in the system of equations (3.4.67).

If $i$ and $j$ are corresponding degrees of freedom at a contact node, then the corresponding constraint can be expressed as:

$$d_i^{(n+1)}(t) - d_j^{(n+1)}(t) = g_{ij}(t) \tag{3.4.68}$$

where the jump $g_{ij}$ is known once the incident-reflected wave system $\mathbf{x}_{IR}$ is given. If there are $N_D$ degrees of freedom in the problem and $c$ constraints, then all of the constraint equations of the form (3.4.68) can be written in a matrix equation as:

$$\mathcal{C}\mathbf{d}^{(n+1)} = \mathbf{g}_c \tag{3.4.69}$$

where $\mathbf{g}_c$ is a $c \times 1$ vector containing the $g_{ij}$ terms and $\mathcal{C}$ is a $c \times N_D$ matrix. If the degrees of freedom at the contact nodes were to be numbered sequentially, first on one side of $\Gamma_{MO}$ and then on the other side such that the contact degrees

of freedom are the last to be numbered in the problem, then $C$ would be of the form:

$$C = \begin{pmatrix} 0 \ldots 0 & 1 & 0 \ldots & & \ldots 0 & -1 & 0 \ldots \ldots & 0 \\ 0 \ldots \ldots 0 & 1 & 0 \ldots & & \ldots 0 & -1 & 0 \ldots & 0 \\ \vdots & \ddots & \ddots & \ddots & & \ddots & \ddots & \ddots & \vdots \\ 0 \ldots & \ldots 0 & 1 & 0 \ldots & & \ldots 0 & -1 & 0 \\ 0 \ldots & \ldots 0 & 1 & 0 \ldots & & \ldots 0 & -1 \end{pmatrix} . \tag{3.4.70}$$

In the actual finite element model there is no restriction on the numbering of the degrees of freedom. It is done here only for clarity.

There is more than one way to show how the constraints of Eq. (3.4.69) can be included in the finite element formulation of the problem. One way is as follows.

One can think of the system of equations (3.4.67) (which are not correct since they do not include the constraints of Eq. (3.4.69)) as resulting from extremizing the quadratic form:

$$\Pi = \frac{1}{2}\mathbf{d}^{(n+1)\mathrm{T}} G \mathbf{d}^{(n+1)} - \mathbf{g}^{\mathrm{T}} \mathbf{d}^{(n+1)} \tag{3.4.71}$$

over the components of $\mathbf{d}^{(n+1)}$. Then the correct system of equations can be obtained by extremizing this quadratic form subject to the constraints of Eq. (3.4.69). One way to proceed is to use the method of Lagrange multipliers. Let $\mathbf{\Lambda}$ represent a $c \times 1$ vector containing the Lagrange multipliers. Then the appropriate quadratic form to extremize in order to obtain the correct set of equations is:

$$\Pi' = \frac{1}{2}\mathbf{d}^{(n+1)\mathrm{T}} G \mathbf{d}^{(n+1)} - \mathbf{g}^{\mathrm{T}} \mathbf{d}^{(n+1)} + \left(\mathbf{d}^{(n+1)\mathrm{T}} C^{\mathrm{T}} - \mathbf{g}_c^{\mathrm{T}}\right) \mathbf{\Lambda} . \tag{3.4.72}$$

The extremization must be carried out over the components of $\mathbf{\Lambda}$ as well as the components of $\mathbf{d}^{(n+1)}$; i.e.,

$$\frac{\partial \Pi'}{\partial \mathbf{d}^{(n+1)}} = \mathbf{0} \qquad \text{and} \qquad \frac{\partial \Pi'}{\partial \mathbf{\Lambda}} = \mathbf{0} \quad . \tag{3.4.73}$$

This leads to the following system of equations.

$$\left.\begin{aligned} G\mathbf{d}^{(n+1)} + C^{\mathrm{T}}\mathbf{\Lambda} &= \mathbf{g} \\ C\mathbf{d}^{(n+1)} &= \mathbf{g}_c \end{aligned}\right\} \quad . \tag{3.4.74}$$

These equations may be expressed as the following partitioned matrix set of equations:

$$\left(\begin{array}{c|c} G & C^{\mathrm{T}} \\ \hline C & 0 \end{array}\right)\left(\begin{array}{c} \mathbf{d}^{(n+1)} \\ \hline \mathbf{\Lambda} \end{array}\right) = \left(\begin{array}{c} \mathbf{g} \\ \hline \mathbf{g}_c \end{array}\right) \quad . \tag{3.4.75}$$

This system of equations possesses undesirable characteristics from a numerical point of view. First, it has a large bandwidth, and second, it contains a block of zeros along the diagonal. However, starting with this system of equations, one could imagine doing a series of row and column operations which would eliminate the Lagrange multipliers from the problem. In fact, one could perform additional row and column operations and eliminate the degrees of freedom along one side of $\Gamma_{\mathrm{MO}}$ from the problem, leaving only one set, say the ones on the $\Omega_{\mathrm{M}}$ side of $\Gamma_{\mathrm{MO}}$ in the system of equations. This would result in a matrix system of equations:

$$G'\mathbf{d}^{(n+1)'} = \mathbf{g}' \tag{3.4.76}$$

where the vector $\mathbf{d}^{(n+1)'}$ contains the degrees of freedom corresponding to all the nodes not on $\Gamma_{\mathrm{MO}}$, plus the degrees of freedom corresponding only to the contact nodes along $\Gamma_{\mathrm{MO}}$, which are associated with region $\Omega_{\mathrm{M}}$.

In the finite element model, the effects of doing all of these row and column operations are done at the element level, and the system of equations (3.4.76) are assembled directly. Hence, in the finite element model only one set of nodes is needed along the interregion boundary $\Gamma_{\mathrm{MO}}$. The degrees of freedom calculated at these nodes correspond to the wave system on the $\Omega_{\mathrm{M}}$ side of $\Gamma_{\mathrm{MO}}$. The degrees of freedom associated with the nodes in region $\Omega_{\mathrm{M}}$ correspond to the

complete wave system $\mathbf{x}$, and the degrees of freedom associated with the nodes in region $\Omega_O$ correspond to the radiated wave system $\mathbf{x}_R$.

### 3.4.7 Transforming to the Eulerian Description

By the use of the results of Section 3.1.2, the water surface elevations computed by the finite element model can be transformed to the Eulerian description. The water surface elevations computed by the finite element model are the elevations of the water surface at the positions of the fluid particles which at time $t = 0$ were located at the node points. These values can be transformed to the Eulerian description so they correspond to the surface elevations at the locations which the water particles occupied at time $t = 0$. These locations are fixed in space.

From Eqs. (3.1.86) and (3.1.116) the fluid particle displacements computed by the shallow water equations differ from the true particle displacements (which would be computed if the exact three-dimensional equations of motion were solved) by terms of $O(\alpha, \beta)$. From Eqs. (3.1.76), (3.1.86) and (3.1.98) the water surface elevation differs from the true elevation by terms of $O(\alpha^2)$. Hence, Eq. (3.1.67) can be written in terms of the water particle displacements $\mathbf{x}$ and surface elevation $\eta$ computed by the model as:

$$\eta_E(\mathbf{a}, t) = \eta(\mathbf{a}, t) - \alpha \mathbf{x}(\mathbf{a}, t) \cdot \nabla \eta(\mathbf{a}, t) + O(\alpha\beta, \alpha^2) \quad . \tag{3.4.77}$$

But from the momentum equations (3.4.3):

$$\nabla \eta = -\mathbf{x}_{tt} + O(\alpha, \beta, \gamma) \quad . \tag{3.4.78}$$

Substituting this into Eq. (3.4.77) gives:

$$\eta_E(\mathbf{a}, t) = \eta(\mathbf{a}, t) + \alpha \mathbf{x}(\mathbf{a}, t) \cdot \mathbf{x}_{tt}(\mathbf{a}, t) + O(\alpha\beta, \alpha\gamma, \alpha^2) \quad . \tag{3.4.79}$$

In particular, we can evaluate this equation at each time step, i.e., for $t = n\Delta t$ $n = 1, 2, \ldots$ and at each node point $\mathbf{a} = \mathbf{a}_i$ $i = 1, 2, \ldots, N$ where $N$ is the number of node points. Then all of the quantities on the right hand side of Eq. (3.4.79) are nodal quantities which are computed each time step where $\mathbf{x}_{tt}$ can be obtained from Eq. (3.4.57). Hence, the evaluation of $\eta_{\mathrm{E}}$ at the node points is very easy. However, this method will not necessarily give correct results at node points located in the vicinity of a beach where the shoreline moves with time because the fixed locations of the node points may or may not be part of the instantaneous fluid domain. When the shoreline recedes, some of the node points are left behind where there is no fluid. The other shortcoming is that when the shoreline moves up onshore, there are no node points corresponding to locations above the still water line, and so no Eulerian measurements of runup can be made in this region with this technique. Because of the nature of the description, none of these problems are encountered with the quantities computed in the Lagrangian description. Therefore, to resolve the nearshore region in the Eulerian description, a slightly more elaborate technique than Eq. (3.4.79) is needed. However, this method will work well offshore where Eulerian measurements are usually made anyway.

### 3.4.8 Sample Implementation of the Finite Element Model

In order for the finite element model to successfully model the response of a harbour to long wave excitation it is important that it be able to subtract the incident-reflected wave system in the outer region $\Omega_{\mathrm{O}}$ and to permit the remaining radiated wave system to pass through the outer radiation boundary $\Gamma_{\mathrm{O}}$. This allows the outer semi-infinite region to be modelled using a reasonably small finite sized grid, thus saving considerable amounts of computation. The

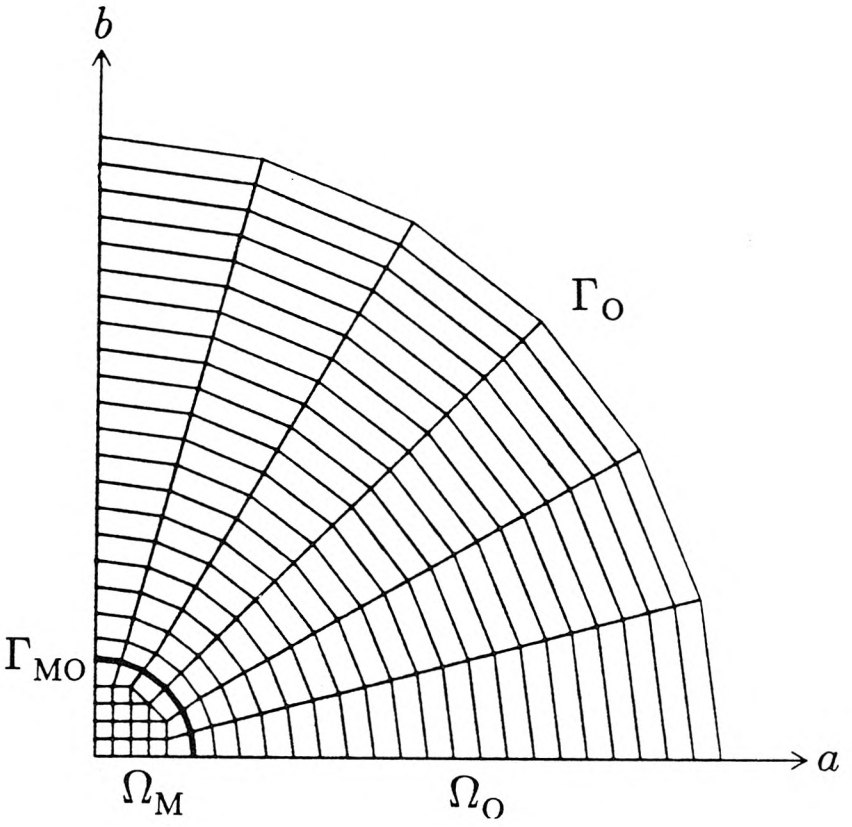


Fig. 3.4.7 Finite element mesh used for the sample implementations.

effectiveness of these two aspects of the model can be demonstrated in two simple implementations of the model.

For both cases the grid shown in Fig. 3.4.7 was used. The disturbances were symmetrical about $b = 0$, so the grid was defined only for $b \geq 0$. The boundary $a = 0$, $b \geq 0$ represents a semi-infinite coastline. It is vertical and perfectly reflecting. The radius of the grid is $R_O = 7.02$, the still water depth is unity everywhere, and the corner element at $(a, b) = (0, 0)$ has the dimensions $0.1 \times 0.1$. Hence, a time step of $\Delta t = 0.05$ was chosen. For both simulations, nonlinear, dispersive, and viscous dissipative effects were neglected.

The first test case investigates the effectiveness of the procedure used to subtract the incident-reflected wave system in region $\Omega_O$. For this case $\Gamma_{MO}$ appears

as the darkened circular arc in Fig. 3.4.7. The incident wave was chosen to be:

$$\eta = H(t+a-\phi)(1-e^{-(t+a-\phi)})\sin(t+a-\phi) \tag{3.4.80}$$

where $H(t)$ is the unit Heaviside step function and the term $(1-e^{-(t+a-\phi)})$ was chosen so that at the leading edge of the incident wave the surface displacement is zero and well as the fluid particle displacement, velocity, *and* acceleration. The phase $\phi$ is simply chosen so that at time $t=0$ the leading edge of the wave has just reached the boundary $\Gamma_{MO}$ where $b=0$. Since there is no harbour in this case and the boundary $a=0$ is a vertical perfectly reflecting wall, there is no radiated wave. Hence, exterior to the boundary $\Gamma_{MO}$ in region $\Omega_O$ there should ideally be no motion, whereas within the boundary in region $\Omega_M$ the incident-reflected wave system should be present. Along $\Gamma_{MO}$ the model computes only the wave heights associated with the region $\Omega_M$. However, the wave heights along this boundary associated with region $\Omega_O$ can easily be obtained using Eq. (3.4.25a).

In Fig. 3.4.8 the computed solution is compared to the theoretical solution along $b=0$ for a number of successive time values. In Fig. 3.4.9 the time record at $(a,b)=(0,0)$ is compared against the theoretical one. The agreement is very good in both cases. Along the boundary $\Gamma_O$, the radiation boundary condition is applied, but since there is almost no motion in the outer region $\Omega_O$, it really does not play a significant role in the simulation.

The second test investigates the effectiveness of the radiation boundary condition applied along $\Gamma_O$. For this case a radially symmetric disturbance is created along the darkened circular boundary, $\Gamma_{MO}$, in Fig. 3.4.7. At time $t=0$ the fluid is quiescent. At $t=0$ the forcing function:

$$H(t-2\pi)\frac{t^2(2\pi-t)^2}{\pi^4}\sin t \tag{3.4.81}$$

is applied along this arc in a similar way as the head loss matching condition is

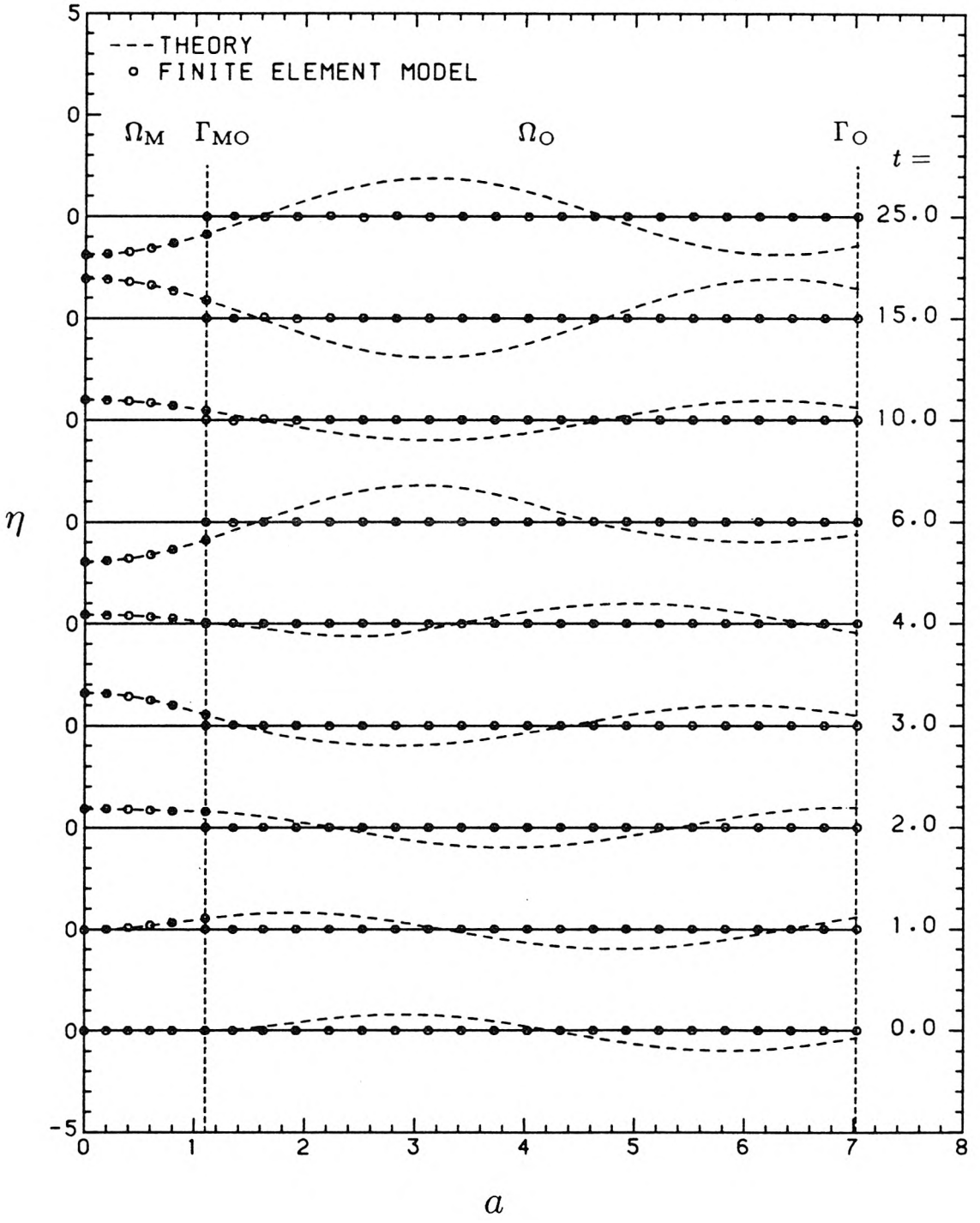


Fig. 3.4.8 Comparison of the computed solution to the theoretical one along $b = 0$.

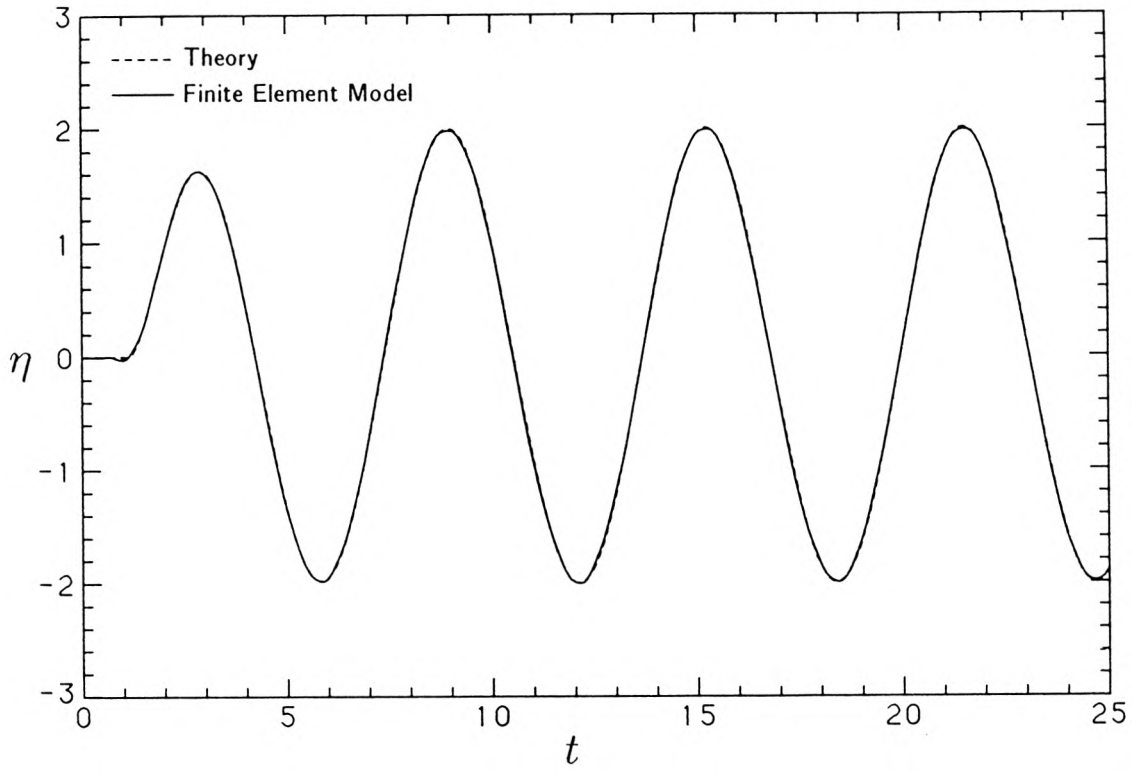


Fig. 3.4.9 Comparison of the computed solution to the theoretical one at $(a, b) = (0, 0)$.

implemented across $\Gamma_{HM}$. A jump in $\eta$ proportional to Eq. (3.4.81) is generated along this arc. In Figs. 3.4.10 and 3.4.11 this jump can be seen at the times $t = 1.0,\ 2.0$ and at $t = 4.0,\ 5.0$. These figures show the wave profile along $b = 0$ for a number of successive time values. At $t = 1.0,\ 2.0$ the jump has the opposite sign to that at the times $t = 4.0,\ 5.0$ in accordance with the sign of the forcing function in Eq. (3.4.81). Since the grid has finite resolution the jump is actually spread over three or four node points but it is still quite sharp. Note from Eq. (3.4.81) that at $t = \pi$ the forcing is zero, and this is reflected by the continuous water surface at the time $t = 3.0$. For $t > 2\pi$ the forcing is zero and so from this time on the waves propagate freely, subject to the boundary conditions imposed. The actual technique used to generate the wave system is not important. The important thing is to generate a localized wave system near the origin so that

its propagation can be followed out to the boundary $\Gamma_O$. An alternate approach would have been to specify an initial localized wave height at time $t = 0$. There is no boundary $\Gamma_{MO}$ in these simulations, and so an incident-reflected wave system is not subtracted off anywhere in the computational domain.

The results of two different tests are shown. Fig. 3.4.10 shows the results when the boundary condition $\eta = 0$ is applied along $\Gamma_O$, and Fig. 3.4.11 shows the results when the radiation boundary condition Eq. (3.4.12) is applied along $\Gamma_O$. Notice that in the first case the wave system is strongly reflected along $\Gamma_O$ since the boundary condition $\eta = 0$ does not allow the transmission of the waves out through $\Gamma_O$. In the second case, the wave system passes freely out of the computational domain across $\Gamma_O$. Fig. 3.4.12 shows the wave heights as a function of time at the origin $(a, b) = (0, 0)$ for both of these cases up to $t = 25$. Note the very large reflection that occurs if the radiation boundary condition is not used.

These computations were performed on a Floating Point Systems FPS 164 Attached Processor hosted by an IBM 4341 computer. Each run required approximately 45 seconds of execution time.

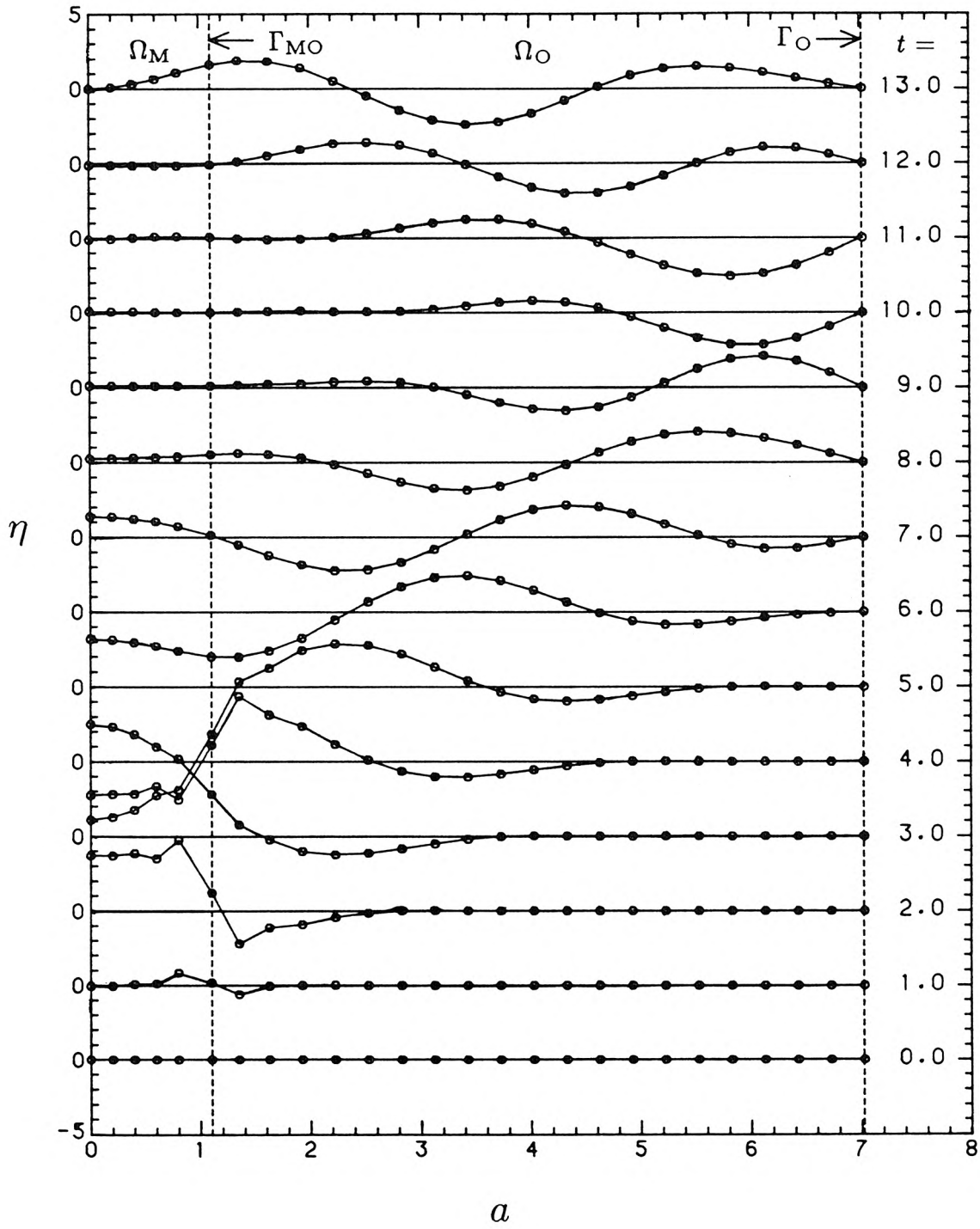


Fig. 3.4.10 Wave profiles along $b = 0$ at successive time values. Boundary condition $\eta = 0$ applied along $\Gamma_O$.

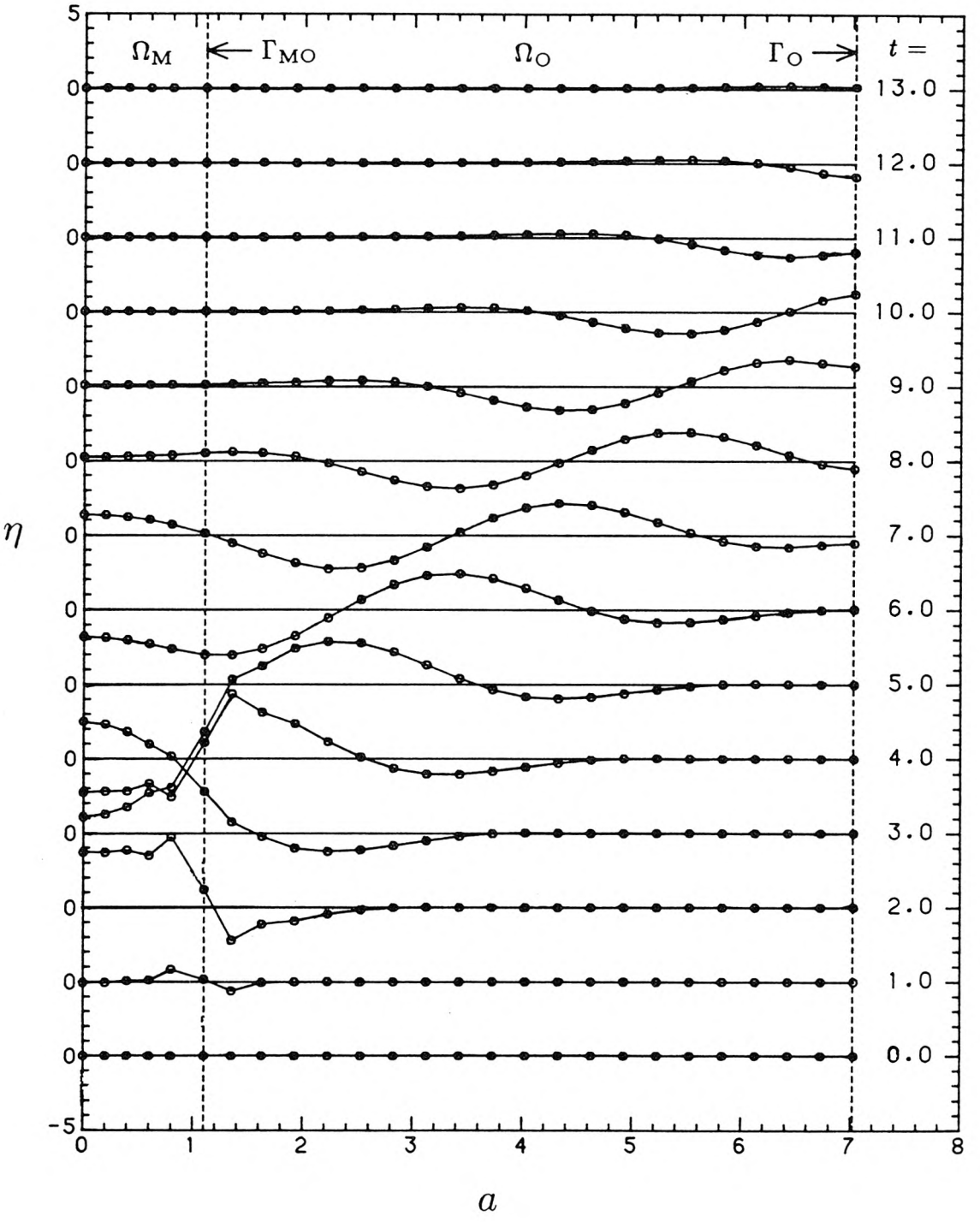


Fig. 3.4.11 Wave profiles along $b = 0$ at successive time values. Radiation boundary condition Eq. (3.4.12) applied along $\Gamma_O$.

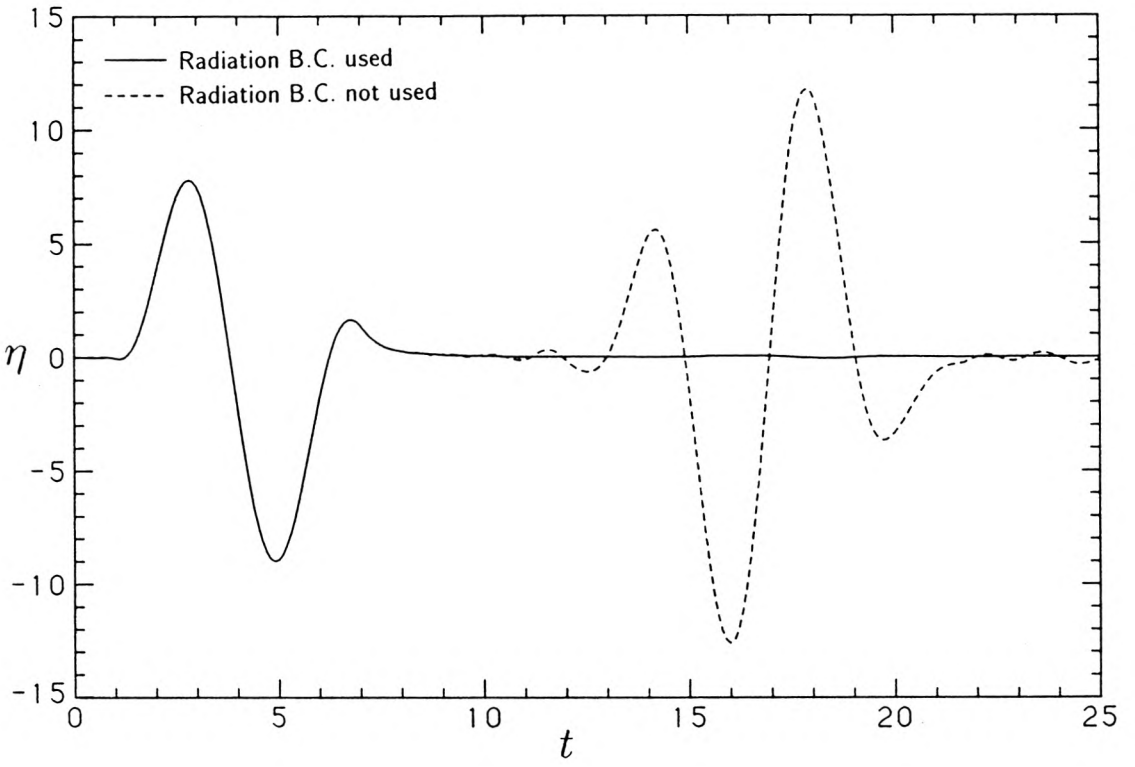


Fig. 3.4.12 Comparison between the two cases with and without the radiation boundary condition.

# CHAPTER 4

# Experimental Equipment and Procedures

## 4.1 The Wave Basin

The experiments for this investigation were conducted in the wave basin shown in Figs. 4.1.1 and 4.1.2. A schematic figure of the basin and the experimental arrangement is shown in Fig. 4.1.3. The basin was 58 cm deep, 4.73 m wide and 9.60 m long. Both the vertical walls and the bottom of the basin were constructed of marine plywood, 1.91 cm (3/4 in) for the sides, and 2.54 cm (1 in) for the bottom. The floor of the basin was raised 25.4 cm (10 in) above the floor of the laboratory on a substructure of wood sills and joists. The substructure was built mainly to allow for proper levelling of the basin floor. In order to ensure water tightness and to provide a level bottom, a layer of polyester resin approximately 0.64 cm (1/4 in) thick was poured onto the basin floor. The resulting bottom was horizontal to within $\pm 0.05$ cm (0.02 in) . For additional details of the construction of this basin see Raichlen (1965).

Also shown in Figs. 4.1.1, 4.1.2, and 4.1.3 are wave energy absorbers along the two sides of the basin. They were built to help simulate the open ocean by partially absorbing the waves which radiated from the harbour entrance out into the basin. Each absorber was 46 cm high, 60 cm thick, 9.15 m long, and was constructed of 50 layers of fiberglass window screen cloth. The screens were composed of 18 wires per inch in one direction and 16 wires per inch in the other direction, with a

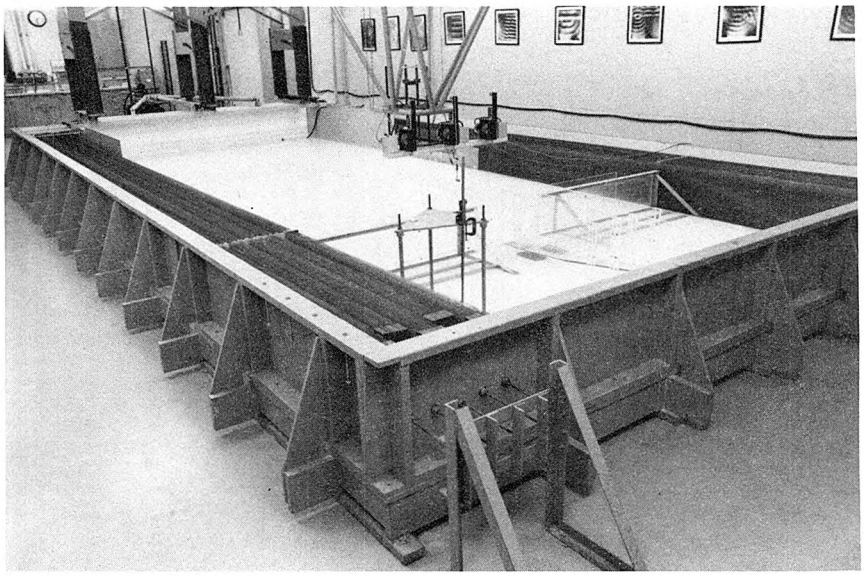

Fig. 4.1.1 Overall view of the wave basin. The wave generator at the left end in this view and the model harbour is at the right end.

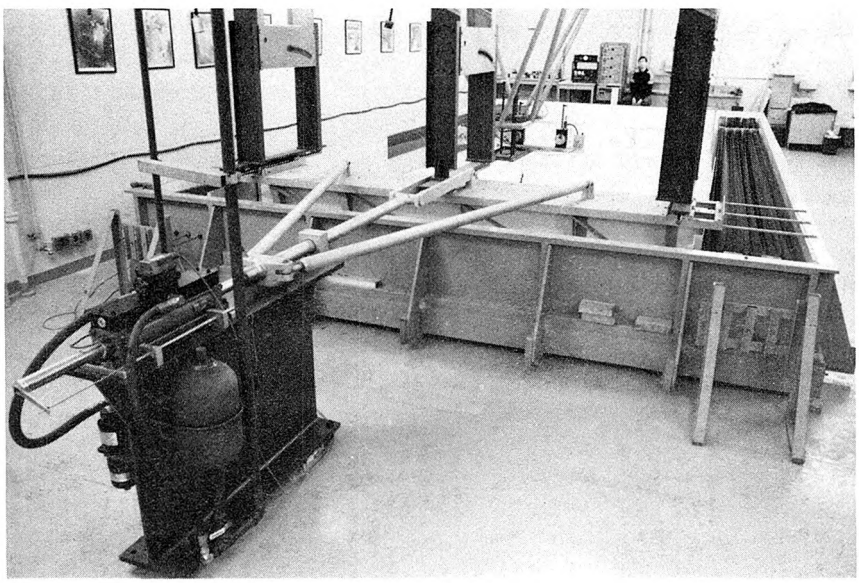

Fig. 4.1.2 Overall view of the wave generator and wave basin.

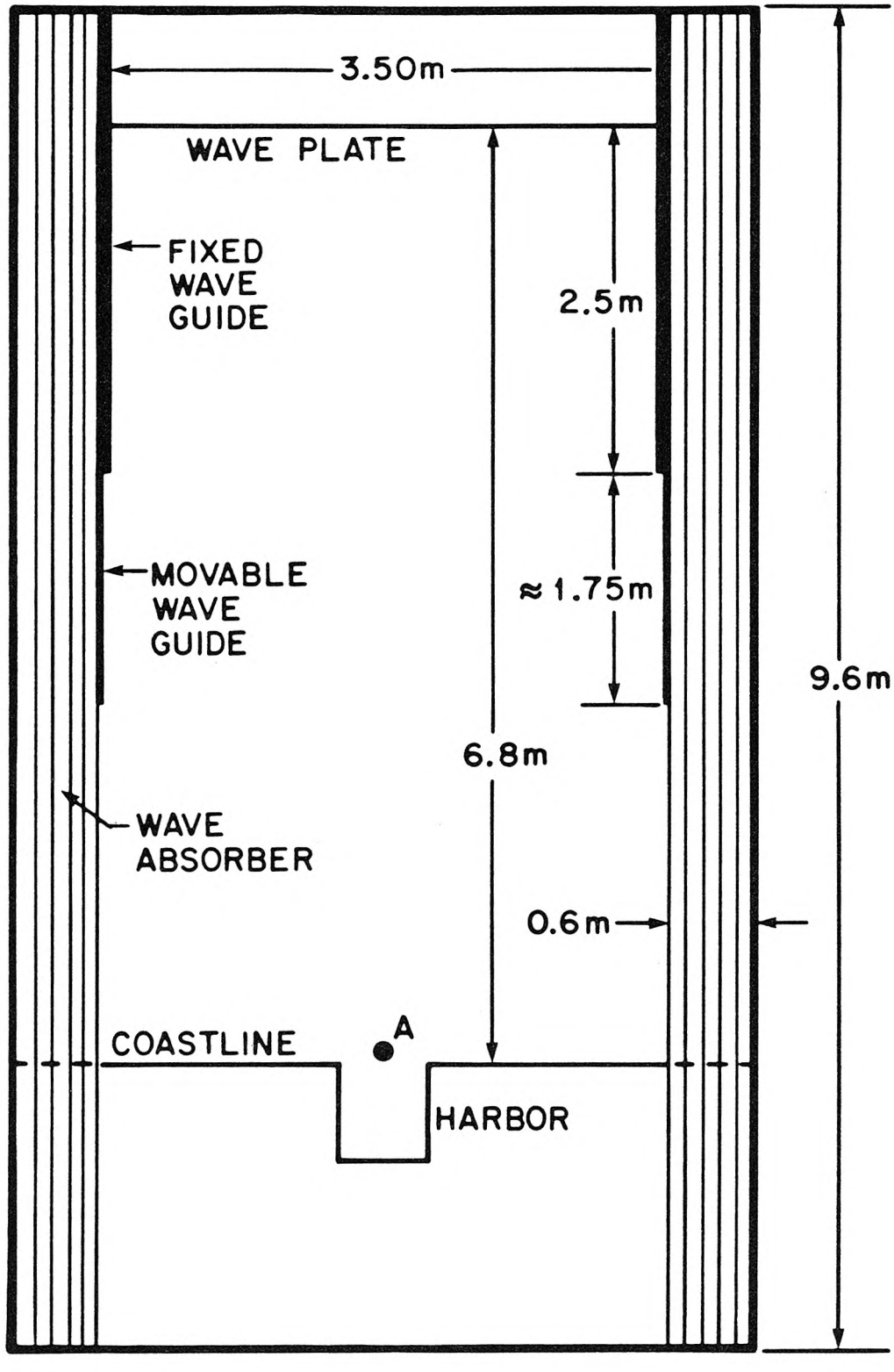


Fig. 4.1.3 Schematic figure of the wave basin and the experimental setup.

wire diameter of 0.3 mm. Both absorbers consisted of five identical units mounted adjacent to each other. Each unit consisted of ten screens spaced 0.95 cm (3/8 in) apart, held together by brackets at each end. They were stretched taut by 0.95 cm (3/8 in) diameter stainless steel rods connected to the brackets and to a structural frame located outside the basin. The rods passed through "O"-ring seals mounted in the walls to prevent leakage.

For the class of waves of interest to this investigation (wavelength $\sim$ 1.5 m, water depth $\sim$ 7 cm), the reflection coefficient for these wave absorbers was estimated to be between 30% and 60% (Lepelletier 1980). This is rather large, and it reflects the difficulty of constructing an efficient long wave absorber that can fit in a small experimental wave basin. However, only a small fraction of the energy radiated from the harbour entrance returned to the harbour before the main reflections return from the wave plate itself. Therefore, simulation of the open sea condition for this investigation was limited by the distance from the wave plate to the harbour, relative to the wavelength of the waves generated, not by the efficiency of the lateral wave absorbers. The experimental conditions used for this investigation limited the simulation of the open sea to approximately eight incident wavelengths.

## 4.2 The Wave Generator

The wave generator used for this study consisted of a vertical plate, driven horizontally by a servo-controlled hydraulic system. The plate motion could be specified in an arbitrary fashion by a microcomputer. The description of this wave generator will be divided into four parts: the wave plate and carriage, the hydraulic system, the servo system, and the microcomputer. The descriptions of the wave plate and support structure, the hydraulics system, and the servo system will be

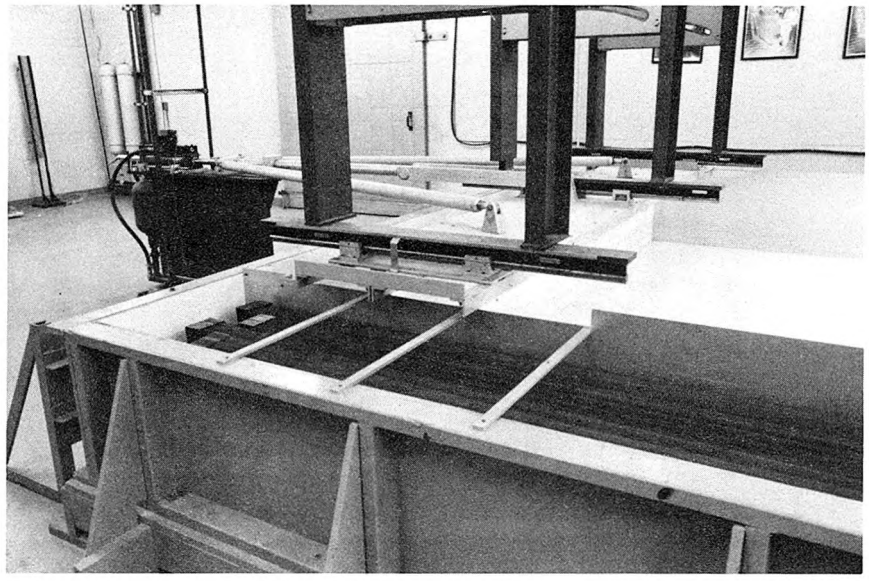

Fig. 4.2.1 View of the wave plate and support structure.

abbreviated since they have been documented elsewhere (Goring 1978, Lepelletier 1980). The microcomputer was designed specifically for this study, so it will be described in somewhat greater detail. However, for a thorough description of the design and operation of the microcomputer the reader is referred to Zelt (1986).

### 4.2.1 The Wave Plate and Carriage

Photographs of the wave plate, overhead support and carriage are shown in Figs. 4.1.1, 4.1.2, and 4.2.1. The vertical wave generating surface was an aluminum plate 3.60 m wide, 61 cm high, and 0.64 cm (1/4 in) thick. In order

to increase its stiffness, it was attached to a structural aluminum angle frame. This assembly was suspended from an overhead structure by three pairs of linear ball bushings which travelled on 3.18 cm diameter (1-1/4 in) hardened steel rails. As seen in Fig. 4.2.1, each rail was connected to two vertical channels which were fastened to the overhead structure using slotted holes to allow for vertical alignment of the rails. The overhead structure was in turn fastened to a reinforced concrete ceiling beam.

The wave plate travelled between two aluminum guide walls 60 cm high, 3.30 m long, and 0.95 cm (3/8 in) thick which were aligned parallel to the side-walls of the basin between the wave absorbers and the wave plate. These guide walls can be seen in Figs. 4.1.1, 4.2.1 and, schematically, in Fig. 4.1.3. One end of each guide plate was connected to the backwall of the basin and each plate was held vertical by three braces from the top of the plate to the sidewall of the basin. To reduce diffraction effects around the ends of the wave guides, they were extended 1.75 m with movable vertical walls constructed from 16 gauge galvanized iron. Lepelletier (1980) reported that such an arrangement improved the quality of the incident wave at the harbour entrance without significantly altering the open sea characteristics of the wave basin. To avoid problems of leakage around the wave plate, it was sealed against the guide walls and the bottom of the of the wave basin by rubber windshield wiper blades. The mounting arrangement for the wiper blades is shown in Fig. 4.2.2. It consisted of two identical aluminum bars with grooves cut out to accept the body of the wiper blade. The blade is held in place by bolting the two bars together tightly.

As seen in Fig. 4.1.2, the wave plate assembly was connected to the rod of the hydraulic cylinder by three arms made of aluminum tube 6.35 cm (2-1/2 in) in diameter with a wall thickness of 3.18 mm (1/8 in). As a safety precaution to guard against a malfunction of the servo-hydraulic system, the cylinder rod was

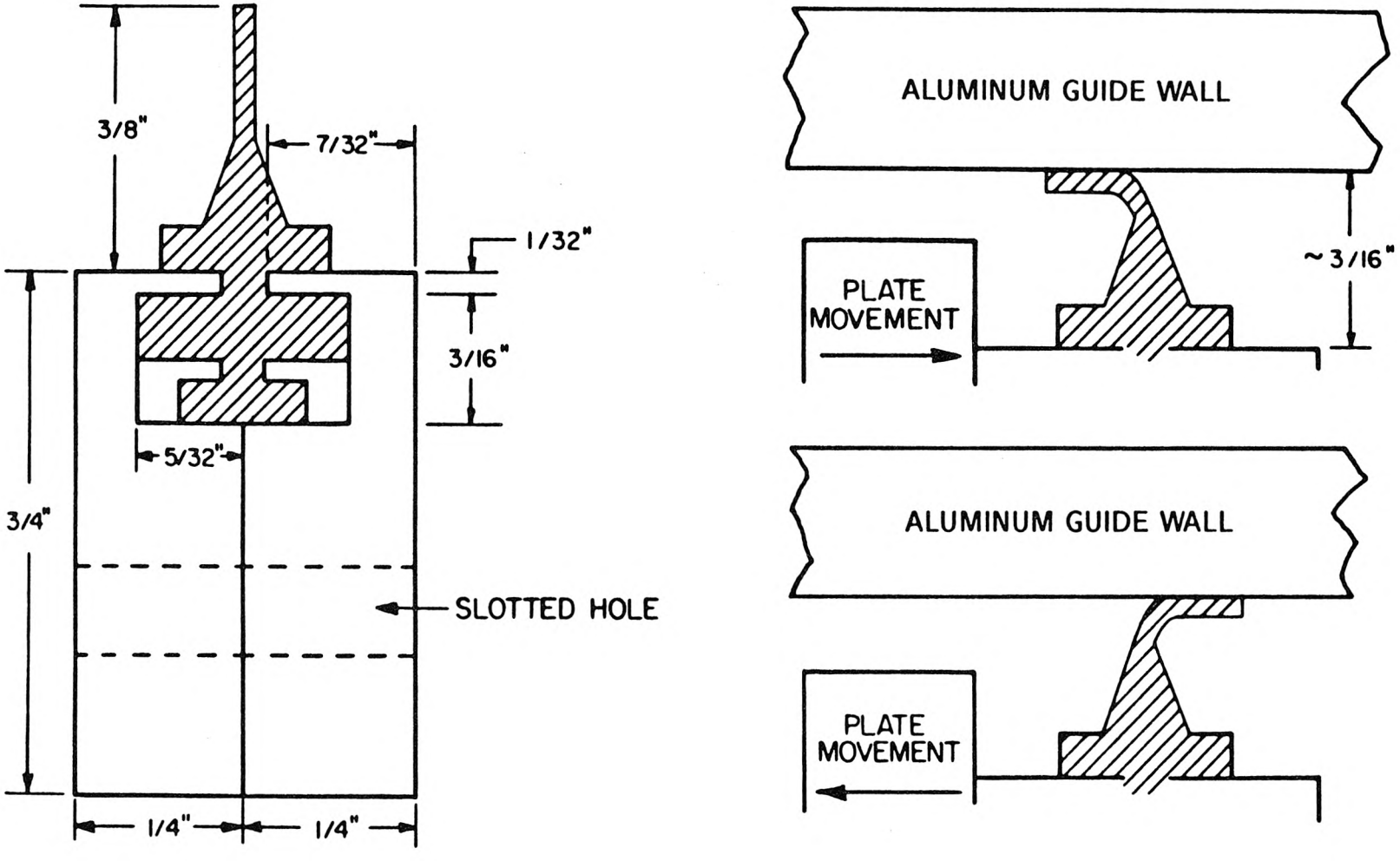


Fig. 4.2.2 Wiper blade and holder (after Goring, 1978).

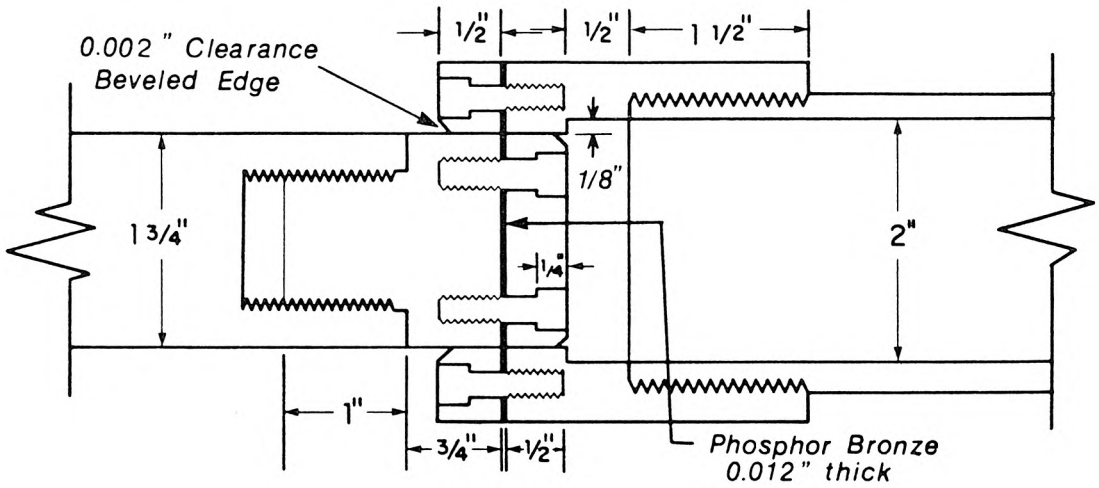


Fig. 4.2.3 Drawing of the safety device connecting the hydraulic cylinder rod to the drive arm assemby (after Lepelletier, 1980).

connected to the drive arm assembly via a safety device designed to rupture if it was subjected to excessive force. A drawing of this device is shown in Fig. 4.2.3. The connection was made using a shear plate 0.03 cm (0.012 in) thick, made of Phosphor Bronze, which was designed to break if the shear load exceeded 13300 N (3000 lb). This was the maximum load which could be taken safely by the ball bearing and plate assembly. If the shear plate ruptured under an excessive load, the cylinder rod could slide freely inside the central arm. The shear plate did not rupture during this study.

### 4.2.2 The Hydraulic System

The hydraulic system is shown schematically in Fig. 4.2.4. The main

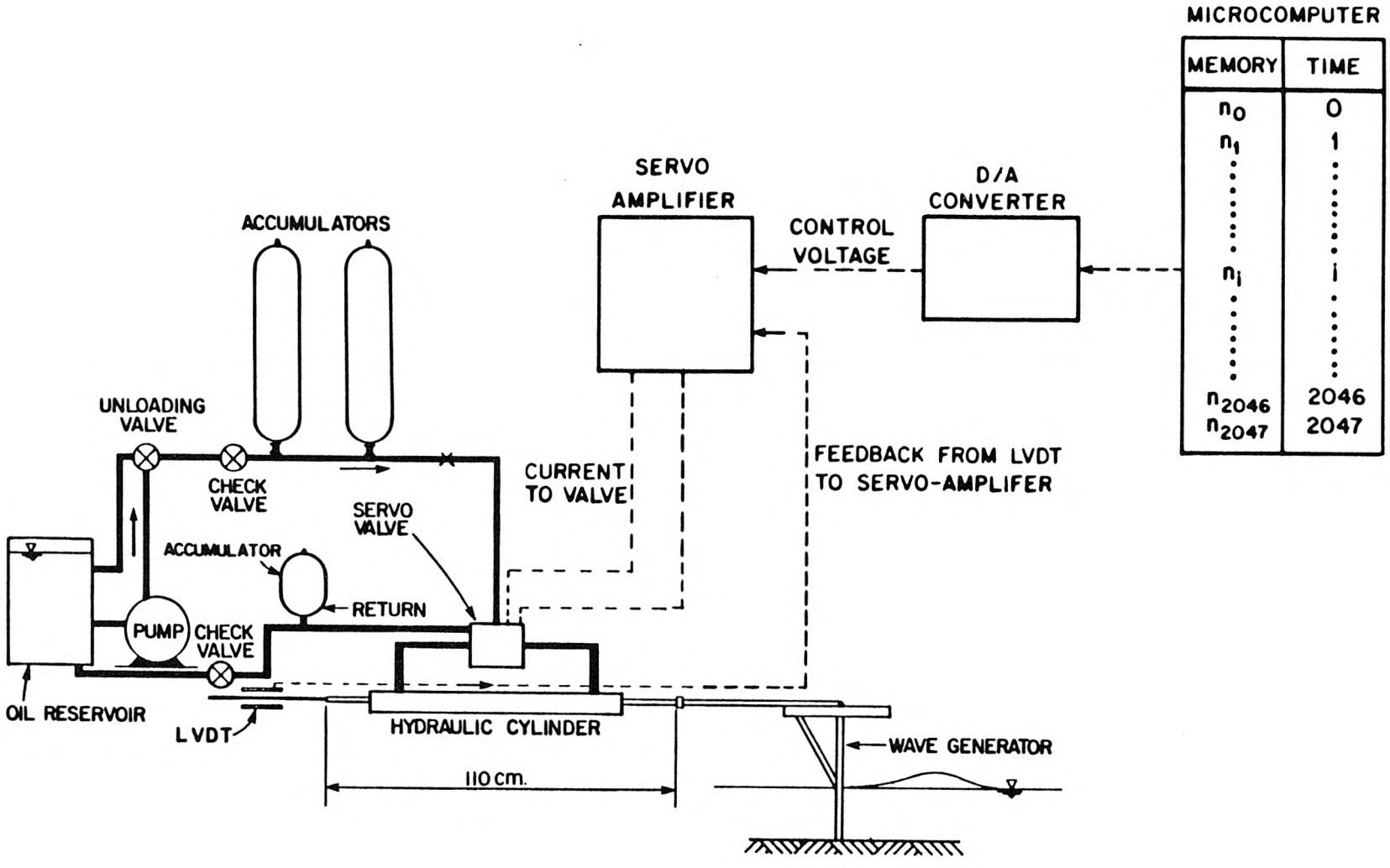


Fig. 4.2.4 Schematic drawing of the hydraulic system (modified from Goring, 1978).

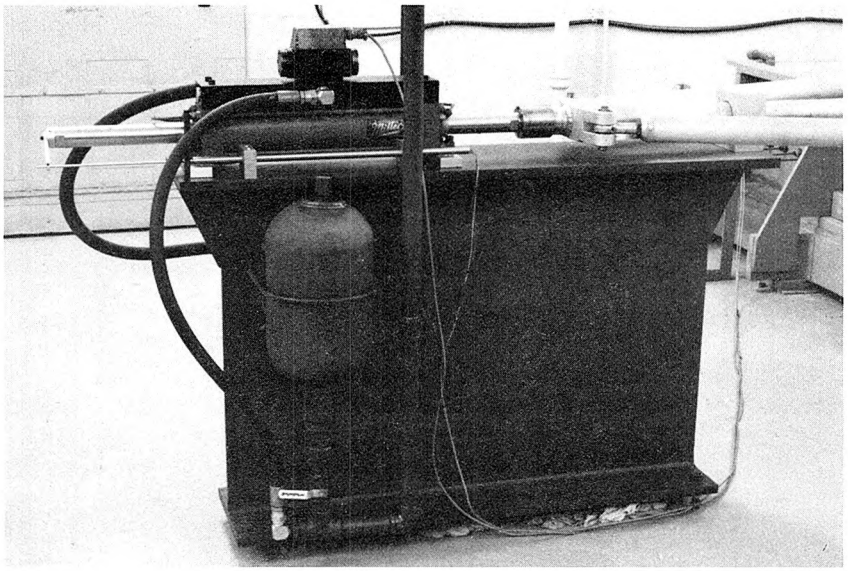

Fig. 4.2.5 View of the hydraulic system showing the LVDT and the small accumulator.

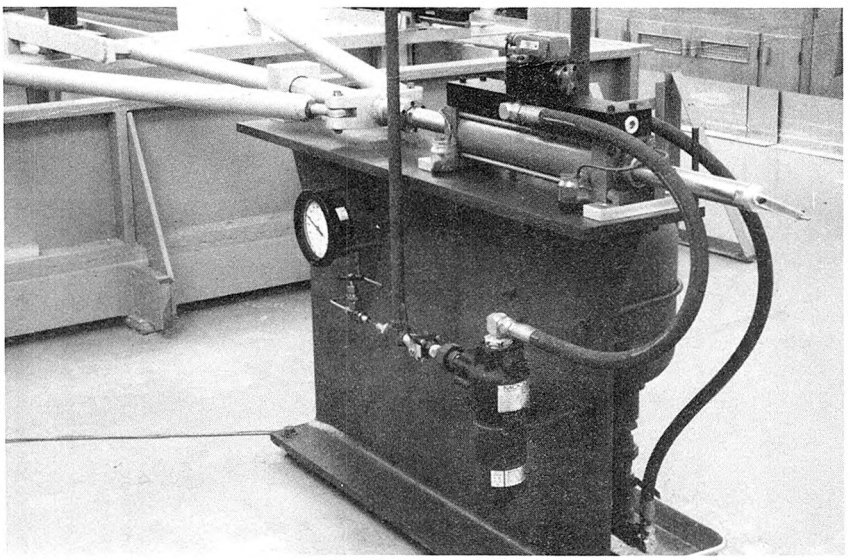

Fig. 4.2.6 View of the hydraulic system showing the filter and the pressure gauge.

components in the system were an oil reservoir, a pump, two accumulators, a servo valve, and a hydraulic cylinder. The reservoir had a capacity of 151 litres of hydraulic oil. The pump, used to fill the accumulators with oil, was a Denison constant volume, axial-piston-type pump, rated at 11 litres/min at a pressure of approximately 20.7 MPa (3000 psi). It was powered by a 5.6 kW (7.5 hp) 1800 rpm electric motor. Immediately downstream of the pump was a filter with a nominal particle diameter rating of 10 $\mu$m, followed by an unloading valve and then a check valve. The unloading valve directed the flow of oil back into the reservoir if the pressure exceeded a preset value of 17.2 MPa (2500 psi). The check valve prevented a reverse flow through the pump from the pressurized system when power to the pump was turned off. The pump supplied oil to two 37.9 litre accumulators which were precharged to 3.1 MPa (450 psi) with nitrogen gas bladders. Their maximum rated operating pressure was 20.7 MPa (3000 psi). The pressurized oil was supplied to the hydraulic cylinder by a servo valve (Moog Model 71-103) with a rated flow of 227 litres/min when supplied with 40 ma of current from the servo amplifier. The double ended hydraulic cylinder had a 10.2 cm (4 in) bore within which travelled a 4.45 cm (1-3/4 in) diameter rod with a 40.6 cm (16 in) stroke. Immediately downstream of the servo valve, a small 5.7 litre accumulator was installed to reduce pressure fluctuations caused by rapid changes of the flow rate through the servo valve. Finally, a check valve, which opened at 97 kPa (14 psi) was placed just before the reservoir to keep the return line full of oil.

The hydraulic supply system and pump were located one floor below the wave basin. As a result, the accumulators and the hydraulic cylinder which drove the wave plate were about 5 m above the oil reservoir and pump. The hydraulic cylinder and rod can be seen in Figs. 4.2.5 and 4.2.6. The servo valve, with its electrical connection to the servo amplifier, is the object seen located on top of the cylinder. The small accumulator can be seen in Fig. 4.2.5.

### 4.2.3 The Servo System

The servo system controlled the flow of the oil to the hydraulic cylinder and, hence, the generation of waves with the wave plate. The system consisted of a servo amplifier and a linear feedback device. The feedback device generated a voltage proportional to the instantaneous position of the wave plate carriage. The microcomputer supplied an accurate time varying analog control voltage to the servo amplifier. This voltage defined the motion of the wave plate in the following way. The voltage from the feedback device and from the microcomputer were of opposite signs and were added together by the servo amplifier to give an "error" voltage. The servo amplifier amplified this error signal and then supplied a current proportional to it to the servo valve. This current controlled the flow of hydraulic oil to the hydraulic cylinder, and, thus, the velocity of the hydraulic piston and wave plate carriage. Since the feedback loop was very stable, the gain of the servo amplifier could be adjusted to be large enough so that the instantaneous position of the wave plate was almost directly proportional to the instantaneous control voltage supplied by the microcomputer to the servo amplifier. In reality, the gain must be kept finite, and for this reason the instantaneous position of the wave plate cannot be *exactly* proportional to an arbitrary input control voltage. However, for the range of wave plate velocities and accelerations needed to generate waves for this investigation, the errors were very small. By iteratively adjusting the input control voltage to account for the finite response time of the servo system, these errors could have been eliminated. However, this was not necessary because the waves generated with this system were measured with a wave gauge and this *measured* wave was used in all the analysis, not the *theoretical* wave which would have been generated, assuming the servo system had a perfect response. The servo amplifier can be seen above the microcomputer on the left in Fig. 4.2.7.


Fig. 4.2.7 Servo amplifier and microcomputer (left), and Sanborn recorder (right).

The feedback device used was an LVDT (Linearly Variable Differential Transformer), Collins Model LMT 711 P38, shown in Fig. 4.2.5 along the side of the hydraulic cylinder. The LVDT generated a current directly proportional to the position of the wave carriage. It consisted of a primary and a secondary coil wound in the form of a tube inside which a ferro-magnetic core moved. The primary coil was supplied with 6 VAC from the servo amplifier unit and the output of the secondary coil was returned to the servo amplifier where it was demodulated into a direct current signal. The core was attached directly to the hydraulic piston rod. Hence, as the piston moved, the core moved within the coils and the demodulated signal from the secondary coil varied linearly with the position of the wave plate carriage.

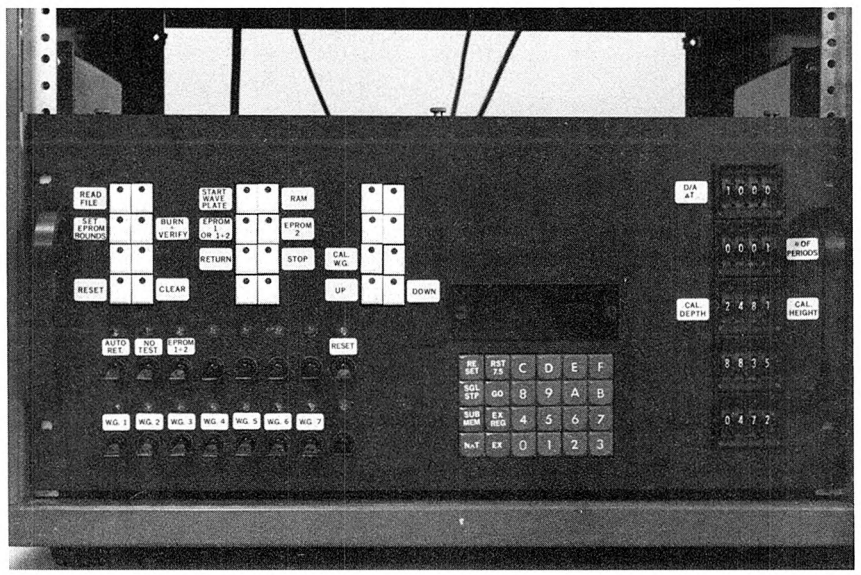


Fig. 4.2.8 The microcomputer.

### 4.2.4 The Microcomputer

The microcomputer is the central control unit of the wave generator. The microcomputer generates the analog control voltage supplied to the servo amplifier, which determines the motion of the wave plate carriage. The trajectory (i.e., the position as a function of time) of the wave plate is stored in the memory of the microcomputer and this information is sent to the servo amplifier in real time with the use of a Digital to Analog (D/A) converter. A photograph of this unit is shown in Fig. 4.2.8 (it can also be seen in Fig. 4.2.7). Information and commands from the user are entered through the front panel of the unit via the switches and the keyboard shown in this figure. The microcomputer consists of seven main hardware units, which communicate over a 72-line system bus. Each of these units

will be described separately. There is a Central Processing Unit (CPU) board, memory board, programmable Input/Output (I/O) board, programmable interrupt controller and timer board, Digital to Analog (D/A) converter board, and an Erasable Programmable Read-Only Memory (EPROM) programmer board. Each of these units was constructed on wire wrap circuit boards which plugged directly into the system bus. There is also a wire wrapped keyboard/display unit, which communicates to the CPU over the system bus, although it is physically interfaced directly to the CPU board. A block diagram of the microcomputer is shown in Fig. 4.2.9. All of the hardware is managed by a monitor and a control program, which will be discussed following the descriptions of the hardware units.

#### 4.2.4.1 Central Processing Unit

The CPU was adapted from an existing design (Nosenchuck, 1982). It is the only bus master in the microcomputer (the only device capable of initiating bus cycles). It performs all memory and I/O data transfers, instruction and data processing, and interrupt handling. The CPU is constructed from an Intel 8085A microprocessor, 4 kbytes of 2716 EPROM, an Intel 8155 2048-bit static Random Access Memory (RAM) with I/O ports and timer chip, and various logic gates, latches, bus drivers, and bus transceivers.

The 8085A is an 8-bit data, 16-bit address microprocessor and is run with a clock speed of 2 MHz. The 8085A transfers data over an 8-bit bidirectional 3-state bus which is time multiplexed with the 8 low-order address bits. Eight additional high-order dedicated address bits complete the 16-bit address bus. The 8085A can therefore directly address up to 64 kbytes of memory. The 8085A has twelve addressable 8-bit registers. Four of them can function only as two 16-bit register pairs (stack pointer and program counter). Six others can be used interchangeably

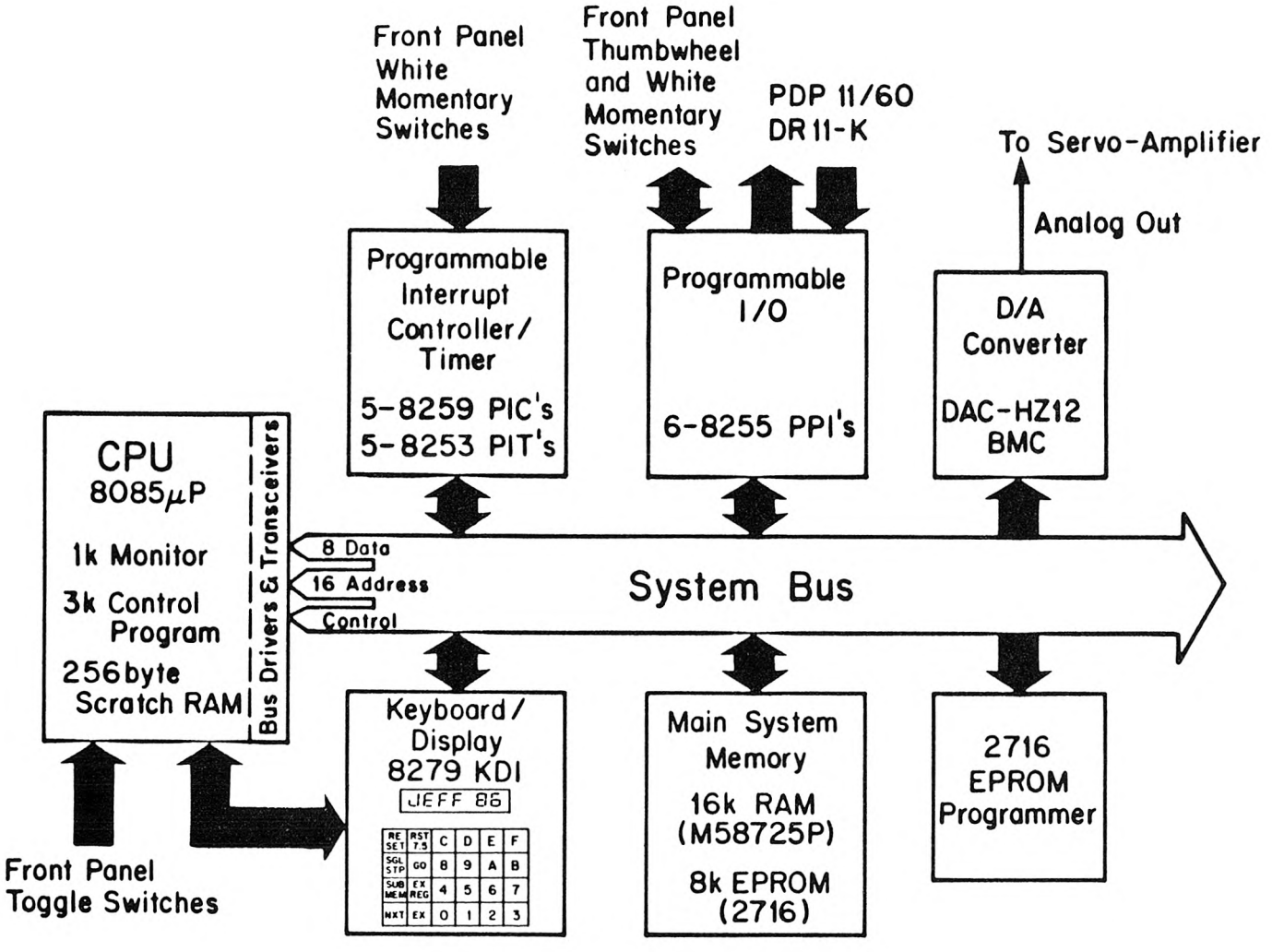


Fig. 4.2.9 Block diagram of the microcomputer.

as 8-bit registers or as 16- bit register pairs. There is also an 8-bit accumulator and a flag register.

The 8085A has five interrupt inputs which from the lowest to the highest priority are: INTR, RST 5.5, RST 6.5, RST 7.5, and TRAP. When either of the interrupts RST 5.5, 6.5, 7.5, or TRAP is recognized, program execution is transferred to fixed low memory addresses. The TRAP interrupt is used for single step program execution from the keyboard/display interface. The RST 7.5 interrupt is directly wired to the key [RST 7.5] (see Fig. 4.2.8) on the front keyboard and is used to transfer program execution to the monitor from the software routine which the microcomputer executes while waiting for commands from the bank of white momentary switches. The RST 6.5 interrupt is not used. The RST 5.5 interrupt is used by the keyboard/display interface to interrupt the CPU when a key closure from the keyboard is detected. The INTR interrupt is very different from the other interrupts. When action is requested by pressing one of the 24 white momentary switches, an INTR interrupt is requested by the programmable interrupt controller. When it is recognized by the 8085A, the interrupt controller then places a call instruction and then a two-byte address onto the bus. When this instruction is executed by the 8085A, program execution is then transferred to the particular software routine located at that address to provide the specified action. Hence, pressing one of the white switches will normally cause program execution to transfer to a corresponding software service routine. The actual process is somewhat more complicated and will be explained more fully when the operation of the interrupt controller is covered.

Four kbytes of 2716 EPROM are provided at memory locations 0000 H to 0FFF H (H $\leftrightarrow$ Hexadecimal). It is used to store the software which controls the operation of the microcomputer. The first one kbyte (0000 H to 03FF H) contains a monitor program that contains utility routines to perform many simple operations

such as front panel keyboard/display scanning and single step program execution. It also allows the user to examine and modify memory locations and 8085A internal registers. The final three kbytes of EPROM are used to store the software which the microcomputer executes to perform each of its specialized tasks after one of the white switches is pressed. This software will be discussed later after all of the hardware has been described.

The 8085A is also connected to an 8155 chip which contains 256 bytes of RAM (address locations from 2000 H to 20FF H), three general purpose I/O ports (with port numbers 21 H, 22 H and 23 H), and a 14-bit programmable counter/timer. The RAM is used for scratchpad memory and various other purposes such as storing default values for quantities which may be modified by the user. The 8-bit I/O ports 21 H and 22 H are used to read the status of the 16 toggle switches. Each of the switches form one bit of an 8-bit byte. I/O port 23 H is not used in the present configuration. The programmable timer/counter is used by the monitor for the single step routine to interrupt the processor following the execution of each instruction.

Apart from the chip select decoder circuitry the rest of the CPU board contains system bus interface circuitry. All of the devices on the system bus require a demultiplexed address bus. Therefore, an Intel 8212 I/O port is used to latch the lower eight bits of the address/data bus from the 8085A when the Address Latch Enable (ALE) is asserted by the 8085A. The high-order address byte is buffered by an 8212. The data lines and the 8085A control signals are buffered by Intel 8216 bidirectional bus transceivers before being sent to the system bus.

#### 4.2.4.2 Keyboard and Display

The keyboard/display unit is a single board mounted on the front

panel of the microcomputer and contains a 24-key keyboard, a six-digit general purpose hexadecimal LED display, plus the keyboard/display scanning and driving circuitry. It was built from an existing design (Nosenchuck, 1982). It interfaces directly with the CPU board.

The keyboard is comprised of 16 hexadecimal data entry keys and 8 command keys. Two of the command keys, [RESET], and [RST 7.5] (see Fig. 4.2.8) are connected directly to the CPU (after passive debouncing). The other keys are scanned for key closure by an Intel 8279 programmable Keyboard/Display Interface (KDI) chip.

The keyboard is arranged in three logical rows and eight columns (the last row has only six columns due to the hard connection, directly to the CPU, of the two keys just mentioned). The 8279 KDI generates row scan signals with a 3-to-8 line decoder (74LS156). When a key closure (debounced by the KDI) is detected by one of the eight column return lines, the KDI interrupts the 8085A via the RST 5.5 interrupt. The code of the detected key is passed to the 8085A during the keyboard interrupt service routine stored in the monitor. The monitor program then decides what action to take, based on which key was struck.

The 8279 KDI is also used to output hexadecimal information to a 6-digit 7-segment LED display. Data are multiplexed to the LED display digits via two 4-bit KDI ports. The output ports are synchronized to the decoded line scan signals (shared by the keyboard), which are used to multiplex the 7-segment display data to the individual LED displays. The 6-digit hexadecimal display can be used to display memory addresses, the data stored at these locations, and the contents of the 8085A internal registers.

#### 4.2.4.3 Memory

The memory board contains sixteen kbytes of M58725P static RAM (memory locations 4000 H to 7FFF H) and eight kbytes of EPROM (memory locations D000 H to EFFF H). The EPROM consists of four 2716 chips mounted in zero insertion force sockets to facilitate entry and removal. In the present configuration the two EPROM's at memory locations E000 H–E7FF H and E800 H–EFFF H can be used to store two separate 1024-point wave plate trajectories or a single 2048-point trajectory. The RAM can also be used to store a wave plate trajectory of up to 8192 points. The trajectory is computed on the W.M. Keck Laboratory PDP 11/24 or PDP 11/60 computer and then sent to the microcomputer unit from the PDP 11/60 (or any other computer with a DR11–K compatible parallel interface), where it is placed in RAM. This transmission process will be described later. After the trajectory is placed in RAM, it can be used to control the motion of the wave plate. When the power to the microcomputer is switched off, this trajectory is lost. However, if this trajectory is needed for future use, the EPROM programmer can be used to burn the trajectory into one or more 2716 EPROM's, which can then be placed into the zero insertion force sockets for later use.

#### 4.2.4.4 Programmable Input/Output Unit

The programmable I/O board performs most of the digital input and output to and from the microcomputer. The board holds six 8255A Programmable Peripheral Interfaces (PPI's) which will be denoted PPI 1 to PPI 6. Each contains 24 programmable I/O pins which can be software configured to operate in a number of different modes, usually as three groups of 8-bit memory mapped I/O ports denoted as ports A, B and C.

The I/O pins of PPI 1, PPI 2, PPI 3, and port C of PPI 6 are all configured as

8-bit input ports to read the status of the thumbwheel switches seen on the right side of the microcomputer in Fig. 4.2.8. The data from the thumbwheel switches are read in BCD so that each 8-bit port is capable of reading two decimal digits from the thumbwheel switches. The flashing lights on the 24 white momentary switches are fully software controlled. The 24 I/O pins of PPI 4 are configured in three 8-bit output ports where each bit is used to enable or disable the flashing of one of these lights.

PPI 5 and sixteen of the I/O pins of PPI 6 are used to transfer data between the microcomputer and the laboratory PDP 11/60 computer. With the addition of some circuitry external to the PPI's on the programmable I/O board, the microcomputer is interfaced directly to the PDP 11/60 computer through its existing DR11-K parallel interface. This allows 16-bit words to be transferred either from the microcomputer to the PDP 11/60 or from the PDP 11/60 to the microcomputer over separate parallel lines. Data transfer is performed asynchronously, using handshaking signals. For each data transfer from the PDP 11/60 to the microcomputer the following sequence of events occurs. A 16-bit data word is placed on the output lines of the DR11-K. When the voltages on these lines have stabilized, the DR11-K issues an Internal Low Data Ready signal in the form of a zero voltage pulse lasting for a duration of no greater than $0.5\,\mu s$, which tells the microcomputer that a word is present to be read. When this handshake signal is received by the programmable I/O board, it is used to latch the lower 8 bits of the word by an 8212 I/O port and also to trigger a one-shot multivibrator, which is wired directly to the $\overline{STB}_A$ input of PPI 5. This strobes the higher 8 bits of the word into the input latch of port A of PPI 5 and also causes PPI 5 to assert the $IBF_A$ (Input Buffer Full) line and the $INTR_A$ (interrupt request) line. The $INTR_A$ signal is sent to the programmable interrupt controller and timer board via the IRA line of the main system bus. This causes an interrupt request to be

issued to the CPU, whereupon execution is vectored to an interrupt service routine which reads and stores the word that is being transferred from the DR11-K. The lower 8 bits of the word are read from the 8212 I/O port by port A of PPI 6, and the higher 8 bits (which were latched into port A of PPI 5 by the $\overline{STB}_A$ signal) are read by port A of PPI 5. Meanwhile, the $IBF_A$ signal is used to trigger a one-shot multivibrator to send out a short voltage pulse on the External Data Accepted line of the DR11-K. This signals the DR11-K that the word being sent to the microcomputer has been captured. The DR11-K is then free to output the next word, completing the cycle.

Data are transferred from the microcomputer to the DR11-K in a similar way. For each 16-bit word transferred from the microcomputer to the PDP 11/60, the following sequence of events occurs. When the previous word sent to the PDP 11/60 has been accepted by the DR11-K, it issues a pulse of zero voltage on its Internal Data Accepted line lasting for at least $5\,\mu s$. This signal tells the microcomputer that it is free to send the next word of data. When this signal is received by PPI 5, it asserts the $INTR_B$ line. This signal is sent to the programmable interrupt controller and timer board via the IRB line of the main system bus. This causes an interrupt request to be issued to the CPU. Execution is then transferred to an interrupt service routine which outputs the next word to be sent to the PDP 11/60. The low-order 8-bit byte is written out to port B of PPI 6. The high-order 8-bit byte is then written out to port B of PPI 5. This causes the voltage to go low on the $\overline{OBF}_B$ (Output Buffer Full) line of PPI 5. This transition triggers a one-shot multivibrator which sends a zero voltage pulse to the External Data Ready input of the DR11-K to inform the DR11-K that there is a word present to be read. After the DR11-K reads this word, it issues a low voltage pulse on its Internal Data Accepted line, completing the cycle.

As just mentioned, the $INTR_A$ and $INTR_B$ signals are used to generate

interrupts to transfer execution to service routines to read or write data words from or to the PDP 11/60. These signals are not sent directly to an 8259 programmable interrupt controller but to an 8253 programmable interval timer, which delays the signals to the 8259 for approximately 1 ms. This slows the data transfer rate between the microcomputer and the PDP 11/60, so that the resources of the PDP 11/60 will not be monopolized by the microcomputer when data transfers are being made. However, it still allows a data transfer rate of approximately one thousand 16-bit words per second.

#### 4.2.4.5 Programmable Interrupt Controller and Timer Unit

This board is used to coordinate all of the CPU interrupt requests via the INTR line of the main system bus and to provide all of the hardware timing control signals apart from the system clock signal CLK. The timing is performed by five 8253 Programmable Interval Timers (PIT's). Each timer contains three independent general purpose 16-bit counters, each of whose modes of operation are software programmable. These timers are used to generate interrupt requests to the interrupt controller in order to:

1) output a word to the D/A converter to control the motion of the wave plate

2) return the wave plate to its initial position in the auto-return mode

3) read a word from and write a word to the lab PDP 11/60 computer

4) program a byte of data into a 2716 EPROM by the EPROM programmer

Several of the timers are not used at the present and so may be dedicated for future uses.

Interrupt requests are handled by five 8259 Programmable Interrupt Controllers (PIC's). One PIC is used as a master, leaving four cascaded slave controllers. An interrupt initiated through these controllers is used to transfer program execution to one of the service routines in the main control program. The sequence of events to accomplish this is as follows:

1. One of the Interrupt Request lines (IR0–IR7) of a slave controller is raised high. As the names of these lines suggest, this is done when an interrupt is necessary to transfer execution to one of the service routines.

2. If this interrupt has not been masked (disabled), the slave then sends an INT to the master controller, which in turn sends an INT to the CPU via the INTR line of the main system bus. This tells the CPU that an interrupt is being requested.

3. As soon as the CPU can service this request, it responds with an $\overline{\text{INTA}}$ (INTerrupt Acknowledge) pulse.

4. Upon receiving the $\overline{\text{INTA}}$ from the CPU, the master controller releases a CALL instruction code (11001101) onto the 8-bit data bus.

5. This CALL instruction initiates two more $\overline{\text{INTA}}$ pulses from the CPU.

6. These two $\overline{\text{INTA}}$ pulses enable the slave controller that is requesting the interrupt to release a preprogrammed subroutine address (corresponding to the service routine) onto the data bus. The lower 8 bits of the address are released at the first $\overline{\text{INTA}}$ pulse, and the higher 8 bits of the address are released at the second $\overline{\text{INTA}}$ pulse.

7. The CALL instruction is executed and program execution is transferred to the specified service routine.

All of the interrupts are assigned a priority. Hence, two or more interrupt requests can occur simultaneously. The highest priority interrupt is acknowledged first, then the next highest, etc.

This approach to executing the service routines allows more than one operation to be performed "simultaneously" by the microcomputer. The microcomputer, of course, can execute only one program at any instant in time but by using the interrupt controller, the CPU can quickly jump between different interrupt service routines and *appear* to be performing more than one job simultaneously.

#### 4.2.4.6 Analog Output

The position of the wave plate is determined by the analog voltage supplied to the input of the servo amplifier. In order to convert the digital representation of the wave plate trajectory stored in the memory of the microcomputer to an analog signal, a 12-bit D/A converter is used. An 8255A PPI is used to provide the digital input to a DAC-HZ12BMC D/A converter manufactured by Datel-Intersil. Port A and the upper four bits of Port C of the PPI are used to output the 12 bits of data each time the D/A output interrupt service routine is executed. For a typical wave plate trajectory, a new voltage is output every 0.5–2 ms, depending on the number of points in the trajectory and the duration or period of the wave plate motion.

#### 4.2.4.7 EPROM Programmer

A wave plate trajectory or a portion of executable code can be programmed into one or more 2716 EPROM's using the EPROM programmer board. Apart from a small amount of support circuitry this board contains an 8255A PPI connected to a zero insertion force socket. The three ports on the 8255A are

used to output the address, data, and control signals necessary to program a 2716 EPROM placed in the zero insertion force socket.

#### 4.2.4.8 Control Software

There are two separate software packages that run on the microcomputer. The first package is a one kbyte monitor program. The monitor is a collection of utility routines used to perform many simple operations such as front panel keyboard/display scanning and single step program execution. It also allows memory locations and 8085A internal registers to be examined and modified. Since this software is not central to the use of the microcomputer as a wave maker controller, and because its operation is transparent to the user, it will not be described in detail here. The second package is the wave generator control program. It consists of numerous service routines that coordinate the hardware units throughout the various operations associated with the wave generation process. This software will be described briefly in this section.

When power to the microcomputer is switched on via the line switch at the rear of the unit, a hardware reset occurs and program execution is transferred to location 0000 H in the monitor program. The monitor performs several initialization operations and then transfers execution to the wave generator control program at location (address) 0400 H. This portion of the control program initializes and programs the 8259 programmable interrupt controllers, the 8255A programmable peripheral interfaces, the 8155 RAM;I/O;timer, and the 8253 programmable interval timers for subsequent use. The user need not be aware of the many operations in this procedure since it is all done automatically when the unit is powered up. After the microcomputer has been successfully started up it then executes a four step endless loop starting at locations 0614 H. This is the code that the micro-

computer executes when not performing any other special tasks. When the CPU receives an interrupt request, control is transferred to the appropriate interrupt service routine. After this routine is executed, program execution returns to this endless loop.

The control program, that includes software to allow a file containing a wave plate trajectory, can be transferred from the lab PDP 11/60 computer to the microcomputer. This operation is initiated when the white button READ FILE is pressed on the front panel of the microcomputer (see Fig. 4.2.8). The appropriate interrupts to enable the data transfers are then unmasked, and execution is returned to the endless loop. Interrupts are then generated approximately every 1 ms to execute the service routine, which reads one word of the file being transferred and then stores it in RAM. This continues until the entire file is received. With sixteen kbytes of RAM, the trajectory can be up to 8192 16-bit words long. After the file is send to the microcomputer, it is then automatically sent back to the PDP 11/60 where it is compared against the copy of the file just sent to the microcomputer to check whether there were any transmission errors.

Software is also provided to allow a wave trajectory or a block of executable code to be programmed into a 2716 EPROM so that it can be retained for future use. For a description of this software, see Zelt (1986).

The bulk of the code in the wave generator control program is dedicated to controlling the motion of the wave plate carriage. A wave plate trajectory is stored in the microcomputer as a sequence of integer numbers (ranging from 0–4095) stored in contiguous memory locations. These numbers are output, in sequence, to the D/A converter in order to supply a time-varying analog control voltage to the servo amplifier (see Fig. 4.2.4). The wave plate trajectory can be stored in either RAM or EPROM. The rate at which these numbers are sent to the D/A converter can be chosen by the user by entering the time interval,

in microseconds, in the thumbwheel switches labelled "D/A $\Delta$T" in Fig. 4.2.8. In addition, the number of wave periods to be generated can be entered in the thumbwheel switches labelled "# OF PERIODS."

The waveplate is set in motion by pressing the white button [START] . Before the motion is actually initiated, the microcomputer performs a test on the selected wave trajectory. Each successive point in the trajectory is checked to see that it does not differ widely from the previous value. In addition, the D/A $\Delta$T value entered in the thumbwheel switches is checked to see that it is not too small. Both of these conditions could cause a violently quick motion of the wave plate carriage, which could damage the wave generator equipment or persons nearby. If either of these conditions is found, the wave plate is not started, the user is informed of the condition via the front panel LED display, and program execution returns to the endless loop to await further instructions. However, if the trajectory is determined to be safe, then a programmable timer/counter is loaded with the D/A $\Delta$T value entered on the thumbwheel switches, the appropriate interrupt which allows data to be written out to the D/A converter is unmasked, and then control is transferred back to the endless loop routine. These tests are performed very quickly so that the user will not notice the slight delay necessary to perform them before the wave plate is started in motion.

The timer/counter then generates interrupt requests to the interrupt controller every "D/A $\Delta$T" microseconds. When each interrupt is serviced, the next word in the wave plate trajectory is written out to the D/A converter. When the last point in the trajectory is reached, it is checked against the first point to check that the two do not differ widely. If they do, then the wave plate is stopped. If they do not, then another period is generated, provided more than one period was requested. Therefore, if the trajectory does not correspond to oscillatory motion, the user need not worry that the wave plate will slam back to its initial position

after it is fully extended, even if the number of periods requested is greater than one. An example of such a trajectory is one that will generate a solitary wave. After the requested number of periods has been generated then the wave plate is stopped.

The motion of the wave plate may be stopped by the user at any time before the requested number of periods has been completed simply by pressing the button STOP . The wave plate will not come to an immediate stop but will complete the present period of motion and stop when it is finished.

If the wave plate motion is not oscillatory (such as the plate motion which generates a solitary wave), then the plate must be returned to its starting point after the wave is generated. This can be done by pressing the button RETURN . The wave plate then slowly ramps back to its initial position. One can also choose to let the microcomputer return the plate automatically. After the wave has been generated, the microcomputer checks to see if the toggle switch labelled "AUTO RET." is turned on. If it is, then a programmable timer/counter is loaded with a predetermined value to provide a delay of approximately 17 seconds. After this time period the wave plate is then automatically returned to its initial position.

## 4.3 The Harbour Model

A lucite harbour model with variable dimensions was used for this investigation. It was rectangular in planform and the still water depth decreased linearly from the entrance to the shoreline, as can be seen in Fig. 4.3.1. A "U" shaped outer frame composed of three lucite walls surrounded the harbour to reinforce the rigidity of the model. The harbour sidewalls consisted of two parallel walls 178 cm long, 44 cm high, and 1.27 cm (1/2 in) thick, connected to the backwall of the outer U-frame. The distance between these side walls could be varied in a continuous

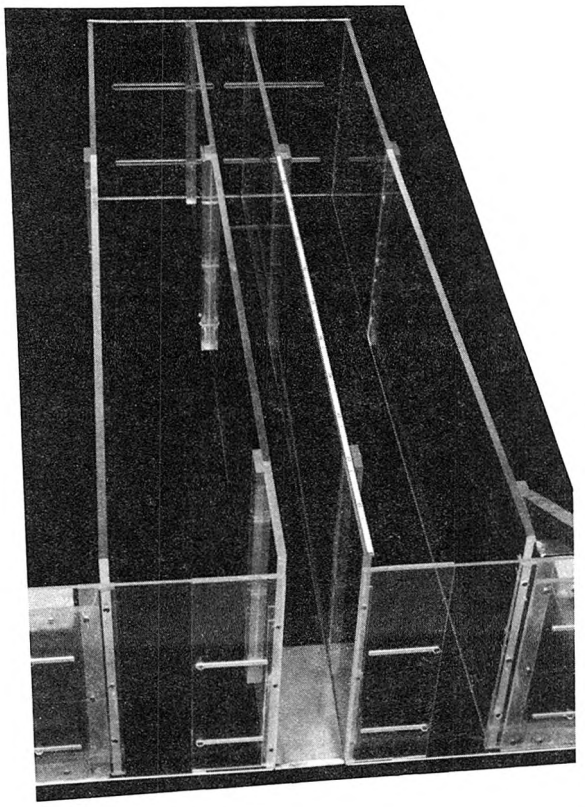

Fig. 4.3.1 The lucite harbour model.

manner. The sloping bottom of the harbour consisted of a single piece of 1.27 cm (1/2 in) thick lucite. One end of the piece of lucite forming the bottom was extended with a piece of 1.59 mm (1/16 in) thick stainless steel plate, sharpened to a knife edge along its free end. This permitted the harbour bottom to meet flush with the floor of the wave basin. The plate can be clearly seen at the harbour entrance in Fig. 4.3.1. The harbour bottom was placed in its proper position, and then the harbour sidewalls were pressed against it. The two side edges of the lucite bottom and its stainless steel end were lined with weather stripping foam to eliminate leakage. The injection of dye near these edges showed that there was, in fact, no leakage. A series of eight harbour bottoms were used in the experiments, each with a slightly different width, varying from 2.85 cm to 11.0 cm wide. Hence,

the harbour width was varied in discrete steps, although its length could be varied continuously simply by varying the angle of the harbour bottom. The entrance to the harbour was fully open for all the experiments.

A small amount of dissipation due to capillary hysteresis occurs from wave action on solid surfaces (Miles 1967). This effect is particularly noticeable for surfaces that are not wetted by the liquid (e.g., lucite and distilled water). This effect can be minimized by adding a small amount of wetting agent to the liquid (Keulegan 1959). For this investigation, a small amount of Photo-Flo 200 solution (manufactured by Kodak) was added to the water before each experiment.

The harbour model was designed so that it would fit into a gap in a false wall simulating a perfectly reflecting coastline (see Fig. 4.1.3). The coastline was parallel to, and about 7 m from, the wave plate. The coastline was 40 cm high and made of 0.95 cm (3/8 in) thick lucite, mounted on a frame of galvanized iron angles. There were two identical walls, one on either side of the harbour entrance. Lucite spacers, 0.95 cm (3/8 in) thick, 2.54 cm (1 in) wide, and 45 cm high, were placed between each screen of the lateral wave absorbers, in line with the coastline. They are represented in Fig. 4.1.3 by the dashed lines passing through the wave absorbers in line with the coastline. These extended the coastline to the outer walls of the wave basin and prevented wave energy from penetrating the absorbers into the still water region behind the coastline.

## 4.4 Measurement of the Water Surface Elevation

A resistance wave gauge was used to measure the wave amplitude in the harbour for each of the experiments. A photograph of a typical wave gauge used can be seen in Fig. 4.4.1. The wave gauge consisted of two parallel stainless steel rods 0.74 mm in diameter, 9 cm long, and spaced 0.5 cm apart. The rods had sufficient

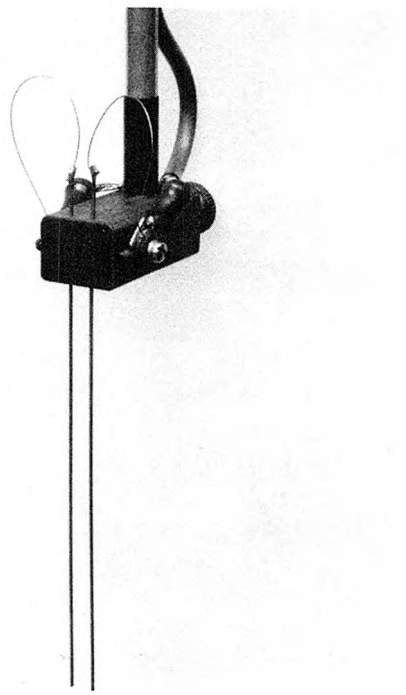

Fig. 4.4.1 A wave gauge.

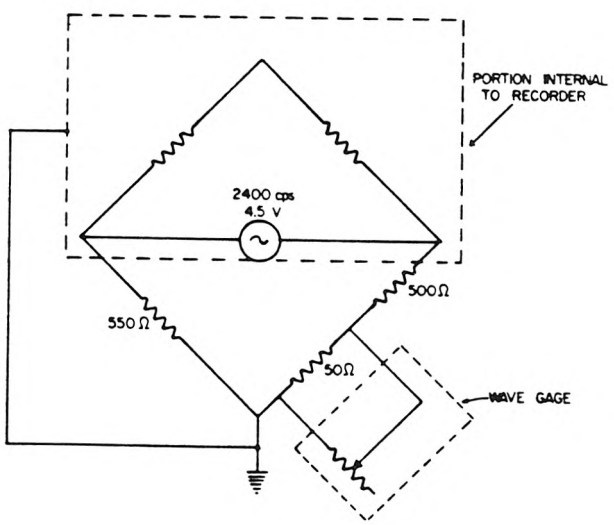


Fig. 4.4.2 Circuit diagram for the wave gauge (after Raichlen, 1965).

stiffness to allow them to be supported at only one end; the other ends penetrated the free surface. The wave gauge was used in conjunction with a Sanborn (150 series) recorder (see Fig. 4.2.7). A Sanborn Carrier Preamplifier supplied a 2400 Hz, 4.5 volt excitation for the gauge and also received the output signal from the wave gauge which, after demodulation and rectification, was displayed on the recording unit. The circuit diagram for the wave gauge is presented in Fig. 4.4.2. The immersion of the wave gauge in water causes an imbalance in the full bridge circuit and induces an output voltage proportional to the change of depth of immersion of the wave gauge relative to its balanced position.

In addition to the recording obtained from the Sanborn recorder, the demodulated and rectified signal from the wave gauge was recorded by the laboratory's PDP 11/60 computer with an Analog-to-Digital (A/D) converter (the same computer used to send the wave plate trajectory to the microcomputer). The signal from the Sanborn recorder still retained some of the 2400 Hz excitation and its voltage was too high to be recorded directly by the A/D converter. Therefore, the voltage had to be reduced and the signal had to be filtered to eliminate this electrical noise. In addition, since the A/D converter was located several hundred feet away from the Sanborn unit, it was necessary to convert the signal into a differential signal which was transmitted to the PDP 11/60 computer via a twisted pair of cables. At the computer the signal was converted back to a single ended signal referenced to the user's ground potential. By the use of this technique to transmit the signal, noise picked up during transmission automatically cancelled, since all the information was encoded into the *difference* in the transmitted potentials. For a detailed description of this additional signal conditioning circuitry, see Lepelletier (1980).

The wave gauge was attached to a remotely controlled calibration device shown in Fig. 4.4.3, which consisted of a rack and pinion driven by a synchronous

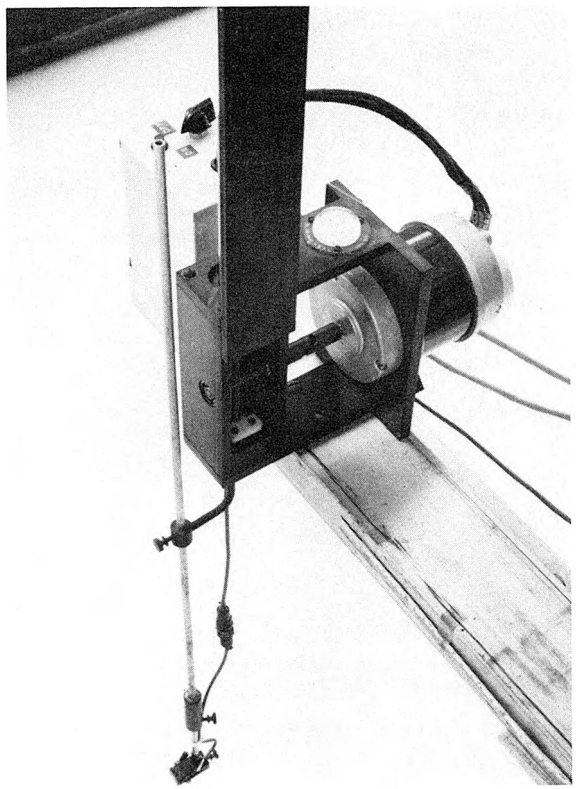

Fig. 4.4.3 Wave gauge and calibration device.

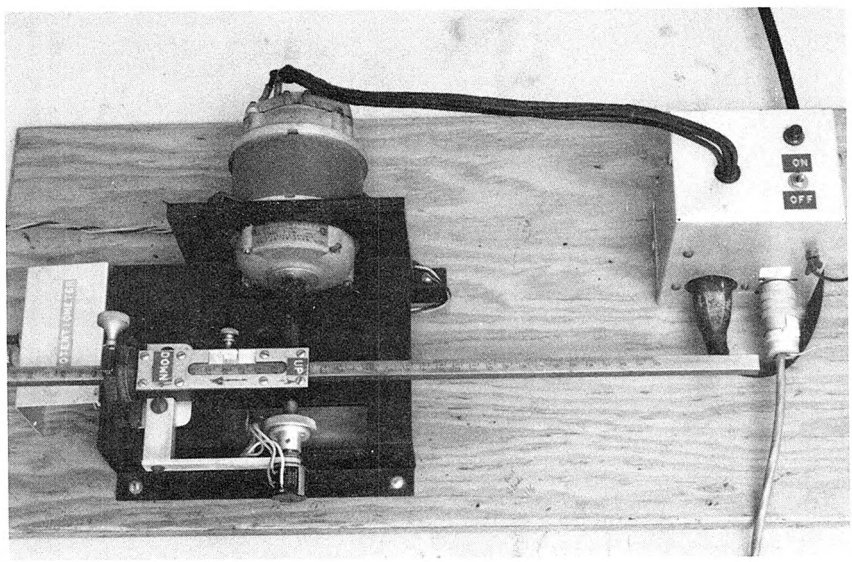


Fig. 4.4.4 Wave gauge master control unit.

motor. The wave gauge was attached to the rack with its weight counterbalanced by a lead weight. The synchronous motor was connected to a master control unit shown in Fig. 4.4.4, which consisted of a synchronous generator driven by a pinion and the rack of a point gauge. Therefore, when the point gauge was moved, a current was generated and relayed to the motor, which moved the wave gauge vertically in a one-to-one ratio. This arrangement allowed a quick calibration of the wave gauge before each run. To record the calibration data with the A/D converter of the laboratory's PDP 11/60 computer, the motion of the rack of the point gauge was converted to an electrical signal by a multiturn potentiometer and constant voltage signal.

## 4.5 Experimental Procedure for Data Acquisition

The computer aided A/D data acquisition system made it possible to calibrate the wave gauge, record the wave amplitudes, and then reduce the data very quickly and accurately. Calibration of the wave gauge was performed before every run. Each experiment consisted of three consecutive steps:

(1) Calibration Step: The wave gauge was placed in its equilibrium position and the bridge circuit was balanced. Then the wave gauge was immersed downward a distance greater than the maximum positive wave height expected. The gauge was then raised slowly by manually turning the wheel on the point gauge of the master unit until the wave gauge was raised above its equilibrium position a distance greater than the maximum negative wave height expected. During this phase the voltages from both the wave gauge and the potentiometer of the master unit were recorded with the A/D system of the PDP 11/60. This information was sufficient to calibrate the wave gauge after the experiment was finished. Before the experiment was started, the wave gauge was returned below its equilibrium posi-

tion and then raised back up again precisely to that level to avoid gear backlash in the synchronous motors.

(2) Run Step: The microcomputer was activated to generate the incident waves, and then the A/D data acquisition on the PDP 11/60 computer was started to record the voltage from the wave gauge.

(3) Data Reduction Step: A software package was run on the PDP 11/60 computer to calibrate the wave gauge and reduce the voltages recorded during the experiment to wave amplitudes. The calibration routine fitted a fourth degree polynomial to the calibration curve of the wave gauge. Very good agreement was obtained between the measured calibration curve and the fitted curve. The correlation coefficient was typically 0.998 or greater.

Since the last two steps could be performed very quickly, usually within two to three minutes, there was no need to recalibrate again after the experiment.

# CHAPTER 5

## Comparison of Results of the Finite Element Model with Those from Theory and Experiments

In order to test the validity of the finite element model, it is important to compare its predictions to both theoretical and experimental results. Theoretical solutions for many different conditions often can be obtained, allowing one to isolate individual aspects of the flow. In addition, a parametric analysis is much easier to conduct theoretically since physical experiments are, in general, very time-consuming. Unfortunately, theoretical solutions cannot include all of the real fluid effects found in nature; therefore, comparison with experimental data is also important. From such a comparison one can determine whether the approximations made to develop the numerical model were valid. One can also determine which real fluid effects are not important and therefore need not be modelled.

## 5.1 Comparison With Theory

In this section the finite element model will be compared to three different theoretical solutions. The first comparison will primarily investigate the model's capability to compute the nonlinear effects associated with wave runup (for non-breaking waves). The second comparison will validate the model's ability to treat nonhydrostatic vertical fluid accelerations. Such accelerations are responsible for frequency dispersion. The final comparison will focus on the harbour resonance


Fig. 5.1.1 Finite element mesh used for modelling the runup of a plane wave on a linearly sloping beach.

process for three harbours with very different bathymetries. This comparison will test the model's ability to handle different bathymetries, and it will also be useful to investigate some of the numerical problems associated with modelling flow through a harbour entrance.

### 5.1.1 Comparison With a Nonlinear Theoretical Solution

Exact solutions to nonlinear wave theories are rare, especially if the fluid boundaries are free to deform with the runup and rundown of waves on a sloping boundary. For that reason the Carrier-Greenspan solution of Section 3.3 is remarkable. It is the ideal solution to test the finite element model's ability to handle the nonlinear aspects of wave runup, since this aspect can be isolated and all other real fluid effects eliminated from the problem.

Simulations were performed using the finite element mesh shown in Fig. 5.1.1. Since the finite element model treats two horizontal dimensions, a 2-D mesh was

used even though the problem involves only one horizontal coordinate. Eight node quadrilateral elements were used very successfully although linear elements also worked well. Since shoaling causes the local wavelength scale to decrease as a wave approaches the shoreline, the nodal spacing was decreased in this direction accordingly. The nodal spacing was chosen to vary roughly with the square root of the depth, so that there would be no time step penalty due to the smaller node spacing near the shoreline. The mesh consisted of 57 elements. The same nondimensional variables as given by Eq. (3.3.6) in Section 3.3 were used for the finite element numerical computations. For convenience they are repeated here:

$$x = \frac{x^*}{\ell} \qquad t = \frac{t^*}{T} \qquad h = \frac{h^*}{\phi\ell} = x$$

$$h = \frac{h^*}{\phi\ell} = x \qquad u = \frac{u^*}{u_0} \quad . \tag{5.1.1}$$

Also, the same length scale, $\ell = \phi g/\omega^{*2}$, was chosen. Since the same depth scale (i.e., $\phi\ell$) was used to nondimensionalize the water depth, $h^*$, as well as the wave height, $\eta^*$, the nonlinear parameter $\alpha$ is equal to unity in the finite element model. The importance of the nonlinear terms is governed by the wave amplitude parameter $A_0$ defined in Eqs. (3.3.37) and (3.3.39), and which appears in Eq. (5.1.2) below. As shown in Section 3.3 the steady-state solution exists only over the range $0 \leq A_0 \leq 1$. The shoreline was located at $a = 0$ and the offshore boundary at $a = a_{\max} = 95.0$. The nodal spacing at the shoreline was: $\Delta a = 0.229$, and at the offshore boundary was: $\Delta a = 1.62$. The longshore nodal spacing was: $\Delta b = 2.0$. A time step of $\Delta t = 0.05$ was chosen. At time $t = 0$ the fluid was quiescent. For $t > 0$ the wave amplitude:

$$\eta = \Re\left\{\frac{A_0}{2} H_0^{(1)}(2\sqrt{a_{\max}})e^{i(t+\phi)}\right\}(1 - e^{-0.2t^2}) \tag{5.1.2}$$

was applied at the offshore boundary. Here $\Re$ refers to the real part of the quantity

enclosed within the braces. The phase $\phi$ was chosen so that $\eta = 0$ at $t = 0$. The exponential factor was included so that the particle accelerations would be zero at $t = 0$. Equation (5.1.2) represents a plane wave normally incident to the shoreline. This wave will reflect from the shore ( $a = 0$ ) and propagate back toward the offshore boundary ( $a = a_{\max}$ ), setting up a standing wave system. Since the boundary condition given by Eq. (5.1.2) will not permit this reflected wave to pass freely through the offshore boundary, the reflected wave will be re-reflected back into the computational domain, changing the standing wave system. Thus, the simulation must stop before this "re-reflected" wave contaminates the region of interest.

Since the distance to the offshore boundary, $a = a_{\max}$ , is large, the amplitude of the incident wave given by Eq. (5.1.2) is very small; hence, nonlinear effects are negligible in the offshore region. Although the boundary condition represented by Eq. (5.1.2) is a solution to the *linear* shallow water equations, it will set up a standing wave which is a solution to the *nonlinear* shallow water equations corresponding to the potential of Eq. 3.3.36 (for $\varrho = 1$ ).

Figure 5.1.2a shows the elevation of the shoreline as a function of time as computed by the finite element model for six different values of the amplitude parameter $A_0$. The lowest amplitude runup record corresponds to $A_0 = 0.2$ and in order of increasing amplitude the other records correspond to $A_0 = 0.5$, 0.8, 0.9, and 1.0. The dashed curve corresponds to $A_0 = 1.15$. The shoreline is quiescent until the wave arrives at about $t = 19$. The re-reflected wave, i.e., the wave reflected from the outer computational boundary, returns at about three times this value: about $t = 57$. Its return can be noticed by the slightly decreased height of the last runup crest. The numerical solution for the case $A_0 = 1.15$ (dashed curve) could only be computed until approximately $t = 23.5$, at which point the wave had reached the point of maximum rundown. At this time the

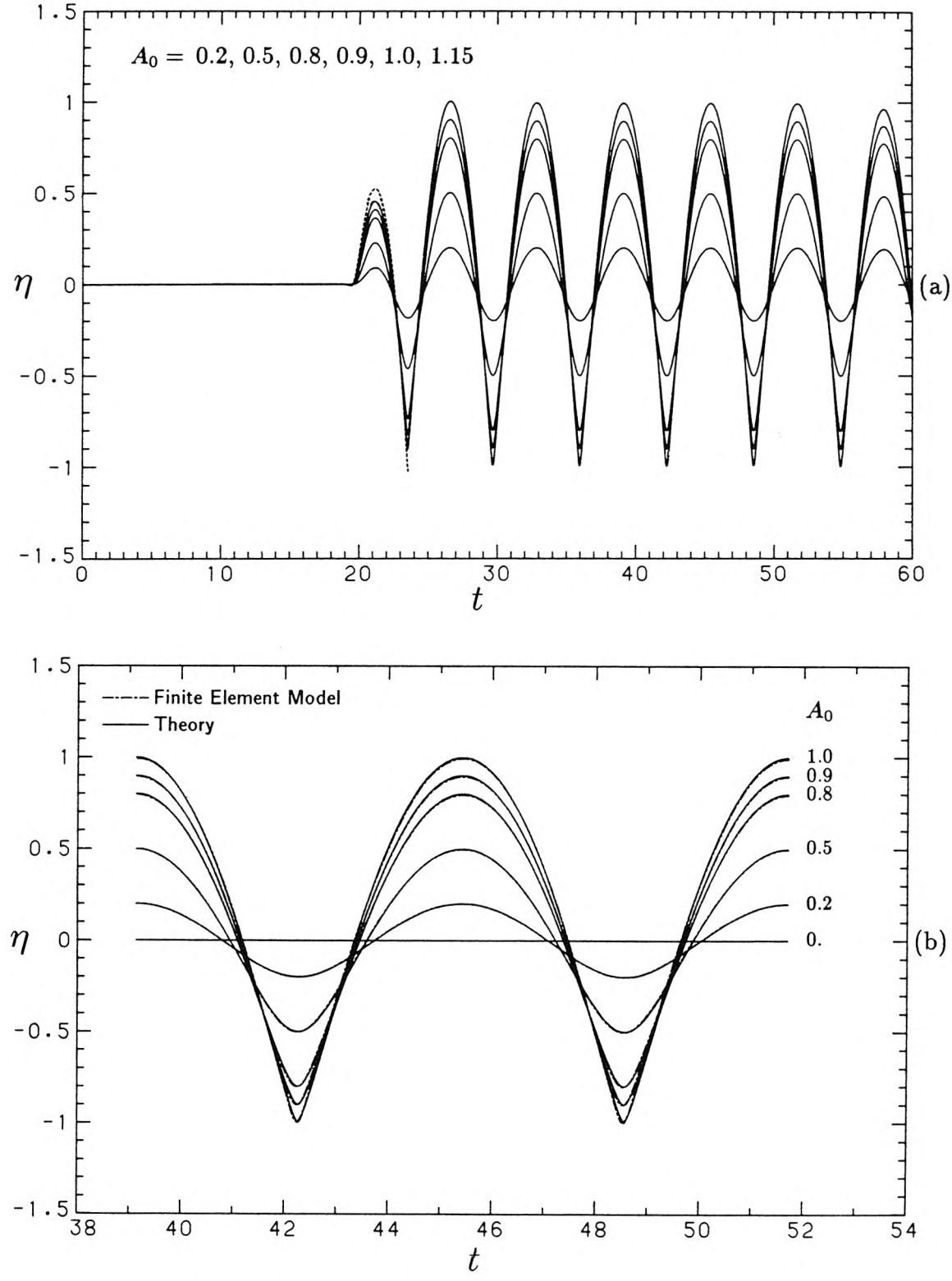


Fig. 5.1.2 (a) shoreline elevation computed by the finite element model: $A_0 = 0.2, 0.5, 0.8, 0.9, 1.0, 1.15$ (b) two periods compared with theory $(\eta = \eta^* \omega^{*2}/\phi^2 g \quad t = \omega^* t^*)$

quantity $1 + \alpha\nabla\cdot\mathbf{x}$ computed for the shoreline element was less than a small tolerance parameter (which had been arbitrarily set to 0.01 in the numerical model). Since $1 + \alpha\nabla\cdot\mathbf{x}$ is the first order approximation for the Jacobian of the transformation between the Lagrangian and the Eulerian frames (see the simple derivation of the nonlinear long wave Lagrangian equations in Appendix A), this means that the water surface is almost vertical and is trying to fold over on itself to become multivalued. Since the quantity $1 + \alpha\nabla\cdot\mathbf{x}$ appears in the denominator of the equation to determine the water surface displacment (Eq. 3.4.2), the finite element model calculations had to be stopped. Theoretically, this should have occurred for $A_0 = 1.$, but since the finite element mesh has a finite resolution at the shoreline, it is difficult to compute these large gradients accurately. In fact, the numerical solution could be computed even for the case $A_0 = 1.1$. If a finer mesh were used, then presumably the shoreline gradient would be more accurate and the numerical solution would break down closer to $A_0 = 1$.

Two periods of the motion in Fig. 5.1.2a from about $t = 39.$ to $t = 52.$ are compared to the theory of Carrier & Greenspan (1958) (Section 3.3) in Fig. 5.1.2b. This plot is similar to Fig. 3.3.5a, where only the theory is shown. Since the Carrier-Greenspan solution is a steady-state solution, the phase of the theoretical result is arbitrary. The theoretical results were shifted in time to line up with the finite element results. The agreement is very good even for the case $A_0 = 1$. That is quite remarkable.

Figure 5.1.3a shows both the Lagrangian and the Eulerian surface elevations for the case $A_0 = 0.5$ associated with the two nodes located at $a = 0.688$, very near the shoreline. The Lagrangian surface elevations are computed directly by the finite element model (FEM) and the Eulerian elevations are computed from these Lagrangian elevations using the procedure of Section 3.4.7. The Eulerian elevations are the ones that would be measured by a wave gauge fixed at $a =$

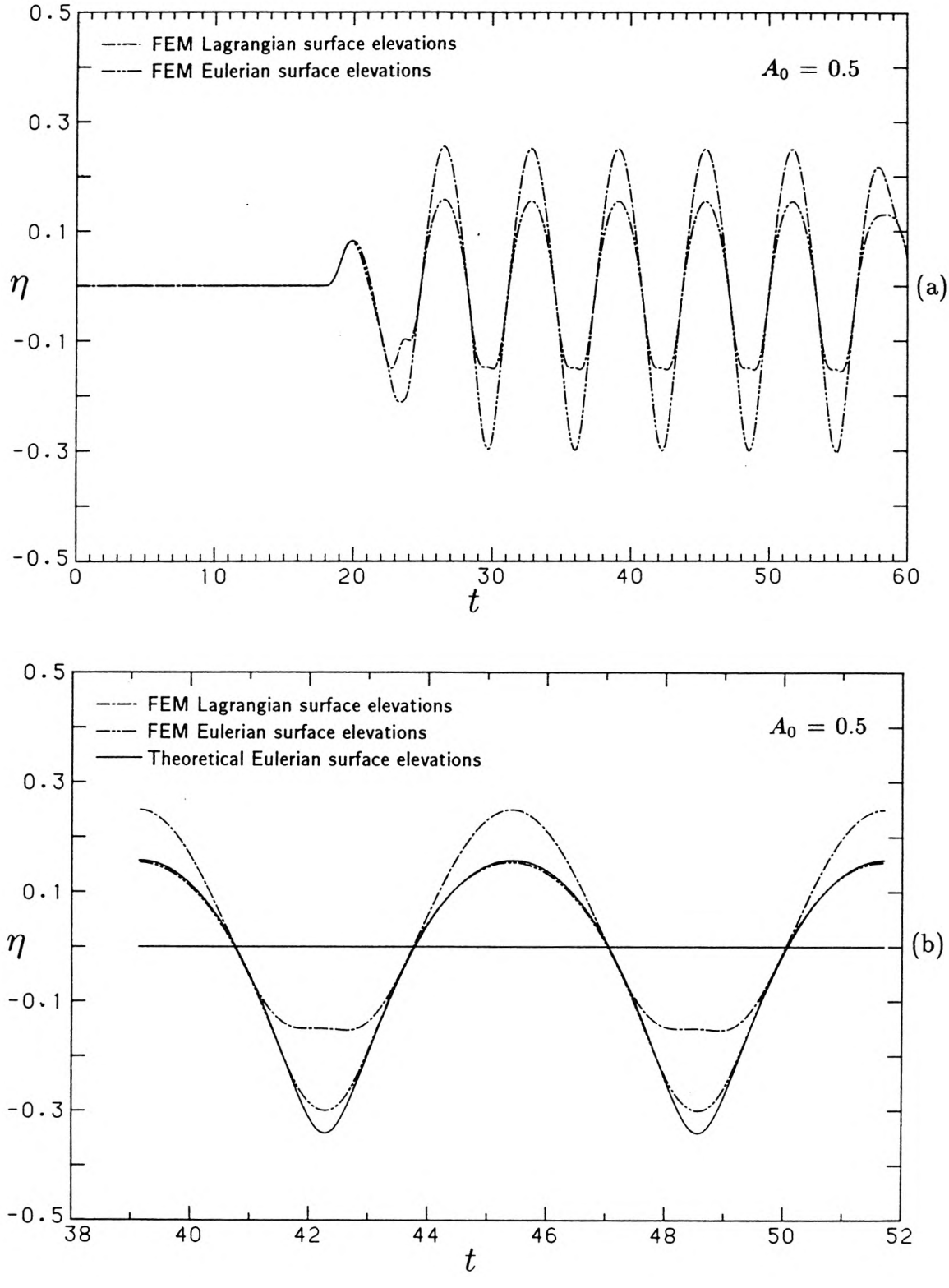


Fig. 5.1.3 (a) Eulerian and Lagrangian wave records associated with a node at $a = 0.688$ (b) two periods compared against theory $(\eta = \eta^* \omega^{*2}/\phi^2 g \quad t = \omega^* t^*)$

0.688, and the Lagrangian elevations are the ones that would be measured by a wave gauge that moved with the particle which at time $t = 0$ was located at $a = 0.688$. Notice there is a large difference between the two since the Lagrangian fluid particle associated with the node at $a = 0.688$ moves sufficiently far from its initial position so that the instantaneous wave heights at these two points are quite different. The greater the nonlinear parameter $A_0$, the greater the difference will be between these two descriptions. Figure 5.1.3b compares two periods of the motion in Fig. 5.1.3a from about $t = 39.$ to $t = 52.$ with the theoretical Eulerian result. Notice that the agreement between theory and the numerical Eulerian result is very good except near the times of maximum rundown. The reason for this is related to the fact that the curvature of $\eta$ in the nearshore region is greatest at the time of maximum rundown (see Fig. 3.3.4a). Therefore, near these times it is most difficult to numerically differentiate $\eta$ to obtain an accurate estimate for $\nabla\eta$. By virtue of Eq. (3.4.78) it is also most difficult to obtain accurate values for $x_{tt}$ at these times as well. Since $\nabla\eta$ or $x_{tt}$ are needed to compute $\eta_E$ using Eqs. (3.4.77) or (3.4.79), respectively, these estimates of $\eta_E$ will also be the least accurate at the times of maximum rundown. Hence, the discrepancy between the theoretical Eulerian result and the numerical result at the times of maximum rundown is due to errors introduced in the transformation from the Lagrangian to the Eulerian description as described in Section 3.4.7, not in the quantities that are directly computed by the finite element model in the Lagrangian description.

Figures 5.1.4 & 5.1.5 compare the wave profiles as predicted by the theory of Carrier & Greenspan (1958) and by the finite element model. These figures are similar to Figs. 3.3.3 & 3.3.4 where only the theory is shown. The theory is plotted for the times $t = i\pi/4, \quad i = 0,1,2,3,4$. The numerical results are plotted for the times: $t = 39.1$, 39.9, 40.7, 41.5, & 42.25. If these values are offset by the first time value, $t = 39.9$, they become: $t = 0.$, 0.8, 1.6, 2.4, & 3.15.

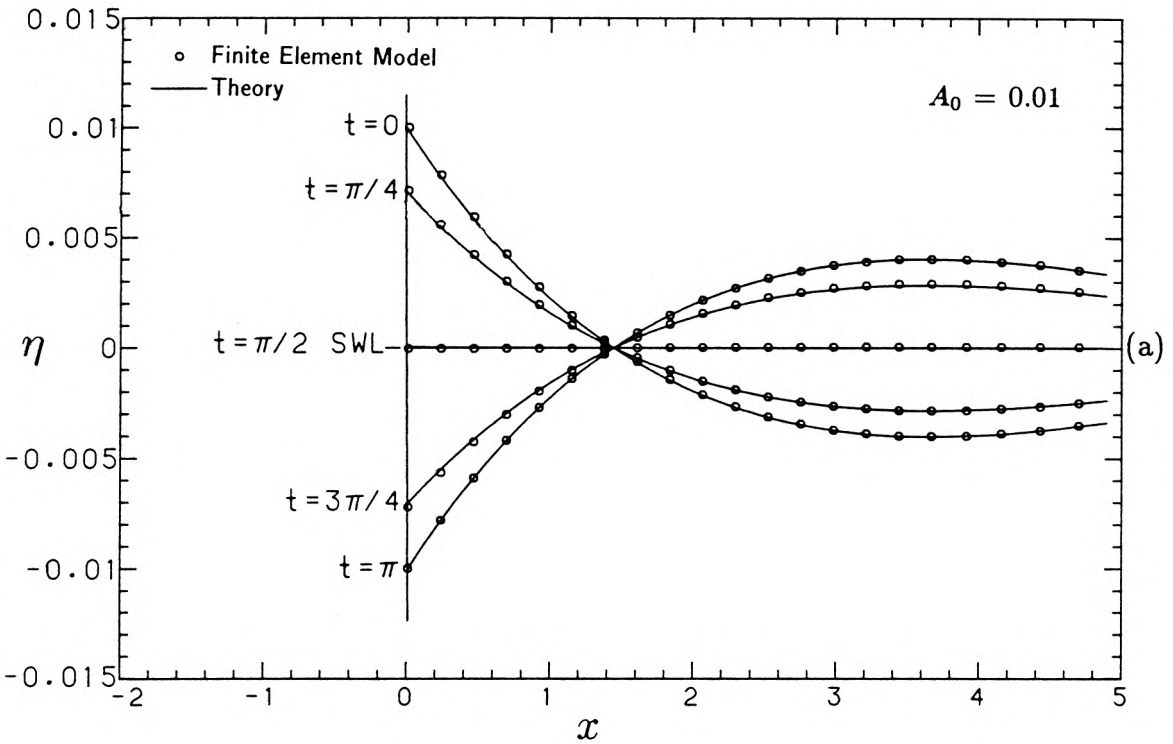


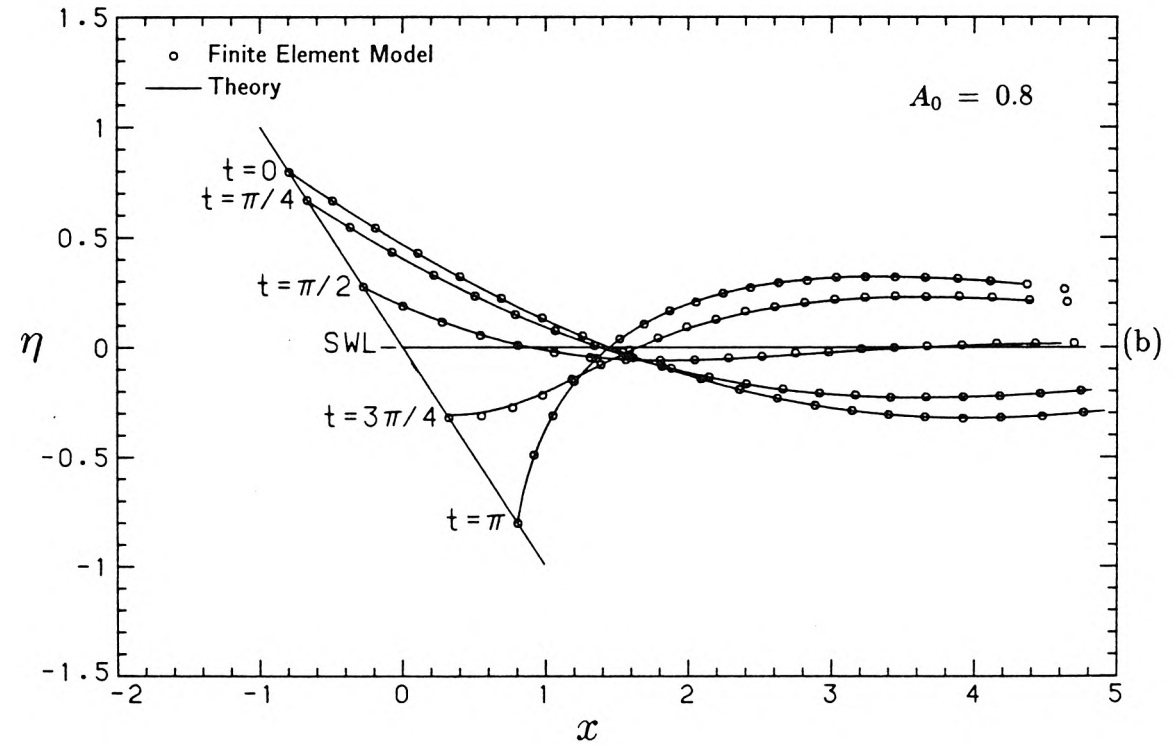


Fig. 5.1.4 Comparison between the wave profiles as predicted by theory and the finite element model; (a) $A_0 = 0.01$ (b) $A_0 = 0.8$ $\quad (\eta = \eta^* \omega^{*2}/\phi^2 g \quad x = x^* \omega^{*2}/\phi g)$

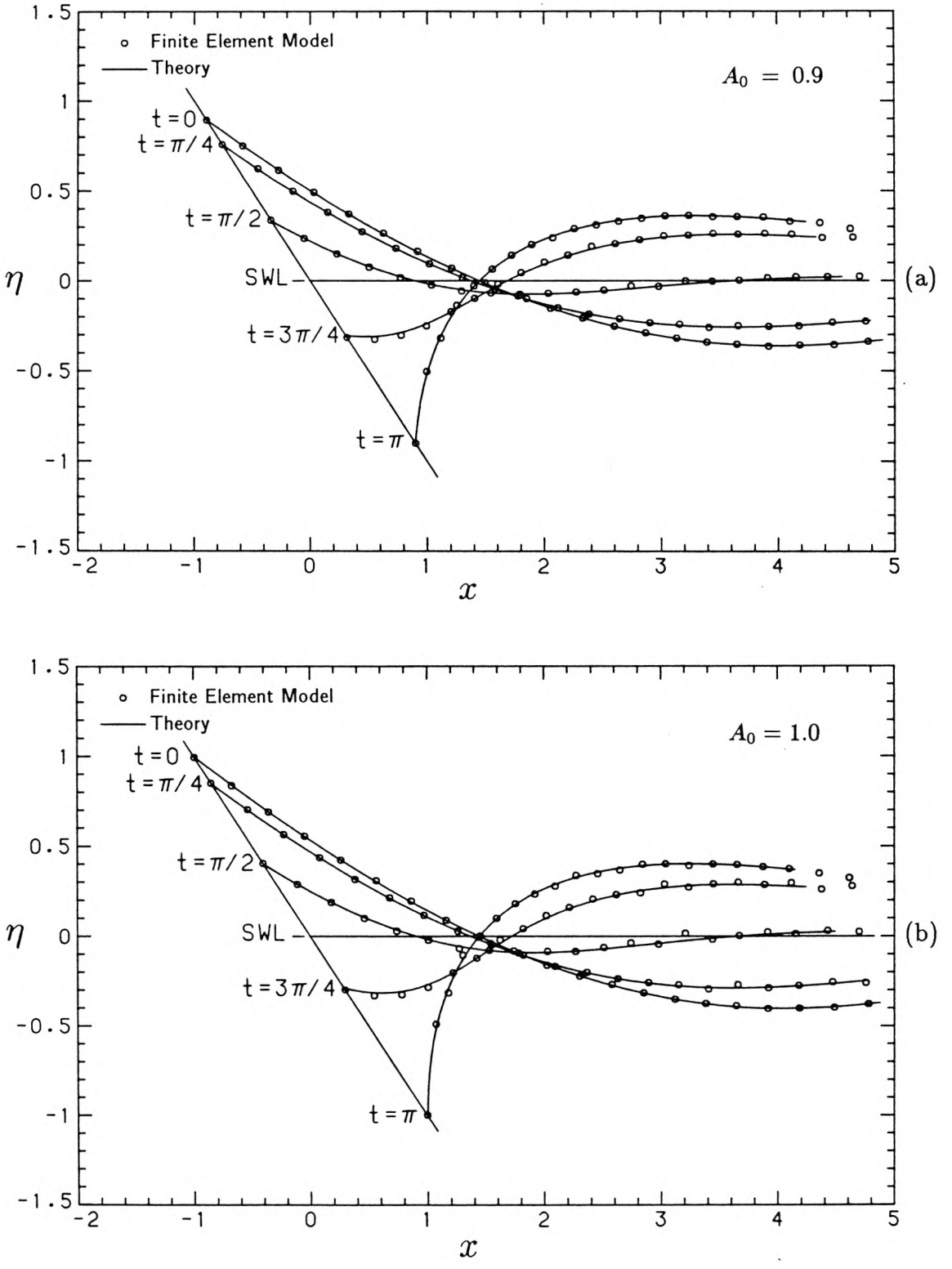


Fig. 5.1.5 Comparison between the wave profiles as predicted by theory and the finite element model; (a) $A_0 = 0.9$ (b) $A_0 = 1.0$ $\left(\eta = \eta^* \omega^{*2}/\phi^2 g \quad x = x^* \omega^{*2}/\phi g\right)$

Note that these values are not equal to $i\pi/4$ for any $i$, but they are the closest possible values to compare with theory, given the discrete time step $\Delta t = 0.05$, since temporal interpolation was not performed. Hence, most of the error in Figs. 5.1.4 & 5.1.5 is due to the fact that the theoretical and numerical results are, in fact, being compared at slightly different values of the time $t$. Nevertheless, the agreement is very good. By following the symbols plotted for the finite element solution, one can get an idea of the trajectories of the particles throughout the fluid, since those symbols indicate the surface elevation at the average location of the fluid particles whose horizontal coordinates coincided with the node points at time $t = 0$. Up until $A_0 = 0.8$ the numerical results are perfectly well behaved. However, for $A_0 = 0.9$, one can see a slight oscillation in Fig. 5.1.5a, with a wavelength roughly equal to twice the grid spacing, superimposed on the wave profiles. The oscillations are small but a little more obvious in the case $A_0 = 1.0$. These oscillations were introduced at the time of the first rundown trough shown in Fig. 5.1.2a at about $t = 23.5$ where the model tried to compute the large accelerations at the shoreline. However, these high frequency oscillations did not grow noticeably over the duration of the simulation. Unfortunately they do make it difficult to make accurate local estimates for $\nabla\eta$ or $\mathbf{x}_{tt}$ and hence make it difficult to transform the output from the model to the Eulerian description as described in Section 3.4.7. Notice also the extreme gradients near the shoreline at the time of maximum rundown in Figs. 5.1.5a and 5.1.5b. That is the main reason why a relatively fine finite element mesh was used; for small values of the nonlinear parameter $A_0$ a much coarser mesh can be used with little degredation in accuracy.

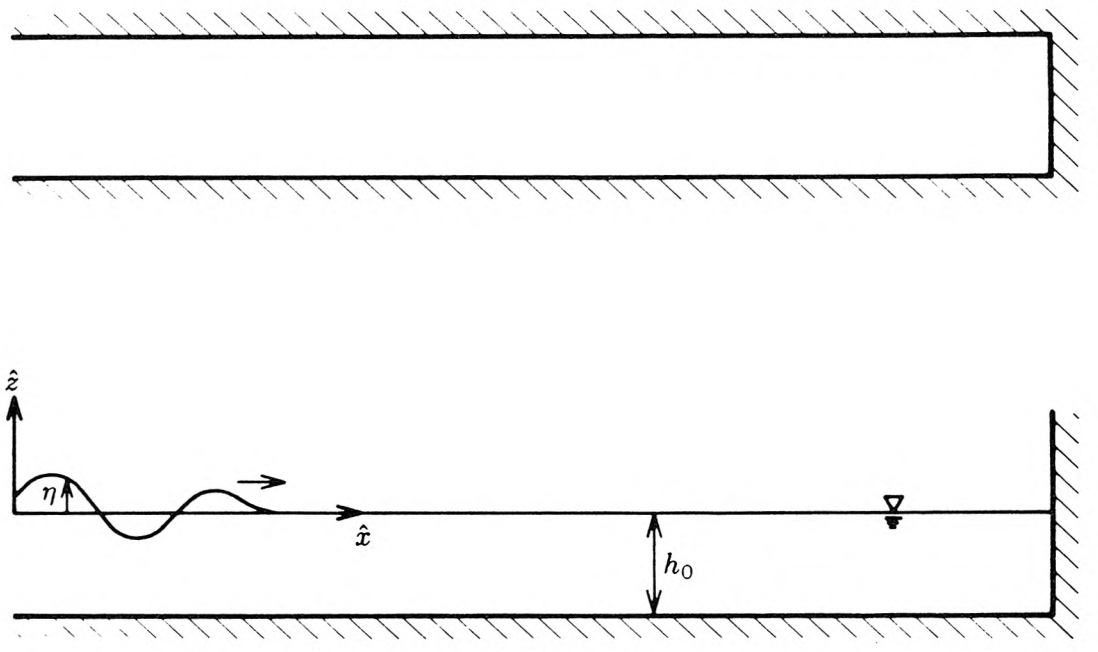


Fig. 5.1.6 Definition sketch of the channel geometry.

### 5.1.2 Comparison with Theoretical Dispersion Relations

The derivation of the long wave equations in Section 3.1.3 included terms that accounted for deviations of the pressure from the hydrostatic law caused by vertical fluid accelerations. As a result, the dispersion relation for these equations predicts that waves with short wavelengths propagate more slowly than waves with longer wavelengths. In order to test the ability of the finite element model to treat properly the effects of vertical accelerations, the dispersion relation for these equations will be computed numerically in this section. The results will be compared to the theoretical dispersion relation for these equations as well as the theoretical dispersion relations for fully dispersive linear theory and for nondispersive long wave theory.

The following numerical simulation will be conducted. Waves of a single har-

monic frequency will be generated in a long constant depth channel with straight parallel sides; see Fig. 5.1.6 for a definition sketch of the channel geometry. Although there is little reason for confusion here, the axis coordinate labels, $\hat{x}$ and $\hat{z}$, have hats to emphasize that they represent the Cartesian coordinates relative to the common origin $(\hat{x}, \hat{z}) = (0, 0)$, not relative to a particle's initial position. Initially the free water surface is quiescent. The waves will be generated at one end of the channel with a perfectly reflecting vertical wall at the other end, although this latter boundary condition is irrelevant, since the simulation will be terminated before reflections from this boundary reach the domain of interest. The waves generated will be uniform across the width of the channel, so the problem is strictly two-dimensional with wave propagation along a single coordinate direction. Hence, the wave celerity can be determined easily by measuring the time for a point of constant phase, e.g., a zero crossing, to propagate a known distance. By repeating this procedure for several different frequencies the wave celerity can be determined numerically as a function of the wave frequency.

The theoretical dispersion relation for the linearized long wave equations corresponding to Eqs. (3.1.117) and (3.1.118) of Section 3.1.3 for wave propagation in one horizontal dimension in a fluid of constant depth is given by Eq. 3.1.131 and is repeated here for the convenience of the reader:

$$\omega_{\mathrm{wd}}^2 = \frac{g h_0 \, k^2}{1 + \frac{1}{3}(k h_0)^2} \quad . \tag{5.1.3}$$

Here $\omega$ is the dimensional wave frequency, $k$ is the dimensional wave number $(= 2\pi/\lambda)$, $h_0$ is the dimensional still water depth, $\lambda$ is the wavelength, and $g$ is the acceleration of gravity. The subscript $(\,)_{\mathrm{wd}}$ refers to the weakly dispersive theory represented by Eqs. (3.1.117) and (3.1.118) of Section 3.1.3. All quantities in this section will be dimensional.

In comparison with Eq. (5.1.3), the dispersion relations for the fully dispersive linear theory and the nondispersive linear long wave theory are, respectively:

$$\omega_{\mathrm{fd}}^2 = gk \tanh kh_0 \tag{5.1.4}$$

$$\omega_{\mathrm{nd}}^2 = gh_0k^2 \quad . \tag{5.1.5}$$

Here the subscripts $(\,)_{\mathrm{fd}}$ and $(\,)_{\mathrm{nd}}$ refer to the fully dispersive wave theory and the nondispersive long wave theory, respectively. Corresponding to these three dispersion relations are the following expressions for the phase velocity, $c$.

$$c_{\mathrm{fd}} = \sqrt{gh_0}\sqrt{\frac{\tanh kh_0}{kh_0}} \tag{5.1.6}$$

$$c_{\mathrm{wd}} = \frac{\sqrt{gh_0}}{\left[1 + \frac{1}{3}(kh_0)^2\right]^{1/2}} \tag{5.1.7}$$

$$c_{\mathrm{nd}} = \sqrt{gh_0} \quad . \tag{5.1.8}$$

The deviations of expressions (5.1.7) and (5.1.8) from the exact linear dispersive result of Eq. (5.1.6) are tabulated in Table 3.1.1.

However, Eqs. (5.1.6), (5.1.7), and (5.1.8) are not the most convenient expressions to compare with the results of the finite element model. This is because the wave speed in these expressions is expressed in terms of the wave number $k$, not in terms of the temporal frequency $\omega$. The waves will be generated by forcing them at one end of the channel at a known frequency. Hence, the wave frequency is a known input parameter to the problem, but not the wave number (or wavelength). The wavelength must be determined by measuring it as the waves are generated. Therefore, it is best to rewrite the celerity relations in Eqs. (5.1.6)-(5.1.8) in terms of the wave frequency, $\omega$. For the weakly dispersive theory and the nondispersive

theory one obtains:

$$c_{\mathrm{wd}} = \sqrt{gh_0}\,\sqrt{1-\beta/3} \tag{5.1.9}$$

$$c_{\mathrm{nd}} = \sqrt{gh_0} \tag{5.1.10}$$

where $\beta$ is defined to be:

$$\beta = \frac{\omega^2 h_0}{g} \quad . \tag{5.1.11}$$

It is not possible to write down a simple closed form expression for $c_{\mathrm{fd}}$ as a function of $\beta$. However, one can, in principal, eliminate $kh_0$ between Eqs. (5.1.4) and (5.1.6) to obtain $c_{\mathrm{fd}}$ as a function of $\beta$.

The parameter $\beta$ is a measure of the importance of frequency dispersion in the problem. For very small values of $\beta$ it is clear from Eq. (5.1.4) that $\beta \approx (kh_0)^2$. However, for larger values of $\beta$ this is not so.

The relations between $c$ and $\beta$ are interesting. Equation (5.1.10) is the familiar nondispersive result which states that the wave celerity is independent of the wave frequency. This is valid for small values of $\beta$ but not so for larger values. Equation (5.1.9) is a better approximation to the wave celerity for small to moderate values of $\beta$, but it is interesting to note that it goes to zero at a finite value of $\beta = 3$. The same is true for the group speed as well. Figure 5.1.7 shows the dependence of $c_{\mathrm{fd}}$, $c_{\mathrm{wd}}$, and $c_{\mathrm{nd}}$ on $\beta^{1/2}$ over a large range of $\beta$. This figure shows that both long wave theories are very inaccurate for large $\beta$, where dispersion is most important, but in the region $\beta < 1$, where dispersion is weak, both long wave theories approach the exact solution, although the weakly dispersive theory is considerably more accurate over this range. Since this investigation is concerned only with long waves (small $\beta$), the weakly dispersive wave theory is entirely adequate and is more accurate than the nondispersive theory. Very little energy will be distributed in wave frequencies where $\beta > 1$; therefore, the error

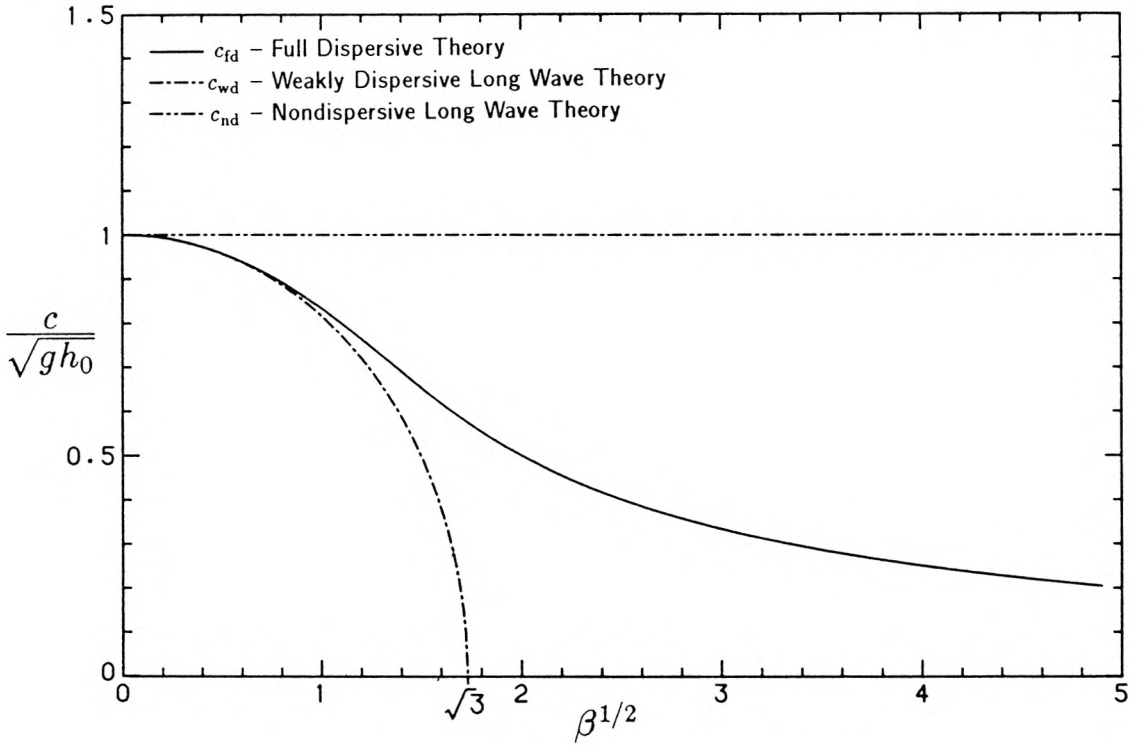


Fig. 5.1.7 Phase speed as a function of $\beta^{1/2} = \omega\sqrt{h_0/g}$ for linear dispersive theory, weakly dispersive long wave theory, and nondispersive long wave theory.

in the dispersion relation for $\beta > 1$ will have little influence. Nevertheless, the case $\beta \geq 3$ will be investigated numerically to show that this situation does not pose any numerical problems.

The finite element mesh corresponding to the domain shown in Fig. 5.1.6 consisted of a single row of linear quadrilateral elements. The node spacing was chosen so that there were forty elements per nondispersive wavelength, $\lambda_{nd}$. The nondispersive wavelength, $\lambda_{nd}$, is the wavelength associated with the temporal frequency $\omega$ computed from the nondispersive relation of Eq. (5.1.5). For $\beta > 0$ the wavelength is shorter than $\lambda_{nd}$, and therefore, in general for $\beta > 0$, there were *fewer* than forty elements per wavelength. With this nodal spacing, the time step $\Delta t$ was chosen to be: $\Delta t = 0.01\,\lambda_{nd}/\sqrt{gh_0}$. The mesh was 280 elements long; therefore, it could accommodate seven nondispersive wavelengths. At one

end of the channel the following forcing was applied for $t \geq 0$:

$$\eta = H(1 - e^{-p(\omega t)^2}) \sin \omega t \quad . \tag{5.1.12}$$

The exponential factor was included to ensure that the applied fluid acceleration was zero at $t = 0$. The parameter $p$ was chosen to be $6.9/(2\pi)^2$, which leads to $(1 - e^{-p(\omega t)^2}) \approx 0.999$ after one period of the generation. The amplitude $H$ is irrelevant since nonlinear effects are not considered here.

Equation (5.1.12) is plotted in Fig. 5.1.8a as a function of $t/T$ where $T = 2\pi/\omega$ is the wave period, and with time increasing to the left to provide easy comparison with the spatial wave records in Fig. 5.1.8b. These spatial wave records are plotted as a function of $x/\lambda_{nd}$ where $x$ is the distance from the end of the channel and $\lambda_{nd}$ is the nondispersive wavelength defined previously. The waves are generated at $x = 0$ and propagate to the right with the vertical endwall indicated by the hatched line at $x/\lambda = 7$. Each of the three spatial wave profiles are plotted for the time $t/T = 6$.

The first spatial wave profile in Fig. 5.1.8b is for $\beta = 0$, i.e., no dispersion. This corresponds to the case where the wavelength is so much greater than the still water depth ($h_0/\lambda \to 0$) that vertical fluid accelerations are negligible. The wave propagates to the right at the speed $c_{nd}$ where $c_{nd}$ is defined by Eq. (5.1.10). Since the origin, $t/T = 0$, of the water surface time history in Fig. 5.1.8a is aligned with $x/\lambda_{nd} = 6$ in Fig. 5.1.8b, the two records should be identical, since for the nondispersive case the spatial wave profile can be determined by moving the input time record along the $x$ axis at the speed $c_{nd} = \sqrt{gh_0}$. Indeed, it can be seen that the two records are nearly identical, and the only perceptible difference is the very slight negative depression at the leading edge of the spatial profile. This is presumably due to numerical dispersion. Thus, if the parameter $p$ were reduced (i.e., if the curvature of the leading edge of the wave were reduced)

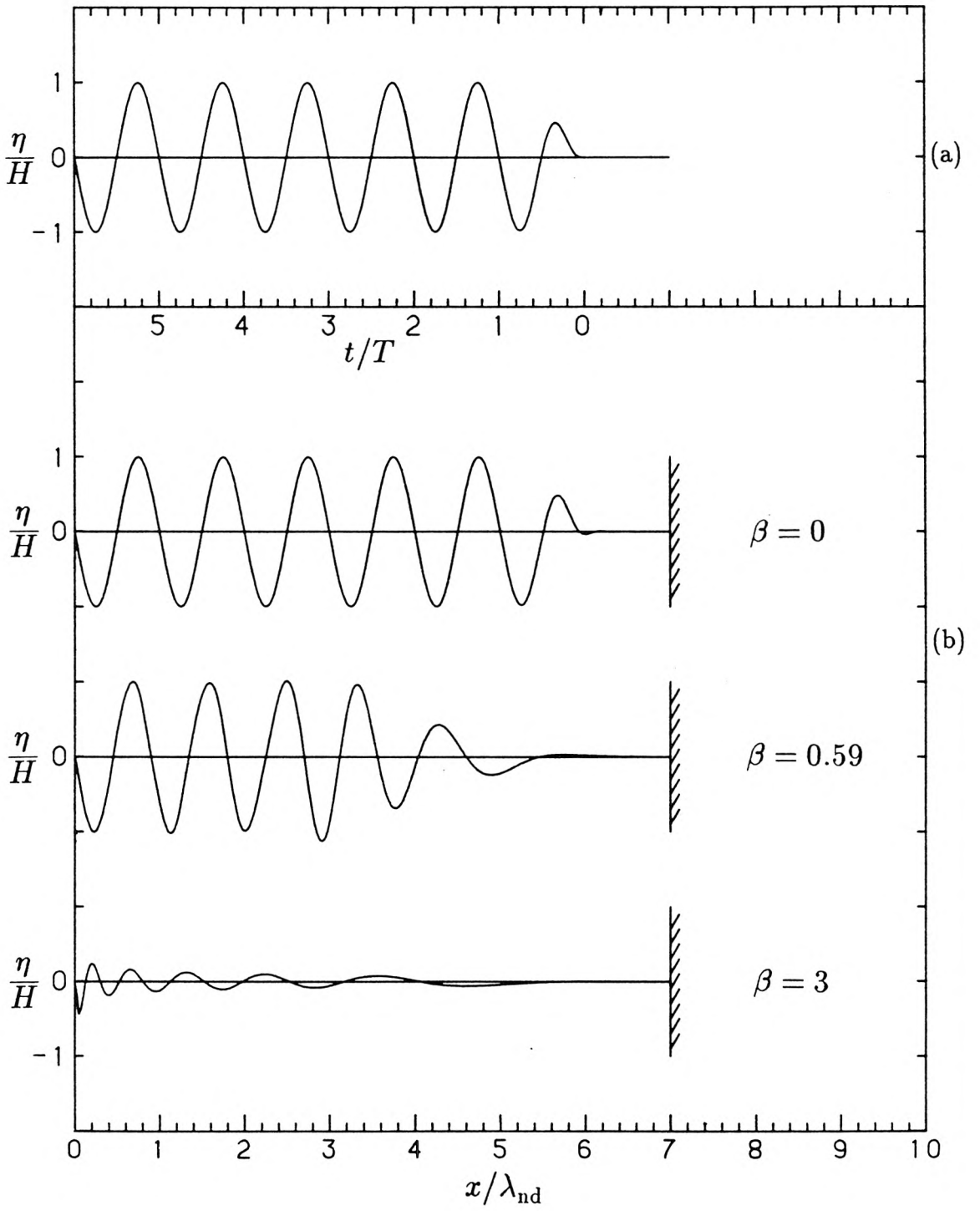


Fig. 5.1.8 Dispersion test: (a) time record of the wave forcing at the end of the channel, (b) spatial wave profiles at time $t/T = 6$ for three different values of $\beta = \omega^2 h_0/g$.

then this depression could also be reduced. At $t/T = 7$ the wave will strike the vertical endwall and reflect back upon itself.

The second spatial wave profile is for $\beta = 0.59$. This represents the case where dispersion is small but certainly not negligible. It can be seen that the wavelength is noticeably shorter than the nondispersive case and, as a result, the wave travels correspondingly more slowly. The effect of dispersion can also be seen by the distortion of the leading edge of the wave. The leading edge of the wave in Fig. 5.1.8a contains the highest concentration of wave numbers different from the fundamental associated with the forcing frequency; therefore, the effect of dispersion is especially noticeable in this region. The first half wavelength for the case $\beta = 0.59$ (corresponding to $0 < t < 0.5$ in the time record of the forcing function in Fig. 5.1.8a) is no longer readily apparent. As a result, the wave appears to start with a large negative depression (corresponding to $0.5 < t < 1$ in the time record of the forcing function). Hence, this depression is fundamentally different than the depression visible at the leading edge of the wave for the nondispersive case. Another interesting dispersive effect for $\beta = 0.59$ is that the third trough has an amplitude greater than the steady-state amplitude of the wave train. This is presumably due to a superpostition of the main wave with the slower moving wave number components near the leading edge of the wave.

The final spatial wave profile is for the special case $\beta = 3$. As seen in Fig. 5.1.7 and Eq. (5.1.9), this profile corresponds to the value of $\beta$ at which the phase speed goes to zero. As mentioned previously, the group speed also goes to zero at $\beta = 0$. This is easy to see from Eqs. (3.1.132) and (3.1.133) because they can be combined to give:

$$(c_g)_{\mathrm{wd}} = \frac{c_{\mathrm{wd}}^3}{g h_0} \tag{5.1.13}$$

where $(c_g)_{\mathrm{wd}}$ is the group speed according to the weakly dispersive theory. There-

fore, the group speed goes to zero when the phase speed goes to zero at $\beta = 3$. For $\beta > 3$, the group speed, wave speed, and wave number become imaginary. This means that the corresponding waves cannot propagate but will decay exponentially with distance. Therefore, the spatial wave profile shown at the bottom of Fig. 5.1.8b corresponds to the maximum value of $\beta$ for which the wave energy can freely propagate away from the generation point at $x = 0$. For the case $\beta > 3$ (not shown in Fig. 5.1.8b) the wave amplitude computed numerically is even smaller than for the case $\beta = 3$ and the wave envelop dies out much more quickly with $x$.

It is clear that the propagation of high frequency (short wavelength) waves corresponding to $\beta > 1$ (see Fig. 5.1.7) is not modelled well by the weakly dispersive theory, but at least these wave components do not cause any numerical problems. As mentioned previously, this investigation is concerned only with long waves (small $\beta$), so very little energy will be distributed in wave frequencies where $\beta > 1$. However, this alone is not enough to conclude that these high wave number components are not important, since it is also important that these wave components do not cause numerical instability problems for the finite element model. If they did cause numerical problems, the amount of energy in these higher modes, however small, would not matter; eventually, the associated instability could contaminate the solution.

One reason why Eqs. (3.1.117) and (3.1.118) were chosen over Eqs. (3.1.112) and (3.1.114) for the finite element model was due to the potential of numerical problems associated with the dispersion relation of Eqs. (3.1.112) and (3.1.114). If Eqs. (3.1.112) and (3.1.114) are linearized, the dissipative terms neglected, and wave propagation is restricted to a single horizontal coordinate direction in a region

of constant depth, then the following dispersion relation is obtained:

$$\omega'^2_{wd} = g h_0 k^2 [1 - \tfrac{1}{3}(k h_0)^2] \quad . \tag{5.1.14}$$

Notice that $\omega'$ argrees with $\omega$ as given by Eq. (5.1.3) for small $kh_0$ to $O((kh_0)^2)$. This should be expected since both pairs of equations, (3.1.117) & (3.1.118) and (3.1.112) & (3.1.114) were derived to be first order accurate in terms of the dispersion parameter $\beta$.

On the other hand, Eqs. (5.1.14) and (5.1.3) behave very differently for *large* values of $kh_0$. From Eq. (5.1.3), the frequency $\omega_{wd}$ is defined for all wave numbers $k$, but the wave number $k$ is defined only for finite values of the frequency $\omega_{wd}$. For large values of $\omega_{wd}$ (or more precisely for large values of $\beta$ where $\beta$ is defined by Eq. (5.1.11)), the wave number $k$ becomes imaginary as mentioned and the wave amplitude decays exponentially with distance. However, for Eq. (5.1.14) the situation is different. The wave frequency $\omega'_{wd}$ is defined only for a finite range of values of $kh_0$. For large $kh_0$ the wave *frequency* $\omega'_{wd}$ becomes imaginary. In this case numerical problems can occur because small amplitude perturbations with large wave numbers can grow with time (Whitham 1974). Therefore, for numerical work, the dispersion relation (5.1.3) is preferred over Eq. (5.1.14).

As mentioned earlier, the wave celerity can be determined by measuring the time for a point of constant phase to propagate a known distance. Using the finite element model, waves were generated for six different values of $\beta$ ranging from $\beta = 0$ to $\beta = 0.99$, and the wave celerity was determined by measuring the time it took for a zero crossing to propagate three wavelengths. The measurements were made in the steady-state region behind the transient leading edge of the wave. These results are plotted in Fig. 5.1.9a as a function of the dispersion parameter $\beta$, using square point plot symbols. Also plotted are the expressions for the wave celerity according to linear dispersive theory (Eq. (5.1.4) and (5.1.6)), weakly

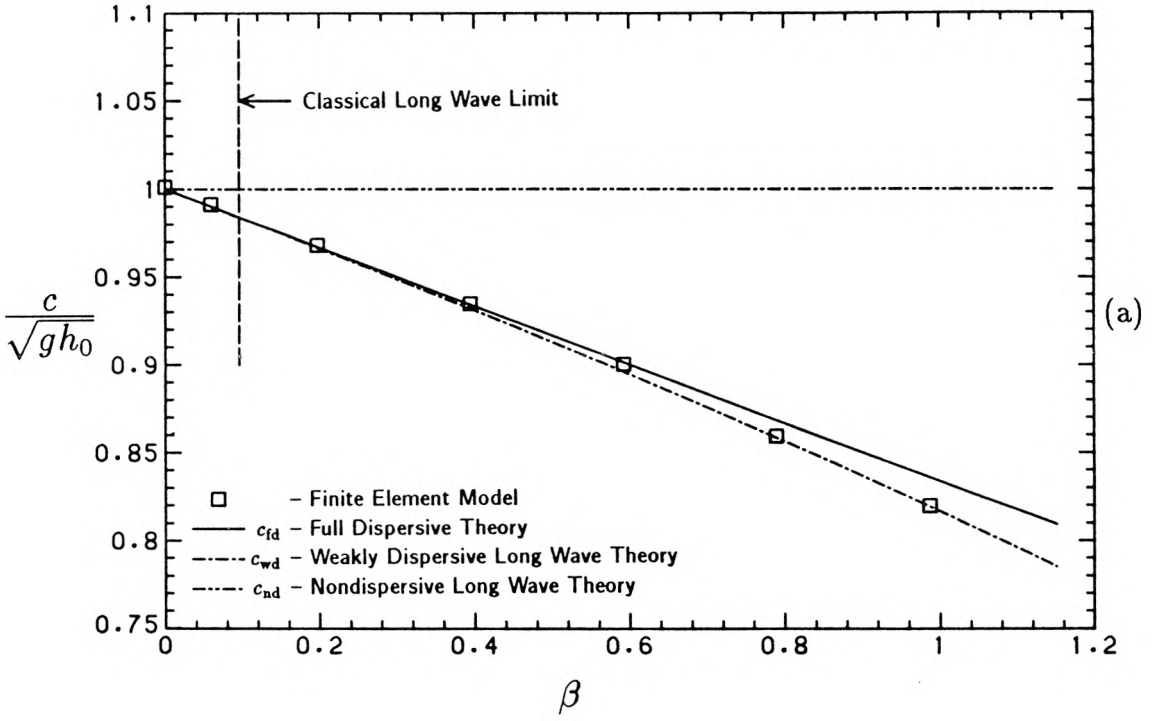


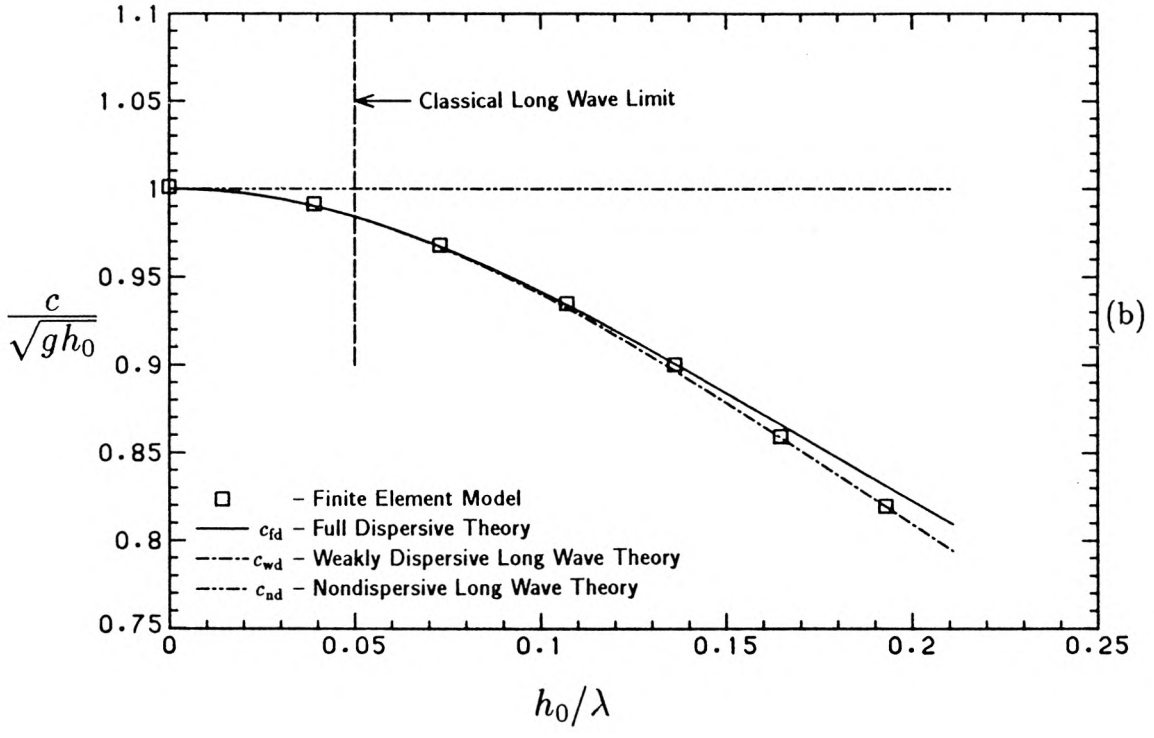


Fig. 5.1.9 Wave celerity as a function of (a) the dispersion parameter $\beta = \omega^2 h_0/g$, (b) the still water depth relative to the wavelength.

dispersive long wave theory (Eq. (5.1.9)), and nondispersive long wave theory (Eq. (5.1.10)). Notice how the expressions for the celerity from the dispersive and weakly dispersive theories vary linearly with the dispersion parameter $\beta$. The quadratic behaviour near $\beta = 0$ in Fig. 5.1.7 occurs because the abscissa is $\beta^{1/2}$, not $\beta$. The finite element model results agree very well with the weakly dispersive theory from which the model was developed. This comparison shows that the model can accurately treat the effects of frequency dispersion caused by vertical fluid accelerations.

Figure 5.1.9b shows the same celerity data plotted against the still water depth relative to the wavelength, $h_0/\lambda$. The linear dispersive theory, weakly dispersive theory, and nondispersive theory correspond to Eqs. (5.1.6), (5.1.7), and (5.1.8), respectively. The values of $h_0/\lambda$ for the finite element results were obtained by averaging over three wavelengths of each of the spatial profiles. Hence, for the finite element results in Fig. 5.1.9b, both the ordinate *and* the abscissa represent measured quantities, whereas in Fig. 5.1.9a only the ordinate is a measured quantity. It is important to remember that points with constant values of $\beta$ in Fig. 5.1.9a *do not* correspond to points with constant values of $h_0/\lambda$ in Fig. 5.1.9b. Since the dispersion relations for each of the theories plotted are different, a single value of $\beta$ will correspond to different values of $h_0/\lambda$, depending on which theory is used.

Also plotted in Figs. 5.1.9a and 5.1.9b is the classical long wave limit. This is not a precisely defined quantity, but it is generally agreed to correspond to approximately $h_0/\lambda \approx 0.05$ (Eagleson & Dean 1966). This corresponds to $\beta \approx 0.1$. Beyond these values, the error between nondispersive long wave theory (the horizontal dashed line) and fully dispersive theory (solid line) grows unacceptable for many applications. However, from these figures it can be seen that the weakly dispersive theory (and the finite element model) is much more accurate and can

be applied to much larger values of $h_0/\lambda$ (or $\beta$), as discussed in Section 3.1.3.1.

### 5.1.3 Comparison With a Harbour Response Theory

The finite element model can also be compared to the harbour response theory of Section 3.2. Three harbours each with a rectangular planform but with three different bathymetries were chosen: (1) constant depth, (2) linearly sloping bottom, and (3) parabolic bottom. A typical finite element mesh used for the simulations is shown in Fig. 5.1.10a although near the second resonant mode for the harbour with the linearly sloping bottom the nodes were concentrated near the shoreline as shown in Fig. 5.1.10b for the same reason that the nodes were concentrated near the shoreline in Section 5.1.1 as seen in Fig. 5.1.1. Figure 5.1.11 shows the harbour regions for these two meshes in more detail. Since the problem is symmetric about the centreline of the harbour, the mesh represents only one-half of the domain. This reduces the amount of computation by a factor of two. Hence, a mesh of the entire harbour would have 4 elements and 5 nodes across its width. The ratio of the width of the harbour to its length, $L$, was 0.2. Therefore, the ratio of the width of the harbour region to its length in Fig. 5.1.10 is half this value, $\epsilon = 0.1$, where $\epsilon$ is defined in Eq. (3.2.10) of Section 3.2. The interregion boundary $\Gamma_{MO}$ in Figs. 5.1.10a and 5.1.10b is the circular arc, which has been darkened for better definition. The interregion boundary $\Gamma_{HM}$ is the darkened vertical line across the entrance to each harbour.

The incident wave was chosen to be sinusoidal. To nondimensionalize the problem, the length scale $\ell$ was chosen to be the length of the harbour $L$, the water depth scale $h_0$ was chosen to be the uniform still water depth exterior to the harbour, and the wave height scale $H$ was chosen to be equal to the amplitude of the incident wave. With this nondimensionalization the incident wave was defined

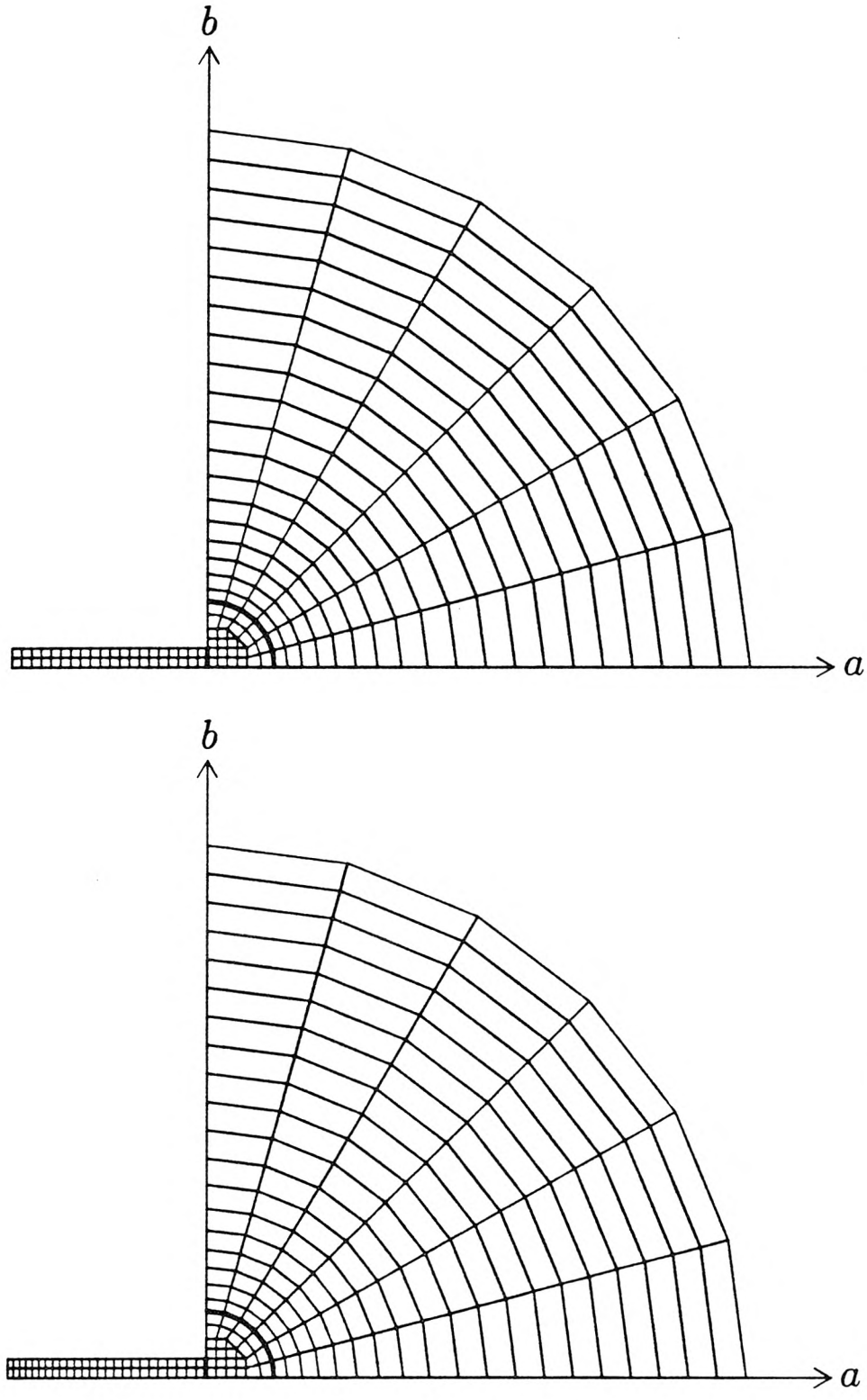


Fig. 5.1.10 Typical finite element meshes used for the harbour response simulations; (a) nodes not concentrated near shoreline, (b) nodes concentrated near shoreline.

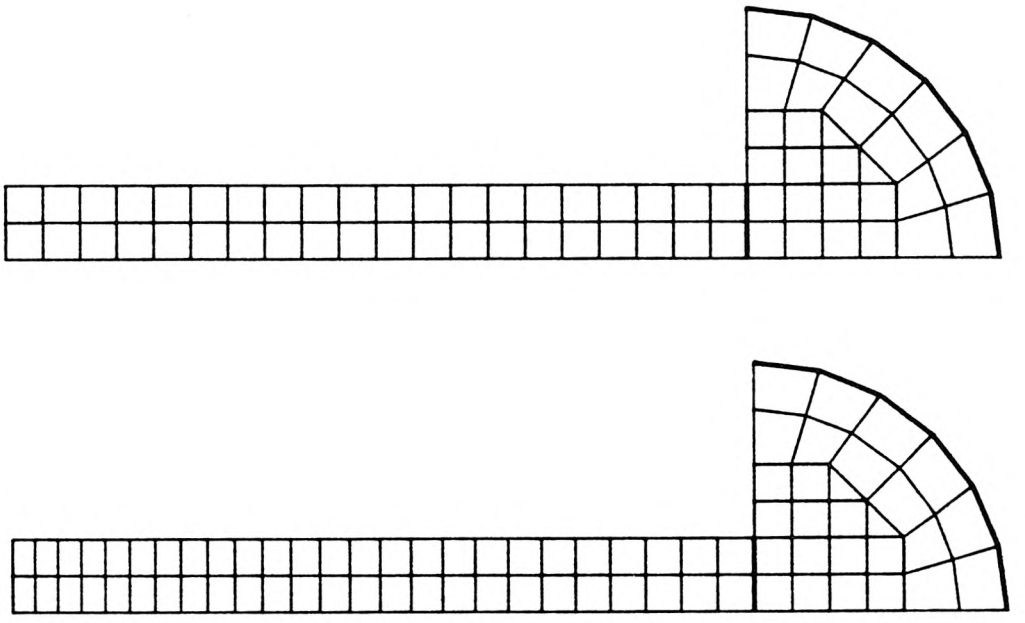

Fig. 5.1.11 Enlarged view of the harbour regions for the two meshes in Figs. 5.1.10a and 5.1.10b.

as:

$$\eta = H(\xi)(1 - e^{-p\xi^2}) \sin kL\xi \tag{5.1.15}$$

where $\xi = a+t-\phi$, $H(\xi)$ is the Heaviside step function, and $k$ is the dimensional wave number of the wave system. The exponential factor was included so that the particle accelerations associated with the waves would be zero at its leading edge $\xi = 0$. The phase $\phi$ was chosen to be equal to the radius of the arc $\Gamma_{MO}$ so that at time $t = 0$ the wave had just reached this interregion boundary. The parameter $p$ was chosen to be 0.02, a conservative value, which generates a gentle transition between the quiescent fluid preceding the waves ( $\xi < 0$ ) to the steady-state oscillations behind the wavefront ( $\xi \gg 1$ ). In order to compare the results of this section with the theory of Section 3.2, the nonlinear and dispersive terms in the equations of motion were neglected. However, the full nonlinear head loss formula (Eq. (3.4.22)) was used in the finite element model, whereas the theory

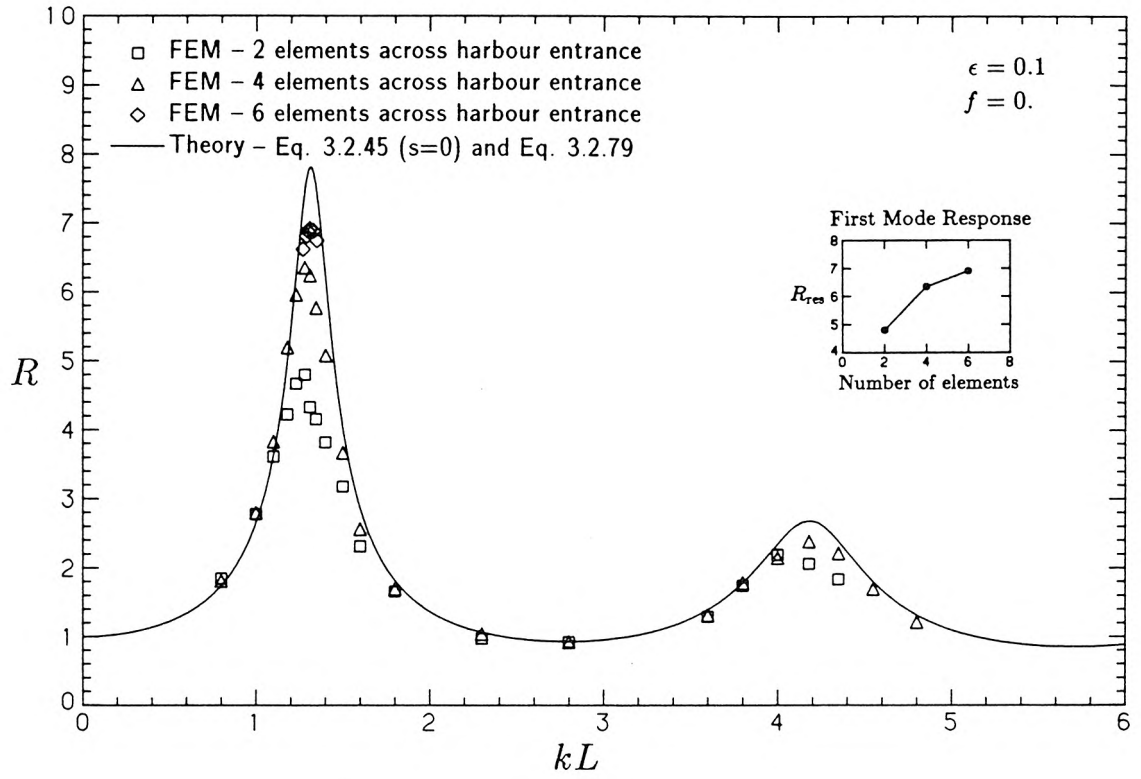


Fig. 5.1.12 Response of a constant depth rectangular harbour as computed by the finite element model with three different finite element meshes.

of Section 3.2 uses the simpler *equivalent* head loss formula (Eq. (3.2.23)). For these head loss formulae the nonlinear parameter $\alpha$ was chosen to be 0.025 and the head loss coefficient $f$ chosen to be 0.8, the maximum value suggested by Lepelletier (1980) for a fully open harbour (see Eq. (3.2.21)).

The first set of comparisons focuses on one of the numerical problems of modelling the flow through the harbour entrance. A constant depth harbour was chosen and entrance losses were neglected ($f = 0$). The results are shown by the triangles in Fig. 5.1.12 (cf. Fig. 3.2.2a). Notice the finite element model underpredicts the height of both of the first two resonant peaks as predicted by the analytical theory (Eq. (3.2.79)). The following reason for this is proposed. The finite element procedure involves integrating quantities over each of the element

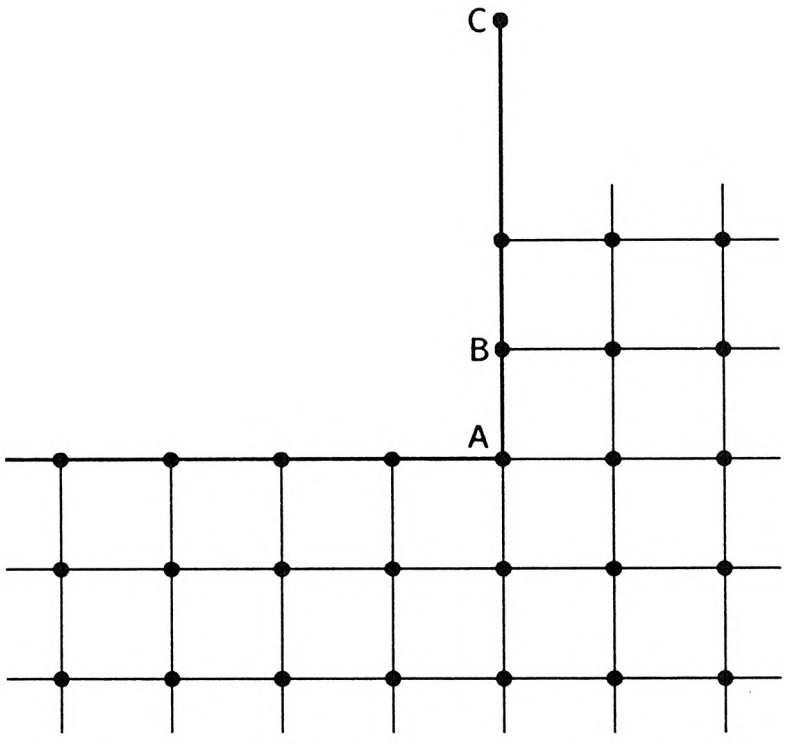


Fig. 5.1.13 Geometry where the boundary turns sharply through a large angle, e.g., at a harbour entrance.

domains and along some of their boundaries. The fluid particle displacements and surface elevations are computed only for each of the node points, but to evaluate the integrals the variables are interpolated between the node points. This procedure works well if the domain of the problem varies smoothly everywhere. However, at the entrance to the harbour, the boundary direction changes sharply through 90 degrees from the harbour sidewall to the coastline, e.g., at the node labelled "A" in Fig. 5.1.13. Along the coastline (represented by the line AC in Fig. 5.1.13) there should, ideally, be no component of the particle displacement vector normal to this wall since the wall is vertical and perfectly reflecting. In the numerical model, that will be true for each of the nodes on this wall *except* for the corner node (node A) joining the harbour with the coastline. This node will have a component of displacement normal to the line AC associated with it. Therefore,

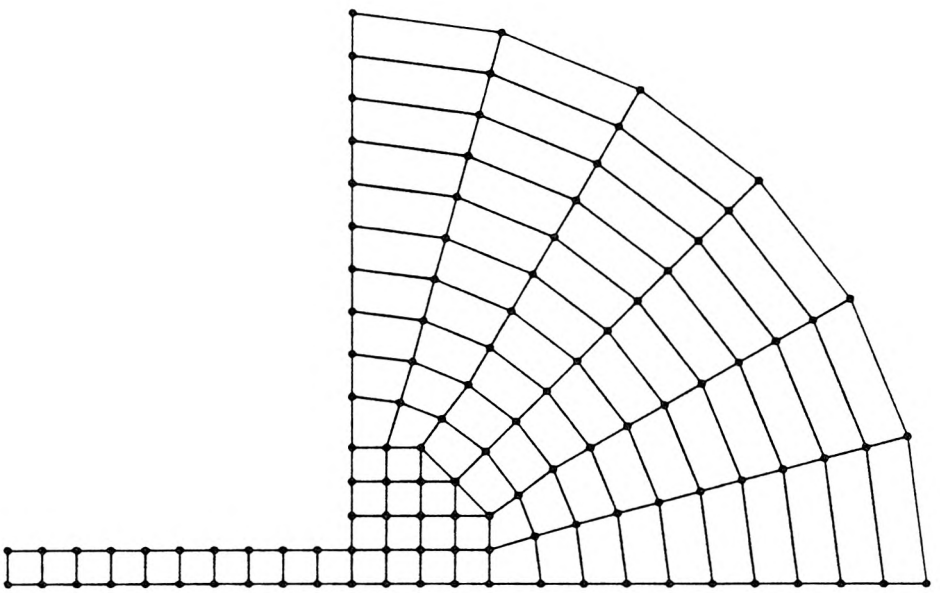

Fig. 5.1.14 Coarse finite element mesh with only one row of elements in the harbour region.

if the particle displacements are interpolated between this node and the one next to it (labelled "B") along the coastline, the interpolation will yield a nonzero component of particle displacement normal to the coastline along the entire line segment AB. Hence, the harbour will in some sense look wider than it actually is near the mouth. The particle displacements at the entrance are the largest at resonance and so this effect will be most noticeable near the resonant peaks of the harbour response curve. The result is that more energy is radiated from the mouth of the harbour than would be if the normal component of displacement were exactly zero along the line segment AB. Thus, the numerical model predicts a slightly lower response near resonance than the theoretical model. A finer finite element mesh would improve the estimate of the harbour response because the distance AB over which there would be a nonzero normal component of particle displacement would decrease.

To test this hypothesis, the simulations were performed again using two different type meshes. One mesh was coarser than that in Fig. 5.1.10. As shown in Fig. 5.1.14 it had only one row of elements instead of two along the length of the half-harbour (i.e., 2 elements across the full width of the harbour). These results are represented by the squares in Fig. 5.1.12. The other mesh (not shown) was finer. It had *three* rows of elements along the length of the half-harbour (i.e., 6 elements across the full width of the harbour). The results for this harbour are represented by the diamonds in Fig. 5.1.12. As expected, the maximum response corresponding to the first two modes increases in height for the finer mesh and decreases in height for the coarser mesh.

The maximum value of the amplification factor corresponding to the first resonant mode, $R_{\text{res}}$, is plotted as a function of the number of elements across the full width of the harbour in the inset of Fig. 5.1.12. It is not clear how close the numerical solution would converge towards the theoretical response curve given an arbitrarily fine mesh, but it is clear that the mesh resolution near the harbour entrance is probably the major source of error near the peaks in the response curve. Notice that away from resonance, where the harbour response is less sensitive to the amount of energy radiated from the entrance, the harbour response, as computed with each of the three different mesh resolutions, shows good agreement with each other and with the theory of Section 3.2. For subsequent simulations it was decided to use the meshes respresented in Figs. 5.1.10a and 5.1.10b. The coarser mesh was too crude and did not give very good results for the larger values of $kL$, and the finer mesh required significantly more computation, although it did yield better results. In any practical application the user must compromise between mesh resolution and computational cost.

It is interesting to note that Lee (1969) obtained similar results to those respresented by the triangles in Fig. 5.1.12. However, he used a boundary integral

technique based on the Helmholz equation, using three segments across the entrance of the harbour. Even though his numerical method was fundamentally different from the finite element technique being used here, it is likely that he, too, would have benefited from a finer discretization as well, particularly near resonance.

It was mentioned in Section 3.2.3 that if the entrance loss coefficient $f$ was determined by simply comparing experimental results to a numerical model and adjusting its value until the two agreed, then the value obtained would likely be a little smaller than the "true" value that would be obtained if the model equations could be solved exactly by an analytical technique. The effect of the finite size of the elements at the harbour entrance is to introduce additional radiation dissipation into the model. Hence, the value of $f$, which would be obtained by matching the experimental results to the numerical results, would not have to account for this additional dissipation introduced by the finite mesh resolution. The "true" value of $f$ (corresponding to infinite resolution at the harbour entrance) would be larger since it would also account for the additional dissipation introduced by the finite mesh resoution. On the other hand, computing the entrance loss coefficient $f$ by matching the experimental results to the numerical results would tend to lump other physical sources of dissipation, which weren't explicitly accounted for in the model, into this coefficient. This would *increase* the value of $f$ somewhat. Therefore, it is important that these sources be included and treated accurately in the model. Nevertheless, the value used in the numerical model for simulations would depend upon the particular geometry and the finite element mesh used. The finer the resolution near the harbour entrance, the larger the value of $f$. Even for a fixed nodal geometry, the value of $f$ would depend upon the type of elements used, i.e., linear or quadratic, quadrilaterals or triangles.

For the remaining comparisons, entrance losses were included. As discussed

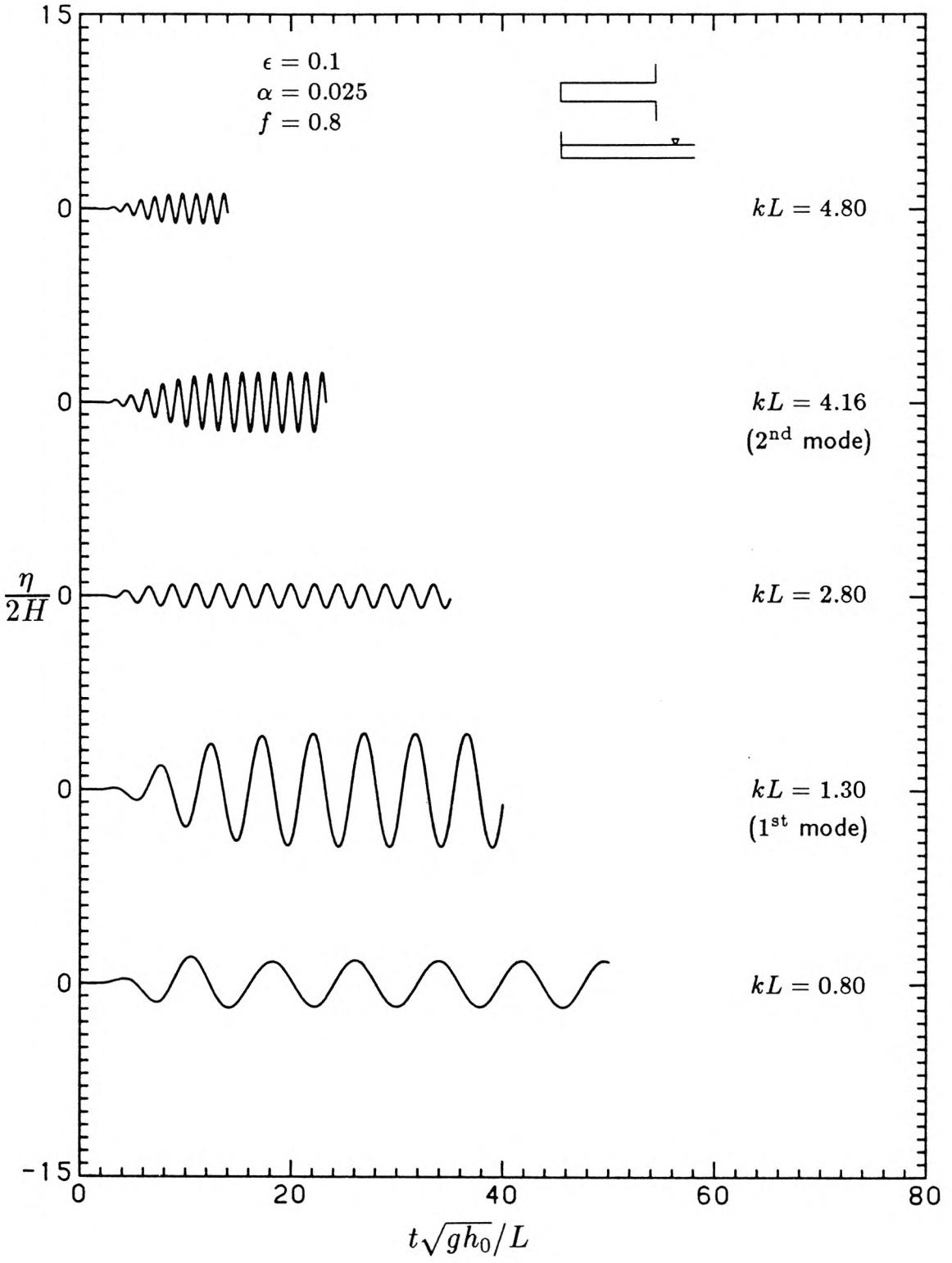


Fig. 5.1.15 Finite element model wave records associated with the 3 nodes along the backwall of a constant depth rectangular planform harbour.

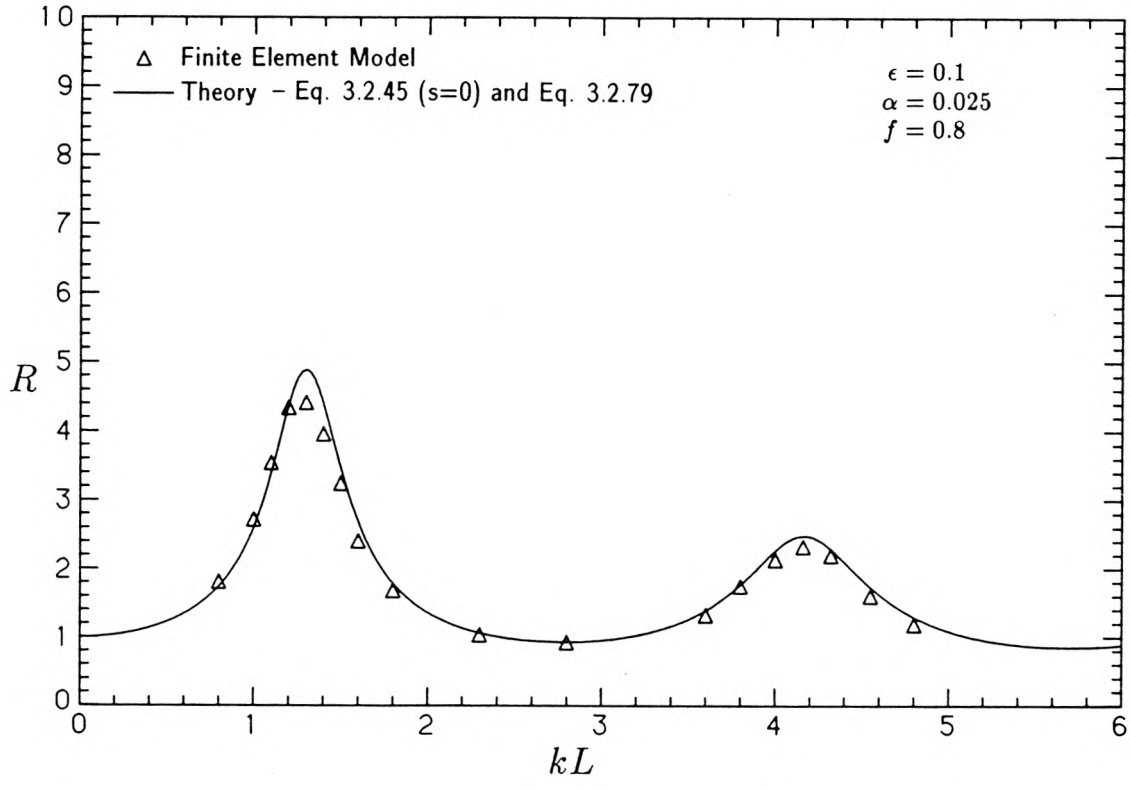


Fig. 5.1.16 Response of a constant depth rectangular harbour. Entrance losses included.

earlier, the entrance loss coefficient, $f$, was chosen to be 0.8. Also, as mentioned previously, three different bathymetries were modelled: (1) constant depth, (2) linearly sloping bottom, and (3) parabolic bottom. For each of these cases two different figures are shown. Figures 5.1.15 & 5.1.16 correspond to the constant depth harbour, Figs. 5.1.17 & 5.1.18 correspond to the harbour with the linearly sloping bottom, and Figs. 5.1.19 & 5.1.20 correspond to the harbour with the parabolic bottom. Each of the first figures, 5.1.15, 5.1.17, and 5.1.19 shows five representative water surface time histories obtained at the backwall of the constant depth harbour or at the shoreline of the sloping bottom harbours. Two of the five water surface time histories correspond to the first and second resonant modes of the harbour and the other three correspond to wave periods different from these. To give an idea of the degree of three-dimensionality within the harbour, each wave

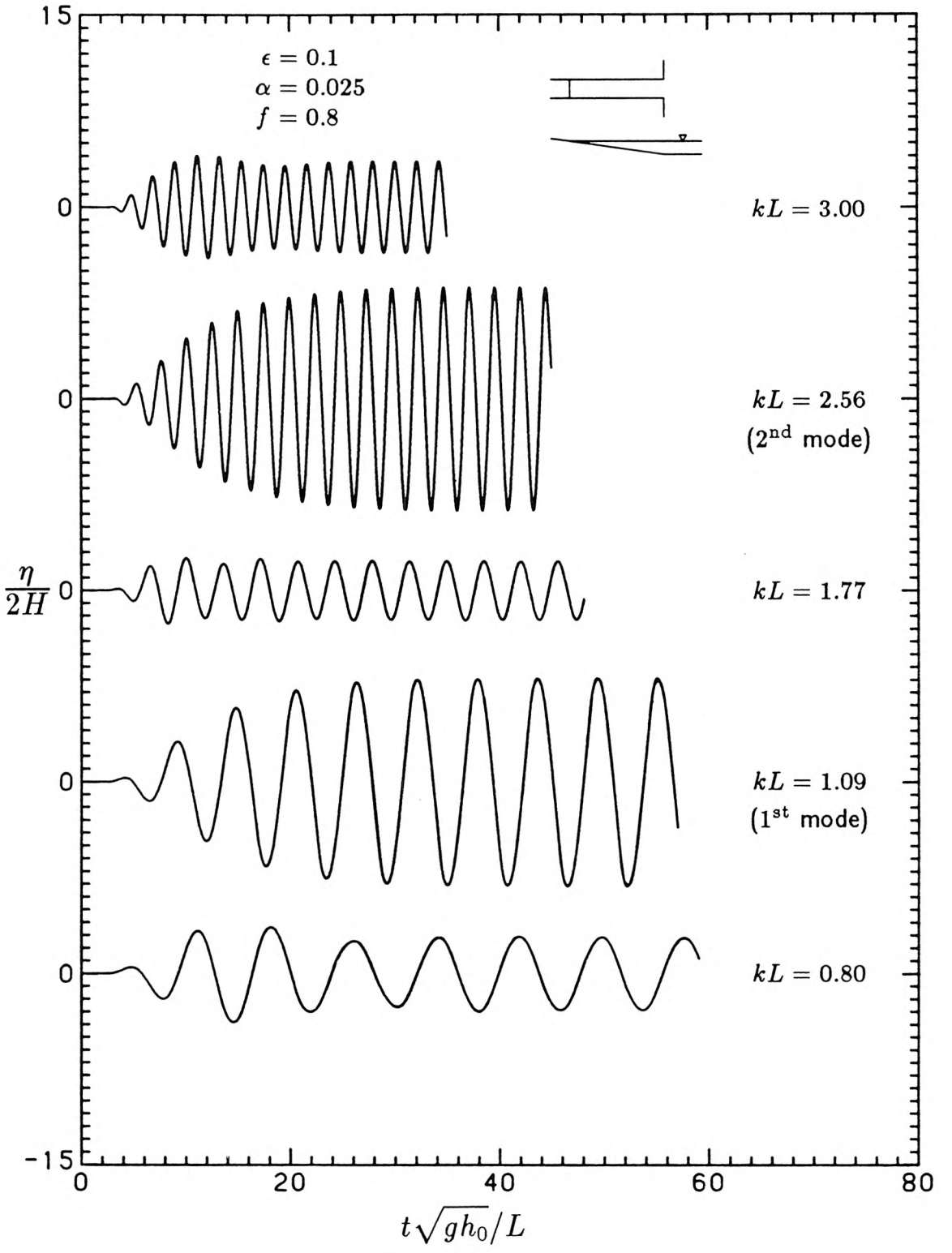


Fig. 5.1.17 Finite element model wave records associated with the 3 nodes along the shoreline of a rectangular planform harbour with a linearly sloping bottom.

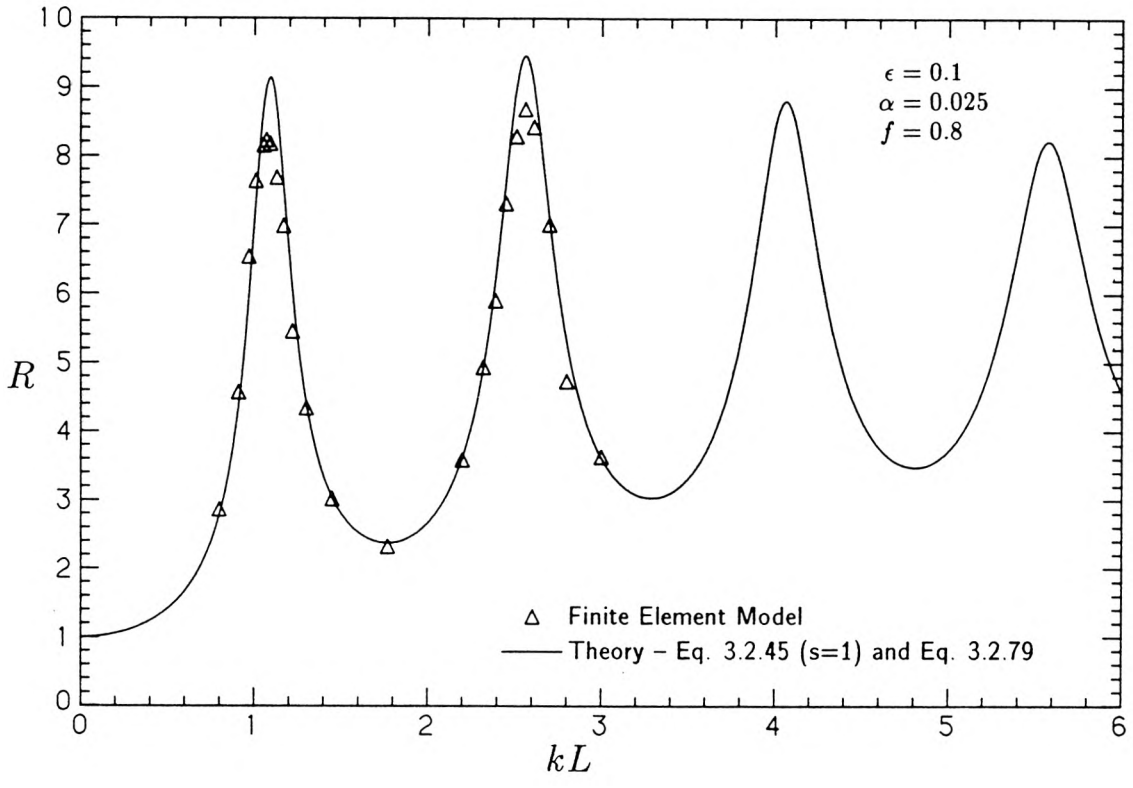


Fig. 5.1.18 Response of a rectangular harbour with a linearly sloping bottom. Entrance losses included.

record is actually a superposition of the three wave records corresponding to the three nodes along the backwall or shoreline of the harbour. The following figures, 5.1.16, 5.1.18, and 5.1.20 show the comparison between the harbour response curve computed from Eq. (3.2.79) of Section 3.2 and from the finite element model. The finite element model results correspond to the centre node at the harbour backwall or shoreline. Notice that the scales for each of the corresponding figures are the same, so one can get a good idea of the relative magnitudes of the response characteristics of each of these harbours.

The response of each of the harbours was very uniform across the width of the harbour at the backwall or shoreline, although there was a small amount of three-dimensionality near the first resonant mode for the harbour with the quadratic bottom (Fig. 5.1.19). The cause of this slight three-dimensionality was not clear.

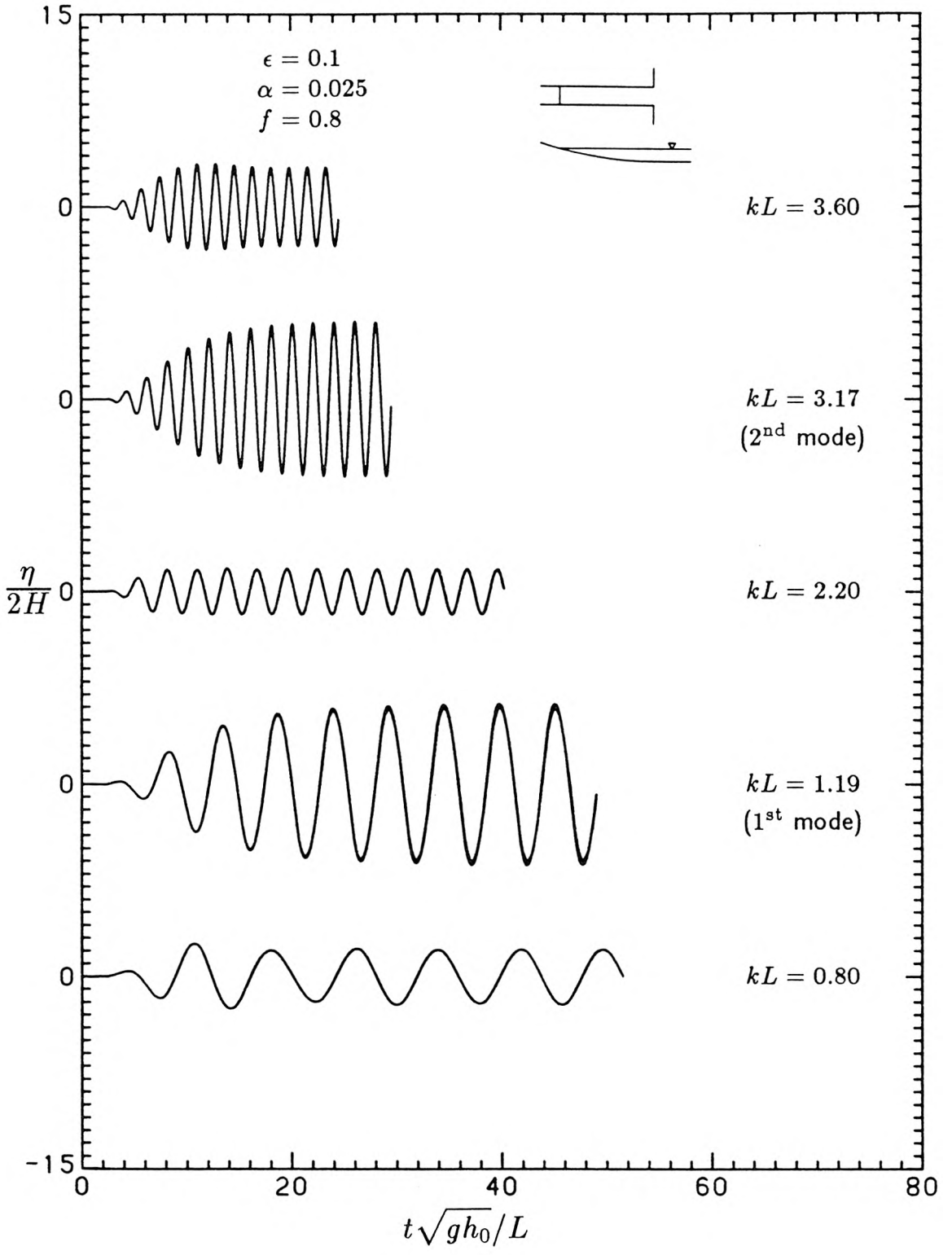


Fig. 5.1.19 Finite element model wave records associated with the 3 nodes along the shoreline of a rectangular planform harbour with a parabolic bottom.

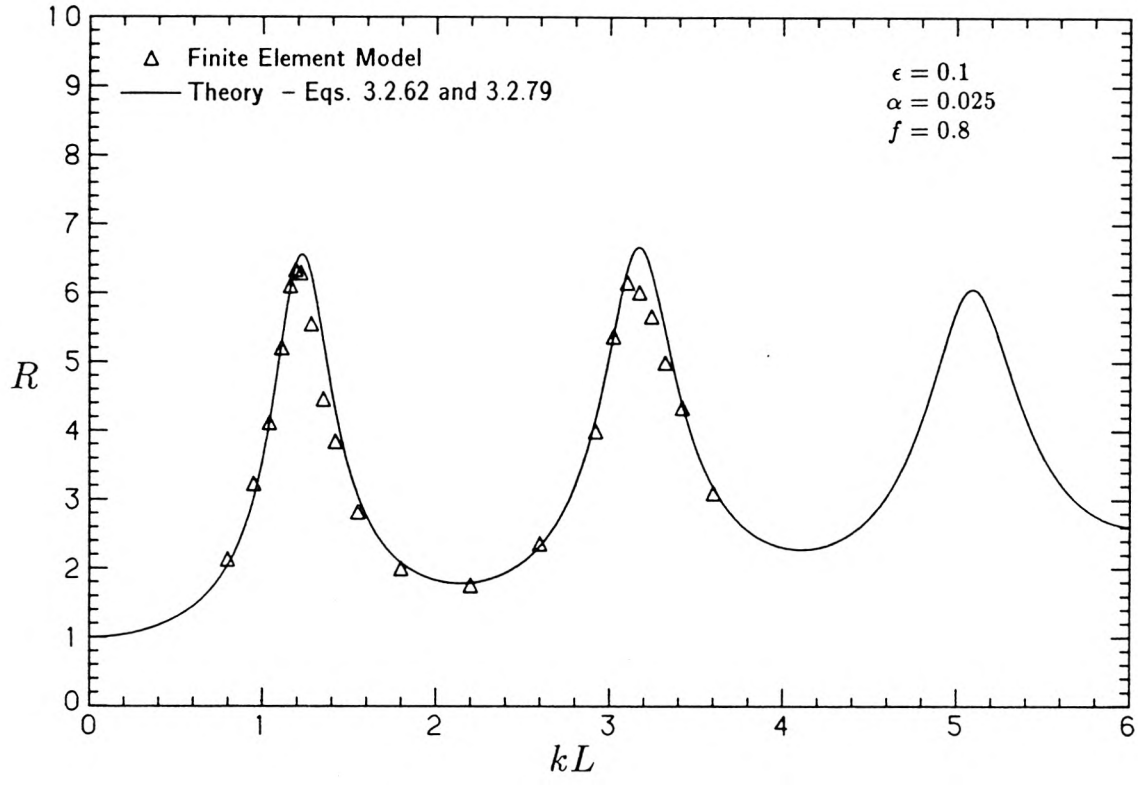


Fig. 5.1.20 Response of a rectangular harbour with a parabolic bottom. Entrance losses included.

The finite element results compare very well with the theory of Section 3.2, although the numerical model slightly underpredicts the height of the resonance peaks, as discussed in the case with $f = 0$ for the constant depth harbour; however, the discrepancy appears to be a little less for these cases with $f = 0.8$. Also, notice that the second resonant mode response is greater than at the first mode for the harbour with the linearly sloping bottom in Fig. 5.1.18. That occurs because the entrance dissipation is much greater for the first mode response; at the second mode the velocities at the harbour entrance are smaller, so there is less entrance dissipation. Also, shoaling effects are much greater for the second mode, so the overall response at this mode is greater than that of the first mode (however, if the effects of shoaling over the sloping bottom were removed from the response curve in Fig. 5.1.18, the second mode response would fall below that of the first mode).

However, for the harbour with the parabolic bottom (Fig. 5.1.20), the response at both the first and second resonant modes is nearly identical, whereas for the constant depth harbour (Fig. 5.1.16) where shoaling plays no role, the response at the first mode is clearly greater than at the second mode.

## 5.2 Comparison With Harbour Response Experiments

Harbour response experiments were conducted in the wave basin facility discussed in Section 4.1 and shown in Figs. 4.1.1 and 4.1.2. A rectangular harbour with a linearly sloping bottom was chosen. In the constant depth outer region, representing the open sea, the still water depth was $h_0 = 7\,\mathrm{cm}$. A train of weakly nonlinear cnoidal waves was generated in the initially quiescent basin with the microprocessor-controlled servo-hydraulic wave generator discussed in Section 4.2. The wave period was $T = 2\mathrm{sec}$; thus, $\omega = \pi\,\mathrm{sec}^{-1}$. Based on cnoidal wave theory, the approximate wavelength of this wave system is $\lambda = 1.64\,\mathrm{m}$ $(\lambda/h_0 = 23.4)$, very close to the linear long wave result computed from $\lambda = T\sqrt{gh_0}$. The wave generator was located approximately $6.9\,\mathrm{m}$ from the harbour entrance. Since the basin outside the harbour was meant to simulate the open ocean, which allows all wave energy radiated from the harbour mouth or reflected from the coastline to propagate away out to infinity without returning, this placed an upper limit on the number of periods of the incident wave system the harbour could be exposed to. Waves that propagated away from the harbour eventually reflected from the wave generator and returned to the harbour. Therefore, for these experiments it was possible to expose the harbour to only approximately eight periods $(2 \times 6.9\,\mathrm{m} \div 1.64\,\mathrm{m} \approx 8)$ of the incident waves. The steady-state wave amplitude at the harbour entrance with the entrance closed was $2H = 0.20\,\mathrm{cm}$. This wave record was used to define the incident-reflected wave record used for input to the finite

element model. The ratio of the width of the harbour to its length $2b/L$ was chosen to be 0.2 as it was in the previous section, where the finite element model was compared with the harbour response theory of Section 3.2. The same incident waves were used for each of the runs so that the spectral energy distribution in the incident wave was fixed and the characteristic time scale $T$ was also fixed. The response of the harbour was varied by changing the length of the harbour, keeping the width to length ratio equal approximately to 0.2, as discussed in Section 4.3. The harbour response parameter $\omega L/\sqrt{gh_0}$ was therefore varied by changing $L$, not $\omega$. See Appendix B for a complete list of the values of $2b$, $L$, and the parameters $2b/L$, and $\omega L/\sqrt{gh_0}$ for each of the experiments.

The parameter $\omega L/\sqrt{gh_0}$ was chosen as the harbour response parameter instead of $kL = 2\pi L/\lambda$ because the wave frequency, $\omega$, was a specified parameter, whereas the wavelength, $\lambda$, would have to be measured experimentally. According to linear nondispersive long wave theory these two parameters are identical since this theory predicts $k = \omega/\sqrt{gh_0}$. However, due to small nonlinear and dispersive effects, which are accounted for in cnoidal wave theory, $kL$ and $\omega L/\sqrt{gh_0}$ differ slightly.

The terms in the long wave equations that relate to boundary layer dissipation must be modified slightly to treat this harbour bathymetry. The derivation of these terms in the equations of motion required the assumption that the water depth $h(a,b)$ was much greater than the boundary layer thickness. This assumption must of course break down at the shoreline, where $h(a,b) \to 0$. From Eq. (3.4.3) the coefficient of these terms is $\gamma/h(a,b)$, where $\gamma$ is the boundary layer dissipation parameter defined in Eq. (3.4.4). The violation of the assumption is reflected by the singular behaviour of this coefficient at the shoreline. In reality the dissipation, of course, does not grow unbounded at the shoreline. The following simple modification to this formula was made to avoid this problem. An estimate of the

boundary layer thickness $\delta$ was made using Eq. (3.1.22). The boundary layer dissipation terms are valid away from the shoreline where the still water depth is much greater than the boundary layer thickness $\delta$; i.e., $h(a,b) > d\delta$ where $d \gg 1$. The coefficient $\gamma/h(a,b)$ was used everywhere away from the shoreline where this was valid, but near the shore where $h(a,b) < d\delta$ the coefficient was replaced with $\gamma/d\delta$, the value of the coefficient near the shoreline where the approximations are still valid. The constant $d$ was chosen to be 10. Although this may seem to be a somewhat crude method of clearing up the difficulty at the shore, it is not necessary to be more accurate for the following reason. For the range of parameters applicable to the experiments performed in this investigation, the amount of power dissipated within the boundary layers is very small in comparison to the dissipation associated with entrance losses and the radiation of energy back out of the harbour entrance to the open basin. The relative importance of these sources of dissipation was discussed by Lepelletier (1980) for a constant depth rectangular harbour. For the conditions corresponding to the experiments in this investigation, the laminar friction losses are approximately an order of magnitude smaller than those associated with radiation. With a linearly sloping bottom the boundary layer losses will be somewhat larger since the average depth throughout the harbour is one-half that for a constant depth harbour, but these losses will still be small compared to the radiation and entrance losses. Hence, a small error in the treatment of the boundary layer losses will have very little effect on the solution computed. However, it should be noted that if the motion were confined to a closed basin with no radiation or entrance loss effects, the relative importance of laminar viscous dissipation would be much greater. It is true that if the waves break the dissipation will be very large near the shoreline. However, that dissipation mechanism is not at all related to the boundary layer dissipation model being considered here. Hence, the present investigation is limited to nonbreaking waves

only.

A further modification to the boundary layer dissipation terms was made to account for contamination of the water surface. Surfactants can form a thin film, which introduces a horizontal laminar shear stress at the surface of the water. The velocity gradient can be expressed, approximately, in a form analogous to Eq. (3.1.71) as:

$$\frac{\partial^2 \mathbf{x}_{bl}}{\partial c \partial t} = -\frac{C}{\gamma \vartheta} \frac{\partial \mathbf{x}}{\partial t} \qquad c = 0 \tag{5.2.1}$$

where $\mathbf{x}_{bl}$ is the horizontal fluid particle displacement vector in the boundary layer at the surface. The parameter $C$ is known as the surface contamination factor. This effect can easily be accounted for in the finite element model by replacing the dissipation parameter, $\gamma$, in Eq. (3.4.3) by $\gamma(1+C)$. Experiments by Van Dorn (1966) indicate that for an initially clean liquid surface in contact with the ambient atmosphere, $C$ rapidly approaches a limiting value of unity, corresponding to a fully contaminated surface film. Therefore, for comparison with the harbour response experiments, a value $C = 1$ was used.

The treatment of dissipation in the boundary layer has been included in the finite element model to allow comparison with the experiments in this section. Therefore, it has been assumed that the boundary layer is laminar as discussed in Section 3.1.1.1. However, in an actual harbour the boundary layer will be turbulent so the associated dissipation must be modelled differently. In that case the bed stress can be modelled proportional to the square of the horizontal velocity. However, since the finite element model will not be compared with field data, this capability was not included, although it would not present a large problem to do so.

A head loss coefficient at the harbour entrance of $f = 0.8$ was used in the numerical simulations of each of the experiments. This is the same value that was

used to compare the results of the finite element model to the harbour response theory developed in Section 3.2. It is also the same value used by Lepelletier (1980) for the harbours with fully open entrances (i.e., no breakwater partially closing the entrance).

The harbours used in the experiments were symmetric about the longitudinal axis of the harbour, so the finite element computations were performed using only one-half of the domain. Finite element meshes similar to that shown in Fig. 5.1.10a were used.

The response parameter $\omega L/\sqrt{gh_0}$ was varied from 0.70 to 2.08. This range fully encompasses the first resonant mode, as shown in Fig. 5.1.18. Figure 5.2.1 compares six of the water surface time histories obtained experimentally with those computed by the finite element model. The measurement location was along the centreline of the harbour midway between the entrance and the quiescent shoreline. For this comparison the results of the finite element model were converted to the Eulerian description using the method of Section 3.4.7. Measurements of the height of the shoreline (runup) as a function of time were not made because of the difficulties in the experimental techniques at the scale of these measurements.

The water surface time history in Fig. 5.2.1 with $\omega L/\sqrt{gh_0} = 0.$ is the experimental wave record obtained at the entrance to the harbour (point A in Fig. 4.1.3) with the harbour entrance closed (i.e., the record obtained when the incident wave reflected from a vertical wall). It was used to define the function $f(t)$ in Eqs. (3.4.18) and (3.4.19). The other six wave records compare the results of experiment and the finite element model for different values of $\omega L/\sqrt{gh_0}$.

The records for $\omega L/\sqrt{gh_0} = 0.70$ and 0.89 correspond to wavelengths below the first resonant mode. The finite element model results agree extremely well with the experimental results for $\omega L/\sqrt{gh_0} = 0.70$. The comparison is still very good for $\omega L/\sqrt{gh_0} = 0.89$ with only a very slight discrepancy in the minimum

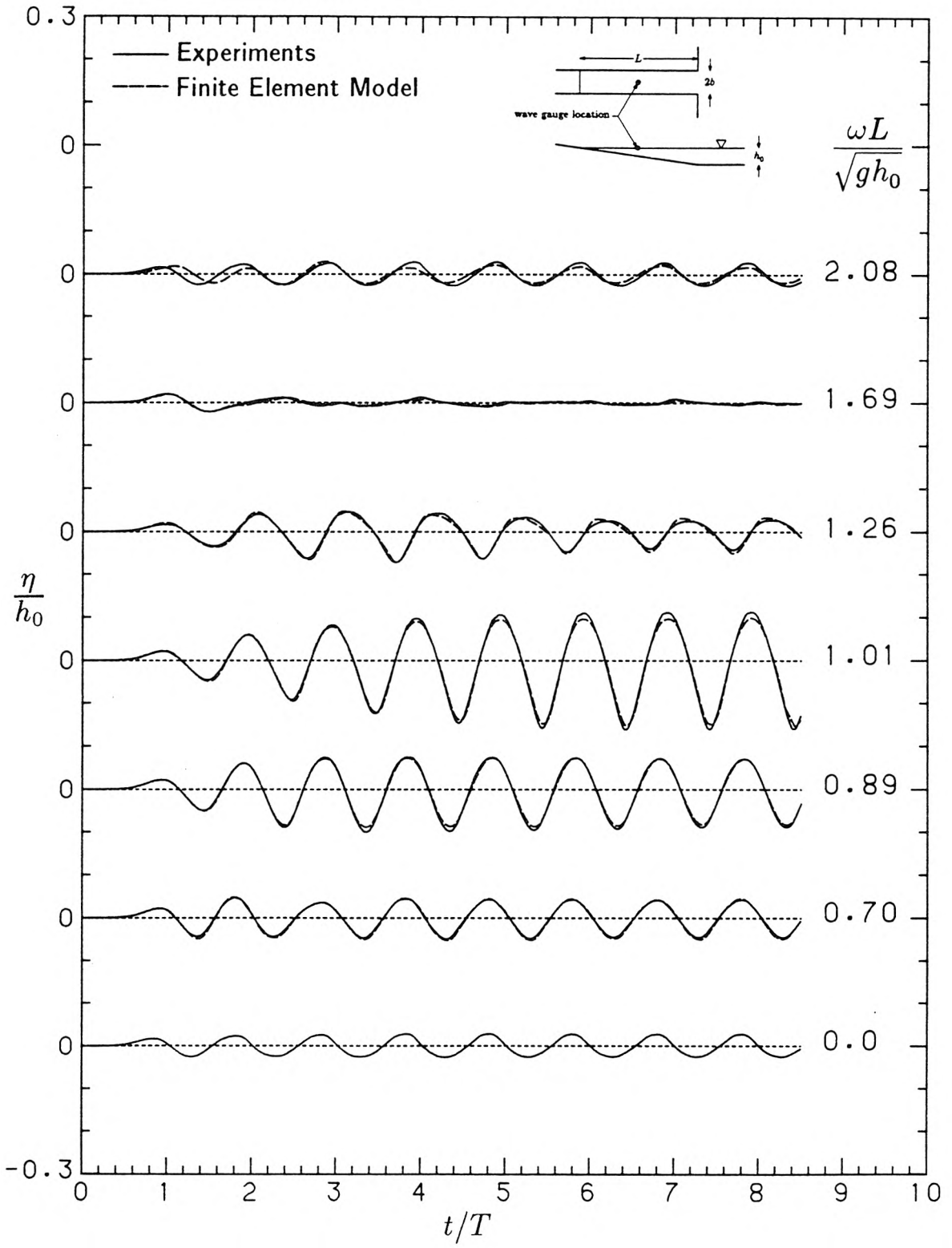


Fig. 5.2.1 Wave records measured at the centre of the harbour. Comparison of experiments with the finite element model for different values of $\omega L/\sqrt{gh_0}$.

wave extrema.

The largest response occurred for the experiment with $\omega L/\sqrt{gh_0} = 1.01$ which corresponded to the first resonant mode of the harbour. The amplitude of the finite element model results is slightly smaller than that of the experimental results but the agreement is still very good. Notice how the troughs are larger than the peaks. That difference is due to the nonlinear effects which were discussed in detail in Section 3.3 and Section 5.1.1 (Fig. 5.1.3). The effect is very noticeable near resonance where the wave heights, and hence the nonlinear effects, are the greatest. The crests and troughs in the experimental wave record are approximately $\eta/h_0 = 0.11$ and $\eta/h_0 = -0.16$, respectively.

The agreement between the experimental results and the finite element model is also very good for normalized frequencies beyond resonance. Of all the records shown, the one corresponding to $\omega L/\sqrt{gh_0} = 1.26$ is the slowest to reach steady state. In fact, it does not reach steady state within the eight periods of excitation shown. In addition, its shows that the maximum harbour response occurs during the transient portion of the motion. It appears that the steady-state response will be lower. These characteristics were present to some degree in most of the experiments for frequencies just above resonance in the region where the harbour response decreased as $\omega L/\sqrt{gh_0}$ increased.

The harbour response for $\omega L/\sqrt{gh_0} = 1.69$ appears to be suprisingly small. Although the steady-state response at the measurement location is indeed very small, the overall harbour response is not this small. At steady state a node is very near the measurement location for $\omega L/\sqrt{gh_0} = 1.69$, so the wave height is very small near this location but not so elsewhere in the harbour. It was shown in Section 3.3 (see Fig. 3.3.2) that periodic waves on a linearly sloping bottom can exhibit a curious behaviour, in a nonlinear sense, at and near the points where nodes are predicted by linear theory. The wave height is not zero

at these points. Instead, at and near these points the wave records exhibit twice as many minima and maxima compared to locations away from these points. The results of Section 3.3 are based on the assumption that the sloping bottom extends to infinity where the motion is perfectly harmonic and two-dimensional. The harbour response experiments do not satisfy these assumptions but the motion was quite two-dimensional within the harbour; the incident wave was very close to a single harmonic plane wave, and the bottom was linearly sloping within the harbour, so one would expect some qualitative agreement between these two cases. Unfortunately, this effect cannot be seen in the record for $\omega L/\sqrt{gh_0} = 1.69$. First of all, the overall response of the harbour for $\omega L/\sqrt{gh_0} = 1.69$ was not large, so the nonlinear effects were not great. Also, the presence of small amplitude higher harmonics in the incident wave would tend to mask this effect. Finally, it is not clear that the transient harbour response had completely died out at the end of eight periods of the incident wave.

The agreement for $\omega L/\sqrt{gh_0} = 2.08$ is still fairly good, although there is a small phase shift between the two records which can be seen during the first period of motion up to $t/T = 2$. The two records were aligned to maximize the agreement of the established motion after the arrival of the incident wave system. The reason for this phase shift is not known. The numerical model actually predicts a slightly larger response than the experimental results.

As mentioned previously, the value of the entrance loss coefficient $f$ was chosen to 0.8 based on the results of Lepelletier (1980). He obtained this value by forcing agreement between many sets of experiments and his numerical model. It appears that a value of $f$ slightly less than 0.8 would provide best agreement between the present experiments and the finite element model. That would cause the amplitude of the finite element results to increase near resonance. The agreement in the response *away* from resonance would remain very good because it is

insensitive to the value of the entrance loss coefficient. However, the overall agreement here for $f = 0.8$ is very good, nonetheless, and any effort spent making small adjustments in the entrance loss coefficient to force even better agreement is of doubtful value since the coefficient depends on many factors. If the same set of experiments were modelled with a different finite element mesh, the value of $f$ which maximized the agreement would be slightly different again, as shown in Section 5.1.3.

The results of the experimental runs are summarized in Fig. 5.2.2 where these results are compared with the linear theory of Section 3.2 and with the nonlinear dispersive finite element numerical model. As mentioned earlier, the measurement location is on the centreline of the harbour midway between the entrance and the quiescent shoreline. In Fig. 5.2.2 three different quantities are displayed, each as a function of the parameter $\omega L/\sqrt{gh_0}$: the wave height maxima, the wave height minima, and the mean water level. The drop in the mean water level can also be seen in Fig. 5.2.1 near resonance ( $\omega L/\sqrt{gh_0} = 1.01$ ) where it is seen that the troughs of the waves are much greater than the peaks. This leads to a negative mean water level as described in Section 3.3 where the nonlinear effects of runup on a beach with a linearly sloping bottom were discussed.

The results of the linear theory of Section 3.2 are indicated in Fig. 5.2.2 by the solid lines which represent the steady-state maximum and minimum wave heights at the measurement location. The steady-state wave record at the harbour entrance with the entrance closed was used to define the incident wave. Using this record, the results shown in Fig. 5.2.2 were then obtained using the Fourier synthesis technique described in Section 3.2.8. It should be recalled that the individual Fourier modes are coupled through the headloss formula of Eq. 3.2.23. Hence, although the theory of Section 3.2 is basically linear in nature, the nonlinear character of the headloss dissipation introduces a weak nonlinear coupling of the

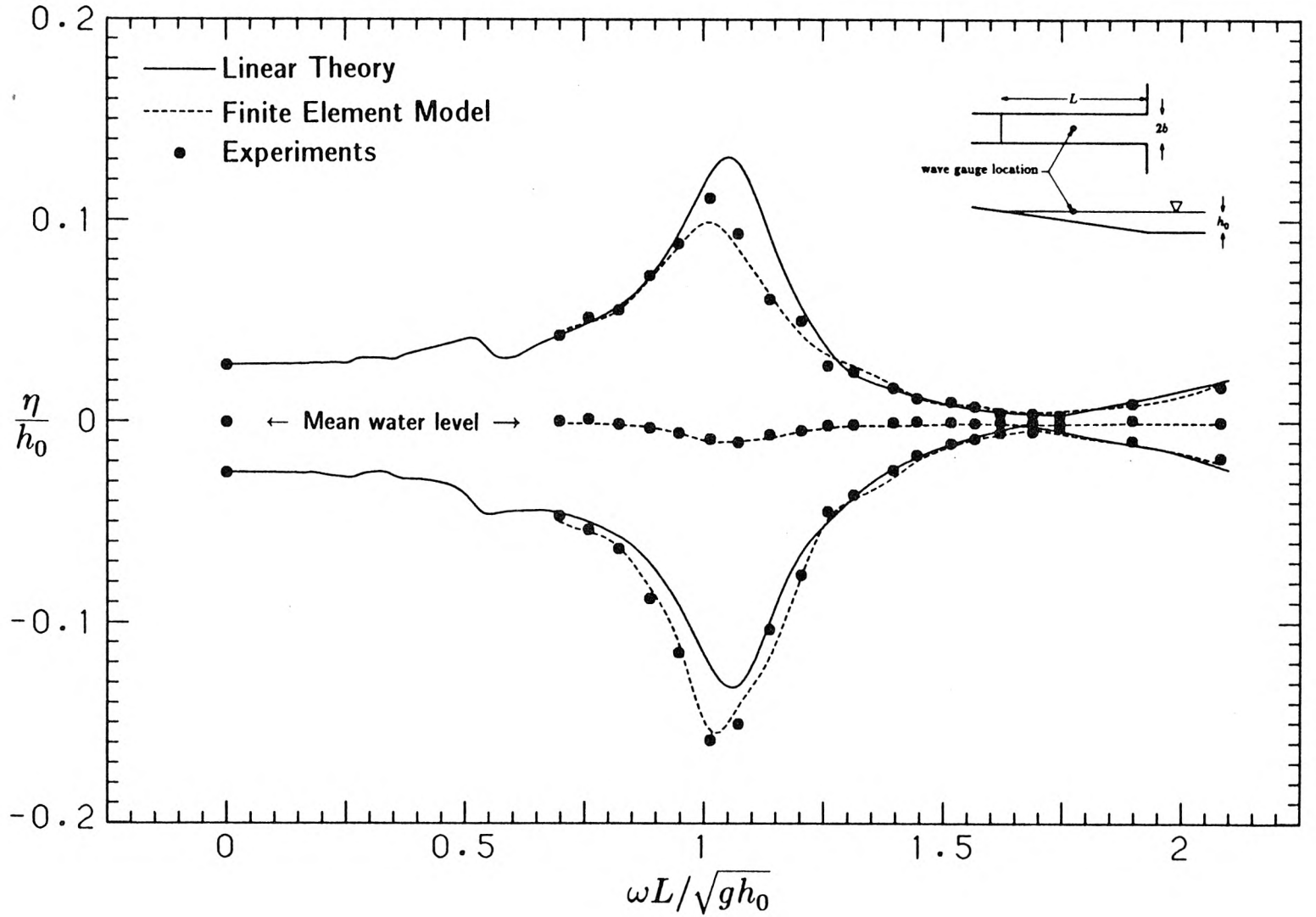


Fig. 5.2.2 Variation of the wave extrema and mean water level with $\omega L/\sqrt{gh_0}$, at the centre of the harbour.

Fourier modes. The small peaks in the linear response curves in Fig. 5.2.2 near $\omega L/\sqrt{gh_0} = 0.5$ are due to the first resonant mode response of the second harmonic component in the incident wave.

Since there is no mechanism provided to transfer energy into the zero frequency harmonic component, the linear theory predicts that the mean water level coincides everywhere with the still water level $\eta/h_0 = 0$. For that reason, the linear theory *over*predicts the maxima and *under*predicts the minima in the harbour response in Fig. 5.2.2.

The finite element model agrees much better with the experimental results than does the linear theory, and the mean water level is reproduced well. Near the resonant peak at $\omega L/\sqrt{gh_0} \approx 1$ (where the wave ampitude is the largest) the mean water level is significantly less than zero, which is consistent with the results discussed in Section 3.3 where the mean water level became more negative as the amplitude of the wave increased. The wave height extrema are also predicted well, although the finite element model underpredicted both the peaks and the troughs slightly near resonance. If an entrance loss coefficient $f$ slightly smaller than 0.8 were used, the agreement near resonance between the experiments and theory would improve without significantly altering the response away from resonance, as discussed previously.

In the discussion of Fig. 5.2.1 it was noted that in the region $\omega L/\sqrt{gh_0} > 1$; i.e., normalized frequencies greater than the first resonant mode, a steady-state response was not always obtained within the first eight oscillations, although the convergence was generally good enough to permit a reasonable estimate. For those cases where a definite steady state had not been reached, the harbour response was arbitrarily defined by the average of the maxima and the average of the minima in the wave record for the $7^{\text{th}}$ and $8^{\text{th}}$ periods of oscillation. Similarly, the mean water level was defined by the mean value of the wave record for the $7^{\text{th}}$ and

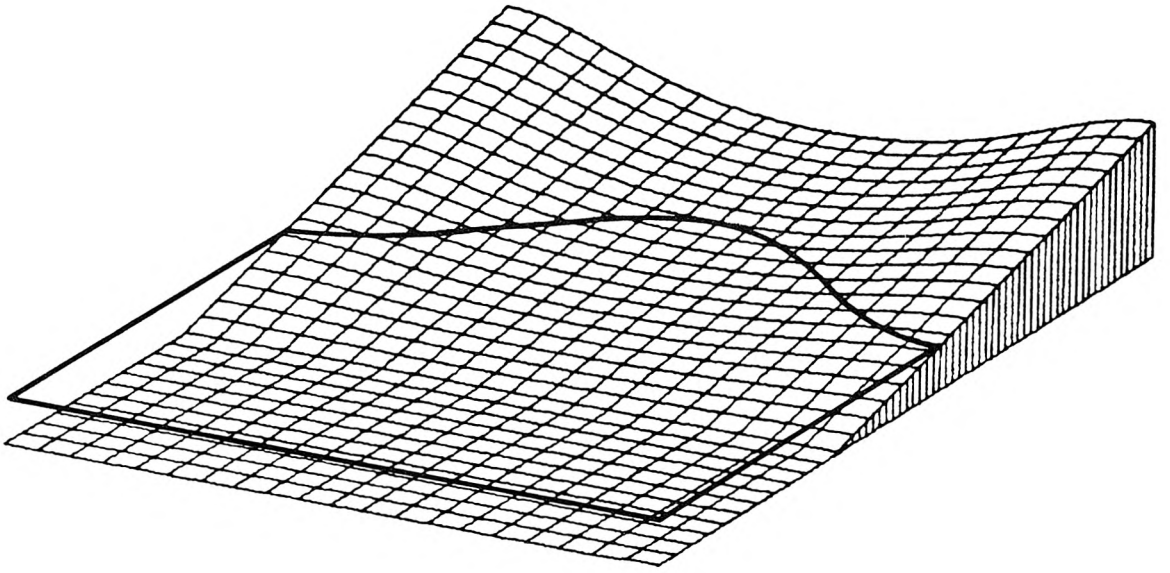

Fig. 5.3.1 Bathymetry of the test case.

$8^{th}$ periods of oscillation. This was done for both the experimental and the finite element model results displayed in Fig. 5.2.2.

## 5.3 Three-Dimensional Application of the Finite Element Model

To further illustrate the capabilities of the finite element model, a strongly three-dimensional test problem was chosen, which combines several aspects of direct importance to harbour or bay resonance. The test case geometry combines a curved shoreline with a sloping nearshore bathymetry that merges with a constant depth region far from shore. This geometry permits a complex interaction of different processes to influence the shoreline runup.

A view of the bathymetry can be seen in Fig. 5.3.1. The bottom is represented

by the rectangular mesh. The outline of the still surface is delineated by the single closed line located above the bottom. The curved portion of this line traces the shoreline which, in plan view, is one period of a sine wave. The constant depth region continues indefinitely offshore. The computations were performed assuming the region was bounded laterally by vertical walls. By symmetry this is also equivalent to treating a periodic coastline formed from bays situated between steep promontories. The slope of the bottom perpendicular to the shoreline at these two extreme lateral extents is 1:5. The slope of the bottom perpendicular to the shoreline at the centre of the bay is 1:10. The vertical scale in Fig. 5.3.1 is correct although it may appear to be exaggerated due to foreshortening caused by the three-dimensional perspective.

It is evident from the view of the bathymetry in Fig. 5.3.1 that many different processes may occur and interact to modify the shoreline runup. Refraction will tend to cause incident waves to bend towards the promontories at either edge of the domain seen in Fig. 5.3.1, whereas reflection from these projections will tend to direct wave energy to the shoreline at the centre of the bay. In addition, the sloping bathymetry can support edge wave type modes that may partially trap energy in the nearshore region. The combination of these above effects may greatly influence the shoreline runup in ways not possible in models that approximate the nearshore geometry with a vertical wall.

A definition sketch of the geometry is shown in Fig 5.3.2. As mentioned previously, this geometry is equivalent to treating a periodic coastline formed from bays situated between steep promontories. This periodic extension is indicated by the dashed lines extending from each lateral boundary of the shoreline. Although there is little reason for confusion, the hats above the coordinate axis labels, i.e., $\hat{x}$ and $\hat{y}$, emphasize that they represent the coordinates relative to the origin $(\hat{x},\hat{y}) = (0,0)$, not relative to a particle's initial position. All quantities in this

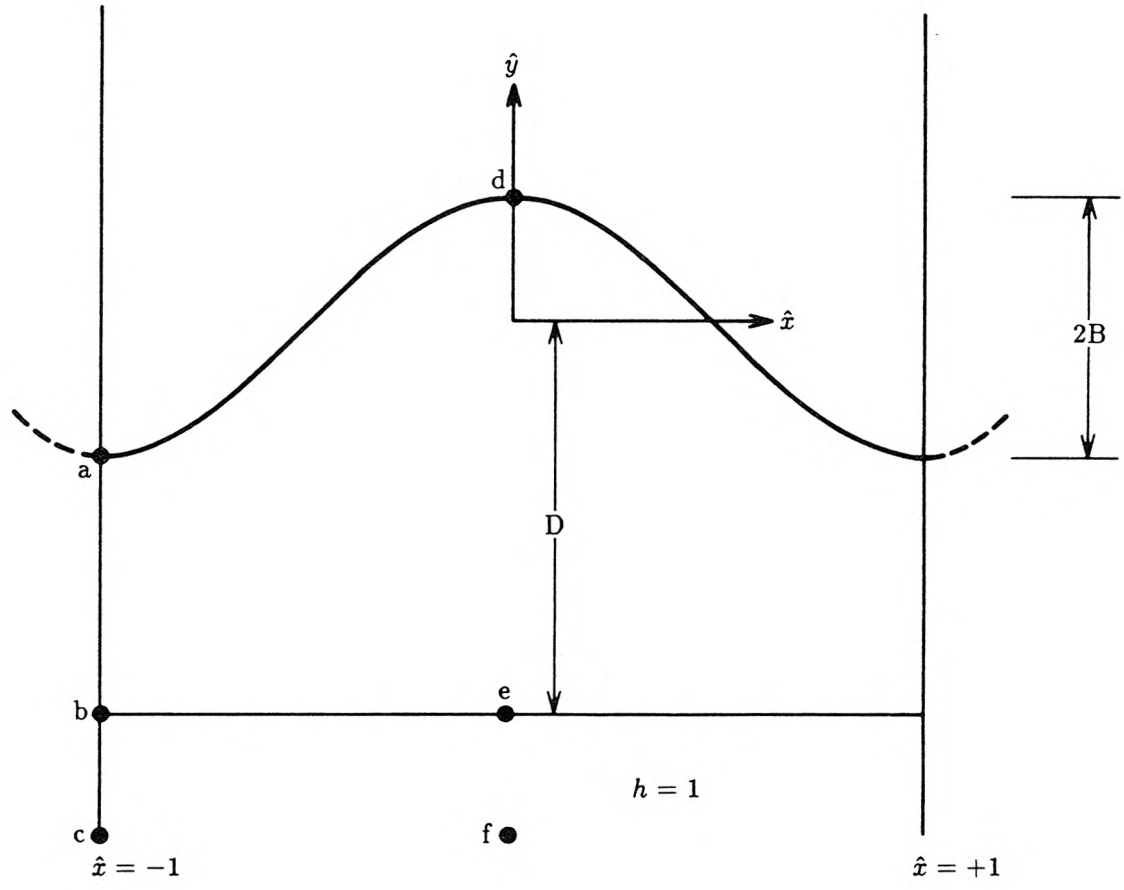


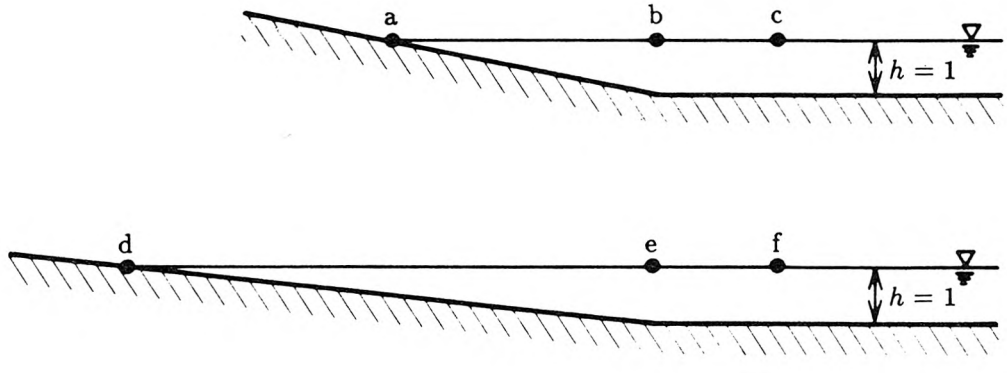


Fig. 5.3.2 Definition sketch of the test case geometry.

figure are nondimensional and all quantities in this section will be nondimensional unless otherwise explicitly stated. The nondimensionalization of Section 3.1.2 was chosen where the characteristic water depth , $h_0$ , was chosen to be the constant offshore water depth, the horizontal length scale, $\ell$ , was chosen to be one-half of the width of the bay in Fig. 5.3.2, and the characteristic wave height, $H$ , was chosen to be the incident wave height, to be discussed shortly. Hence, the offshore nondimensional water depth is $h = 1$ , and the lateral boundaries of the domain are located at $\hat{x} = \pm 1$ . The nonlinear parameter, $\alpha$ , and the dispersion parameter, $\beta$ , are defined exactly as in Section 3.1:

$$\alpha = \frac{H}{h_0} \qquad \beta = \left(\frac{h_0}{\ell}\right)^2 \quad . \tag{5.3.1}$$

In terms of the dimensionless variables, the still water depth was chosen to be:

$$h(\hat{x},\hat{y}) = \begin{cases} 1 - \dfrac{\hat{y}+D}{B\cos\pi\hat{x}+D} & \hat{y} \geq -D \\ 1 & \hat{y} < -D \end{cases} \quad . \tag{5.3.2}$$

For regions above the still water depth, $h$ is negative. The contours in the region $\hat{y} \geq -D$ corresponding to this bathymetry are:

$$\hat{y} = B(1 - \frac{y_0}{D})\cos\pi\hat{x} - y_0 \qquad y_0 \leq D \quad . \tag{5.3.3}$$

The quantity $y_0$ is a free parameter which specifies a particular contour. The shoreline corresponds to $y_0 = 0$ :

$$\hat{y}_{\text{shoreline}} = B\cos\pi\hat{x} \quad . \tag{5.3.4}$$

For the finite element model the parameters $B$ and $D$ were chosen to be:

$$B = \frac{1}{\pi} \tag{5.3.5}$$

$$D = \frac{3}{\pi} \quad . \tag{5.3.6}$$

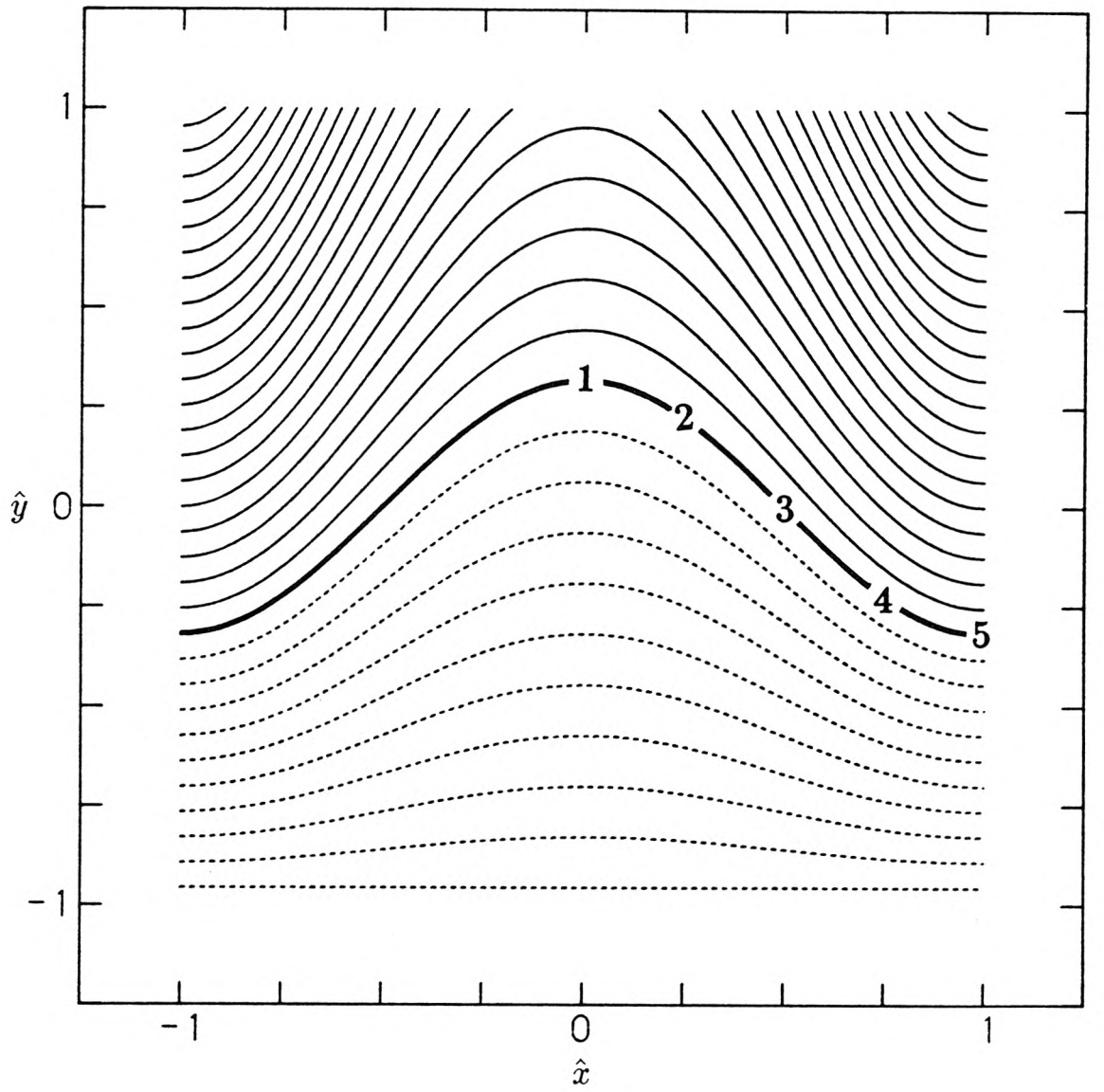


Fig. 5.3.3 Contours of the nearshore bathymetry. Heavy solid line corresponds to shoreline. Dashed lines below still water surface.

The contours of the still water depth are shown in Fig. 5.3.3 for $|\hat{x}| \leq 1$ and $|\hat{y}| \leq 3/\pi$. For $\hat{y} < -3/\pi$ the still water depth is constant. The shoreline corresponds to the heavy solid line. The dashed lines correspond to contours below the still water surface. The contour spacing was chosen to be one-tenth of the offshore still water depth. The labels 1, 2, ..., 5 refer to positions where

runup predictions will be made. They correspond to $\hat{x} = 0.$, 0.25, 0.5, 0.75, and 1.0.

Viscous bed stresses will be neglected. In general, their importance is difficult to judge. For typical laboratory studies of the scale considered in this work where the beach is smooth, the flow will be laminar and the concomitant dissipation will be small; it is likely that it will not alter the runup characteristics significantly. However, for large scale studies where the surface roughness of the shore region is large, the flow will be turbulent and the attendant dissipation may be large enough to be a major factor determining the runup height. Since this test case will be compared with neither laboratory nor field results, it is not possible to estimate "typical" bed stress dissipation rates and so, therefore, they will be neglected entirely.

A typical finite element mesh used for the computations is shown in Fig. 5.3.4. The entire mesh is shown alongside an enlarged view of the nearshore region. It is comprised exclusively of linear quadrilateral elements (see Fig. 3.4.2). Notice how the use of isoparametric elements allows the rectangular mesh to be gradually distorted in the nearshore region so that one of its boundaries conforms exactly to the still shoreline.

The input wave was chosen to be a solitary wave of the form:

$$\begin{aligned} \eta_{\text{E}}(t - \frac{\hat{y}}{c}) &= \operatorname{sech}^2 \sqrt{\frac{3\alpha}{4\beta}(1+\alpha)}\,(t - \frac{\hat{y}}{c}) \\ &= \operatorname{sech}^2 \chi\,(t - \frac{\hat{y}}{c}) \end{aligned} \tag{5.3.7}$$

where

$$\chi = \sqrt{\frac{3\alpha}{4\beta}(1+\alpha)} \tag{5.3.8}$$

and

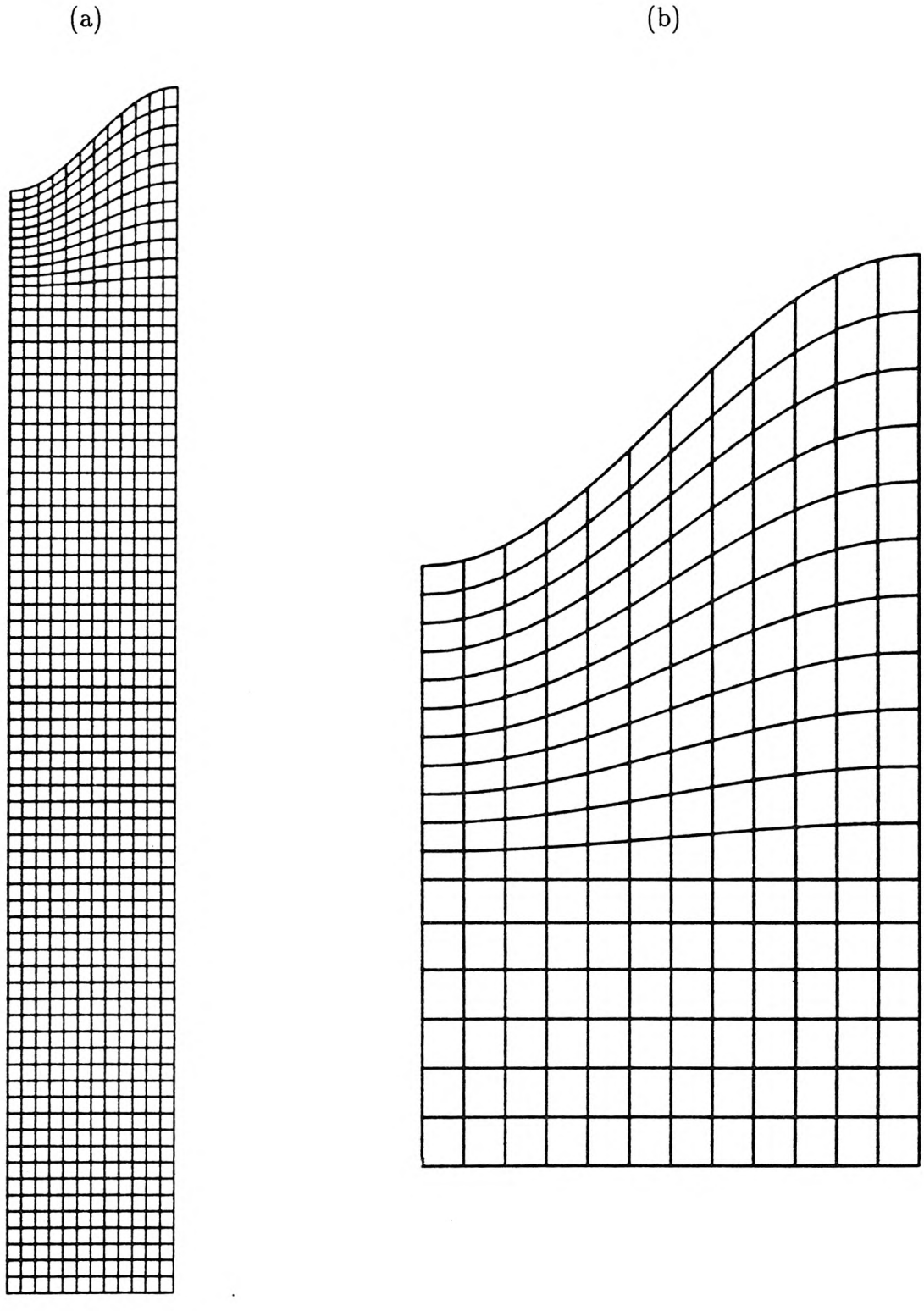


Fig. 5.3.4 (a) Typical finite element mesh, (b) enlarged view of mesh near the shoreline.

$$c = \sqrt{1+\alpha} \tag{5.3.9}$$

where $\alpha = H/h_0$, and the subscript $_E$ on $\eta$ shows that this is the expression for the water surface displacement in the Eulerian description. The characteristic wave height $H$ is the (dimensional) amplitude of the incident solitary wave far offshore in the constant depth region. The solitary wave of Eq. (5.3.7) travels with a nondimensional celerity $c = \sqrt{1+\alpha}$.

The results for eight cases will be shown with $\alpha$ varying from 0.001 up to 0.03. The incident solitary wave will be specified at the offshore boundary represented by the lower boundary of the finite element mesh in Fig. 5.3.4a. For each case the maximum and minumum runup values along the shore will be recorded as well as the time history of the runup at the locations 1, 2, ..., 5 shown in Fig. 5.3.3.

The solitary wave of Eq. (5.3.7) is written in the Eulerian description. However, input to the finite element model must be in the Lagrangian description. Therefore, Eq. (5.3.7) must be transformed to the Lagrangian description. Actually, using Eq. (5.3.7) as input to the model is unlikely to cause significant error since, for the range of amplitudes, $\alpha \leq 0.03$, the difference between the two descriptions at the offshore boundary is small. However, a very simple expression for the solitary wave in the Lagrangian description can be obtained, so it will be used. As a first step in transforming to the Lagrangian description, let us use Eq. (3.1.63) of Section 3.1.2 for the special case $g_E = \eta_E(t - \hat{y}/c)$:

$$\eta(b,t) = \eta_E(t - \frac{b + \alpha\, y(b,t)}{c}) \tag{5.3.10}$$

where now $y$ without the hat refers to the position of a fluid particle relative to its initial position at $\hat{y} = b$. (We have assumed that $\eta_E$ is solely a function of $(t - \hat{y}/c)$, independent of $\hat{x}$. Equation (5.3.10) is the required expression for the surface displacement in the Lagrangian description except that the particle

position $y(b,t)$ is not known. The particle position $y(b,t)$ can be written in terms of the Eulerian velocity of the particle, $v_E(t - \hat{y}/c)$, using Eq. (3.1.61). In turn, the Eulerian velocity can be determined from the water surface elevation, $\eta_E$, for the special case of a permanent form wave. In that case the Eulerian fluid velocity is approximately (e.g., Svendsen 1974):

$$v_E(\hat{y},t) = \frac{c\,\eta_E(\hat{y},t)}{1 + \alpha\,\eta_E(\hat{y},t)} \quad . \tag{5.3.11}$$

If this expression for the Eulerian velocity is substituted into Eq. (3.1.61), then after an integration by parts the expression for the fluid particle displacement, $y(b,t)$, reduces to:

$$y(b,t) = \frac{c\int_0^t \eta_E(b,t')\,dt'}{1 + \alpha\,\eta_E(b,t)} \quad . \tag{5.3.12}$$

This equation is strikingly similar to Eq. (5.3.11). It must be remembered that both Eqs. (5.3.11) and (5.3.12) are valid only for permanent form waves. For the solitary wave of Eq. (5.3.7), Eq. (5.3.12) reduces to (for $b = 0$):

$$y(0,t) = \frac{c\,\tanh\chi\,t}{\chi\,(1 + \alpha\,\mathrm{sech}^2\,\chi\,t)} \quad . \tag{5.3.13}$$

(To generate a solitary wave with a vertical plate piston wave generator, one would move the plate according to Eq. (5.3.13).)

The Lagrangian form of the solitary wave can be obtained by substituting the particle displacement, $y(b,t)$, from Eq. (5.3.12) into Eq. (5.3.10) (with $\eta_E(\hat{y},t) = \eta_E(t - \hat{y}/c)$). Since we are interested only in obtaining an expression for the wave for a constant value of $b$ we can, without loss of generality, set $b = 0$. Then the result is:

$$\eta(t) = \eta_E\Big(t - \frac{\alpha\int_0^t \eta_E(t')\,dt'}{1 + \alpha\,\eta_E(t)}\Big) \quad . \tag{5.3.14}$$

For the solitary wave of Eq. (5.3.7), this expression for the Lagrangian surface displacement (for $b = 0$) becomes:

$$\eta(t) = \operatorname{sech}^2\Big(\chi\, t - \frac{\alpha \tanh \chi\, t}{1 + \alpha \operatorname{sech}^2 \chi\, t}\Big) \quad . \tag{5.3.15}$$

The equivalent Eulerian result for $\hat{y} = 0$ from Eq. (5.3.7) is:

$$\eta_{\mathrm{E}}(t) = \operatorname{sech}^2 \chi\, t \quad . \tag{5.3.16}$$

Equation (5.3.15) was used for input to the finite element model.

Since the characteristic length scale, $\ell$, was chosen to be one-half the width of the bay, independent of the incident solitary wave, the dispersion parameter, $\beta$, is also independent of the incident wave. Since the slope of the bottom at the centre of the bay was chosen to be $1/10$, the dispersion parameter is:

$$\beta = \Big[\frac{h_0}{\ell}\Big]^2 = \big[0.1(B + D)\big]^2 = 0.0162 \quad . \tag{5.3.17}$$

As mentioned previously, the nonlinear parameter, $\alpha$, was varied from 0.001 up to 0.03. This represents a factor of 30 in the difference between the largest and the smallest amplitudes of the solitary waves. Since the shape of the solitary wave in Eq. (5.3.15) depends on $\alpha$ through the parameter $\chi$, where $\chi$ is defined by Eq. (5.3.8), solitary waves of different amplitudes necessarily contain a different frequency content of Fourier wave numbers. Therefore, the solitary wave becomes more peaked as its amplitude increases, so the frequency content of the solitary wave shifts to higher frequencies as its amplitude increases. This is a very important point for interpreting the results of the eight test cases to be presented here. As the amplitude of the incident solitary wave is increased, nonlinear effects increase simply because of this increase in the incident wave height. In addition, as more energy gets placed into the higher wave numbers, frequency dispersion becomes more important; hence, shoaling in the sloping region near the shoreline

intensifies. This shoaling causes a further increase in wave height, thus enhancing the nonlinear effects and increasing the three-dimensionality of the wave field.

Figures 5.3.5–5.3.12 summarize the results for the eight cases: $\alpha = 0.001$, 0.0025, 0.005, 0.010, 0.015, 0.020, 0.025, 0.030. In each figure four plots are shown. Plot (a) shows the runup extrema in the $(\hat{x}, \hat{y})$ plane. It is the same as Fig. 5.3.3 except for the two long-dashed lines that mark the lines of maximum runup and the maximum rundown. Plot (b) is similar to plot (a). It also plots the maximum and minimum runup as a function of $\hat{x}$. However, in this case the shoreline has, in effect, been stretched out into a straight line and the values plotted correspond to the maximum and minimum runup measured *perpendicular* to the shore at a given value of $\hat{x}$. The runup has been normalized by the still water depth, $h_0$, of the constant depth region far offshore. Plot (d) is exactly the same as plot (b) except that the runup values are normalized with respect to the incident solitary wave height, $H$. Plot (c) shows the runup measured perpendicular to the shoreline as a function of time at the five locations shown in Fig. 5.3.3.

Clearly the results for the case $\alpha = 0.001$ shown in Fig. 5.3.5 are very different than for the case $\alpha = 0.030$ shown in Fig. 5.3.12. Since the amplitude of the wave is very small for the case $\alpha = 0.001$, nonlinear effects are negligible. The runup is very small, as can be seen in Figs. 5.3.5a and 5.3.5b. In Fig. 5.3.5a the runup cannot be be distinguished from the width of the line representing the still shoreline. In Fig. 5.3.5b the runup is negligible since it has been normalized by the still water depth. However, in 5.3.5d the runup has been normalized by the amplitude of the incident solitary wave. In this figure it can be seen that the maximum runup is almost uniform across the bay and equal to twice the amplitude of the incident wave. This is the expected result for a small amplitude long wave reflecting from a vertical wall. That is precisely the situation for the case $\alpha = 0.001$ since, from Eqs. (5.3.7) and (5.3.8), the characteristic length scale of a solitary wave

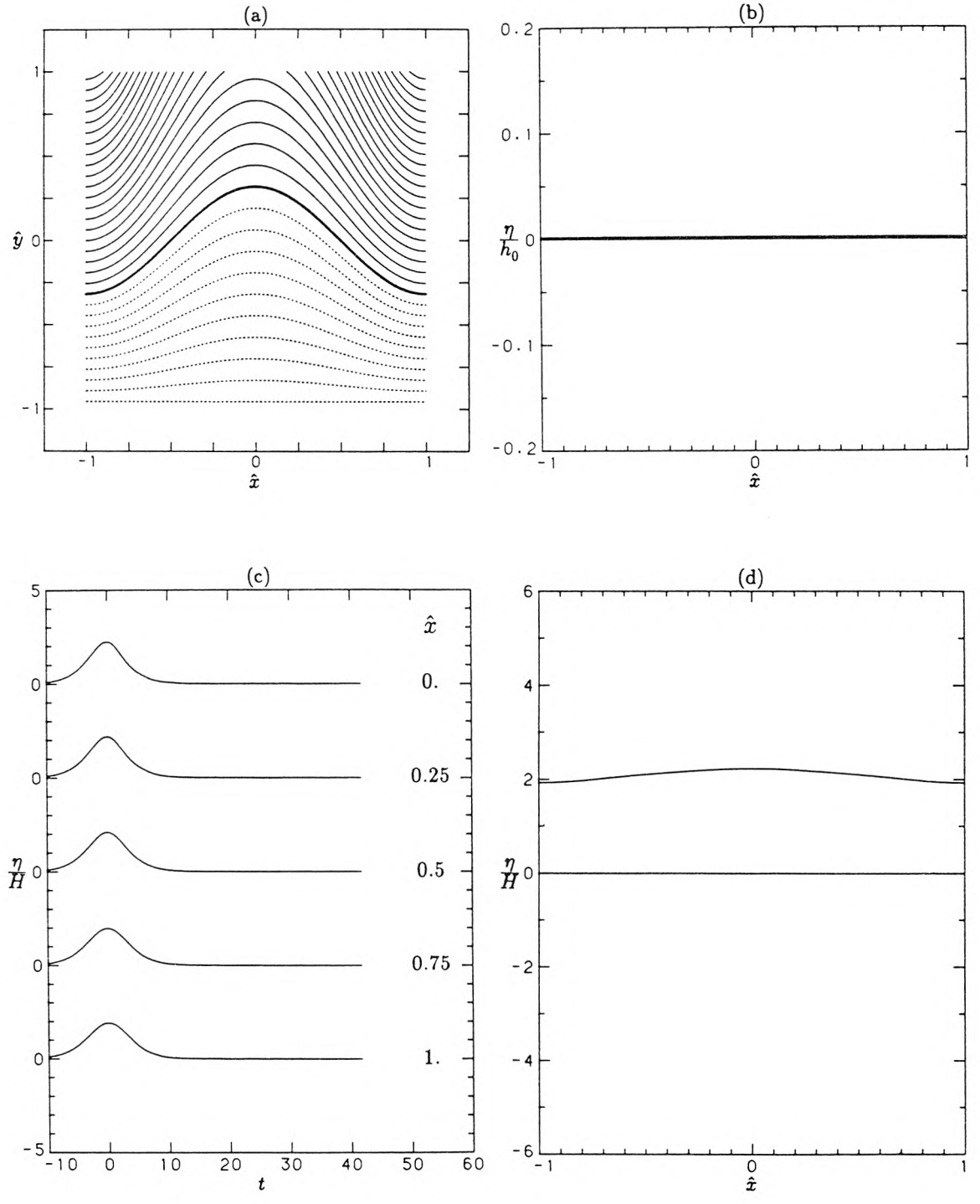


Fig. 5.3.5 $\alpha = 0.001$ (a) runup extrema in the $(\hat{x}, \hat{y})$ plane, (b) & (d) runup extrema perpendicular to the shoreline, (c) time records of runup perpendicular to the shoreline.

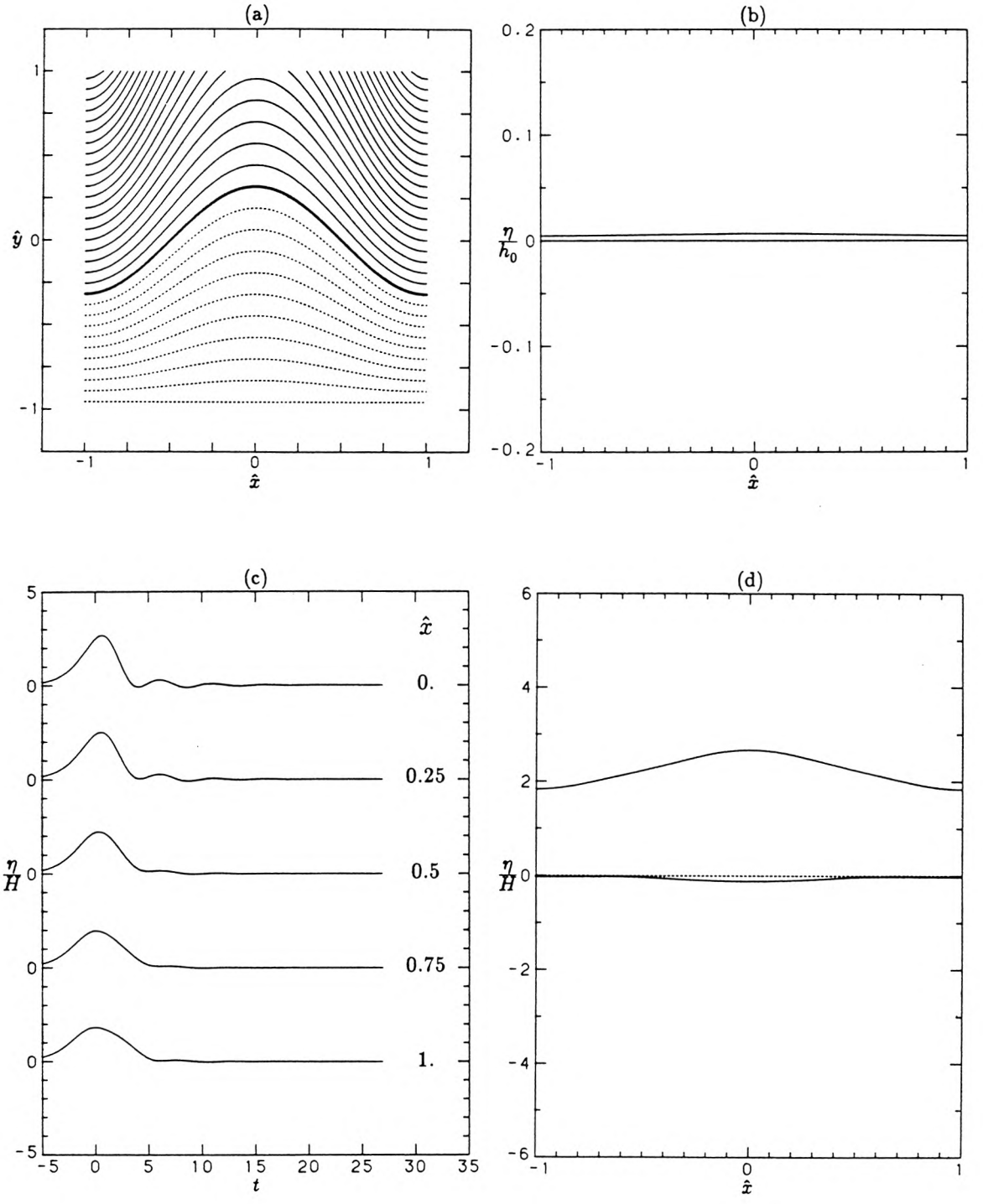


Fig. 5.3.6 $\alpha = 0.0025$ (a) runup extrema in the $(\hat{x}, \hat{y})$ plane, (b) & (d) runup extrema perpendicular to the shoreline, (c) time records of runup perpendicular to the shoreline.

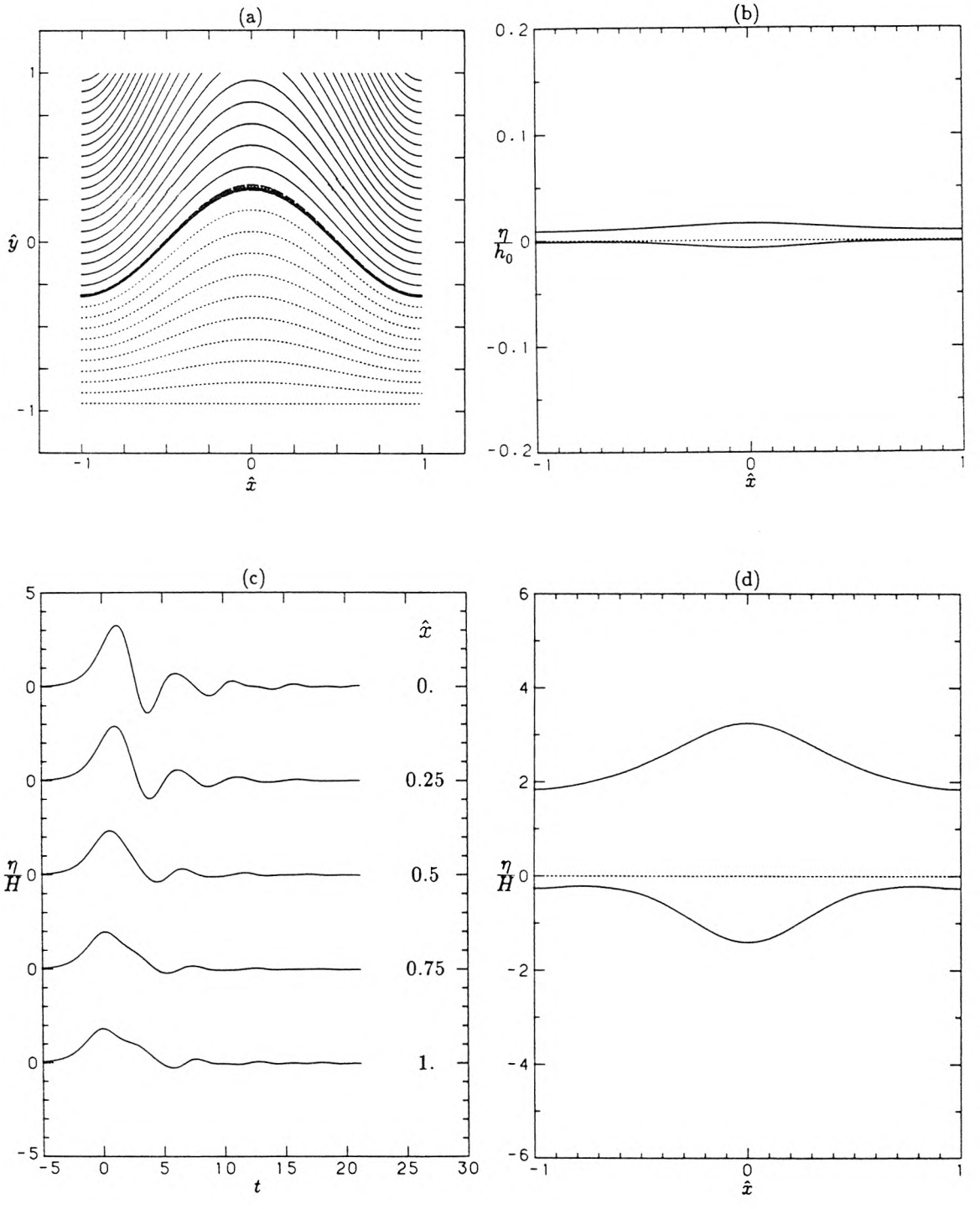


Fig. 5.3.7 $\alpha = 0.005$ (a) runup extrema in the $(\hat{x}, \hat{y})$ plane, (b) & (d) runup extrema perpendicular to the shoreline, (c) time records of runup perpendicular to the shoreline.

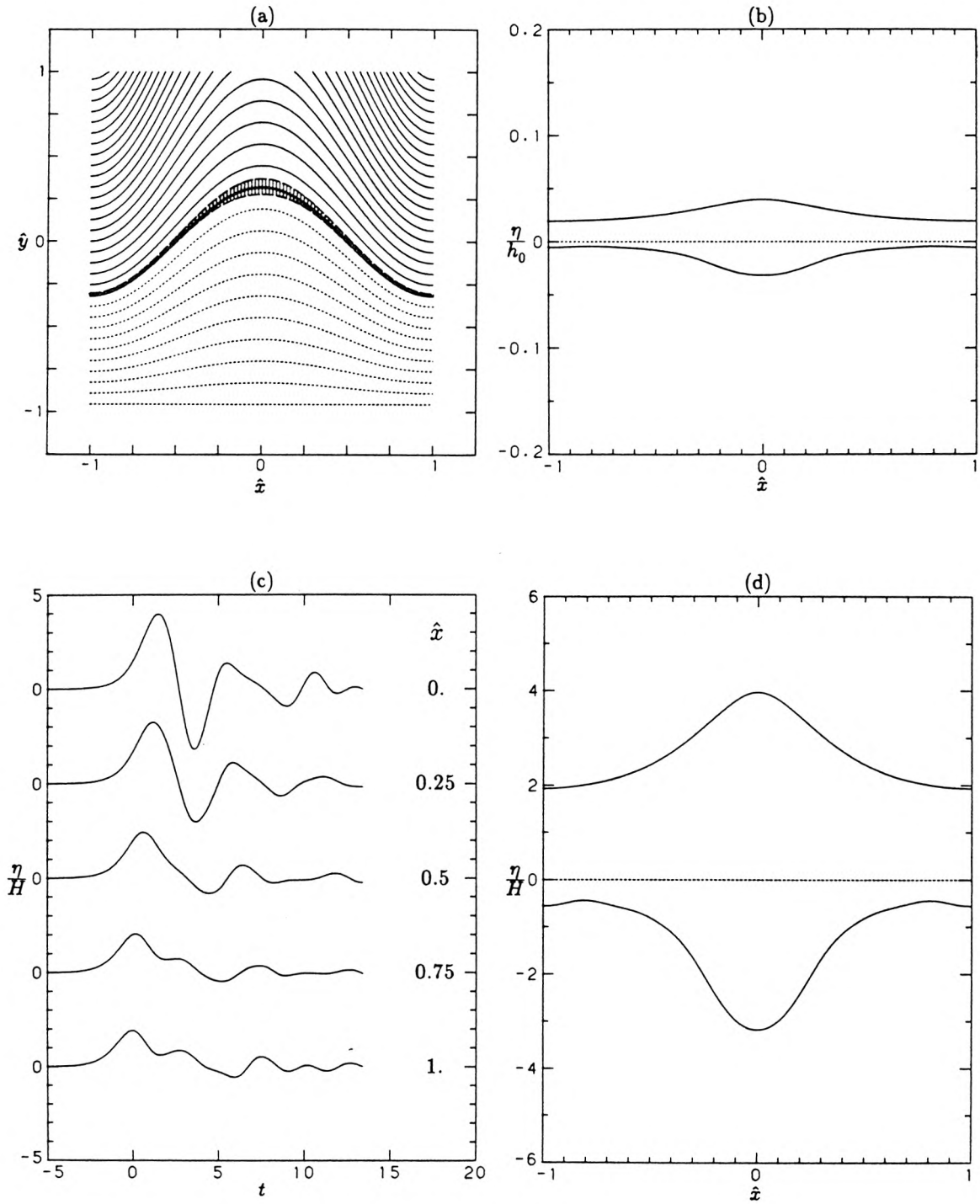


Fig. 5.3.8 $\alpha = 0.01$ (a) runup extrema in the $(\hat{x}, \hat{y})$ plane, (b) & (d) runup extrema perpendicular to the shoreline, (c) time records of runup perpendicular to the shoreline.

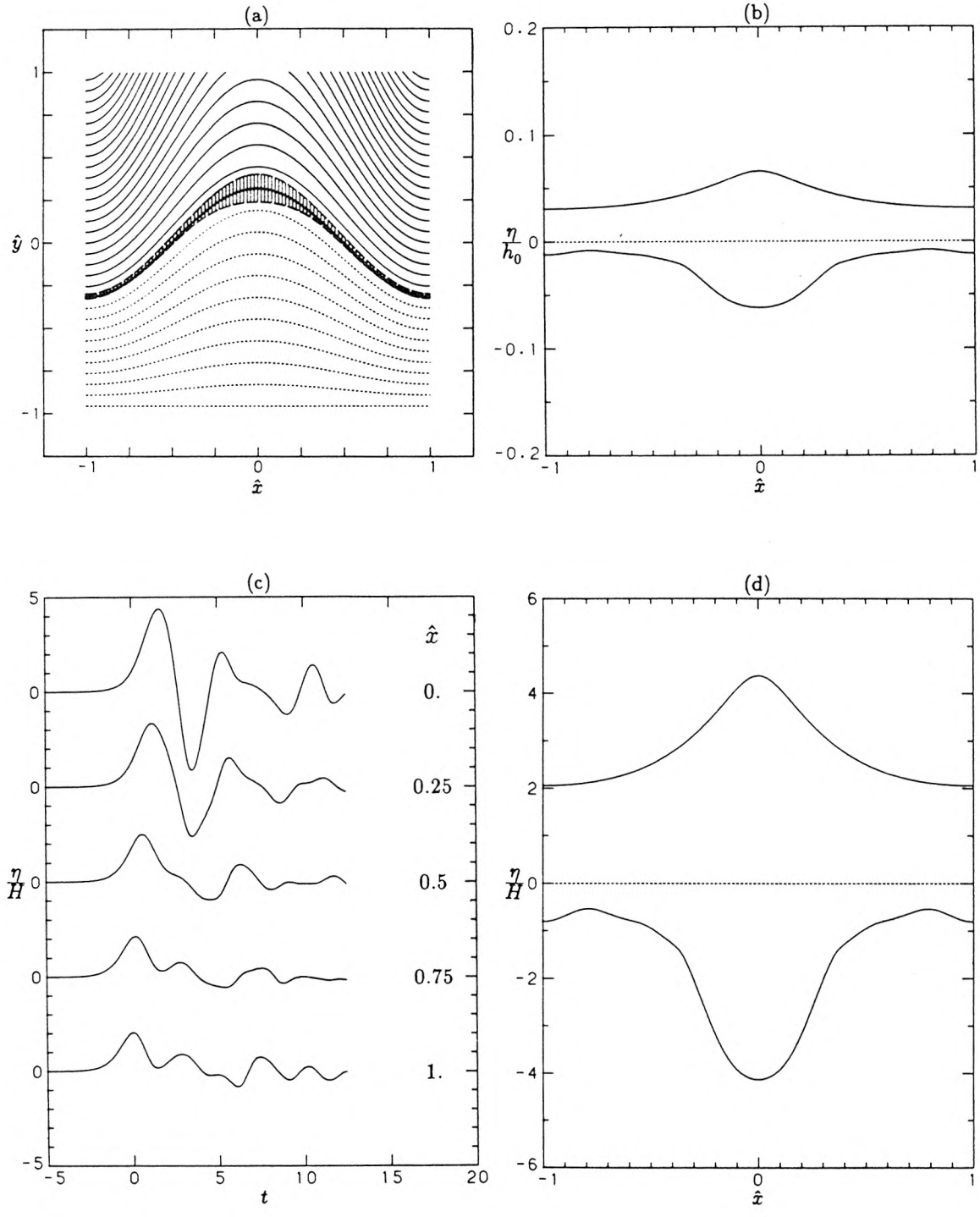


Fig. 5.3.9 $\alpha = 0.015$ (a) runup extrema in the $(\hat{x}, \hat{y})$ plane, (b) & (d) runup extrema perpendicular to the shoreline, (c) time records of runup perpendicular to the shoreline.

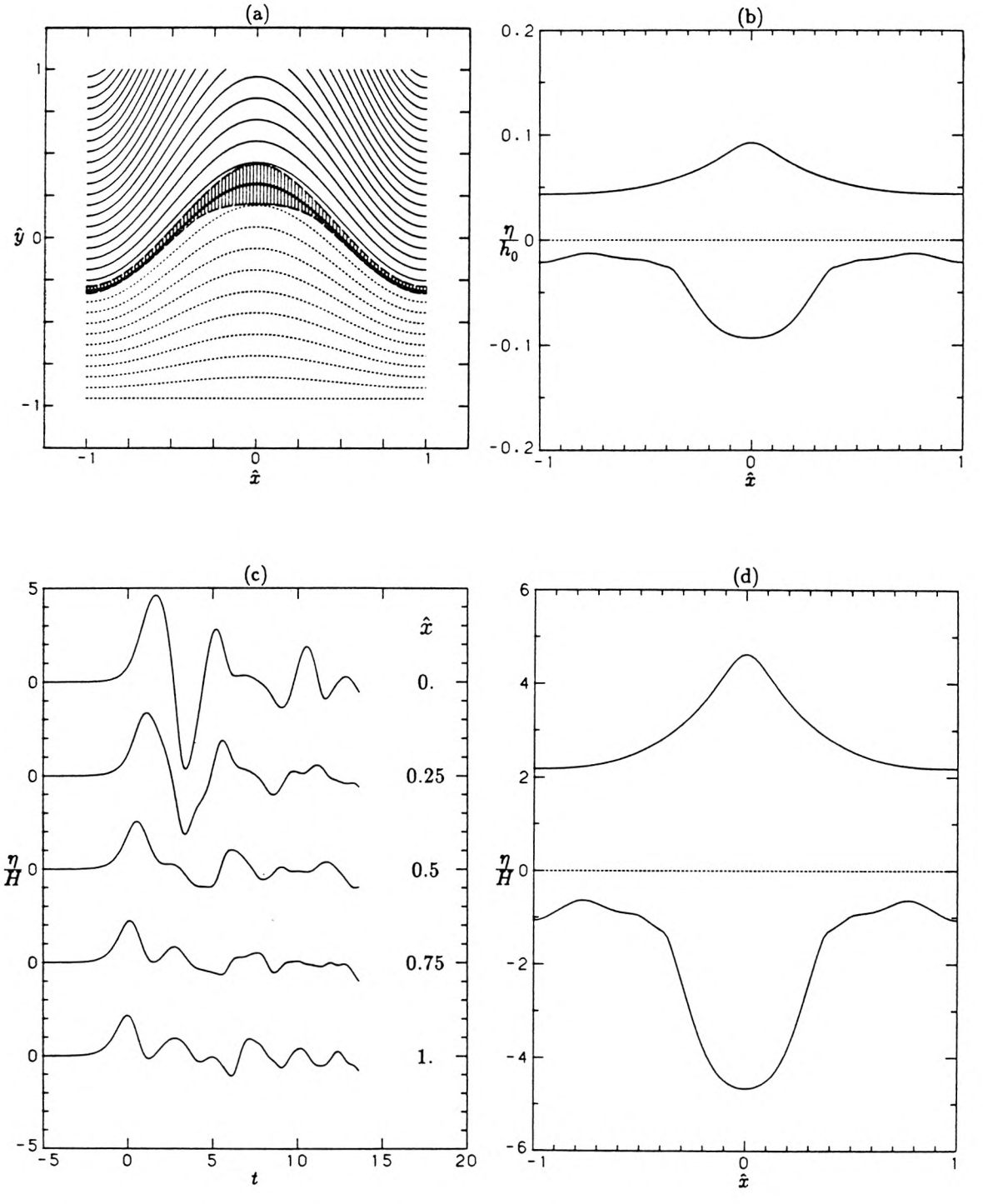


Fig. 5.3.10 $\alpha = 0.02$ (a) runup extrema in the $(\hat{x}, \hat{y})$ plane, (b) & (d) runup extrema perpendicular to the shoreline, (c) time records of runup perpendicular to the shoreline.

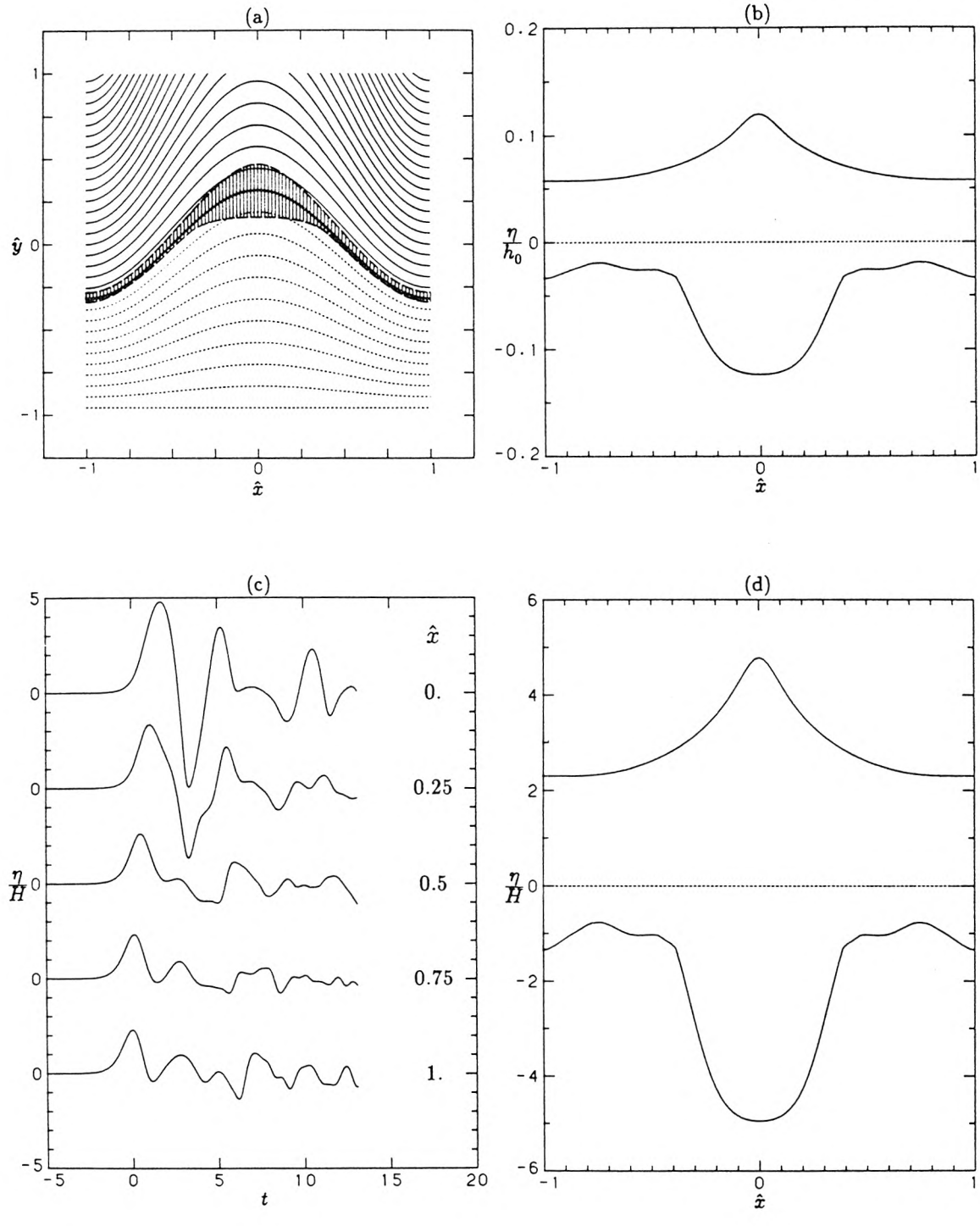


Fig. 5.3.11 $\alpha = 0.025$ (a) runup extrema in the $(\hat{x}, \hat{y})$ plane, (b) & (d) runup extrema perpendicular to the shoreline, (c) time records of runup perpendicular to the shoreline.

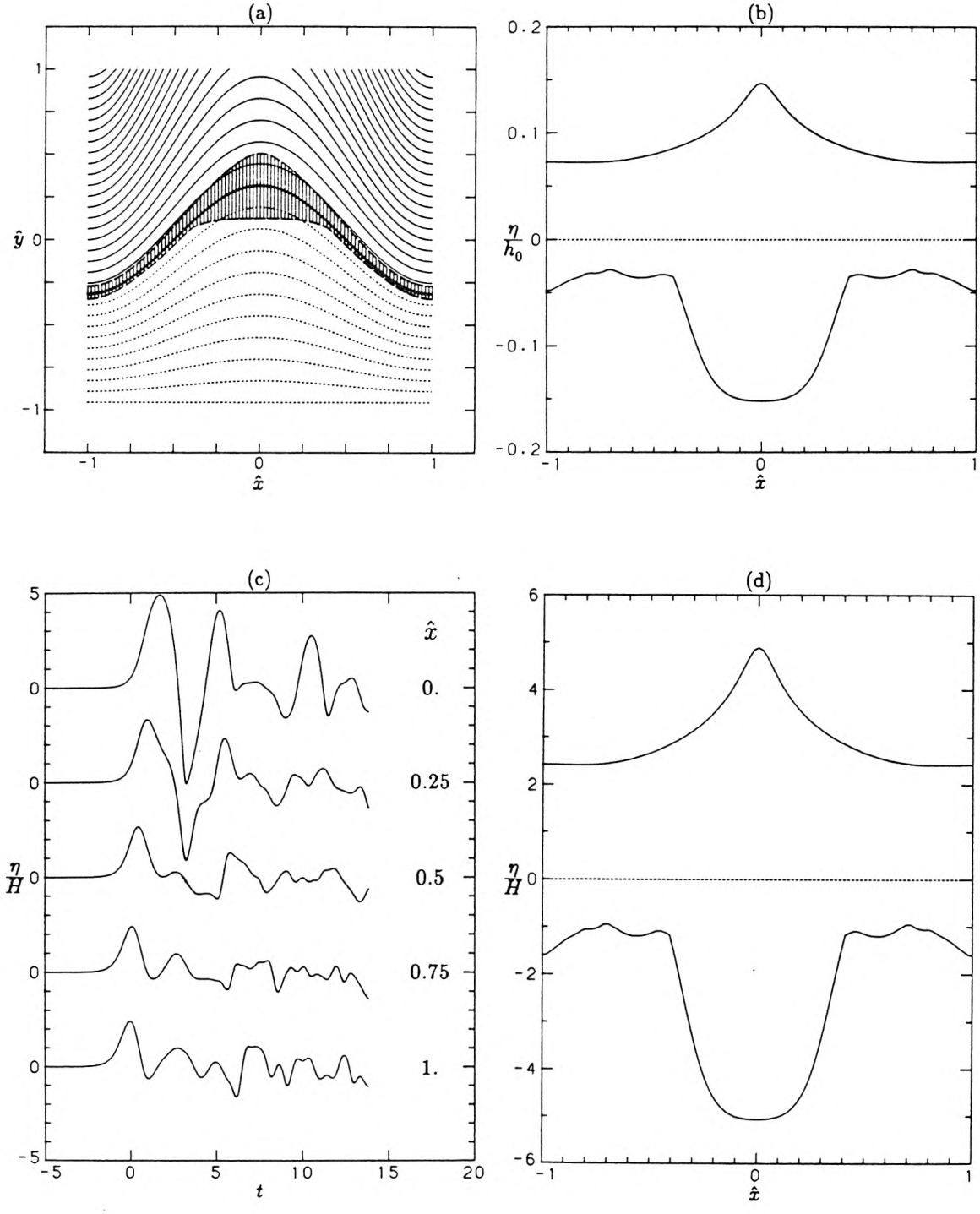


Fig. 5.3.12 $\alpha = 0.03$ (a) runup extrema in the $(\hat{x}, \hat{y})$ plane, (b) & (d) runup extrema perpendicular to the shoreline, (c) time records of runup perpendicular to the shoreline.

is proportional to $1/\sqrt{\alpha}$. Therefore, the solitary wave for the case $\alpha = 0.001$ is very long, much longer than the length of the nearshore sloping region. Hence, the coastline is essentially a vertical wall relative to the characteristic length scale of the incident wave. In Fig. 5.3.5d the runup is slightly larger at the centre of the bay ( $\hat{x} = 0$ ) than at the lateral boundaries $\hat{x} = \pm 1$. That is a small effect of the three-dimensional nature of the nearshore bathymetry; although the incident wave is much longer than the length of the sloping nearshore region, the converging bathymetry is able to reflect some of the wave energy towards the centre of the bay at $\hat{x} = 0$. The rundown is negligible across the entire bay. In Fig. 5.3.5c the runup at the five locations indicated in Fig. 5.3.3 is plotted as a function of time. At each location the runup is almost identical, although it is slightly greater at the centre of the bay ( $\hat{x} = 0$ ) for the reason just mentioned. This figure clearly shows that the bathymetry has very little influence on the wave runup for the case where the length scale of the wave is much greater than the length scale of the nearshore sloping region.

Figures 5.3.6–5.3.12 show the effects of increasing the amplitude of the incident solitary wave beyond $\alpha = 0.001$. The normalization of $\eta$ by the offshore still water depth, $h_0$, in part (b) of each of the figures gives a good representation of the *absolute* magnitude of the shoreline motion within the bay, whereas the normalization of $\eta$ by the incident wave height, $H$, in part (d) of each of the figures gives a good representation of the *relative* amplitude of the shoreline motion along the shore of the bay. Part (c) of each figure not only gives a good indication of the three-dimensionality of the runup within the bay but also includes phase information about the relative times of maximum or minimum runup between each of the locations along the shore of the bay.

In general, as $\alpha$ is increased, the effects mentioned for the case $\alpha = 0.001$ become more pronounced. The runup amplitudes increase and, in fact, the max-

imum rundown eventually exceeds the maximum runup in absolute value at the centre of the bay ( $\hat{x} = 0$ ). Three-dimensionality becomes very pronounced and the runup amplitude becomes very location sensitive. Runup is much greater at the centre of the bay due to reflections from the shores on either side which tend to channel the wave energy to the head of the bay. The maximum run*up* amplitude along the shore always occurs on the first advance of the shoreline, but the maximum run*down* amplitude does not necessarily occur on the first retreat of the shoreline, especially along the promontories away from the centre of the bay. Hence, the maximum run*down* amplitudes across the bay in parts (b) and (d) were not all achieved on the same oscillation of the shoreline. The first rundown of the shoreline at $\hat{x} = 0$ in part (c) of the figures is very large for the larger values of $\alpha$. This, in fact, was the reason why values of $\alpha$ larger than 0.03 are not considered here since for values of $\alpha$ somewhat larger than 0.03 numerical problems occurred at the time of maximum rundown at this location. The numerical problem was precisely the same as occurred in Section 5.1.1 when the parameter $A_0$ was increased beyond 1.1. The water surface approached the vertical at the rundown point in an attempt to become multivalued.

Perhaps the most important result evident for large values of $\alpha$ is the persistent ringing seen in part (c) of the figures long after the forcing from the incident wave has stopped. Such ringing is often associated with bays or harbours with narrow entrances that reflect some of the wave energy back into the basin due to a large jump in the wave impedance across the entrance. However, for the present case being considered here, the bay entrance is fully open. The ringing in this case is due to a coupling of the three-dimensional wave motion within the bay with that in the offshore sloping region, which partially traps the wave energy along the coast. One would not expect such a persistent ringing if the water depth was constant everywhere and the shoreline boundary were a vertical wall. Therefore,

the bathymetry itself, in addition to the shoreline geometry, has an important influence on the overall response of the bay to wave forcing.

If a harbour were situated at some point along the bay in Fig. 5.3.2, then the excitation applied at the mouth of this harbour would be much different than the incident solitary wave time record. Instead, the excitation would be similar to the time records shown in part (c) of Figs. 5.3.5–5.3.12. For the larger values of $\alpha$, the solitary wave loses its identity and the time records become oscillatory in nature; this will lead to an entirely different harbour response than that associated with the solitary wave excitation. The conclusion that the offshore topography can significantly influence the response of a bay is not new but has been expressed by several investigators in the past. However, very little work has been reported on numerical models which can examine this process quantitatively.

Munk (1962) examined tsunami records associated with different recording stations and concluded that the records were governed principally by the topography near the recording station, not by the character of the tsunami at its source. He concluded that some of the tsunami energy became distributed in partially trapped edge or shelf wave modes. Therefore, the wave spectrum in a harbour or bay situated along such a coast would be determined by the combination of two factors: (1) the spectrum of the wave field along the nearshore shelf and slope (predominantly a function of its topography) and (2) the bathymetry of the particular harbour or bay in question.

Olsen and Hwang (1971) examined the wave records of Keauhou Bay, Hawaii, and developed a numerical response model for the harbour. They reported good agreement with the measured wave records *except* for the lowest frequencies. For these low frequencies they concluded that shelf resonance and edge waves played a significant role in determining the bay response.

The coupling of harbours with the offshore topography was studied by Noiseux

(1983), who looked at the effect of depth variations near the mouths of idealized harbour-like geometries. He concluded that the offshore depth variations may be very important in determining the resonance characteristics of a bay or harbour, in addition to the planform geometry within the harbour.

The observations of these investigators are consistent with the results presented in this section. The finite element model developed in Section 3.4 of this work appears to be a very effective tool for investigating these very complicated processes.

As a final comment it should be noted that although the case treated in this section corresponds to a periodic coastline of bays coupled with a sloping offshore region, the results can be applied, at least qualitatively, to the case of a single bay situated on an infinitely long coast with a sloping offshore topography. The coupling of the bay with the offshore region and the spectral response of the offshore region to long wave excitation will be quantitatively different, but most of the discussion of the general processes associated with the periodic coastline is still applicable to the single bay case. The case of a single bay can be treated equally as easily with the finite element model except that a larger finite element mesh is required to represent the solution domain.

# CHAPTER 6

# Conclusions

The major objective of this investigation has been to study the influence of sloping boundaries on the response of bays and harbours to transient long wave excitation. Much of the analysis has been theoretical, with laboratory experiments conducted to compare with some of the theoretical developments. The major conclusions of this invesigation will be divided into three sections, each reflecting a different aspect of the study.

## 6.1 Harbour Response Theory

A theoretical harbour response model was developed, applicable to narrow harbours with fully open entrances, and applied to several harbours, each with a different geometry or bathymetry. The theory includes a rigorous treatment of the combined effects of both entrance width and entrance dissipation. The theory was used to validate the finite element numerical model and, in addition, a number of conclusions can be drawn:

1. In addition to the standard amplification factor, $R$, the modified (or reduced) amplification factor, $R'$, is a useful quantity to describe the response of a narrow harbour. The modified amplification factor removes the effects of geometric amplification and bathymetric shoaling from the standard amplification factor.

2. There are three regimes of the resonant harbour response that depend upon the relative sizes of the nondimensional amplitude of the incident wave, $|A_{\text{inc}}|$, and the nondimensional harbour entrance width, $\epsilon$:

   (i) For large amplitudes ( $|A_{\text{inc}}| > O(\epsilon^2)$ ), the response of the harbour at resonance is limited by entrance losses.

   (ii) For moderate amplitudes ( $|A_{\text{inc}}| = O(\epsilon^2)$ ), the response of the harbour at resonance is limited by both entrance dissipation and radiation of wave energy from the harbour mouth.

   (iii) For small amplitudes ( $|A_{\text{inc}}| < O(\epsilon^2)$ ), the response of the harbour at resonance is limited by radiation. For this case it was found that the harbour paradox still existed in that the amplification factor, $R$, grows arbitrarily large as the harbour entrance width is reduced to zero. However, the actual amplitude within the harbour remains small.

3. The harbour bathymetry and sidewall geometry have a strong influence on both the resonant frequencies and the harbour response at resonance. For a given harbour length and entrance width, the frequency of the first resonant mode was found to vary by nearly a factor of two, and the response of the first mode ranged by nearly a factor of three (entrance losses neglected) for the special geometries and bathymetries considered in this work.

4. In comparison with a constant depth rectangular harbour, the resonant frequencies are lower for a harbour with sloping bottom but are higher for a harbour with converging sidewalls. (If a harbour has both a sloping bottom and converging sidewalls, then it is not possible, in general, to arrive at a similar conclusion.)

## 6.2 Nonlinear Effects of Wave Runup

The nonlinear effects of the runup of nonbreaking periodic waves on a plane beach were investigated using the transformation of Carrier & Greenspan (1958). For most of the analysis the waves were assumed to be harmonic far offshore and frequency dispersion was neglected. Although the conclusions drawn from this analysis are strictly valid only under these assumptions, they are also probably applicable, at least qualitatively, to the general case of the runup of waves on many natural beaches.

1. At a fixed location near the shore, the minimum wave amplitude is larger in absolute value than the maximium wave amplitude; i.e., the troughs are larger than the crests. As a result, the mean wave height near the shore is negative and this effect decreases monotonically offshore. The fact that the crests are smaller than the troughs may have importance in the estimation of tsunami runup from nearshore tide stations.

2. Near the location where nodes are predicted by linear theory, the water surface time history exhibits twice as many oscillations as the incident wave, and precisely at the "nodal" location the surface elevation oscillates between zero and a negative value (which depends on the value of the parameter $A_0 = A_0\omega^2/\phi^2 g$).

3. The maximum fluid acceleration occurs at the shoreline at the point of maximum rundown of the wave.

4. Nonlinear effects do not alter the maximum and minimum runup amplitudes of nonbreaking periodic waves on a beach from the values predicted by linear theory. (This is true for arbitrary periodic waves, not only for waves that are harmonic far offshore.)

## 6.3 Finite Element Model

A finite element model was developed, based on a set of long wave equations in the Lagrangian description, which is capable of treating nonlinear and dispersive effects in regions of arbitrary geometry and bathymetry. In particular, the model can compute the runup of nonbreaking waves on a beach with an arbitrarily curved shoreline. Based on the results of this model, the following conclusions can be drawn:

1. Comparison with nonlinear Carrier-Greenspan (1958) solution was very good, indicating that the model can compute accurately the runup of nonbreaking waves on a beach.

2. Comparison with linear dispersive theory indicates that the model can accurately treat weakly dispersive effects resulting from vertical fluid accelerations.

3. An abrupt change in the boundary geometry at the mouth of a harbour can be responsible for enhanced radiation damping in a finite element model. This reduces the harbour response at resonance, and, therefore, it is important to resolve the geometry at the harbour entrance with as fine a mesh as is practical.

4. Three-dimensional simulations of the runup of solitary waves on a curved beach indicate that some of the wave energy can become partially trapped along the coast. Hence, the excitation of a harbour situated along such a coast is strongly dependent on the bathymetry of the sloping region and it may, in fact, bear little resemblance to the incident wave itself. In such situations it is essential to include in the analysis the sloping region exterior to the harbour.

### 6.3.1 Comparison with Laboratory Experiments

Laboratory experiments were performed to study the response of a rectangular harbour whose still water depth decreased linearly from the entrance to the shoreline. Based on comparisons between the results of these experiments and the finite element model, the following conlusions are evident:

1. Overall agreement between the experiments and the nonlinear, dispersive, dissipative finite element model was very good for both the transient and the steady-state response. The agreement was better than that between the experiments and the linear harbour response theory.

2. The water surface time histories, recorded along the centreline of the harbour midway between the entrance and the quiescent shoreline, were asymmetric, with larger troughs than crests. This nonlinear effect was most apparent near the first resonant mode where the harbour response was the greatest. As a result of this asymmetry, the mean water level, at the point of measurement, was negative. These features were reproduced accurately by the finite element model.

3. Entrance dissipation, due to flow separation, is still a difficult effect to model accurately. Although a quadratic head loss appears to be a useful approximation to model this dissipation mechanism for a narrow harbour entrance, the value of the entrance loss coefficient must still be determined by experiment. Future work to determine this coefficient numerically, without the need to perform laboratory experiments, would be of great benefit.

4. Although this investigation did not treat wave breaking, it is a process of great importance, and future work to incorporate this effect into three-dimensional runup models is warranted.

# REFERENCES


Abramowitz, M. & Stegun, I.A. 1972 *Handbook of Mathematical Functions.* Dover.

Behrendt, L., Jonsson, I.G. & Skovgaard, O. 1983 A Hybrid FEM-Model for Tsunami Amplification in Nearshore Regions. *Proceedings, 1983 Tsunami Symposium*, Hamburg, Germany. 265–273.

Bernard, E.N. & Vastano, A.C. 1977 Numerical Computation of Tsunami Response for Island Systems. *Journal of Physical Oceanography.* **7** No. 3, 389–395.

Carrier, G.F. & Greenspan H.P. 1958 Water Waves of Finite Amplitude on a Sloping Beach. *Journal of Fluid Mechanics.* **4**, 97–109.

Carrier, G.F. 1971 The Dynamics of Tsunamis. *Mathematical Problems in the Geophysical Sciences.* Proceedings of the Sixth Summer Seminar on Applied Mathematics, Rensselaer Polytechnic Institute, 1970. American Mathematical Society.

Chen, H.S. & Mei, C.C. 1974 *Oscillations and Wave Forces in an Offshore Harbor.* M.I.T. Ralph M. Parsons Laboratory for Water Resources and Hydrodynamics. Report #190.

Connor, J.J. & Brebbia, C.A. 1976 *Finite Element Techniques for Fluid Flow.* Butterworth & Co.

Cowper, G.R. 1973 Gaussian Quadrature Formulas for Triangles. *International Journal for Numerical Methods in Engineering.* **7** Issue No. 3, 405–408.

Dean, R.G. & Dalrymple, R.A. 1984 *Water Wave Mechanics for Engineers and Scientists.* Prentice-Hall.

Eagleson, P.S. & Dean, R.G. 1966 Small Amplitude Wave Theory. *Estuary and Coastline Hydrodynamics.* A.T. Ippen [editor]. McGraw-Hill.

Gopalakrishnan, T.C. & Tung, C.C. 1980 Run-up of Non-breaking Waves—A Finite-Element Approach. *Coastal Engineering.* Elsevier Scientific Pub. Co., Amsterdam. **4**, 3–22.

Gopalakrishnan, T.C. & Tung, C.C. 1983 Numerical Analysis of a Moving Boundary Problem in Coastal Hydrodynamics. *International Journal for Numerical Methods in Fluids.* **3** No. 2, 179–200.

Goring, D.G. 1978 *Tsunamis–The Propagation of Long Waves Onto a Shelf.* W.M. Keck Laboratory of Hydraulics and Water Resources, Report No. KH-R-38, California Institute of Technology, Pasadena, California.

Goto, C. 1979 Nonlinear Equation of Long Waves in the Lagrangian Description. *Coastal Engineering In Japan.* **22**, 1–9.

Goto, C. & Shuto, N. 1980 Run-up of Tsunamis by Linear and Nonlinear Theories. *Coastal Engineering.* Proceedings of the Seventeenth Coastal Engineering Conference, Sydney, Australia. ASCE. **1**, 695–707.

Gray, W.G. 1976 An Efficient Finite Element Scheme for Two-Dimensional Surface Water Computation. *Finite Elements in Water Resources.* Pentech. 4.33–4.49.

Gray, W.G. & Lynch D.R. 1977 Time-Stepping Schemes for Finite Element Tidal Model Computations. *Advances in Water Resources.* **1** No. 2, 83–95.

Greenspan, H.P. & Benney, D.J. 1973 *Calculus: An Introduction to Applied Mathematics.* McGraw-Hill.

Hebenstreit, G.T., Bernard, E.N. & Vastano, A.C. 1980 Application of Improved Numerical Techniques to the Tsunami Response of Island Systems. *Journal of Physical Oceanography.* **10** No. 7, 1134–1140.

Hebenstreit, G.T., Reid, R.O. 1980 *The Tsunami Response of the Hawaiian Islands.* Reference 80-2-T. Texas A&M University.

Heitner, K.L. 1969 *A Mathematical Model for Calculation of the Run-up of Tsunamis.* Ph.D. thesis. California Institute of Technology, Pasadena, California.

Heitner, K.L. 1970 *Additional Investigations on a Mathematical Model for Calculation of the Run-up of Tsunamis.* Earthquake Engineering Research Laboratory Report. California Institute of Technology, Pasadena, California.

Heitner, K.L. & Housner, G.W. 1970 Numerical Model for Tsunami Run-up. *Journal of the Waterways Harbors and Coastal Engineering Division.* ASCE. **96** WW3, 701–719.

Horikawa, K. & Nishimura, H. 1970 On the Function of Tsunami Breakwaters. *Coastal Engineering In Japan.* **13**, 103–112.

Houston, J.R. 1978 Interaction of Tsunamis with the Hawaiian Islands Calculated by a Finite-Element Numerical Model. *Journal of Physical Oceanography.* **8** No. 1, 93–102.

Houston, J.R. & Butler, H.L. 1979 *A Numerical Model for Tsunami Inundation.* Technical Report HL-79-2. Hydraulics Laboratory, U.S. Army Engineer Waterways Experiment Station, Vicksburg, Mississippi.

Houston, J.R. & Garcia, A.W. 1974 *Type 16 Flood Insurance Study: Tsunami Predictions for Pacific Coastal Communities.* Technical Report H-74-3. Hydraulics Laboratory, U.S. Army Engineer Waterways Experiment Station, Vicksburg, Mississippi.

Houston, J.R. & Garcia, A.W. 1978 *Type 16 Flood Insurance Study: Tsunami Predictions for the West Coast of the Continental United States.* Technical Report H-78-26. Hydraulics Laboratory, U.S. Army Engineer Waterways Experiment Station, Vicksburg, Mississippi.

Hwang, L.-S., Butler, H.L. & Divoky, D.J. 1972 Tsunami Model: Generation and Open-Sea Characteristics. *Bulletin of the Seismological Society of America.* **62** No. 6, 1579–1596.

Hwang, L.-S. & Lee, Y.K. [editors] 1979 *Tsunamis.* Proceedings of the National Science Foundation Workshop.

Hwang, L.-S. & Tuck, E.O. 1970 On the Oscillations of Harbours of Arbitrary Shape. *Journal of Fluid Mechanics.* **42**, 447–464.

Iida, K. & Iwasaki, T. [editors] 1983 *Tsunamis: Their Science and Engineering.* Proceedings of the International Tsunami Symposium 1981, IUGG Tsunami Commission, May, 1981, Sendai-Ofunato-Kamaishi, Japan. Terra Scientific.

Ippen, A.T. & Goda, Y. 1963 *Wave Induced Oscillations In Harbors: The Solution for a Rectangular Harbor Connected to the Open-Sea.* M.I.T. Hydrodynamics Laboratory. Report #59.

Ippen, A.T. & Raichlen, F. 1962 *Wave Induced Oscillations In Harbors: The Problem of Coupling of Highly Reflective Basins.* M.I.T. Hydrodynamics Laboratory. Report #49.

Ito, Y. 1970 On the Effect of Tsunami-Breakwater. *Coastal Engineering In Japan.* **13**, 89–102.

Iwagaki, Y. & Murakami, H. 1972 Harbor Oscillations Induced by Composite Waves in Rectangular Basins. *Bulletin of the Disaster Prevention Research Institute*, Kyoto University, Japan. **21** Part 4 No. 196, 265–277.

Jonsson, I.G. 1978 *A New Approach to Oscillatory Rough Turbulent Boundary Layers.* Series Paper 17. Institute of Hydrodynamics and Hydraulic Engineering. Technical University of Denmark.

Kato, N. & Hattori, M. 1980 Characteristics in the Pressure Caused by Nonbreaking Waves on a Sloping Surface. *Coastal Engineering In Japan.* **23**, 131–146.

Keller, J.B. & Keller, H.B. 1964 *Water Wave Run-up on a Beach.* Reseach Report for the Office of Naval Research, Department of the Navy. Service Bureau Corporation. New York, N.Y.

Keller, J.B. & Keller, H.B. 1965 *Water Wave Run-up on a Beach, II.* Reseach Report for the Office of Naval Research, Deptartment of the Navy. Service Bureau Corporation. New York, N.Y.

Keulegan, G.H. 1959 Energy Dissipation in Standing Waves in Rectangular Basins. *Journal of Fluid Mechanics.* **6**, 33–50.

Kolman, B. 1970 *Elementary Linear Algebra.* Macmillan.

Lamb, H. 1945 *Hyrodynamics.* Dover. 1932 ed.

Langsholt, M. 1981 *Experimental Study of Wave Run-up.* Thesis. University of Oslo.

Lee, J.J. 1969 *Wave Induced Oscillations in Harbors of Arbitrary Shape.* W.M. Keck Laboratory of Hydraulics and Water Resources, Report No. KH-R-20, California Institute of Technology, Pasadena, California.

Lee, J.J. 1971 Wave-Induced Oscillations in Harbours of Arbitrary Geometry. *Journal of Fluid Mechanics.* **45**, 375–394.

Leendertse, J.J. 1967 *Aspects of a Computational Model for Long-Period Water-Wave Propagation.* Memorandum RM-5294-PR. Rand Corporation, Santa Monica, California.

Lepelletier, T.G. 1980 *Tsunamis–Harbor Oscillations Induced by Nonlinear Transient Long Waves.* W.M. Keck Laboratory of Hydraulics and Water Resources, Report No. KH-R-41, California Institute of Technology, Pasadena, California.

Lighthill, J. 1978 *Waves in Fluids.* Cambridge University Press.

Lynch, D.R. & Gray W.G. 1978 Finite Element Simulation of Shallow Water Problems With Moving Boundaries. *Finite Elements in Water Resources.* Pentech. 2.23–2.42.

Lynch, D.R. & Gray W.G. 1979 A Wave Equation Model for Finite Element Tidal Computations. *Computers and Fluids.* **7** No. 3, 207–228.

Lynch, D.R. & Gray W.G. 1980 Finite Element Simulation of Flow in Deforming Regions. *Journal of Computational Physics.* **36**, 135–153.

Magnus, W., Oberhettinger F. & Soni R.P. 1966 *Formulas and Theorems for the Special Functions of Mathematical Physics.* Springer-Verlag.

Mei, C.C., Liu, P. & Ippen A.T. 1974 Quadratic Loss and Scattering of Long Waves. *Journal of the Waterways, Harbors and Coastal Engineering Division.* ASCE. **100** WW3 August, 217–237.

Miche, A. 1944 Mouvements Ondulatoires de la Mer en Profondeur Constante ou Décroissante. *Annales des Ponts et Chaussées.*

Miles, J.W. 1967 Surface-Wave Damping in Closed Basins. *Proc. Roy. Soc. London.* A **297**, 459–475.

Miles, J.W. 1974 Harbor Seiching. *Annual Review of Fluid Mechanics.* **6**, 17–35.

Miles, J. & Munk, W. 1961 Harbor Paradox. *Journal of the Waterways and Harbors Division.* ASCE. **87** WW3, 111–130.

Mungall, J.C.H. & Reid, R.O. 1978 *A Radiation Boundary Condition for Radially-Spreading Non-Dispersive Gravity Waves.* Technical Report Reference 78-2-T. Texas A&M University.

Munk, W.H. 1962 Long Ocean Waves. *The Sea.* Vol. 1, Interscience, M.N. Hill [editor], 647–663.

Murakami, H. & Noguchi, E. 1977 Effect of Entrance Loss on Wave-Induced Oscillations in Rectangular Harbors. *Coastal Engineering In Japan.* **20**, 27–42.

Murty, T.S. & Boilard, L. 1970 The Tsunami in Alberni Inlet Caused by the Alaska Earthquake of March 1964. *Tsunamis in the Pacific Ocean.* Proceedings of the International Symposium on Tsunamis and Tsunami Research, W.M. Adams [editor]. East-West Center Press, Honolulu, Hawaii. 165–187.

Murty, T.S. 1977 *Seismic Sea Waves Tsunamis.* Department of Fisheries and the Environment, Fisheries and Marine Service, Ottawa.

Noiseux, C.F. 1983 Resonance in Open Harbours. *Journal of Fluid Mechanics.* **126**, 219–235.

Nosenchuck, D.M. 1982 *Passive and Active Control of Boundary Layer Transition.* Graduate Aeronautical Laboratories California Institute of Technology. Pasadena, California.

Olsen, K. & Hwang, L.-S. 1971 Oscillations in a Bay of Arbitrary Shape and Variable Depth. *Journal of Geophysical Research.* **76** No. 21, 5048–5064.

Pedersen, G. & Gjevik, B. 1983 Run-up of Solitary Waves. *Journal of Fluid Mechanics.* **135**, 283–299.

Peregrine, D.H. 1967 Long Waves on a Beach. *Journal of Fluid Mechanics.* **27**, 815–827.

Pinder G.F. & Gray W.G. 1977 *Finite Element Simulation in Surface and Subsurface Hydrology.* Academic.

Raichlen, F. 1965 *Wave-Induced Oscillations of Small Moored Vessels.* W.M. Keck Laboratory of Hydraulics and Water Resources, Report No. KH-R-10, California Institute of Technology, Pasadena, California.

Raichlen, F. 1966 *Estuary and Coastline Hydrodynamics*, A.T. Ippen [editor]. McGraw-Hill.

Raichlen, F. 1976 *Coastal Wave Hydrodynamics–Theory and Engineering Applications.* W.M. Keck Laboratory of Hydraulics and Water Resources. Technical Memorandum 76-1. California Institute of Technology, Pasadena, California.

Raichlen, F., Lepelletier, T.G. & Tam, C.K. 1983 The Excitation of Harbors by Tsunamis. *Tsunamis: Their Science and Engineering*. K. Iida & T. Iwasaki [editors]. Terra Scientific. 359–385.

Reid, R.O. & Bodine, B.R. 1968 Numerical Model for Storm Surges in Galveston Bay. *Journal of the Waterways and Harbors Division*. ASCE. **94** WW1, 33–57.

Rogers, S.R. & Mei, C.C. 1978 Nonlinear Resonant Excitation of a Long and Narrow Bay. *Journal of Fluid Mechanics*. **88**, 161–180.

Shuto, N. 1967 Run-up of Long Waves on a Sloping Beach. *Coastal Engineering in Japan*. **10**, 23–38.

Shuto, N. 1968 Three Dimensional Behavior of Long Waves on a Sloping Beach. *Coastal Engineering in Japan*. **11**, 53–57.

Shuto, N. 1972 Standing Waves in Front of a Sloping Dike. *Coastal Engineering in Japan*. **15**, 13–23.

Shuto, N. & Goto, T. 1978 Numerical Simulation of Tsunami Run-up. *Coastal Engineering in Japan*. **21**, 13–20.

Soloviev, S.L. & Go, Ch.N. 1974 *A Catalog of Tsunamis on the Western Shore of the Pacific Ocean (173–1968)*. Nauka Publishing House, Moscow, USSR. Canadian Translation of Fisheries and Aquatic Sciences 5077, 1984.

Soloviev, S.L. & Go, Ch.N. 1975 *A Catalog of Tsunamis on the Eastern Shore of the Pacific Ocean (1513–1968)*. Nauka Publishing House, Moscow, USSR. Canadian Translation of Fisheries and Aquatic Sciences 5078, 1984.

Spielvogel, L.Q. 1975 Single-wave Run-up on Sloping Beaches. *Journal of Fluid Mechanics*. **74**, 685–694.

Stoker, J.J. 1957 *Water Waves*. Interscience.

Stokes, G.G. 1851 On the Effect of the Internal Friction of Fluids on the Motion of Pendulums. *Trans. Camb. Phil. Soc.* **9** part 2, 8–106.

Svendsen, I.A. 1974 *Cnoidal Waves Over a Gently Sloping Bottom*. Series Paper No. 6, Institute of Hydrodynamics and Hydraulic Engineering. Technical University of Denmark.

Tanaka, T., Ono, Y. & Ishise, T. 1980 The Open Boundary Value Problems in Ocean Dynamics by Finite Elements. *Finite Elements in Water Resources*. Pentech. 5.47–5.63.

Thomson, R.E. 1981 *Oceanography of the British Columbia Coast*. Canadian Special Publication of Fisheries and Aquatic Sciences 56.

Ünlüata, Ü. & Mei, C. 1975 Effects of Entrance Loss on Harbor Oscillations. *Journal of the Waterways Harbors and Coastal Engineering Division.* ASCE. **101** WW2 May, 161–180.

Ursell, F. 1953 The Long-Wave Paradox in the Theory of Gravity Waves. *Proc. Camb. Phil. Soc.* **49**, 685–694.

Van Dorn, W.G. 1965 Tsunamis. *Advances in Hydroscience.* **2**, 1–48.

Van Dorn, W.G. 1966 Boundary Dissipation of Oscillatory Waves, *Journal of Fluid Mechanics.* **24**, 769–779.

Wang J.D. & Connor J.J. 1975 *Mathematical Modelling of Near Coastal Circulation.* M.I.T. Ralph M. Parsons Laboratory for Water Resources and Hydrodynamics. Report #200.

Whitham, G.B. 1974 *Linear and Nonlinear Waves.* Wiley-Interscience.

Whitham, G.B. 1979 *Lectures on Wave Propagation.* Springer-Verlag.

Wiegel, R.L. 1964 *Oceanographical Engineering.* Prentice-Hall.

Wilson, B.W. 1972 Seiches. *Advances in Hydroscience.* **8**, 1–94.

Wu, T.Y. 1979 *Tsunamis.* Proceedings of the National Science Foundation Workshop. L.-S. Hwang & Y.K. Lee [editors].

Wu, T.Y. 1981 Long Waves in Ocean and Coastal Waters. *Journal of the Engineering Mechanics Division.* ASCE. **107** No. EM3, 501–522.

Xanthopoulos, T. & Koutitas, C. 1976 Numerical Simulation of a Two Dimensional Flood Wave Propagation Due to Dam Failure. *Journal of Hydraulic Research.* **14** No. 1, 321–331.

Yeh, G.-T., & Chou, F.-K. 1979 Moving Boundary Numerical Surge Model. *Journal of the Waterway Port Coastal and Ocean Division.* ASCE. **105** WW3, 247–263.

Yeh, G.-T., & Yeh, F.-F. 1976 Generalized Model for Storm Surges. *Coastal Engineering.* Proceedings of the Fifteenth Coastal Engineering Conference, Honolulu, Hawaii. ASCE. **1**, 921–940.

Zelt, J.A. 1986 *The Design and Operation of a Microcomputer Controlled Wave Generator.* W.M. Keck Laboratory of Hydraulics and Water Resources. Technical Memorandum. California Institute of Technology, Pasadena, California. To be published.

# LIST OF SYMBOLS

| | |
|---|---|
| $a$ | $a_1$ |
| $\mathbf{a}$ | the vector $(a, b)$ |
| $A_{\text{inc}}$ | amplitude of incident wave system |
| $\mathbf{A}$ | the vector $(a, b, c)$ |
| $a_i$ | the $i^{th}$ Cartesian coordinate of a fluid particle at time $t = 0$, $i = 1, 2, 3$ |
| $(\ )_a$ | differentiation with respect to the variable $a$; e.g., $x_a = \frac{\partial x}{\partial a}$ |
| $A_0$ | amplitude of periodic runup on a linearly sloping beach |
| $A_{jk}$ | cofactor of $\frac{\partial x_j}{\partial a_k}$ |
| $b$ | $a_2$ |
| $b(x)$ | half the breadth of a narrow harbour at the location $x$ |
| $(\ )_b$ | differentiation with respect to the variable $b$; e.g., $x_b = \frac{\partial x}{\partial b}$ |
| $c$ | $a_3$ or the phase speed of a wave |
| $c_g$ | group speed of a sinusoidal wave |
| $(\ )_c$ | differentiation with respect to the variable $c$; e.g., $x_c = \frac{\partial x}{\partial c}$ |
| $C$ | dissipation matrix in the finite element model, characteristic wave celerity, or surface contamination factor |
| $\mathcal{C}$ | constraint matrix in the finite element model |
| $\mathbf{d}$ | vector which contains the fluid particle dispacements at the node points |
| $\mathbf{D}$ | $\begin{pmatrix} y_b & -x_b \\ -y_a & x_a \end{pmatrix}$ |
| $\Delta E_{\text{bl}}$ | proportional energy density loss per period under a sinusoidal wave due to boundary layer dissipation |
| $\Delta E_{\text{int}}$ | proportional energy density loss per period under a sinusoidal wave due to internal dissipation |

| | |
|---|---|
| $(\ )_{\mathrm{E}}$ | refers to a variable in the Eulerian description, e.g., $\mathbf{U}_{\mathrm{E}}$ |
| $f$ | entrance loss coefficient |
| $\mathbf{f}$ | vector containing the forcing terms for the finite element matrix equation $M\mathbf{d} = \mathbf{f}$ to determine the nodal values of the fluid particle displacements |
| $F_i$ | exact expressions for the viscous terms in the Lagrangian description, $i = 1, 2, 3$ |
| $g$ | acceleration due to gravity |
| $g(\mathbf{A}, t)$ | arbitrary function in the Lagrangian description |
| $g_{\mathrm{E}}(\mathbf{X}, t)$ | arbitrary function in the Eulerian description |
| $h$ | still water depth |
| $H$ | characteristic wave height |
| $\mathcal{H}(\kappa, x)$ | harbour function for $\eta$ corresponding to the nondimensional frequency $\kappa$ |
| $H_0^{(1)}(\ )$ | Hankel function of the first kind of order zero $\equiv J_0(\ ) + iY_0(\ )$ |
| $H_0^{(2)}(\ )$ | Hankel function of the second kind of order zero $\equiv J_0(\ ) - iY_0(\ )$ |
| $\underline{\mathbf{H}}$ | $\begin{pmatrix} h_{aa} & h_{ab} \\ h_{ba} & h_{bb} \end{pmatrix}$ |
| $h_0$ | characteristic still water depth |
| $i$ | $\sqrt{-1}$ |
| $j_s$ | the $s^{\text{th}}$ zero of $J_0(z)$. $s = 1, 2, \ldots$ |
| $J$ | Jacobian $\frac{\partial(x,y,z)}{\partial(a,b,c)}$ |
| $J_n(\ )$ | Bessel function of the first kind of order $n$ |
| $k$ | wavenumber $\equiv \frac{2\pi}{\lambda}$ |
| $\ell$ | characteristic wavelength |
| $L$ | length of a rectangular harbour |
| $M$ | "mass" matrix in the finite element model |
| $M_{jk}$ | minor of $\frac{\partial x_j}{\partial a_k}$ |

| | |
|---|---|
| $\mathbf{n} = (n_a, n_b)$ | outward unit vector of a two-dimensional region |
| $\mathbf{n}_\theta$ | radial unit vector $(\cos\theta, \sin\theta)$ where $\theta$ is the polar angle |
| $N_i$ | finite element shape function corresponding to local node number $i$ |
| $p$ | In the Eulerian description this refers to the static pressure. In the Lagrangian description this refers to the deviation of the pressure from its intitial value. |
| $p_d$ | dynamic pressure |
| $P_\nu(\ )$ | Legendre function of the first kind of degree $\nu$ |
| $Q$ | orthogonal transformation matrix |
| $Q_\nu(\ )$ | Legendre function of the second kind of degree $\nu$ |
| $R$ | amplification factor of a harbour |
| $R'$ | alternate amplification factor of a harbour adjusted to account for the effect of shoaling and geometrical wave amplification, $R' \equiv R/S$ |
| $\Re\{\ \}$ | real part of a complex quantity |
| $\mathrm{Re}_\delta$ | Reynolds number based on the boundary layer thickness $\delta$ and the velocity immediately outside the boundary layer |
| $R_\mathrm{M}$ | Radius of the harbour mouth region |
| $R_\mathrm{O}$ | Radius of the outer region where the radiated wave is computed |
| $(\ )_\mathrm{res}$ | the value of the enclosed variable at resonance |
| $s$ | the ratio of the length of the sloping region in a harbour to its total length |
| $S$ | factor by which the amplitude of a wave will increase within a harbour due to the effects of shoaling and amplification caused by variable bathymetry and harbour sidewall geometry within the harbour. |
| $t$ | time |
| $(\ )_t$ | differentiation with respect to the variable $t$; e.g., $x_t = \frac{\partial x}{\partial t}$ |
| $T$ | wave period |
| $\mathbf{T}$ | horizontal viscous shear force along the bottom |

| | |
|---|---|
| $u$ | $u_1$ |
| $u_i$ | the $i^{th}$ component of velocity in the $i^{th}$ coordinate direction, $i = 1, 2, 3$ |
| $\mathcal{U}(\kappa, x)$ | harbour function for $u$ corresponding to the nondimensional frequency $\kappa$ |
| $\mathbf{u}$ | the vector $(u, v)$ |
| $\mathbf{u}_0$ | amplitude of horizontal velocity |
| $\mathbf{u}_{bl}$ | horizontal velocity within the boundary layer |
| $\mathbf{U}$ | the vector $(u, v, w)$ |
| $U_r$ | Ursell number $\equiv \frac{\alpha}{\beta} = \frac{H\ell^2}{h_0^3}$ |
| $v$ | $u_2$ |
| $w$ | $u_3$ |
| $W$ | energy dissipated per period due to laminar boundary layer dissipation |
| $\mathcal{W}[\ ]$ | approximate operator for the vertical component of vorticity |
| $x$ | $x_1$ |
| $\tilde{x}$ | Cartesian coordinate whose origin is at the harbour entrance |
| $x_i$ | In the Lagrangian description this refers to the $i^{th}$ component of displacement in the $i^{th}$ coordinate direction of a fluid particle from its initial position, $i = 1, 2, 3$.<br>In the Eulerian description this refers to the $i^{\text{th}}$ Cartesian coordinate. |
| $\mathrm{x}$ | the vector $(x, y)$ |
| $\mathrm{x}_{bl}$ | horizontal fluid particle displacement vector within the boundary layer |
| $\mathrm{x}'$ | approximate horizontal fluid particle displacement vector for particles at the free surface |
| $\bar{\mathrm{x}}$ | approximate "depth averaged" horizontal fluid particle displacement vector |
| $\mathrm{x}_E$ | the horizontal absolute coordinates of a fluid particle $\equiv \mathbf{x} + \alpha\mathbf{a}$ |
| $\mathbf{X}$ | the vector $(x, y, z)$ |

| | |
|---|---|
| $y$ | $x_2$ |
| $Y_n(\ )$ | Bessel function of the second kind of order $n$ |
| $z$ | $x_3$ |
| $\alpha$ | nonlinear parameter $\equiv \frac{H}{h_0}$ |
| $\beta$ | dispersion parameter $\equiv (\frac{h_0}{\ell})^2$ |
| $\gamma$ | dissipation parameter $\equiv \frac{\ell}{h_0}\sqrt{\frac{\omega\nu}{2gh_0}}$ or Euler's constant $= 0.57721\ldots$ |
| $\Gamma$ | the boundary of a plane two-dimensional region |
| $\Gamma(\ )$ | gamma function |
| $\Gamma_{HM}$ | the common boundary between the inner harbour region and the harbour mouth region |
| $\Gamma_{MO}$ | the common boundary between the harbour mouth region and the outer region |
| $\Gamma_O$ | the boundary of the outer region where the radiation boundary condition is applied |
| $\delta$ | boundary layer thickness |
| $\delta_{ij}$ | Kronecker $\delta$ symbol: $\delta_{ij} = 1$ if $i = j$, $\delta_{ij} = 0$ if $i \neq j$ |
| $\epsilon$ | one-half the ratio of the width of the entrance of a harbour to its length |
| $\varepsilon_{ijk}$ | permutation symbol: $\varepsilon_{123} = \varepsilon_{312} = \varepsilon_{231} = 1$, $\varepsilon_{213} = \varepsilon_{321} = \varepsilon_{132} = -1$, $\varepsilon_{ijk} = 0$ otherwise |
| $\zeta$ | approximate vertical displacement of the water surface above the mean water level which includes the first order effects of nonlinearity, dispersion, and viscous dissipation |
| $\eta$ | vertical displacement of the water surface above the mean water level |
| $\eta_{inc}$ | incident wave system |
| $\theta$ | angular coordinate in 2-D polar coordinates |
| $\vartheta$ | $\frac{2\sqrt{gh_0}}{\omega\ell}$ |

| | |
|---|---|
| $\kappa$ | nondimensional wavenumber or frequency of an incident wave system $\equiv kL$ |
| $\kappa'$ | deviation of $\kappa$ from $\kappa_i$ |
| $\kappa_i$ | zero order approximation to the $i^{\text{th}}$ nondimensional resonant frequency of a rectangular harbour |
| $\lambda$ | wavelength of a periodic wave |
| $\mu$ | absolute viscosity |
| $\nu$ | kinematic viscosity. It also refers to the order of a Legendre function, e.g., $P_\nu$ or $Q_\nu$. |
| $\pi$ | 3.14159... |
| $\rho$ | fluid density |
| $\phi$ | phase angle or beach slope |
| $\chi$ | $\sqrt{\frac{3\alpha}{4\beta}(1+\alpha)}$ |
| $\psi(\ )$ | psi or digamma function |
| $\omega$ | characteristic wave frequency |
| $\Omega$ | a plane two-dimensional region |
| $\Omega_{\text{H}}$ | the inner harbour region |
| $\Omega_{\text{M}}$ | the harbour mouth region |
| $\Omega_{\text{O}}$ | the outer region where the radiated wave is computed |

## SPECIAL SYMBOLS

| | |
|---|---|
| $\lvert\ \rvert$ | absolute value or modulus of enclosed number or vector |
| $\lvert\ \rvert$ | determinant of enclosed matrix |
| $(\ )^*$ | refers to a dimensional quantity, e.g., $x^*$ |
| $\hat{(\ )}$ | either refers to the absolute quantity of the fluid function as op- |

posed to its deviation from its initial value, e.g., $\hat{\mathbf{X}}$, or refers to a trial or test function used in the weighted residual finite element method.

$\nabla$ — Lagrangian gradient operator $\equiv (\frac{\partial}{\partial a}, \frac{\partial}{\partial b})$

${}_3\nabla$ — three-dimensional Lagrangian gradient operator $\equiv (\frac{\partial}{\partial a}, \frac{\partial}{\partial b}, \frac{\partial}{\partial c})$

$\nabla_E$ — Eulerian gradient operator $\equiv (\frac{\partial}{\partial x}, \frac{\partial}{\partial y})$

${}_3\nabla_E$ — three-dimensional Eulerian gradient operator $\equiv (\frac{\partial}{\partial x}, \frac{\partial}{\partial y}, \frac{\partial}{\partial z})$

$O(\quad)$ — order symbol

$\partial$ — used to denote the boundary of a two-dimensional region; e.g., the boundary of region $\Omega$ is $\partial\Omega$.

$\frac{\partial(\ ,\ )}{\partial(\ ,\ )}$ — two-dimensional Jacobian

$\frac{\partial(\ ,\ ,\ )}{\partial(\ ,\ ,\ )}$ — three-dimensional Jacobian

$\cup$ — set union

# APPENDIX A

## Simplified Derivation of the Nonlinear Long Wave Equations in the Lagrangian Description

The derivation of the long wave equations (3.1.119) and (3.1.118) in Section 3.1.3 was based on the assumptions $O(\alpha) = O(\beta) = O(\gamma) < O(1)$. The quantities $\alpha$, $\beta$, and $\gamma$ represent the relative importance of nonlinear effects, frequency dispersion effects, and viscous disipation, respectively. However, it is difficult to see where each of the terms in the equations comes from and what their physical significances are. In this appendix a simplified derivation of the nonlinear long wave equations will be given based on a set of more restricted assumptions. The advantage of this derivation is that it is based more on physical arguments that reveal the physical significance of each of the terms in the equations of motion.

The assumptions which will be made are that: (1) viscous effects are negligible, (2) the horizontal fluid particle displacements $x$ and $y$ are independent of the verical coordinate $c$, and (3) the pressure is hydrostatic. Assumption (1) allows one to neglect internal as well as boundary layer viscous dissipation. Assumptions (2) and (3) are both long wave assumptions which are so strong that they neglect all dispersive effects. Hence, the long wave equations that will be derived subject to these assumptions will not have dissipative or dispersive terms but *will* include nonlinear correction terms. These are the most important correction terms, since the Lagrangian description was chosen in order to model the nonlinear effects of long wave runup.

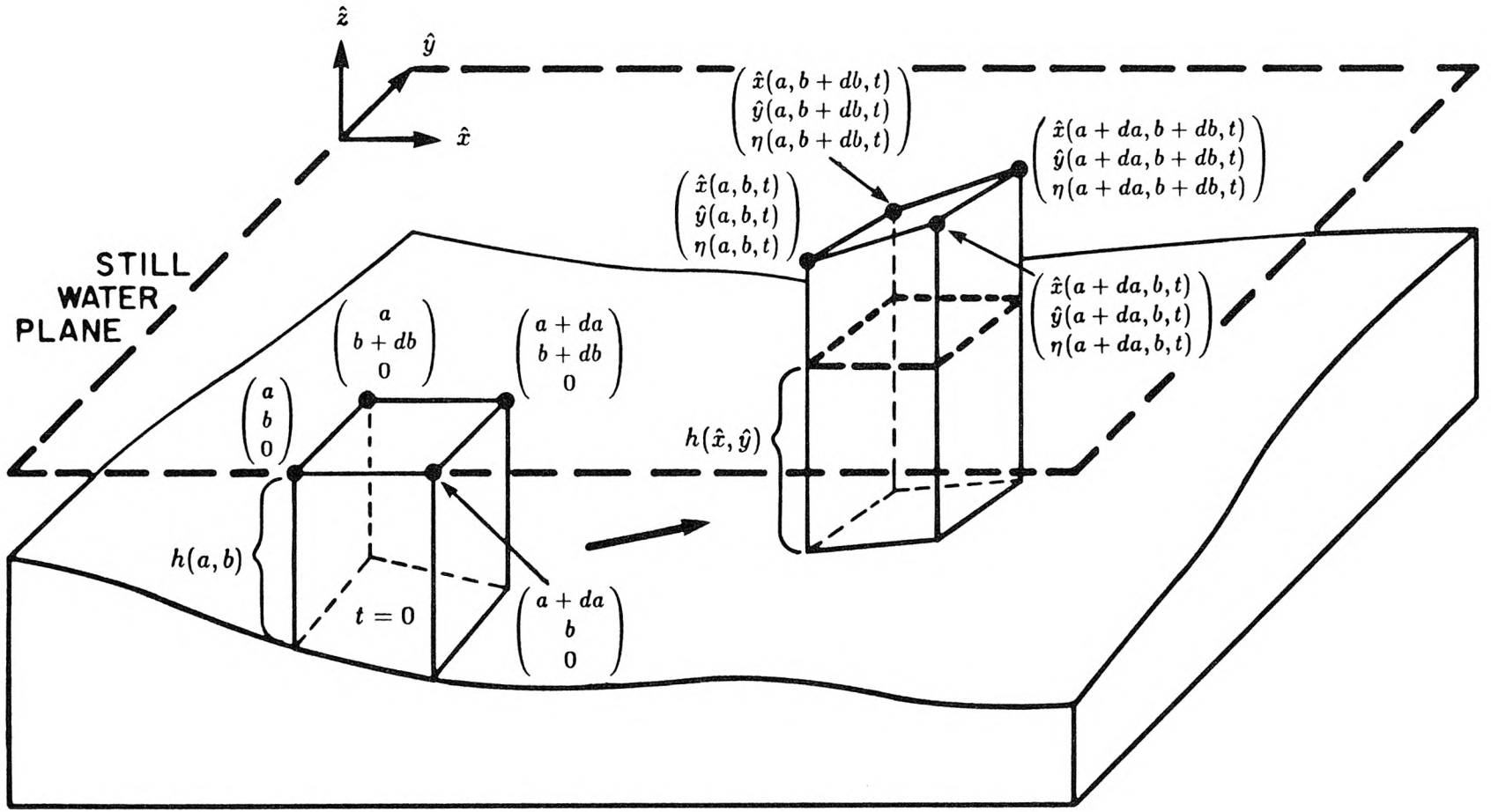


Fig. A.1 A material fluid element at the initial time, $t = 0$, and at an arbitrary time $t$ later.

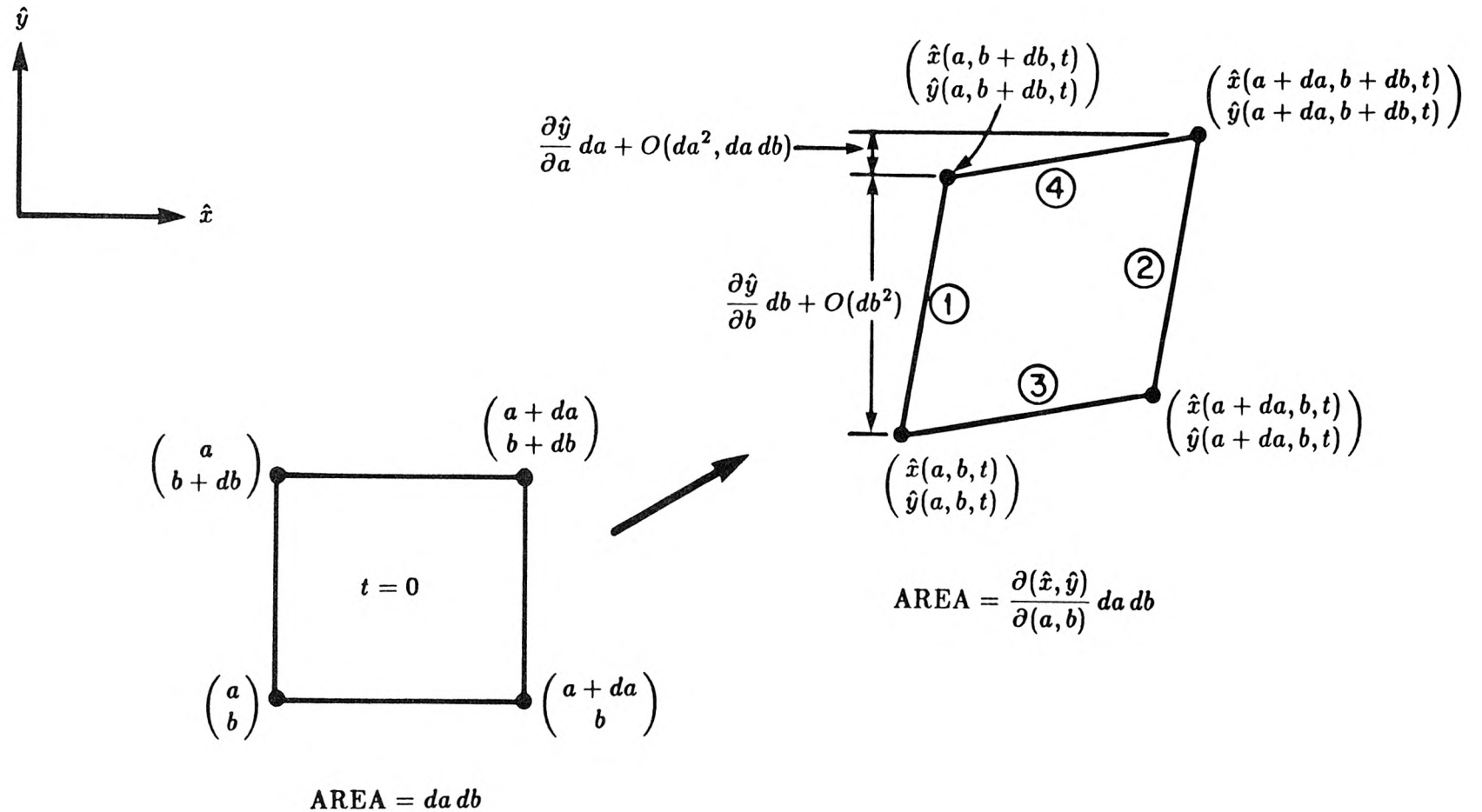


Fig. A.2 Projections of the material fluid element in Fig. A.1 onto the $(\hat{x}, \hat{y})$ plane.

Let us first derive the continuity equation. In Figure A.1 a vertical parallelepiped material element of fluid is shown at both the initial time, $t = 0$, and an arbitrary time $t$ later. At time $t = 0$ the fluid is quiescent and the top surface of the fluid element lies in the plane $\hat{z} = 0$. As before, the $\hat{}$ refers to the absolute quantity rather than to its deviation from its initial value; i.e.,

$$\hat{x} = a + x \qquad \hat{y} = b + y \tag{A.1}$$

so that:

$$\hat{x}(a,b,0) = a \qquad \hat{y}(a,b,0) = b \quad . \tag{A.2}$$

As before, we will *define* $\eta(a,b,t)$ as:

$$\eta(a,b,t) \equiv \hat{z}(a,b,0,t) \tag{A.3}$$

since the free surface corresponds to $c = 0$. At this point all quantities are dimensional. At the initial time, $t = 0$, one corner of the parallelepiped lies at $(a,b,0)$. At time $t$ later it has the coordinates $(\hat{x}(a,b,t), \hat{y}(a,b,t), \eta(a,b,t))$. Figure A.2 shows the projections of this element at these two times onto the $(\hat{x},\hat{y})$ plane. Since the element shown in Figures A.1 and A.2 is a material element and there are no sources or sinks of mass, we must have:

$$\rho h(a,b)\, da\, db = \rho\,[\eta + h(\hat{x},\hat{y})]\frac{\partial(\hat{x},\hat{y})}{\partial(a,b)}\, da\, db \quad ; \tag{A.4}$$

i.e.,

$$\eta(a,b) = \frac{h(a,b)}{\dfrac{\partial(\hat{x},\hat{y})}{\partial(a,b)}} - h(\hat{x},\hat{y}) \quad . \tag{A.5}$$

This is the continuity equation in terms of the dimensional variables $(\hat{x},\hat{y})$.

Now let us derive the momentum equations. Actually, we need only derive one component since the other component will follow directly from the first by

replacing $\hat{x}$ by $\hat{y}$ and $a$ by $b$. Therefore, we will derive only the $a$ component here. Conservation of momentum requires that:

$$\int_{V(t)} \rho \frac{\partial^2 \hat{x}}{\partial t^2}\, dV = -\int_{S(t)} p\, n_a\, ds \tag{A.6}$$

where $V(t)$ and $S(t)$ are the volume and surface area of the element, respectively. The left hand side of Eq. (A.6) is easy to evaluate:

$$\int_{V(t)} \rho \frac{\partial^2 \hat{x}}{\partial t^2}\, dV = \rho \frac{\partial^2 \hat{x}}{\partial t^2}[\eta + h(\hat{x},\hat{y})] \frac{\partial(\hat{x},\hat{y})}{\partial(a,b)}\, da\, db \quad . \tag{A.7}$$

Now let us evaluate the right hand side of Eq. (A.6). It involves computing the net force on the element at time $t$ due to pressure forces acting on the sides and bottom of the element. Since it was assumed the pressure was hydrostatic, we have:

$$p = \rho g(\eta - \hat{z}) \quad . \tag{A.8}$$

Hence, the $a$ component of the pressure force acting on side ① in Fig. A.2 is:

$$\begin{aligned} F_{①} &= \frac{\partial \hat{y}}{\partial b}\, db \int_{-h(\hat{x},\hat{y})}^{\eta} \rho g(\eta - \hat{z})\, d\hat{z} \\ &= \frac{1}{2} \rho g \frac{\partial \hat{y}}{\partial b} [\eta + h(\hat{x},\hat{y})]^2\, db \quad . \end{aligned} \tag{A.9}$$

Similarly, the $a$ component of the pressure force acting on side ④ is:

$$F_{④} = \frac{1}{2} \rho g \frac{\partial \hat{y}}{\partial a} [\eta + h(\hat{x},\hat{y})]^2\, da \quad . \tag{A.10}$$

The $a$ component of the pressure force acting on the bottom of the element is equal to the pressure at the bottom (from Eq. (A.8)) multiplied by the projected area in the $a$ direction. The projected area in the $a$ direction is equal to the cross-sectional area of the element multiplied by the bottom slope $\partial h(\hat{x},\hat{y})/\partial \hat{x}$:

$$\text{projected area} = \frac{\partial(\hat{x},\hat{y})}{\partial(a,b)} \frac{\partial}{\partial \hat{x}} h(\hat{x},\hat{y})\, da\, db \quad . \tag{A.11}$$

From the two-dimensional analog of Eq. (3.1.37) we get:

$$\frac{\partial}{\partial \hat{x}} h(\hat{x},\hat{y}) = \frac{\dfrac{\partial(h,\hat{y})}{\partial(a,b)}}{\dfrac{\partial(\hat{x},\hat{y})}{\partial(a,b)}} \quad . \tag{A.12}$$

Substituting this into Eq. (A.11) we get:

$$\text{projected area} = \frac{\partial(h,\hat{y})}{\partial(a,b)}\, da\, db \quad . \tag{A.13}$$

Hence, the $a$ component of the pressure force acting on the bottom of the element is:

$$F_B = \rho g[\eta + h(\hat{x},\hat{y})] \frac{\partial(h,\hat{y})}{\partial(a,b)}\, da\, db \quad . \tag{A.14}$$

Since from Eq. (A.8) the pressure is zero along the free surface, there is no component of the pressure force associated with that surface. From Eqs. (A.9), (A.10), and (A.14) we find that the total pressure force on the element is:

$$\begin{aligned} -\int_{S(t)} p n_a\, ds &= -\frac{\partial F_{①}}{\partial a}\, da + \frac{\partial F_{④}}{\partial b}\, db + F_B \\ &= \rho g[\eta + h(\hat{x},\hat{y})] \left\{ \frac{\partial \hat{y}}{\partial a}\frac{\partial \eta}{\partial b} - \frac{\partial \hat{y}}{\partial b}\frac{\partial \eta}{\partial a} \right\} \quad . \end{aligned} \tag{A.15}$$

Hence, if we substitute Eqs. (A.7) and (A.15) into Eq. (A.6) the $a$ component of the momentum equation is:

$$\frac{\partial^2 \hat{x}}{\partial t^2}\, \frac{\partial(\hat{x},\hat{y})}{\partial(a,b)} = g \frac{\partial(\hat{y},\eta)}{\partial(a,b)} \quad . \tag{A.16a}$$

Similarly, the $b$ component is:

$$\frac{\partial^2 \hat{y}}{\partial t^2}\, \frac{\partial(\hat{x},\hat{y})}{\partial(a,b)} = g \frac{\partial(\eta,\hat{x})}{\partial(a,b)} \quad . \tag{A.16b}$$

Equations (A.5) and (A.16) don't look like the long wave equations of Section 3.1.3 since they are written in terms of different variables. To show they are

indeed equivalent to $O(\alpha)$, let us first make the change of variables:

$$\hat{x} = a^* + x^* \qquad \hat{y} = b^* + y^* \quad . \tag{A.17}$$

Then let us nondimensionalize exactly as in Section 3.1.2:

$$\begin{aligned} a &= \frac{a^*}{\ell} & b &= \frac{b^*}{\ell} & t &= t^* \frac{\sqrt{gh_0}}{\ell} \\ x &= \frac{x^*}{\ell}\frac{h_0}{H} & y &= \frac{y^*}{\ell}\frac{h_0}{H} & h &= \frac{h^*}{h_0} \quad . \end{aligned} \tag{A.18}$$

Then the continuity equation (A.5) becomes:

$$\boxed{\eta = \frac{1}{\alpha}\left\{ \frac{h(a,b)}{1 + \alpha(x_a + y_b) + \alpha^2 \dfrac{\partial(x,y)}{\partial(a,b)}} - h(a + \alpha x, b + \alpha y) \right\}} \tag{A.19}$$

and the momentum equations (A.16) become:

$$\boxed{\begin{aligned} x_{tt}[1 + \alpha(x_a + y_b) + \alpha^2 \frac{\partial(x,y)}{\partial(a,b)}] + \alpha \frac{\partial(\eta,y)}{\partial(a,b)} + \eta_a &= 0 \\ y_{tt}[1 + \alpha(x_a + y_b) + \alpha^2 \frac{\partial(x,y)}{\partial(a,b)}] + \alpha \frac{\partial(x,\eta)}{\partial(a,b)} + \eta_b &= 0 \end{aligned}} \tag{A.20}$$

where $\alpha = H/h_0$. Equations (A.19) and (A.20) agree with equations (3.1.119) and (3.1.118), respectively, to $O(\alpha)$.

# APPENDIX B

## Harbour Geometry and Experimental Conditions

This Appendix contains the harbour geometry and experimental conditions used for the laboratory experiments discussed in Secion 5.2.

Table B.1

Harbour Geometry and Experimental Conditions.
$h_0 = 7.00\,\text{cm}, \quad T = 2\pi/\omega = 2\,\text{sec}.$

| $\frac{\omega L}{\sqrt{g h_0}}$ | $\frac{2b}{L}$ | $2b$ [cm] | $L$ [cm] |
|---|---|---|---|
| 0. | — | — | 0. |
| 0.698 | 0.223 | 4.1 | 18.4 |
| 0.759 | 0.205 | 4.1 | 20.0 |
| 0.823 | 0.189 | 4.1 | 21.7 |
| 0.888 | 0.222 | 5.2 | 23.4 |
| 0.948 | 0.204 | 5.1 | 25.0 |
| 1.013 | 0.191 | 5.1 | 26.7 |
| 1.073 | 0.219 | 6.2 | 28.3 |
| 1.138 | 0.207 | 6.2 | 30.0 |
| 1.206 | 0.195 | 6.2 | 31.8 |
| 1.259 | 0.217 | 7.2 | 33.2 |
| 1.312 | 0.208 | 7.2 | 34.6 |
| 1.396 | 0.196 | 7.2 | 36.8 |
| 1.445 | 0.215 | 8.2 | 38.1 |
| 1.517 | 0.205 | 8.2 | 40.0 |
| 1.567 | 0.199 | 8.2 | 41.3 |
| 1.620 | 0.218 | 9.3 | 42.7 |
| 1.688 | 0.209 | 9.3 | 44.5 |
| 1.745 | 0.202 | 9.3 | 46.0 |
| 1.897 | 0.208 | 10.4 | 50.0 |
| 2.082 | 0.206 | 11.3 | 54.9 |